The anomalous magnetic moment of the muon and the QED coupling at the Z-boson mass

Thesis submitted in accordance with the requirements of
the university of Liverpool for the degree of Doctor of Philosophy
in the subject of Theoretical Physics

by
Ruofan Liao

September 2011

Declaration

I hearby declare that the work presented in this thesis is the result of my own research activities unless reference is given to others. None of this material has been previously submitted to this or any other university. All work was carried out in the Theoretical Physics Division of the Department of Mathematical Sciences during the period from October 2007 to September 2011.

Contributions to this work have previously been published or are awaiting publication elsewhere in

- K. Hagiwara, R. Liao, A. D. Martin, D. Nomura and T. Teubner, *in preparation.*
- K. Hagiwara, R. Liao, A. D. Martin, D. Nomura and T. Teubner,"$(g-2)_\mu$ and $\alpha(M_Z^2)$ re-evaluated using new precise data," J. Phys. G **G38** (2011) 085003. [arXiv:1105.3149 [hep-ph]].
- K. Hagiwara, R. Liao, A. D. Martin, D. Nomura and T. Teubner, "Muon $g-2$ and $\Delta\alpha$ re-evaluated," *Prepared for the 11th International Workshop on Tau Lepton Physics (TAU 2010), Manchester, UK, 13–17 Sep 2010.* Nucl.Phys.Proc.Suppl. **218** (2011) 225.
- K. Hagiwara, R. Liao, A. D. Martin, D. Nomura and T. Teubner, "$(g-2)_\mu$ and $\Delta\alpha$: Recent developments and status report," *Prepared for the 9th International Conference on Quark Confinement and the Hadron Spectrum (QCHS9), Madrid, Spain, 30 Aug to 3 Sep 2010.* AIP Conf.Proc. **1343** (2011) 340
- K. Hagiwara, R. Liao, A. D. Martin, D. Nomura and T. Teubner, "Update of $g-2$ of the muon and $\Delta\alpha$," *Prepared for the 7th International Workshop on e+e-collisions from Phi to Psi (PhiPsi09), Beijing, China, 13–16 Oct 2009.* Chinese Phys. **C34** (2010) 728. [arXiv:1001.5401 [hep-ph]].

Abstract

In this thesis, we present our updated determinations for the leading order and higher order hadronic vacuum polarisation contributions to the anomalous magnetic moment of the muon ($a_\mu^{\text{had, LOVP}}$, $a_\mu^{\text{had, HOVP}}$), and for the hadronic contributions to the running of the QED coupling at the Z-boson mass ($\Delta\alpha^{(5)}_{\text{had}}(M_Z^2)$).

At present the Standard Model (SM) predictions of the anomalous magnetic moment of the muon a_μ^{SM} is lower than the experimental measurement a_μ^{exp} by about 3 standard deviations. The precision of a_μ^{SM} is limited by hadronic contributions, of which $a_\mu^{\text{had, LOVP}}$ has the largest uncertainty. Therefore improving the accuracy and precision of $a_\mu^{\text{had, LOVP}}$ will help to clarify the origin of the discrepancy between theory and experiment. The running of the QED coupling at the Z-boson mass $\alpha(M_Z^2)$ is the least precise of the three parameters that is usually taken to define the electroweak sector of the SM. Its precision is limited by $\Delta\alpha^{(5)}_{\text{had}}(M_Z^2)$, and is a significant limiting factor for precision electroweak physics, e.g. the indirect determination of Higgs boson mass.

We describe in detail our refined data-driven approach, which processes and combines a large number of e^+e^- hadronic annihilation data for use in our determinations. Error treatment is of course, also discussed in depth. We present a detailed breakdown of all the contributions to $a_\mu^{\text{had, LOVP}}$, including the many new, more precise data used along with discussions on their impacts. We also perform an improved sum rule analysis for a specific energy region, which assists us in discriminating between two different choices of using data. Comparisons with previous analyses as well as with another group's recent determination are also made.

For $\Delta\alpha^{(5)}_{\text{had}}(M_Z^2)$, we summarise the main results, discussing their effects as well as the comparison with other groups. More focus is given to a separate procedure used for preparing a set of new data that will improve the description of $\alpha(q^2)$.

We conclude the thesis by summing our $a_\mu^{\text{had, LOVP}}$, $a_\mu^{\text{had, HOVP}}$ results with the latest predictions of contributions from the other sectors of the SM, leading to our own value for a_μ^{SM}. This is then discussed and compared to other recent determinations. Results for $\Delta\alpha^{(5)}_{\text{had}}(M_Z^2)$ and $\alpha(M_Z^2)$ are also briefly reviewed. Finally, a summary of the whole thesis and future prospects in this area of study are given.

Contents

List of Figures

Acknowledgement

First and foremost I want to deeply thank my supervisor Thomas Teubner, who has been very patient, helpful and generous. Without his guidance and wisdom, I would not have been able to complete this PhD. The same goes for my other collaborators, Alan Martin, Karou Hagiwara, and in particular, Daisuke Nomura, who I had worked the closest with. I would also like to thank the Science and Technology Facilities Council in the UK for providing full funding for this research and the University of Liverpool for their support.

Second, I would like to express my sincerest gratitude for everyone at the Theoretical Physics division and the Mathematical Sciences department. Big thanks to the support staff such as Jean Settle, Ingrid Harper, Steve Downing and Dave Muskett for keeping everything running smoothly. Warm thanks to the lecturers/researchers for their help and creating a great work environment. Of course this extends to all of my friends at the department, who have made these last four years into an unforgettable experience. Special thanks to Gary, my fantastic office-sing-along-mate and unrivalled opponent in 5-a-side; Kyriakos, for his unique style of humour and advices; Stephen, for the many stimulating and helpful discussions on physics, computing etc. and being a good friend; Elisa, Ben, Cathy, Rob, Kirk, Adriano and Owen for the numerous fun times we shared; Viraf, Will and Paul for their amazing and hilarious banters; Chris, for the many PC vs Xbox 'debates'; Warren, my fellow Trekkie; and finally Jackie, it was a pleasure to have briefly shared an office with you. In addition, I would like to thank Hiro and Andrea, two post-docs previously at Liverpool for their assistance and friendship.

Third, I would like to thank from the depth of my heart, my wonderful girlfriend Jennifer. Her love, care and encouragement kept me motivated, and helped me through a very difficult period when my ankle was seriously injured. More than that, the time we spent together are the happiest in my life.

Last but definitely not the least, I would like to thank my family, particularly my Mum, her boyfriend and my Dad. I am forever grateful for the sacrifices they have made, their time dedicated to me and their financial and moral support. This is for you...

Chapter 1

Introduction

1.1 Background

The anomalous magnetic moment and its measurement, especially that of the electron and muon, has played an important role in constructing a relativistic quantum field theory (RQFT), which is the theoretical framework for modern particle physics. In particular, for quantum electrodynamics (QED), the famous 1-loop contribution to the anomalous magnetic moment computed by Schwinger in 1948 [1]

$$a_l^{\mathrm{QED},\,1l} = \frac{1}{2}\frac{\alpha}{\pi}, \quad (l = e,\, \mu,\, \tau), \tag{1.1}$$

was one of the first QED predictions at higher order; and the precise determination of the magnetic moment of the electron from Kusch and Foley [2], was one of the very first tests of quantum corrections predicted by a RQFT. QED eventually developed into the Standard Model (SM) of particle physics, incorporating electromagnetic, weak and strong interactions. Since its inception in the 1970s, the SM has withstood the rigours of nearly all the experimental tests and remains as the best theory for the description of nature at the microscopic scale.

In quantum mechanics, a charged elementary particle has an intrinsic magnetic moment $\vec{\mu}$ due to its spin $\vec{s}$. The relation is given by[1]

$$\vec{\mu} = g\frac{e}{2m}\vec{s}, \tag{1.2}$$

where g is the gyromagnetic factor, e is the electric charge and m is the mass of the particle. The first observation for the magnetic moment of the electron came from the Stern-Gerlach experiment [3] in 1922, which led to the postulate that an electron has spin 1/2 from Goudsmit and Uhlenbeck [4]. Then in 1928, Dirac's relativistic theory of the electron [5] predicted that $g = 2$ for spin-1/2 particles. This can be seen by taking the non-relativistic limit of the Dirac equation with an electromagnetic field A_μ, which results in the Hamiltonian [6],

$$H = \left[\frac{1}{2m}\left(\vec{p} - e\vec{A}\right)^2 - \frac{e}{2m}\vec{\sigma}\cdot\vec{B} + eA^0\right], \tag{1.3}$$

[1] Unless stated otherwise, we adopt natural units where $c = \hbar = 1$.

where $\vec{B} = \vec{\nabla} \times \vec{A}$ and $|eA^0| \ll m$. Now the potential energy of a magnetic moment in an external magnetic field is $U = -\vec{\mu} \cdot \vec{B}$ and for a spin-1/2 particle $\vec{s} = \vec{\sigma}/2$. Hence, comparing U with the interaction term in the Hamiltonian

$$-\frac{e}{2m}\vec{\sigma} \cdot \vec{B}, \tag{1.4}$$

and recalling $\vec{\mu}$ is given by (1.2), finally gives $g = 2$. However, with the development of QED and then later the SM, it is understood that effects such as radiative corrections (see e.g. Fig. 1.1) make g differ slightly from 2. This difference is quantified by a

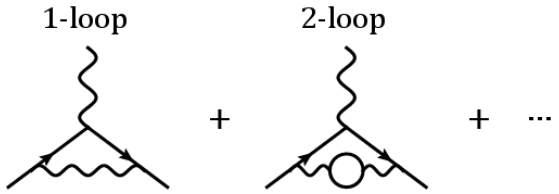

Fig. 1.1: Some higher order Feynman diagrams that contribute to the deviation of $g = 2$.

dimensionless number,

$$a_l = \frac{g_l - 2}{2}, \quad (l = e,\, \mu,\, \tau) \tag{1.5}$$

which is known as the anomalous magnetic moment.

Berestetskii *et al.* [7] in 1956 made the observation that contribution to a_l from new physics at high energy scales or heavy particles is proportional to

$$\delta a_l \sim \left(\frac{m_l}{M}\right)^2, \quad (M \gg m_l) \tag{1.6}$$

Since the muon is about 200 times more massive than the electron, a_μ is then more sensitive to such effects than a_e by a factor of $(m_\mu/m_e)^2 \sim 40\,000$. Thus the anomalous magnetic moment of the muon became a quantity of great interest for testing, at first QED, and then later on the SM. For both a_e and a_μ, the continued searches for their deviations from theory and speculations about their contributions due to new physics, has been and still is a motivation for better and more precise experiments. Indeed, with a precision of 0.24 parts per *billion* [8], a_e is one of the most precisely measured quantities in physics. This is also one of the biggest triumphs of QED and the SM, since the theoretical prediction [9] is still in good agreement with this measurement. For a_μ, experiments have achieved a combined precision of 0.54 parts per million [10], which is still very formidable and only matched by theory recently. At this level of precision, the theoretical prediction need to account for contributions from all the sectors of the SM (i.e. QED, electroweak, and hadronic) in order to be meaningful. These contributions are reviewed in Sections 1.3 to 1.5 but first, a brief discussion on the experimental measurement of a_μ is given.

1.2 Experimental measurements of a_μ

We give a brief overview on the experimental measurement of a_μ. The basic principle behind the measurement exploits the fact that a_μ is responsible for the spin precession of polarised muons travelling in a circular orbit with a constant magnetic field, as shown in Fig. 1.2. Specifically, the angle between the muon's spin and momentum oscillates

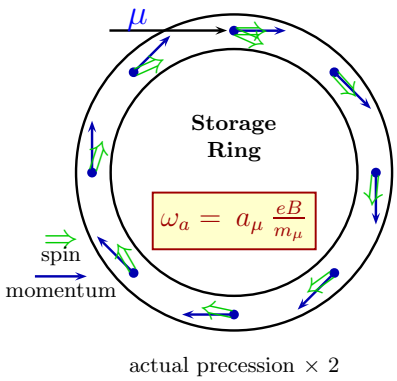

Fig. 1.2: Spin precession of the muon in a magnetic storage ring. The graphics is taken from [11].

with the angular frequency

$$\vec{\omega}_a = a_\mu \frac{e}{m_\mu} \vec{B}, \tag{1.7}$$

which allows a direct measurement of a_μ. To realise this however, one must: 1) have knowledge of the initial direction of the muon spin; 2) allow sufficiently many precession cycles to occur before the muon decays; 3) have knowledge of the final direction of the muon spin; 4) have a precise determination of the magnetic field. The past experiments at the European Organisation for Nuclear Research (CERN) from around 1960 to 1980 [12–15] and more recently at Brookhaven National Laboratory (BNL) around 2000 [16–20], are all based on this idea. For example at BNL, a proton beam is fired towards a target creating pions, which then decays to muons and then injected into a magnetic storage ring. Due to parity violation of the weak interaction, these muons are polarised, meaning the direction of their spin and momentum are identical. In order to keep the muons focused in the plane transverse to the magnetic field, a quadrupole electric field $\vec{E}$ must be applied. However, this means the precession frequency is now [21, 22]

$$\vec{\omega} = \frac{e}{m_\mu} \left[a_\mu \vec{B} - \left(a_\mu - \frac{1}{\gamma^2 - 1} \right) \vec{v} \times \vec{E} \right], \tag{1.8}$$

where $\gamma = 1/\sqrt{1 - v^2}$ is the Lorentz factor and $\vec{v}$ is the muon velocity. This dependence on $\vec{E}$ is undesirable as precise knowledge of the electric field is then also required in order to extract a_μ. Fortunately, one can choose γ such that $a_\mu - 1/(\gamma^2 - 1) = 0$, by tuning

the energy of the muon. This corresponds to $\gamma = \sqrt{1 + 1/a_\mu} \simeq 29.3$ giving $E_{\text{magic}} = \gamma m_\mu \simeq 3.1$ GeV, which is known as the 'magic' energy. The added benefit of having such a high γ value is the large time dilation effect on the muon. At rest, muon has a lifetime of around $2\mu s$, but in this case, the lifetime is extended to around $60\mu s$, allowing the muon spin to oscillate many times before decaying into an electron/positron plus two neutrinos (e.g. $\mu^- \to W^- \nu_\mu \to e^- \bar{\nu}_e \nu_\mu$). Again owing to parity violation of the weak interaction, these electrons prefer to be emitted in the direction of the muon spin. Thus measuring the direction of the electron momentum would give the final spin direction for the muon. Finally, the precise determination of the magnetic field is achieved by measuring the proton spin precession frequency in water with nuclear magnetic resonance, and then using the ratio of the muon-to-proton magnetic moments measured by experiments involving muonium.

Of course the above description is only meant to provide the very basic ideas behind the experimental measurements of a_μ. For a more detailed discussion and further references see the review by Jegerlehner and Nyffeler [11].

Experiment	Year	Type	a_μ $[10^{-10}]$	Precision [ppm]	References
CERN I	1961	μ^+	11 450 000(220000)	4300	[12]
CERN II	1962-68	μ^+	11 661 600(3100)	270	[13]
CERN III	1974-76	μ^+	11 659 100(110)	10	[14]
CERN III	1975-76	μ^-	11 659 360(120)	10	[15]
BNL	1997	μ^+	11 659 251(150)	13	[16]
BNL	1998	μ^+	11 659 191(59)	5	[17]
BNL	1999	μ^+	11 659 202(15)	1.3	[18]
BNL	2000	μ^+	11 659 204(9)	0.7	[19]
BNL	2001	μ^-	11 659 214(9)	0.7	[20]
Average			11 659 208(6.3)	0.54	[10]

Table 1.1: Summary of the experimental measurements of a_μ from CERN and BNL. Reproduced from [11].

Table 1.1 summarises the results of the experimental measurements of a_μ conducted by CERN and BNL. It is clear that the most recent experiments at BNL dominates the precision of the all the measurements. They were able to achieve a 14-fold improvement in precision over the experiments at CERN. Therefore the latest world average of the experimental measurement of a_μ is [10]

$$a_\mu^{\text{exp}} = 1169208.0(6.3) \times 10^{-10}, \tag{1.9}$$

corresponding to a precision of 0.54 parts per million (ppm).

1.3 The QED contribution to a_μ

For the Quantum Electrodynamics (QED) sector, the theoretical prediction is characterised by its fundamental constants. These are the fine structure constant (α) and

the ratios of the lepton masses (m_e, m_μ, m_τ). Thus the precision of this sector is essentially limited by the knowledge of these constants and the order of the perturbative expansion. For α, its most precise determination uses the electron anomalous magnetic moment measured by the Havard group [8]

$$a_e^{\rm exp} = 11\,596\,521.8073(28) \times 10^{-10}. \tag{1.10}$$

This leads to a value for the inverse of α [8]

$$\alpha^{-1} = 137.035999084(51). \tag{1.11}$$

For the lepton masses, they are [23]

$$m_e = 5.109989918(44) \times 10^{-4}\ \text{GeV}, \tag{1.12}$$

$$m_\mu = 0.1056583692(94)\ \text{GeV}, \tag{1.13}$$

$$m_\tau = 1.77699(29)\ \text{GeV}. \tag{1.14}$$

The leading order contribution is universal, i.e. independent of any masses and thus applies to the electron and tau as well as the muon. It comes from the 1-loop diagram as shown in Fig. 1.1, and was first computed by Schwinger in 1948 [1] with the result shown in Eq. (1.1). The lepton mass ratios appear as a result of the closed lepton loops in the higher order contributions like the second diagram in Fig. 1.1. These extra loops can introduce additional mass scales. A more systematic classification [24] results in

$$a_\mu^{\rm QED} = A_1 + A_2(m_\mu/m_e) + A_2(m_\mu/m_\tau) + A_3(m_\mu/m_e, m_\mu/m_\tau). \tag{1.15}$$

Now A_1 is the universal contribution common for all leptons. This includes the Schwinger result, diagrams with additional photon loops and also when the closed lepton loops involve the muon (i.e. same as the external particle). A_2 starts at the 2-loop level and contains lepton loops of the same type except the muon. A_3 begins at 3-loops and involves lepton loops of all types. Each of the terms can be written as a perturbative expansion in α,

$$A_i = \sum_{j=i}^{\infty} A_i^{(2j)} \left(\frac{\alpha}{\pi}\right)^j, \tag{1.16}$$

where $i = 1, 2, 3$ and j counts the number of loops. Therefore in general, to order N,

$$a_\mu^{\rm QED} = \sum_{n=1}^{N} C_n \left(\frac{\alpha}{\pi}\right)^n, \tag{1.17}$$

where the complete 4-loop ($N = 4$) results are known and calculation of $N = 5$ terms are ongoing.

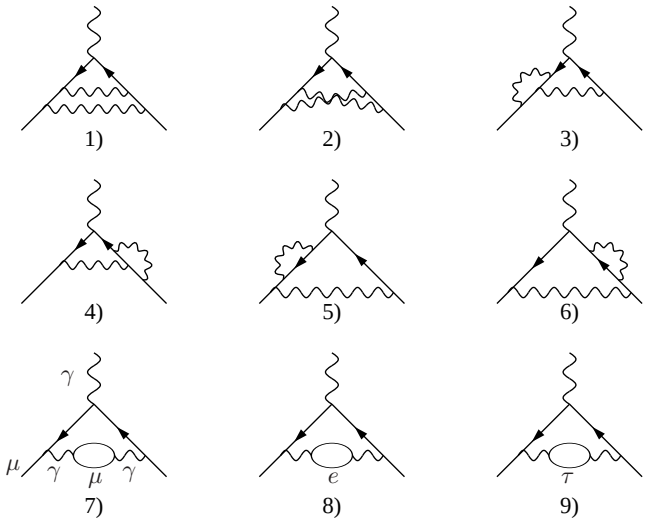

Fig. 1.3: The 2-loop diagrams of the QED contribution to a_μ. Graphics taken from [11].

1.3.1 Universal contributions

The 1-loop contribution is the aforementioned Schwinger result in Eq. 1.1. For the 2-loop level, there are 7 diagrams labelled $1) - 7)$ in Fig. 1.3. These make up the $A_1^{(4)}$ coefficient and was first computed by Petermann [25] and Sommerfield [26] in 1957. The result reads

$$A_1^{(4)} = \frac{197}{144} + \frac{\pi^2}{12} - \frac{\pi^2}{2}\ln 2 + \frac{3}{4}\zeta_3 = -0.32847\ldots \tag{1.18}$$

where $\zeta_3 \approx 1.20205$ is a Riemann Zeta function. The final two diagrams in Fig. 1.3 contribute to the mass dependent term $A_2^{(4)}$.

Going up to 3-loops, the mass independent contribution come from the 72 diagrams in Fig. 1.4, where only the closed muon loops contribute. The result was computed numerically by Kinoshita [27] in 1995 and was confirmed analytically by Laporta and Remiddi [28] in 1996, which was based on prior work by Remiddi and collaborators stretching back to 1969. The final result is given by

$$\begin{aligned} A_1^{(6)} = {} & \frac{83}{72}\pi^2\zeta_3 - \frac{215}{24}\zeta_5 + \frac{100}{3}\left[\left(a_4 + \frac{1}{24}\ln^4 2\right) - \frac{1}{24}\pi^2\ln^2 2\right] - \\ & \frac{239}{2160}\pi^4 + \frac{139}{18}\zeta_3 - \frac{298}{9}\pi^2\ln 2 + \frac{17101}{810}\pi^2 + \frac{28259}{5184} \\ = {} & 1.18123\ldots, \end{aligned} \tag{1.19}$$

where $\zeta_5 \approx 1.03692$ and $a_4 = \mathrm{Li}_4(1/2) = \sum_{n=1}^{\infty} 1/(2^n n^4) \approx 0.51747$ is a polylogarithm.

With 4-loops, the number of diagrams jumps to 891 and their complexity is much greater also. Thus, analytical results have been obtained for only a limited number of diagrams by various groups [29, 30]. However, a numerical approach was established

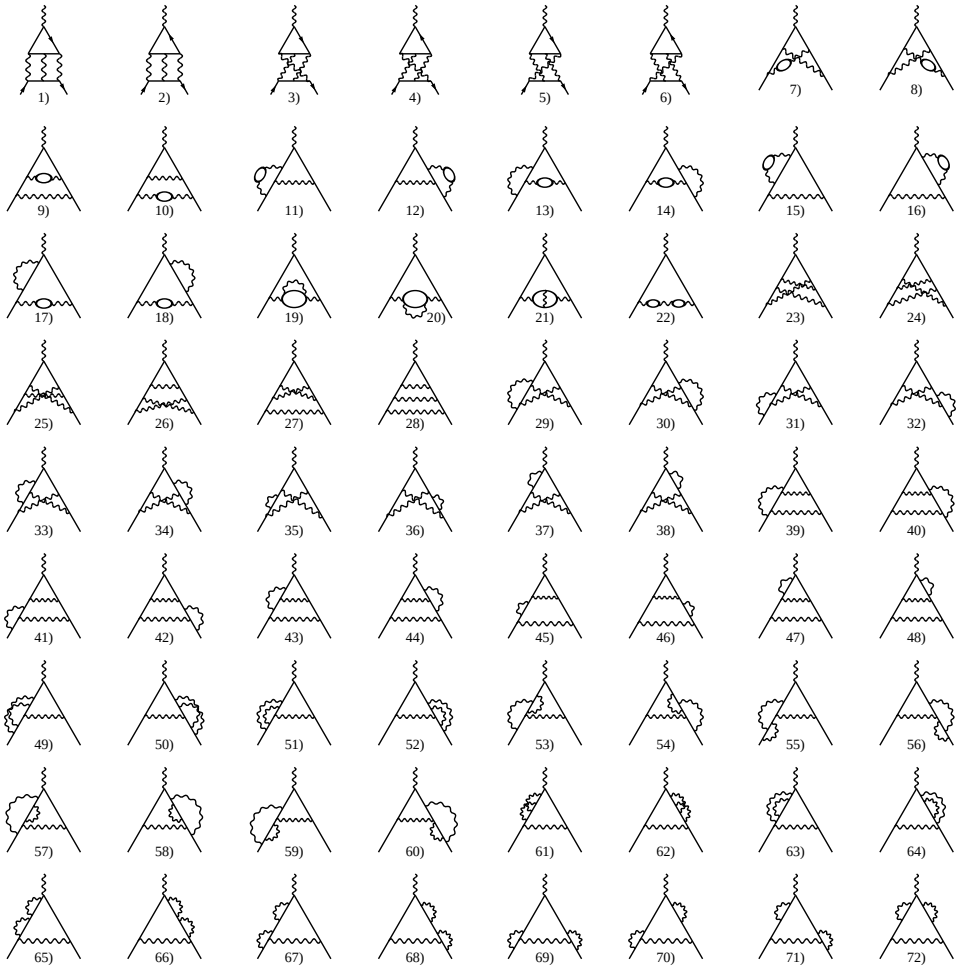

Fig. 1.4: The 3-loop diagrams of the QED contribution to a_μ. Graphics taken from [11].

and matured by Kinoshita and collaborators since 1981 [31, 32]. The mammoth effort undertaken by them over the years culminated in a refined result for the complete 4-loop universal QED contribution in 2008 from Aoyama, Hayakawa, Kinoshita and Nio [9, 33], giving

$$A_1^{(8)} \left(\frac{\alpha}{\pi}\right)^4 = -1.9144(35) \left(\frac{\alpha}{\pi}\right)^4, \tag{1.20}$$

where the uncertainty is due to numerical integration. Now its size is $\sim 0.55 \times 10^{-10}$, which is small compared to the experimental precision of the muon $g-2$, where $\delta a_\mu^{\rm exp} = 6.3 \times 10^{-10}$. However, it is much larger than $\delta a_e^{\rm exp} = 0.0028 \times 10^{-10}$, so although it is not immediately relevant for a_μ, it is crucial for the electron $g-2$.

The calculation for the contribution at 5-loops is still ongoing (see e.g. [34–36]). The number of diagrams for $A_1^{(10)}$ is 12672, an enormous number, and none are dominant so they all have to be evaluated [34] (see also talk given by Thomas Teubner on behalf

of Masashi Hayakawa at the PhiPsi11 conference [37]). An upper bound used by [11] is

$$A_1^{(10)} = 0.0(4.6), \tag{1.21}$$

which was calculated from the method suggested in Appendix B of [38]. Due to the suppression by $(\alpha/\pi)^5$, the 5-loop contribution is even less relevant for a_μ. However, the size of its uncertainty is similar to δa_e^{exp} and thus still important for a_e.

1.3.2 Mass dependent contributions

Mass dependent contributions first appear at the 2-loop level through lepton loop insertions as a result of photon VP effects and the fact that e, μ, τ have different masses. At 3-loops, they appear, for example, from light-by-light scattering diagrams.

For 2-loops the exact mass dependent expression was first found in 1966 [39] and then later compactified in [40]. The numerical results are

$$A_2^{(4)}(m_\mu/m_e) = 1.0942583111(84), \tag{1.22}$$
$$A_2^{(4)}(m_\mu/m_\tau) = 0.000078064(25), \tag{1.23}$$

where the uncertainties come from the mass ratios (m_μ/m_e) and (m_μ/m_τ). Hence the total 2-loop QED contribution from the diagrams in Fig. 1.3 is given by the coefficient,

$$C_2 = A_1^{(4)} + A_2^{(4)}(m_\mu/m_e) + A_2^{(4)}(m_\mu/m_\tau) = 0.765857410(27), \tag{1.24}$$

which results in

$$a_\mu^{\text{QED},\,2l} = C_2 \left(\frac{\alpha}{\pi}\right)^2 = (41321.7620 \pm 0.0014) \times 10^{-10}, \tag{1.25}$$

where the total uncertainty is negligible.

At 3-loops, there are contributions from light-by-light (LbL) diagrams in addition to the VP insertions, and the two mass ratios (m_μ/m_e), (m_μ/m_τ) can now appear simultaneously in a diagram. The numerical results for these contributions are summarised below (for more details and further references, see the review by [11]),

$$A_{2,\,\text{LbL+VP}}^{(6)}(m_\mu/m_e) = 22.86838002(20), \tag{1.26}$$
$$A_{2,\,\text{LbL+VP}}^{(6)}(m_\mu/m_\tau) = 0.00036051(21), \tag{1.27}$$
$$A_{3,\,\text{VP}}^{(6)}(m_\mu/m_e, m_\mu/m_\tau) = 0.00052766(17). \tag{1.28}$$

Note that the majority of the contribution in $A_{2,\,\text{LbL+VP}}^{(6)}(m_\mu/m_e)$ come from the electron light-by-light scattering. This is due to large logarithms of the form $\ln(m_\mu/m_e)$. Together with the universal contribution, the total 3-loop QED contribution is given by,

$$C_3 = 24.05050964(46), \tag{1.29}$$

leading to,

$$a_\mu^{\mathrm{QED},\,3l} = C_3 \left(\frac{\alpha}{\pi}\right)^3 = (3014.1902 \pm 0.0001) \times 10^{-10}. \tag{1.30}$$

The 4-loop mass dependent contributions were calculated by Kinoshita *et al.* [41]. The total is given by,

$$C_4 = 130.8105(85), \tag{1.31}$$

which means

$$a_\mu^{\mathrm{QED},\,4l} = C_4 \left(\frac{\alpha}{\pi}\right)^4 = (38.0807 \pm 0.0025) \times 10^{-10}. \tag{1.32}$$

However, recently Kinoshita *et al.* revised their calculations but only published results for the electron $g-2$ case [9], thus the latest results will be different from above.

Finally, an estimate for the mass dependent 5-loop contribution is given in [34]. So the total 5-loop estimate is

$$a_\mu^{\mathrm{QED},\,5l} \sim (663 \pm 20 \pm 4.6) \left(\frac{\alpha}{\pi}\right)^5 \simeq (0.4483 \pm 0.0135 \pm 0.0031) \times 10^{-10}, \tag{1.33}$$

where the second uncertainty is from the universal contribution estimate in Eq. (1.21).

Summing all the universal and mass dependent contributions together, the final result given by [9, 34] is,

$$a_\mu^{\mathrm{QED}} = (11\,658\,471.808 \pm 0.015) \times 10^{-10}. \tag{1.34}$$

This accounts for over 99.99% of the total contribution to a_μ and it is clear that the uncertainty is very well under control and much less than that from the experimental measurements of a_μ.

1.4 The electroweak contribution to a_μ

The theoretical calculation of the electroweak (EW) contribution to the muon $g-2$ (a_μ^{EW}) gained traction after the renormalisation of the Yang-Mills fields was solved in the early 1970s [42–44] and the SM started to take shape. However, a_μ experiments at CERN during that time [12–15] did not have the precision necessary to verify the theoretical predictions, which became a driving force behind a new g-2 experiment. This finally came to fruition with E821 experiment at BNL, and one of its major goals was to test a_μ^{EW}.

The 1-loop contribution involves exchanges of the Z, $W^\pm$ and H bosons given by Fig. 1.5. The Higgs contribution, however, is negligible. It is suppressed by the Higgs-muon coupling, which is tiny due to the mass of the muon. Thus the contribution at 1-loop is given by [45–49]

$$a_\mu^{\mathrm{EW},\,1l} = \frac{\sqrt{2} G_F m_\mu^2}{16\pi^2} \left[\frac{10}{3} + \frac{(1 - 4\sin^2\theta_W)^2 - 5}{3}\right] + \mathcal{O}\left(\frac{m_\mu^2}{m_{W,Z,H}^2}\right), \tag{1.35}$$

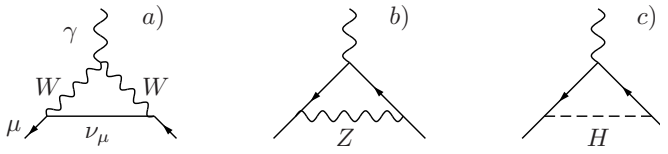

Fig. 1.5: The leading order contributions to $a_\mu^{\rm EW}$. Graphics taken from [11].

where the first and second terms in the square bracket come from the Z and W bosons respectively. Here, $G_F = 1.16637(1) \times 10^{-5}$ GeV^{-2} is the Fermi constant, $\sin^2\theta_W = 1 - m_W^2/m_Z^2 = 0.22276(56)$ is the weak mixing parameter, so

$$a_\mu^{\rm EW,\,1l} = (19.482 \pm 0.002) \times 10^{-10}. \tag{1.36}$$

The 2-loop contributions involve bosonic corrections (part of which is the EM corrections to the 1-loop diagrams in Fig. 1.5) and fermion loop insertions shown in Fig. 1.6. Note that the total amplitude of fermion loops with three photon legs vanishes due to Furry's theorem for QED, thus they do not appear in Fig. 1.6. However, since weak interactions violate parity, the amplitudes of the different orientations of the fermion triangles with $\gamma\gamma Z$, γZZ legs do not cancel. As for the γWW case, there is only one possible orientation due to charge conservation thus its amplitude cannot vanish either. A first calculation with quarks omitted was computed in 1992 by KuKhto, Kuraev, Schiller and Silagadze [50]. They found the 2-loop corrections are enhanced by large logarithms of the form $\ln(M_Z/m_f)$. However, since individual fermion triangle diagrams contain the Adler-Bell-Jackiw (ABJ) or VVA anomaly [51–53], quarks (of the same generation) must also be included to ensure anomaly cancellation. Now the quark triangle loops in reality contain non-perturbative hadronic effects, thus properly accounting for these effects is non-trivial.

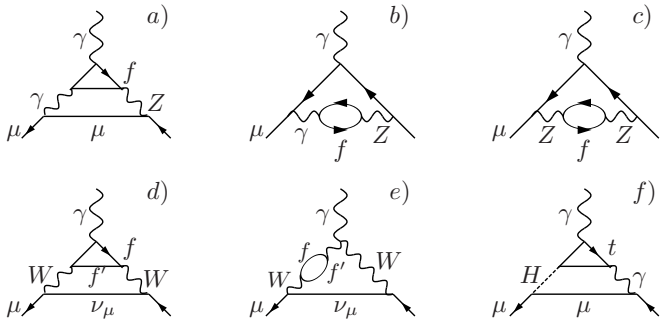

Fig. 1.6: The fermion loop insertion diagrams of the 2-loop contribution to $a_\mu^{\rm EW}$. Graphics taken from [11].

Nevertheless, the entire contribution at 2-loop level including a full treatment of the hadronic effects of the quark triangles summed together with the lepton loops was done by Czarnecki, Krause and Marciano [54] and then later refined by Czarnecki, Marciano

and Vainshtein [55]. Their result, when added to the 1-loop calculation gives [55],

$$a_\mu^{\rm EW} = (15.4 \pm 0.1_{\rm had} \pm 0.2_{m_H,\, m_t,\, 3-{\rm loop}}) \times 10^{-10}. \tag{1.37}$$

The first error comes from the hadronic effects in the 2-loop quark triangle diagrams. The second error includes an estimated mass range for the Higgs boson $114 \lesssim m_H \lesssim 250$ GeV, uncertainty on the top quark mass and an estimation for the leading 3-loop effect. This is consistent with a very similar estimation by [11],

$$a_\mu^{\rm EW} = (15.32 \pm 0.10_{\rm had} \pm 0.15_{m_H,\, m_t,\, 3-{\rm loop}}) \times 10^{-10}, \tag{1.38}$$

and another computation by [56] with the result

$$a_\mu^{\rm EW} = (15.2 \pm 0.1) \times 10^{-10}. \tag{1.39}$$

Thus the uncertainties in the electroweak contribution to a_μ are clearly under control. For this analysis we use Eq. (1.37) with the errors added in quadrature,

$$a_\mu^{\rm EW} = (15.4 \pm 0.2) \times 10^{-10}. \tag{1.40}$$

1.5 The hadronic contribution to a_μ

1.5.1 Introduction

The hadronic contributions have the largest uncertainty in the SM prediction of a_μ. They are normally broken into three separate pieces, the leading order (LO), higher order (HO) vacuum polarisation (VP) contributions, and the light-by-light (LbL) scattering contribution,

$$a_\mu^{\rm had} = a_\mu^{\rm had,\ LOVP} + a_\mu^{\rm had,\ HOVP} + a_\mu^{\rm had,\ LbL}. \tag{1.41}$$

Note that in terms of counting powers of the coupling α, the light-by-light contributions are also sub-leading. Unfortunately none of these three contributions can be computed to the desired precision using perturbative QCD (pQCD). This is because

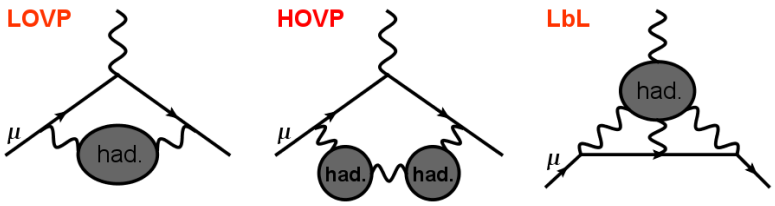

Fig. 1.7: The Feynman diagrams for the LO VP, and one of the HO VP and the LbL hadronic contributions to a_μ.

virtual photons with low q^2 dominate the loop integrals and the running of the strong coupling 'constant' $\alpha_s(q^2)$. At low energies, $\alpha_s(q^2)$ becomes large and pQCD is no

longer reliable. Therefore, a semi-phenomenological method involving hadronic e^+e^- annihilation experimental data is used in the most precise determination of LO and HO VP contributions. However for light-by-light, the mainstream calculations are still model dependent, although there are some promising developments on the lattice front [57,58] and a calculation using an alternative approach based on Dyson-Schwinger equations [59].

1.5.2 The leading order vacuum polarisation contribution

The leading order hadronic vacuum polarisation (LOVP) contribution can be visualised by replacing the internal lepton loop in the QED case with a 'blob' containing all possible hadronic states. This 'blob' thus represents the hadronic contribution to the

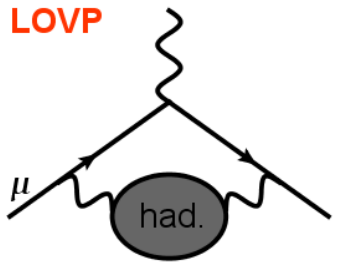

Fig. 1.8: The leading hadronic contribution to a_μ.

photon VP $\Pi'_{\rm had}(q^2)$ and it is this quantity that can be equated to $\sigma(e^+e^- \to \text{hadrons})$.

We take this opportunity to define our conventions on the vacuum polarisation (VP) tensor $\Pi^{\mu\nu}(q^2)$. Using the time-ordered product of two electromagnetic (EM) currents $j^\mu(x)$ it is,

$$\Pi^{\mu\nu}(q^2) \equiv i \int \mathrm{d}^4x e^{iqx} \langle 0|Tj^\mu(x)j^\nu(0)|0\rangle\Big|_{\rm 1PI}. \tag{1.42}$$

The subscript '1PI' stands for 1-particle irreducible, so we only include these type of diagrams. The normalisation for the EM current is

$$j^\mu(x) = \sum_{f,\alpha} Q_f \bar{\psi}^\alpha_f(x)\gamma^\mu\psi^\alpha_f(x), \tag{1.43}$$

where the sum over fermion f should be taken over all the quarks and leptons, and α is the $SU(3)_C$ colour index and thus does not apply for leptons. Q_f is the electric charge of fermion f so for example, $Q_u = 2/3$. Due to current conservation, the VP tensor is purely transverse,

$$\Pi^{\mu\nu}(q) = (q^\mu q^\nu - q^2 g^{\mu\nu})\Pi'(q^2) \tag{1.44}$$

where $\Pi'(q^2) = \Pi(q^2)/q^2$ is known as the VP function. $\Pi'(q^2)$ (or its real part) can be related to its imaginary part via an once subtracted dispersion relation. By virtue of analyticity,

$$\Pi'(q^2) - \Pi'(0) = \frac{q^2}{\pi}\int_{s_{\rm th}}^\infty \mathrm{d}s \frac{\mathrm{Im}\,\Pi'(s)}{s(s-q^2-i\epsilon)}. \tag{1.45}$$

Thus, taking the real part gives

$$\mathrm{Re}\left[\Pi'(q^2) - \Pi'(0)\right] = \frac{q^2}{\pi}\mathcal{P}\int_{s_{\rm th}}^{\infty} \mathrm{d}s \frac{\mathrm{Im}\,\Pi'(s)}{s(s-q^2)}, \tag{1.46}$$

where $\mathcal{P}$ denotes taking the principal value prescription. We also work in the on-shell scheme where the renormalisation condition $\Pi'(q^2 = 0) = 0$ is imposed. Thus $\Pi'(0)$ can be safely omitted.

In case of the hadronic contribution to the VP function, we can then write

$$\Pi'_{\rm had}(q^2) = \frac{q^2}{\pi}\int_{s_{\rm th}}^{\infty} \mathrm{d}s \frac{\mathrm{Im}\,\Pi'_{\rm had}(s)}{s(s-q^2-i\epsilon)}, \tag{1.47}$$

where we have dropped the $\Pi'_{\rm had}(0)$ notation. Then, with the use of the optical theorem (Fig. 1.9), the imaginary part of the photon VP can be written as

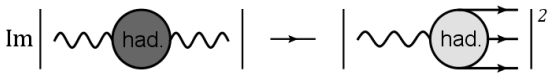

Fig. 1.9: Optical theorem for the hadronic contribution to the photon propagator.

$$\mathrm{Im}\,\Pi'_{\rm had}(s) = \left(\frac{s}{4\pi\alpha}\right)\sigma_{\rm had}(s), \tag{1.48}$$

where $\sigma_{\rm had}(s)$ is the total $e^+e^- \to$ hadrons cross section. This deals with the photon VP, but we also need to account for the one-loop contribution from the coupling of the virtual photon to the muon. This is given by a well known function [7, 60],

$$\left(\frac{\alpha}{\pi}\right)K(s > 4m_\mu^2) = \frac{\alpha}{\pi}\left\{\frac{x^2}{2}(2-x^2) + \frac{(1+x^2)(1+x)^2}{x^2}\left[\ln(1+x) - x + \frac{x^2}{2}\right] + \frac{1+x}{1-x}x^2\ln x\right\} \tag{1.49}$$

where $x = (1-\beta)/(1+\beta)$ and $\beta = \sqrt{1-4m_\mu^2/s}$. Note that the expression here is written with a different normalisation compared to the previous analysis HMNT (03) [61]. Namely, it differs by a factor of $m_\mu^2/(3s)$ compared to Eq.(45) of [61]. This $K(s)$, which is also known as the kernel function, has a relatively simple behaviour,

$$K(s) = \frac{m_\mu^2}{3s}(0.4..1) \tag{1.50}$$

where $(0.4..1) \equiv \tilde{K}(s)$ is a function that monotonically increases from 0.4 to 1 as s increases from $s_{\rm th}$ to ∞. Finally, convoluting this with the imaginary part of the photon VP function gives,

$$a_\mu^{\rm had,\ LOVP} = \frac{1}{4\pi^3}\int_{s_{\rm th}}^{\infty} \mathrm{d}s\, \sigma^0_{\rm had}(s)K(s). \tag{1.51}$$

The quantity $\sigma^0_{\rm had}(s)$ is the undressed or 'bare' e^+e^- hadronic annihilation cross section and $s_{\rm th} = m_\pi^2$ is the invariant mass squared threshold for the hadronic system, which

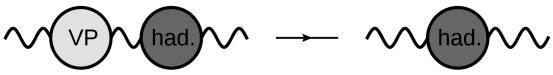

Fig. 1.10: Undressing the photon propagator of all VP effects, otherwise double counting occurs with higher order VP diagrams.

Fig. 1.11: Example of an FSR event and its corresponding diagram in terms of photon VP. These type of diagrams contribute to a_μ and they are not counted in the HOVP contributions. Hence FSR in the cross section data needs to be included.

is defined by the process $e^+e^- \to \pi^0\gamma$. 'Bare' means the photon propagator must be 'undressed' of all (leptonic and hadronic) VP effects (see Fig. 1.10), however final state radiation (FSR) corrections need to be included (see Fig. 1.11). This is required in order to avoid double counting with contributions to $a_\mu^{\text{had, HOVP}}$, specifically in Fig. 1.13 the first diagram in class (a) along with diagrams from classes (b) and (c). Eq. (1.51) can also be written in terms of $R_{\text{had}}(s)$, the hadronic R-ratio,

$$\begin{aligned} a_\mu^{\text{had, LOVP}} &= \frac{1}{4\pi^3}\int_{s_{\text{th}}}^{\infty} \mathrm{d}s\, \frac{\sigma^0_{\text{had}}(s)}{\sigma_{\text{pt}}(s)}\frac{4\pi\alpha^2}{3s}K(s) \\ &= \frac{\alpha^2}{3\pi^2}\int_{s_{\text{th}}}^{\infty}\frac{\mathrm{d}s}{s}R_{\text{had}}(s)K(s), \end{aligned} \tag{1.52}$$

where

$$R_{\text{had}}(s) = \frac{\sigma^0_{\text{had}}(s)}{\sigma_{\text{pt}}(s)} = \frac{\sigma^0_{\text{had}}(s)}{4\pi\alpha^2/(3s)} \tag{1.53}$$

and $\sigma_{\text{pt}}(s)$ is the $e^+e^- \to \mu^+\mu^-$ cross section. For $s \gg m_\mu^2$, $K(s) \sim m_\mu^2/s$ and $R_{\text{had}}(s)$ is independent of s. Hence the integral is dominated by contributions coming from low energies. There are numerous low energy e^+e^- hadronic annihilation data available from experiments as far back as the 1970s. However, this also introduces the difficulty of systematically combining data of different final states, quality and normalisation to give the most accurate result with the correct error estimate. The exact procedures on how we achieved this are detailed in the next chapter. Previous analyses from HMNT (03) [61] and (06) [62] give

$$a_\mu^{\text{had, LOVP}}(\text{HMNT (03)}) = (692.4 \pm 6.4) \times 10^{-10}, \tag{1.54}$$

$$a_\mu^{\text{had, LOVP}}(\text{HMNT (06)}) = (689.4 \pm 4.5) \times 10^{-10}. \tag{1.55}$$

There is an alternative method in using data to calculate the hadronic VP contributions through the use of hadronic τ-decays. Specifically, the $I = 1$ part of the

$e^+e^- \to$ hadrons data can be obtained by using the spectral function data available for the $\tau \to \nu_\tau +$ hadrons processes. This idea was instigated by Alemany, Davier and Höcker [63] when precise $\tau-$spectral data became available after 1997 from ALEPH [64–66], OPAL [67], CLEO [68] and then much later, Belle [69]. In principle, this technique can be used for any hadronic τ decay below the τ mass. However, it is the $e^+e^- \to \gamma^* \to \pi^+\pi^-$ data have that been given the most attention since it alone accounts for over 70% of the contribution to $a_\mu^{\text{had, LOVP}}$. Although other final states such as the 4π channel, have also been calculated. The corresponding τ-decay to the $e^+e^- \to \gamma^* \to \pi^+\pi^-$ is $\tau \to \nu_\tau W \to \nu_\tau \pi\pi^0$, which involves a charged current rather than a neutral one as well as a different final state (see Fig. 1.12). These differences

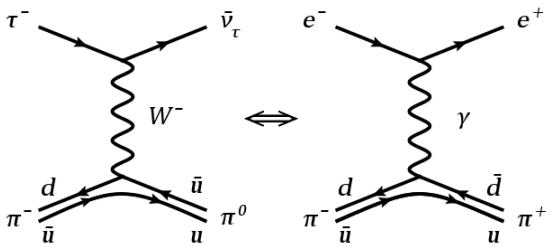

Fig. 1.12: τ-decay vs e^+e^- annihilation.

mean an isospin rotation along with isospin breaking corrections are required to relate the τ-decay process to the e^+e^- data. Comparing the diagrams in Fig. 1.12 we have

$$\sigma(e^+e^- \to \pi^+\pi^-) = \frac{4\pi\alpha^2}{s} v_0(s), \tag{1.56}$$

and

$$\frac{1}{\Gamma}\frac{\mathrm{d}\Gamma}{\mathrm{d}s}(\tau^- \to \pi^-\pi^0\nu_\tau) = \frac{6|V_{ud}|^2 S_{EW}}{m_\tau^2} \frac{\mathcal{B}(\tau^- \to \nu_\tau e^- \bar{\nu_e})}{\mathcal{B}(\tau^- \to \nu_\tau \pi^-\pi^0)} \left(1 - \frac{s}{m_\tau^2}\right)\left(1 + \frac{2s}{m_\tau^2}\right) v_-(s). \tag{1.57}$$

Here, $|V_{ud}|$ is the CKM weak mixing matrix element (its value can be found in e.g. PDG2010 [23]), S_{EW} is the electroweak radiative corrections [70–76], and the $\mathcal{B}$'s are branching ratios. The spectral functions $v_i(s)$ are defined by

$$v_i(s) = \frac{\beta_i^3(s)}{12} |F_\pi^i(s)|^2, \tag{1.58}$$

where $F_\pi^i(s)$ are the pion form factors, $\beta_i(s)$ are phase space factors and $i = 0, -$. The SU(2) isospin symmetry implies $v_-(s) = v_0(s)$, which allows the isospin rotation. However, mass differences between m_u and m_d along with electromagnetic and weak effects break the isospin symmetry. These effects for example, include: $\rho - \omega$ mixing; the phase space factor $\beta^3_{\pi^-\pi^+}/\beta^3_{\pi^-\pi^0}$ due to $m_{\pi^\pm} - m_{\pi^0} \neq 0$; form-factor differences due to charged vs neutral current; and QED effects (real and virtual photon emissions) on the $\tau^- \to \nu_\tau \pi^-\pi^0$ decay. However, even after all known isospin breaking effects are accounted for, differences are still reported between the τ and e^+e^- data. This is seen

in the recent analyses by Davier *et al.* [77,78], which give a discrepancy of around 1.8σ between the prediction for $a_\mu^{\rm had}$ based on isospin corrected τ data, and the one based on e^+e^- data. This difference has decreased compared to their earlier studies, but it is still sizeable and is at odds with results from two other groups. The analysis from Benayoun *et al.* [79–81] based on hidden local symmetry (HLS) and dynamical (ρ, ω, ϕ) mixing, found agreement between the τ and e^+e^- data. Jegerlehner and Szafron's recent study [82] examines the effect of $\rho - \gamma$ mixing, which is not present in the τ spectral function, but can be calculated from the e^+e^- data. They show that by accounting for the $\rho - \gamma$ mixing, the τ and e^+e^- data agree but improvement in the precision of $a_\mu^{\rm had}$ is only minor. Very recently, Benayoun *et al.* in collaboration with Jegerlehner, released an updated analysis based on the HLS model [83]. They report an $a_\mu^{\rm had,\ LOVP}$ result that is slightly lower than, but still consistent and has comparable precision with recent determinations based on the e^+e^- data. Using this result, they arrive at a SM prediction of a_μ that is 4.1σ away from the experimental measurement. A full exploration of these issues goes beyond the scope of this project, but the recent results appear quite encouraging for the τ versus e^+e^- puzzle.

1.5.3 The higher order vacuum polarisation contribution

The HO ($O(\alpha^3)$) hadronic vacuum polarisation contribution ($a_\mu^{\rm had,\ HOVP}$) involves various types of diagrams. One categorisation appears in [84], which split the diagrams into three classes, denoted by (a), (b) and (c) here. Fig. 1.13, which is taken from [61], displays all three classes of diagrams:

(a) diagrams with a single hadronic 'blob' along with the muon as the only leptons present;

(b) diagrams containing one hadronic 'blob' with either an electron or a tau loop;

(c) diagrams with two hadronic 'blobs'.

Their contribution to a_μ then involves the appropriate modifications to the dispersion relation and the kernel $K(s)$ giving,

$$a_\mu^{\rm had,\ HOVP(a)} = \frac{\alpha}{4\pi^4}\int_{s_{\rm th}}^{\infty} {\rm d}s\, \sigma_{\rm had}^0(s) K^{\rm (a)}(s), \tag{1.59}$$

$$a_\mu^{\rm had,\ HOVP(b)} = \frac{\alpha}{4\pi^4}\int_{s_{\rm th}}^{\infty} {\rm d}s\, \sigma_{\rm had}^0(s) K^{\rm (b)}(s), \tag{1.60}$$

$$a_\mu^{\rm had,\ HOVP(c)} = \frac{1}{16\pi^2\alpha}\int_{s_{\rm th}}^{\infty} {\rm d}s \int_{s_{\rm th}}^{\infty} {\rm d}s'\, \sigma_{\rm had}^0(s)\sigma_{\rm had}^0(s') K^{\rm (c)}(s,s'). \tag{1.61}$$

The expressions for the different kernel functions can be found in [84]. The analysis from HMNT (03) [61] gives

$$a_\mu^{\text{had, HOVP(a)}} = (-20.73 \pm 0.18_{\text{exp}} \pm 0.07_{\text{rad}}) \times 10^{-10}, \tag{1.62}$$

$$a_\mu^{\text{had, HOVP(b)}} = (10.60 \pm 0.09_{\text{exp}} \pm 0.04_{\text{rad}}) \times 10^{-10}, \tag{1.63}$$

$$a_\mu^{\text{had, HOVP(c)}} = (0.34 \pm 0.01_{\text{exp}} \pm 0.00_{\text{rad}}) \times 10^{-10}. \tag{1.64}$$

Hence, as is done in the LO determination, we also assign an error due to the radiative corrections. Now the errors of (a) and (b) are almost completely anti-correlated, so their combined uncertainty is the difference between the two errors. The uncertainties of (c) are very small compared to those from (a) and (b), thus they are ignored. With these in mind, the sum of these contributions gives[2],

$$a_\mu^{\text{had, HOVP}} = (-9.79 \pm 0.09_{\text{exp}} \pm 0.03_{\text{rad}}) \times 10^{-10}, \tag{1.65}$$

which is consistent with the original calculation from Krause [84],

$$a_\mu^{\text{had, HOVP}} = (-10.1 \pm 0.6) \times 10^{-10}. \tag{1.66}$$

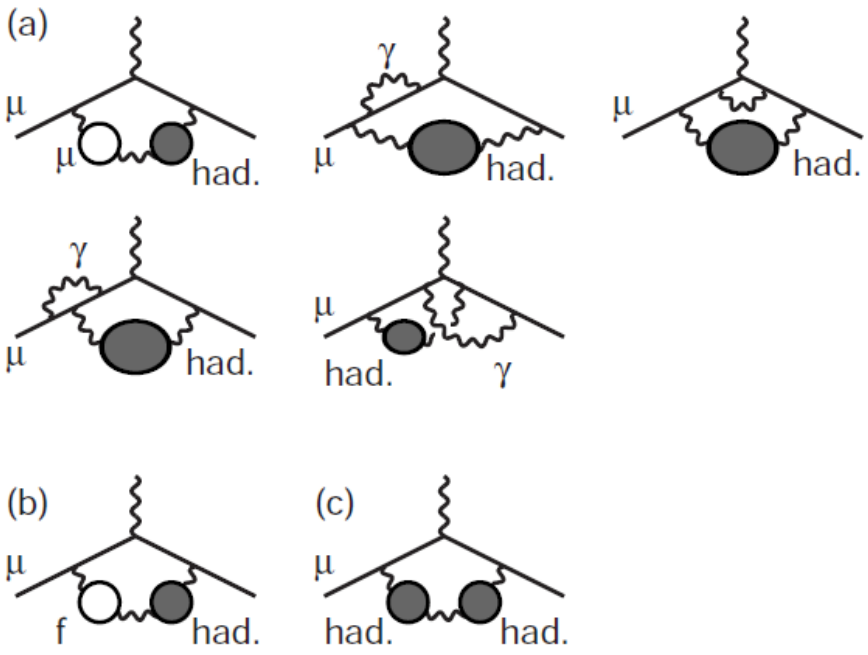

Fig. 1.13: Feynman diagrams that contribute to $a_\mu^{\text{had, HOVP}}$. For the class (b) diagram, $f = e, \tau$ only. Note that mirror counterparts and diagrams where the massless and 'massive' photon propagator are swapped are implied.

[2]The HMNT (06) [62] result is identical apart from a slightly lower experimental error of 0.08×10^{-10}.

1.5.4 The light-by-light contributions

The hadronic light-by-light (LbL) scattering is conceptually the hardest contribution to deal with. This section serves to give a brief overview of the history, difficulties and results of the calculation of $a_\mu^{\text{had, LbL}}$. A detailed discussion of these issues goes beyond the scope of this project, see [11] for a detailed review.

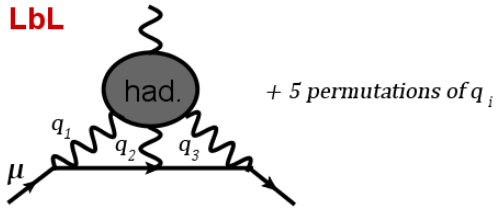

Fig. 1.14: Hadronic light-by-light diagram, note the 3 virtual photons ($q_{1,2,3}$).

The hadronic LbL contribution enters at $\mathcal{O}(\alpha_s^3)$ from the diagrams shown in Fig. 1.14. This process cannot be related to experimental data easily due to three of the photons being virtual. Furthermore, even for LbL scattering involving real photons, pQCD gives a smooth continuum rather than the π^0, η and η' resonances seen by the Crystal Ball detector [85] shown in Fig. 1.15. Therefore, non-perturbative QCD effects must play an important role in this process. The QED counterpart of Fig. 1.14 can receive significant enhancement, therefore we cannot simply neglect this contribution. We can, however, turn to low energy effective representations of the strong interaction, such as chiral perturbation theory (ChPT) [86–88]. Nevertheless, a main difficulty in calculat-

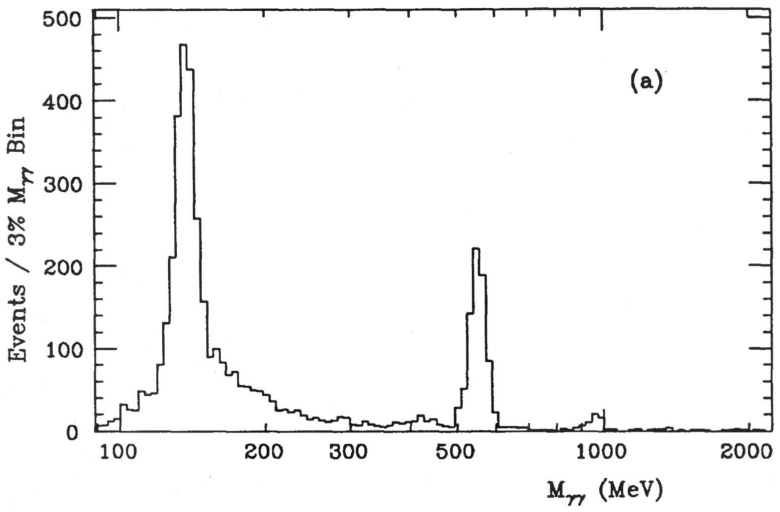

Fig. 1.15: Plot of the $\gamma\gamma$ mass spectrum measured at the Crystal Ball detector.

ing $a_\mu^{\text{had, LbL}}$ is the multi-scale problem due to the 3 virtual photons shown Fig. 1.14. Suppose the low energy effective approach we wish to use, only applies below some scale Λ^2 and above which, pQCD is valid. Then these theories can only reasonably control

the fully soft ($q_1^2, q_2^2, q_3^2 < \Lambda^2$) or the fully hard ($q_1^2, q_2^2, q_3^2 > \Lambda^2$) regions. However, in domains where high and low virtualities are mixed, one has to rely on experimental constraints or operator product expansions (OPE) and/or factorisation schemes to separate the short and long distance physics. Thus in general, there is no single all encompassing model to deal with this problem. A further complication is that behaviours of the low energy effective models (e.g. form factors) have to match QCD at high energy. However, no single model in general satisfies all the constraints or symmetries imposed by QCD. This introduces cut-off dependent results that give relatively large uncertainties (see below), which can be interpreted as a dependence on the model used. Therefore, reducing the effect of or features subject to model dependence, is another obstacle that the computation of $a_\mu^{\text{had, LbL}}$ faces.

Various models have been proposed and utilised throughout the complicated history in calculating $a_\mu^{\text{had, LbL}}$. Early works using constituent quark approximations (quark loops, summed over all flavour) [89,90] for the hadronic blob were received with caution due to not-understood low energy hadronic effects. A more realistic model was also presented by KNO [90] as an alternative to the constituent quark approximation. It assumed a pion or light hadron loop along with low energy resonances (e.g. π^0 exchange) for the hadronic blob. In addition, the vector meson dominance (VMD) model was also incorporated, where the photon has a hadronic structure and can effectively couple to hadrons via $\rho - \gamma$ mixing. Although this model seemed to confirm their approximation using quark loops [90][3]

$$a_\mu^{\text{had, LbL}}(\text{KNO; } \pi \text{ loop+resonance}) = (4.9 \pm 0.5) \times 10^{-10}, \tag{1.67}$$

$$a_\mu^{\text{had, LbL}}(\text{KNO; quark loop}) = (6.0 \pm 0.4) \times 10^{-10}, \tag{1.68}$$

it was pointed out later that quark and pion loop approximations should not be equivalent, but are two separate contributions [91,92]. Furthermore, the application of these types of effective descriptions of QCD modified with VMD, which is only valid at low energies, reinforced the belief that the main contributions came from momentum regions close to the mass of the muon. However, as was considered in [93] and observed in [92,94–96], momentum regions around m_ρ are also important. Therefore, resonances of hadronic states in higher energy domains have to be considered too.

A more systematic method based on the extended Nambu-Jona-Lasinio (ENJL) model [97, 98] was proposed by [91]. It used chiral expansion and the large-N_c QCD picture [99, 100] (see also [101, 102]) to do N_c counting of the different contributions. This is followed by two comprehensive evaluations by BPP [94, 95] using the ENJL effective model of QCD, and HKS/HK [92,103] using the slightly different hidden local symmetry (HLS) model [104]. Their results suggested that the pseudoscalar-exchanges (see Fig. 1.16) is the dominant contribution. Both evaluations however, had the now

[3]The constituent quark approximation from [89] differed not only in size but also in the sign.

'famous' sign error in the dominating π^0-exchange, which was identified by KN [105,106] and then confirmed by [107, 108]. Nonetheless, these approaches became recognised as the framework for computing $a_\mu^{\text{had, LbL}}$. The corrected results from BPP and HKS/HK are

$$a_\mu^{\text{had, LbL}}(\text{BPP; } \pi^0) = (5.9 \pm 0.9) \times 10^{-10}, \tag{1.69}$$

$$a_\mu^{\text{had, LbL}}(\text{BPP; tot}) = (8.3 \pm 3.2) \times 10^{-10}, \tag{1.70}$$

$$a_\mu^{\text{had, LbL}}(\text{HKS/HK; } \pi^0) = (5.7 \pm 0.4) \times 10^{-10}, \tag{1.71}$$

$$a_\mu^{\text{had, LbL}}(\text{HKS/HK; tot}) = (8.96 \pm 1.54) \times 10^{-10}. \tag{1.72}$$

Some recent developments were focused on the dominant neutral pion exchange contri-

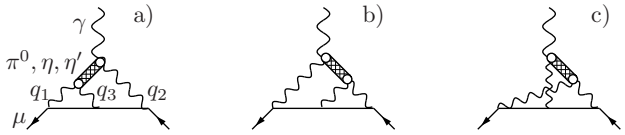

Fig. 1.16: Leading contribution: neutral pseudoscalar-exchange diagrams. Graphics taken from [11].

bution, specifically the pion-photon-photon transition form factors $\mathcal{F}_{\pi^{0(*)}\gamma^{(*)}\gamma^{(*)}}(q_3^2, q_1^2, q_2^2)$ with $q_3 = -(q_1 + q_2)$ in accordance with 4-momentum conservation. The * symbol enclosed in the bracket signifies that if a * is present then the particle is off-shell and if there is no *, then the particle is on-shell. In general, at the internal photon vertex the form factor is fully off-shell $\mathcal{F}_{\pi^{0*}\gamma^*\gamma^*}(q_3^2, q_1^2, q_2^2)$ and at the external photon vertex one has $\mathcal{F}_{\pi^{0*}\gamma^*\gamma}(q_3^2, q_3^2, 0)$, since the external photon is real and soft, corresponding to the external magnetic field. MV [96, 109] discovered that some short distance QCD constraints were overlooked in [92, 94, 95, 103, 105, 106], this meant that the form factor used at the external vertex should not depend on momentum and thus proposed the use of a constant, completely on-shell form factor $\mathcal{F}_{\pi^0\gamma\gamma}(m_\pi^2, m_\pi^2, 0)$. This had the effect of enhancing the pion exchange and the total contribution[4]

$$a_\mu^{\text{had, LbL}}(\text{MV; } \pi^0) = (7.7 \pm 0.7) \times 10^{-10}, \tag{1.73}$$

$$a_\mu^{\text{had, LbL}}(\text{MV; tot}) = (13.6 \pm 2.5) \times 10^{-10}. \tag{1.74}$$

However, N/NJ [11, 111] argued that in doing this, MV have only computed the so called pion-pole contribution and not the complete pion exchange contribution, which requires the use of fully off-shell form factors. Thus in their latest evaluation [11, 111] they used fully off-shell form factors that also satisfies the constraints derived by MV.

[4]However, BP [110] noted that the increase in the total was not due to the enhanced π^0 contribution alone. There was a different treatment of the pseudovector contribution and negative contributions from the scalars and $\pi^\pm$ loop were missed and taken as zero respectively.

The results are,

$$a_\mu^{\text{had, LbL}}(\text{N/JN; } \pi^0) = (7.2 \pm 1.2) \times 10^{-10}, \tag{1.75}$$

$$a_\mu^{\text{had, LbL}}(\text{N/JN; tot}) = (11.6 \pm 4.0) \times 10^{-10}. \tag{1.76}$$

This can be compared with another recent compilation by PdRV [112][5]

$$a_\mu^{\text{had, LbL}}(\text{PdRV; tot}) = (10.5 \pm 2.6) \times 10^{-10}, \tag{1.77}$$

where they altered the values or/and enlarged the errors for some of the individual contributions computed by different groups. Note that the total error above came from individual uncertainties added in quadrature whereas in Eq. (1.76), the errors are added linearly.

Contribution	BPP	HKS/HK	KN	MV	BP	PdRV	N/JN
π^0, η, η'	8.5 ± 1.3	8.27 ± 0.64	8.3 ± 1.2	11.4 ± 1.0	-	11.4 ± 1.3	9.9 ± 1.6
π, K loops	-1.9 ± 1.3	-0.45 ± 0.81	-	0 ± 1.0	-	-1.9 ± 1.9	-1.9 ± 1.3
Pseudovectors	0.25 ± 0.10	0.17 ± 0.17	-	2.2 ± 0.5	-	1.5 ± 1.0	2.2 ± 1.5
Scalars	-0.68 ± 0.20	-	-	-	-	-0.7 ± 0.7	-0.7 ± 0.2
Quark loops	2.1 ± 0.3	0.97 ± 1.11	-	-	-	0.23	2.1 ± 0.3
Total	8.3 ± 3.2	8.96 ± 1.54	8.0 ± 4.0	13.6 ± 2.5	11.0 ± 4.0	10.5 ± 2.6	11.6 ± 4.0
Reference	[94, 95]	[92, 103]	[105, 106]	[96, 109]	[110]	[112]	[11, 111]

Table 1.2: Summary of the most recent results for the various contributions to $a_\mu^{\text{had, LbL}}$, all numbers are in units of 10^{-10}. This is reproduced from Table 13 in [11]. Note that the MV result for the π, K loops also includes other contributions that are subleading in terms of the N_c counting.

In summary, despite the difficulties in calculating $a_\mu^{\text{had, LbL}}$, there is actually quite a good agreement between the various results from different groups, especially in the dominant pseudoscalar exchange contributions. However, other results from subleading contributions show more disparity (see Table 1.2). Thus pinning down their values and reducing their uncertainties would improve the overall prediction for $a_\mu^{\text{had, LbL}}$. As mentioned in the introduction, an alternate method for calculating $a_\mu^{\text{had, LbL}}$ using Dyson-Schwinger equations appeared [59], where Goecke *et al.* reported a very large contribution from quark loops $(13.6 \pm 5.9) \times 10^{-10}$, making their estimate for the total contribution to LbL larger than the other groups by a factor of two. Soon after, a counter-argument was presented in [113] by studying the quark loop contribution using the constituent quark model including QCD radiative effects. Very recently however, Goecke *et al.* released a cross check of their method by computing $a_\mu^{\text{had, LOVP}}$ and the Adler function [114]. They reported a value for $a_\mu^{\text{had, LOVP}}$ that is around 2% less than results based on the e^+e^- data, and found good agreement with the Adler function. Therefore, this issue remains unresolved at present. With the new $g-2$ experiment from

[5] They do not provide a separate value for the π^0 exchange contribution, but instead, quote $(11.4 \pm 1.3) \times 10^{-10}$ for the whole pseudoscalar exchange (including π^0, η and η'), using the mean from MV [96, 109] and the largest error from BPP [94, 95].

Fermilab and J-PARC striving for a precision of 1.4×10^{-10}, independent determination of the hadronic light-by-light contribution from Lattice QCD [57, 58] will prove to be very useful and important in the near future.

1.6 Summary

Table 1.3 summaries the typical results of the different theoretical contributions to a_μ. It is clear that $a_\mu^{\text{had, LOVP}}$ and $a_\mu^{\text{had, LbL}}$ have the largest uncertainties. In particular, due to the difficulties mentioned above, the error from the hadronic light-by-light contribution is not very well under control. Fig. 1.17 compares the total SM predictions of a_μ as computed by various groups (shown by the markers) with the then world average of the experimental measurement of a_μ (shown by the (green) band). This deviation between theory and experiment was first observed at around 2000. Although its size was only around 2 standard deviations (σ), a far cry from claiming discovery, it has not disappeared and recent analyses showed that it is now around 3σ. Therefore, it became important to reduce the uncertainties of these two hadronic contributions in order to clarify the source of this deviation. Furthermore, if new physics beyond the SM (BSM) is indeed responsible for this deviation

$$a_\mu^{\text{BSM?}} = a_\mu^{\text{exp}} - a_\mu^{\text{SM}} \sim (29 \pm 9) \times 10^{-10}, \tag{1.78}$$

then this difference can be used to constrain the parameters of the various models that describe BSM physics. For a discussion on how a_μ (and the latest electroweak data) has affected the minimal supersymmetric extension of the SM, see [115].

Contribution	Value (10^{-10})	Error	References
a_μ^{QED}	11 658 471.81	0.02	[9, 34]
$a_\mu^{\text{had, LOVP}}$	690.30	5.26	[116]
$a_\mu^{\text{had, HOVP}}$	-10.03	0.11	[117]
$a_\mu^{\text{had, LbL}}$	10.5	2.6	[112]
a_μ^{EW}	15.4	0.2	[55]

Table 1.3: Summarises typical results for the various SM contributions to a_μ.

This thesis therefore will focus on improving the calculation and precision of the leading order vacuum polarisation contribution to the anomalous magnetic moment of the muon, based on the well established data-driven approach used in HMNT (03) and (06) [61, 62]. This also allows the determination of the running of the QED coupling as an added benefit. The organisation of the rest of the thesis will be as follows. Chapter 2 is the main focus of the thesis, discussing the computation and results of $a_\mu^{\text{had, LOVP}}$. The exact procedures used in the calculation is presented first, followed by a detailed breakdown of the results obtained, along with their discussion and comparison

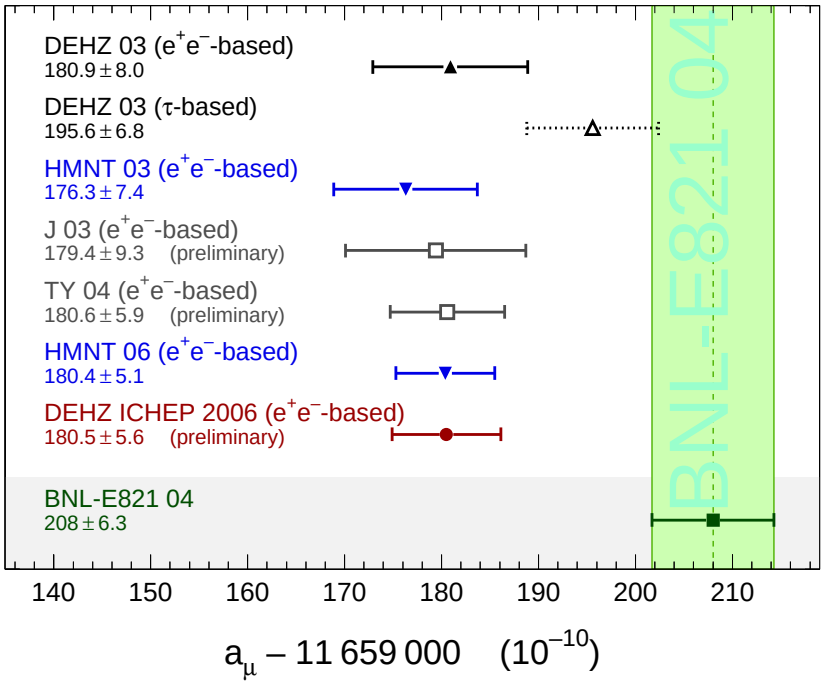

Fig. 1.17: Comparison of a_μ^{exp} and SM predictions of a_μ from various collaborations. Graphics taken from [118].

with other works. Chapter 3 is the secondary focus, introducing the QED coupling and summarising the results of its running, in particular, its value at the Z-boson mass. In addition, the procedure on the inclusion of an important data set and its preliminary impacts is also discussed. Finally Chapter 4 summarises the final results on the anomalous magnetic moment of the muon and the running of the QED coupling at the Z-boson mass, along with a discussion on their implications and the future prospects in this field.

Chapter 2

Computing the LO Hadronic Vacuum Polarisation Contributions

2.1 Method

The procedures used to calculate a_μ^{had} will be presented in this section. Since there are numerous e^+e^- hadronic annihilation data available with different final states and covering different energy ranges, we have decided to group them according to their final state or 'channel' and compute their contributions to a_μ^{had} separately before summing them together. Corrections to the data due to radiative and VP effects will be explained in Section 2.1.1. The details on how data are combined and then fitted for a particular final state will be described in Sections 2.1.2 and 2.1.3 respectively. The integration procedure for the dispersion integral and final remarks can be found in Sections 2.1.4 and 2.1.5. See Section 2.3 for details of the actual data used and their contributions to $a_\mu^{\text{had, LOVP}}$.

2.1.1 Data processing

Vacuum polarisation corrections

As mentioned earlier, the σ_{had}^0 that enters the dispersion relation have the photon VP effects subtracted. However, the observed cross sections σ_{had} for the e^+e^- annihilation process have these effects included. Since VP effects screen the electric charge, this amounts to having a running effective coupling $\alpha(q^2)$ rather than the constant α. Now the running coupling can be expressed using the real part of the photon VP [119],

$$\alpha(q^2) = \frac{\alpha}{1 - \Delta\alpha(q^2)} = \frac{\alpha}{1 - \text{Re}\,\tilde{\Pi}(q^2)}, \tag{2.1}$$

where we define $\tilde{\Pi}(q^2) = -e^2\Pi'(s)$. This is possible since the full photon propagator is proportional to the sum of the 1-particle irreducible (1PI) blobs therefore one can

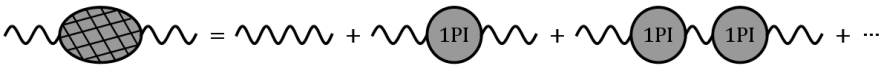

Fig. 2.1: The full photon propagator expressed as a sum of 1-particle irreducible (1PI) blobs.

write

$$1 + \tilde{\Pi} + \tilde{\Pi} \cdot \tilde{\Pi} + \cdots \simeq \frac{1}{1 - \tilde{\Pi}}, \tag{2.2}$$

if $\tilde{\Pi}$ is small. We note that there are both leptonic and hadronic contributions to $\Delta\alpha(q^2)$, thus we can define

$$\Delta\alpha(q^2) = \Delta\alpha_{\rm lep}(q^2) + \Delta\alpha^{(5)}_{\rm had}(q^2) + \Delta\alpha_{\rm top}(q^2). \tag{2.3}$$

The first and third term correspond to the leptonic and top contributions respectively, and they are calculable perturbatively. The middle term is the five flavour hadronic contribution that contains non-perturbative effects, hence $\Delta\alpha^{(5)}_{\rm had}(q^2)$ can be computed by a dispersion integral similar to Eq. (1.52). This will be covered in more detail in Chapter 3. Now the observable cross sections $\sigma_{\rm had}$ contain the absolute square of the full photon propagator, i.e. $|1 + \tilde{\Pi} + \tilde{\Pi} \cdot \tilde{\Pi} + \cdots|^2$, so formally the photon VP includes the imaginary part, i.e. $\tilde{\Pi} = e^2(P + iA)$, although A is suppressed by e^2,

$$|1 + e^2(P + iA) + e^4(P + iA)^2 + \cdots|^2 = 1 + 2e^2P^2 + e^4(3P^2 - A^2) + \cdots \tag{2.4}$$

In the previous analyses [61, 62], $\mathrm{Im}\,\Pi'$ is not included on the grounds that the effect would be small. However, in this analysis we have a new routine that can calculate the full photon VP, hence we now include its imaginary part.

Now the exact details of how the VP is included in each measurement depend on the normalisation the experiment uses along with other factors and there are six different cases to consider, which remain unchanged from the previous analyses [61, 62]. Case (1), for experiments that do not subtract the photon VP effects and the (normalisation) luminosity measurement have already taken these effects into account, then a correction factor

$$C^{(1)}_{\rm VP} = \left(\frac{\alpha}{\alpha(s)}\right)^2 \tag{2.5}$$

need to be applied. For example,

$$R_{\rm had}(s) = \frac{\sigma^0_{\rm had}(s)}{4\pi\alpha^2/(3s)} \simeq C^{(1)}_{\rm VP}\frac{\sigma_{\rm had}(s)}{4\pi\alpha^2/(3s)}. \tag{2.6}$$

Case (2), for experiments that use the $e^+e^- \to \mu^+\mu^-$ process as the normalisation cross section, the photon VP effects will cancel out exactly. Thus the correction factor is simply unity,

$$C^{(2)}_{\rm VP} = 1. \tag{2.7}$$

Case (3), many experiments use the Bhabha scattering as the normalisation process. If VP effects were not removed in the normalisation cross section, then the correction that need to be applied will mostly come from t channel photon exchange amplitudes at $t_{\rm min}$. This is because the Bahbah differential cross section is $\sim \alpha^2/t^2$. Thus the correction for the Bhabha process can be estimated by taking $\alpha^2 \to (\alpha(t_{\rm min}))^2$ where

$$t_{\rm min} = -\frac{s}{2}(1-\cos\theta_{\rm cut}). \tag{2.8}$$

Thus the correction factor for the cross section should be

$$C^{(3)}_{\rm VP} = \left(\frac{\alpha}{\alpha(s)}\right)^2 \left(\frac{\alpha(t_{\rm min})}{\alpha}\right)^2 = \left(\frac{\alpha(t_{\rm min})}{\alpha(s)}\right)^2, \tag{2.9}$$

where for example: if $|\cos\theta_{\rm cut}| \lesssim 1$, then $\alpha(t_{\rm min}) \simeq \alpha$ and the correction factor is closer to Eq. (2.5); if $|\cos\theta_{\rm cut}| \lesssim 0.5$ however, then $\alpha(t_{\rm min}) \sim \alpha(s)$ and the factor is close to Eq. (2.7). Case (4), sometimes the leptonic (electron and muon) part of the photon VP effects have been subtracted. So for those experiments that uses the Bhabha scattering process for normalisation (the ones using the muon pair production process are not affected since the VP effects cancel exactly), the correction factor should be

$$C^{(4)}_{\rm VP} = \left(\frac{\alpha^{e,\mu}(s)}{\alpha(s)}\right)^2 \left(\frac{\alpha(t_{\rm min})}{\alpha^{e,\mu}(t_{\rm min})}\right)^2. \tag{2.10}$$

Here, $\alpha^{e,\mu}(s)$ is the running effective coupling that only contains the electron and muon parts in the photon VP function. Case (5) is a variation of Case (4) where only the electron part of the VP effect was subtracted in some of the older $e^+e^- \to$ all hadrons data. Thus we have,

$$C^{(5)}_{\rm VP} = \left(\frac{\alpha^{e}(s)}{\alpha(s)}\right)^2 \left(\frac{\alpha(t_{\rm min})}{\alpha^{e}(t_{\rm min})}\right)^2. \tag{2.11}$$

Case (6) applies once again to certain data sets for the $e^+e^- \to$ all hadrons process. The assumption is similar to Case (5) in that these data sets have only the electron part of the VP effect subtracted, however, they do not use the Bhabha process for normalisation. Thus the correction factor is a variation of Eq. (2.5),

$$C^{(6)}_{\rm VP} = \left(\frac{\alpha}{\alpha(s)}\right)^2 \left(\frac{\alpha^{e}(s)}{\alpha}\right)^2 = \left(\frac{\alpha^{e}(s)}{\alpha(s)}\right)^2. \tag{2.12}$$

Since applying these correction factors can lead to shifts in the contribution to a_μ that are on the level of the experimental uncertainties and documentation on the exact VP correction used are not available for some older experiments, we thus take a separate error estimate $\delta a_\mu^{\rm VP}$ based on our treatment of the VP corrections. This remains unchanged from [61, 62]

$$\delta a_\mu^{\rm VP,\ data} = \frac{1}{2}\left[\sum_i^{\text{all channels}} (\delta a_\mu^{{\rm VP},i})^2\right]^{\frac{1}{2}}, \tag{2.13}$$

where the difference between applying VP or not in each channel $\delta a_\mu^{{\rm VP},i}$ is summed in quadrature and the resulting total halved.

Final state radiative corrections

Final state radiation (FSR) effect corrections are needed for most of the data sets in the $e^+e^- \to \pi^+\pi^-$ final state (see Section 2.3.2 for the list) and all the data sets in $e^+e^- \to K^+K^-$ channels. This is done by applying the formula for the total inclusive 1-photon correction

$$C_{\rm FSR} = 1 + \eta(s)\frac{\alpha}{\pi}, \tag{2.14}$$

where the factor $\eta(s)$ is given by [120, 121],

$$\begin{aligned}\eta(s) = \frac{1+\beta^2}{\beta}\Bigg[&4\mathrm{Li}_2\left(\frac{1-\beta}{1+\beta}\right) + 2\mathrm{Li}_2\left(-\frac{1-\beta}{1+\beta}\right) - 3\ln\left(\frac{2}{1+\beta}\right)\ln\left(\frac{1+\beta}{1-\beta}\right) - \\ &2\ln(\beta)\ln\left(\frac{1+\beta}{1-\beta}\right)\Bigg] - 3\ln\left(\frac{4}{1-\beta^2}\right) - 4\ln(\beta) + \\ &\frac{1}{\beta^2}\left[\frac{5}{4}(1+\beta^2)^2 - 2\right]\ln\left(\frac{1+\beta}{1-\beta}\right) + \frac{3}{2}\frac{1+\beta^2}{\beta^2}\end{aligned} \tag{2.15}$$

with $\beta = \sqrt{1-4m^2/s}$. Therefore for the $\pi^+\pi^-$ and K^+K^- channels $m = m_\pi$ and m_K respectively. The above equation assumes the particles are charged scalar bosons, which is a reasonable approximation. This is because the cross section is significant close to threshold, where the photon propagator is also less energetic and thus less able to resolve the structures of the π and K, minimising their effects. This correction factor includes both real photon emissions and virtual photon effects. However, there is insufficient information available on how each data set corrected for FSR effects, thus we take 50% of $\eta(s)$ into account along with a 50% error. Therefore,

$$C_{\rm FSR} = \left(1 + \frac{1}{2}\eta(s)\frac{\alpha}{\pi}\right) \quad \text{and} \quad \Delta C_{\rm FSR} = \frac{1}{2}\eta(s)\frac{\alpha}{\pi}, \tag{2.16}$$

covering the entire spectrum of the degree of correction. Although other final states do not receive such a correction, we do apply an additional 1% (of their a_μ values) error as an estimate of the uncertainty due to FSR corrections. The numerical values for these corrections are,

$$\delta a_\mu^{\mathrm{FSR},\,\pi^+\pi^-} = 0.32 \times 10^{-10}, \tag{2.17}$$

$$\delta a_\mu^{\mathrm{FSR},\,K^+K^-} = 0.40 \times 10^{-10}, \tag{2.18}$$

$$\delta a_\mu^{\mathrm{FSR,\,others}} = 1.15 \times 10^{-10}. \tag{2.19}$$

These are added linearly to give a total of,

$$\delta a_\mu^{\mathrm{FSR,\,tot}} = 1.86 \times 10^{-10}. \tag{2.20}$$

Radiative corrections for narrow resonances

The narrow resonance contributions to a_μ include J/ψ, ψ' and $\Upsilon(1S-6S)$ states. They are added separately since they are not resolved by data (see Fig. 2.32). Radiative

corrections to these contributions come from the physical electronic widths $\Gamma(V \to e^+e^-)$ where V represent the different resonances. Their values can be found from the PDG [23] or Table 2.1, and they contain vacuum polarisation effects as well as FSR corrections. These must be removed to obtain the bare electronic width

$$\Gamma^0_{ee} = C_{\rm res}\Gamma(V \to e^+e^-) \tag{2.21}$$

before the contribution can be added. The correction factor $C_{\rm res}$ is given by

$$C_{\rm res} = \left(\frac{\alpha}{\alpha_{{\rm no}\,V}(M_V^2)}\right)^2 \left(1 + \frac{3}{4}\frac{\alpha}{\pi}\right)^{-1}, \tag{2.22}$$

where $\alpha_{{\rm no}\,V}(M_V^2)$ is the running of the QED coupling at the mass of the resonance M_V but with the resonance contribution subtracted. In previous analyses [61, 62], the space-like $\alpha(-M_V^2)$ was used instead because there are no reliable determinations for $\alpha(M_V^2)$. However, this is not fully correct due to the differences between space-like and time-like runnings (see Section 3.3). The differences in this case can be seen in Table 2.1, where bare electronic width when using both the time-like $\alpha_{{\rm no}\,V}(M_V^2)$ and space-like $\alpha(-M_V^2)$ couplings are listed along with the physical width.

Resonance	Γ_{ee}	Γ^0_{ee}	$\Gamma^{0,\,\rm space-like}_{ee}$
J/ψ	5.55	5.31	5.27
ψ'	2.33	2.22	2.20
$\Upsilon(1S)$	1.34	1.25	1.24
$\Upsilon(2S)$	0.612	0.569	0.568
$\Upsilon(3S)$	0.443	0.412	0.411
$\Upsilon(4S)$	0.272	0.253	0.252
$\Upsilon(5S)$	0.310	0.288	0.287
$\Upsilon(6S)$	0.130	0.121	0.120

Table 2.1: Values of the physical and bare electronic width for the narrow resonance states in units of KeV. The last column lists the value of the bare width calculated using $\alpha(-M_V^2)$ instead of $\alpha_{{\rm no}\,V}(M_V^2)$.

The total uncertainty from these VP corrections to the narrow resonances is similar to Eq. (2.13) earlier, except the differences between applying these corrections or not for each resonance $\delta a_\mu^{{\rm VP},\,V}$ are added linearly, giving

$$\delta a_\mu^{{\rm VP,\,res}} = \frac{1}{2}\sum_{V=J/\psi,\,\psi',\,\Upsilon} \delta a_\mu^{{\rm VP},\,V}. \tag{2.23}$$

Therefore the total uncertainty for all the VP corrections including the narrow resonances is,

$$\delta a_\mu^{{\rm VP,\,tot}} = \delta a_\mu^{{\rm VP,\,data}} + \delta a_\mu^{{\rm VP,\,res}} = 0.96 \times 10^{-10}. \tag{2.24}$$

2.1.2 Data combination

The combination procedure have been improved since [61], but the main principles remain the same. When computing $R_{\text{had}}(s)$ for a particular channel, we aim to minimise the amount of theoretical assumption on its shape and normalisation. To this end, we do not fit the data with the use of parametrisations such as Breit-Wigner functions in general[1]. Furthermore, the usage of pQCD is only limited to energies from 2.6 to 3.73 GeV, where it agrees with the data (see Fig. 2.34), and above 11.09 GeV. Therefore the issue now lies with in how to use all the data from different experiments in a particular channel to compute its contribution to a_μ^{had}. One way is to calculate the integral (1.52) for each experiment separately and then do a weighted average of the results. However, there are a few problems with this setup such as incorrect error evaluation (see footnote 4 in [63]), what to do with data sets with only a single point or sparsely populated and the fact that a_μ^{had} as it is computed here, is not an observable. Going to the other extreme, we can integrate over all data point-by-point within a channel. Again there are issues with this approach. For example, the weighting of precise data may be suppressed by points with large uncertainties in its proximity, which leads to an overestimation of the total error. Therefore for each channel, a combination procedure should be applied to the data before integration.

First of all, data points from different experiments have different energy bins, so a re-binning of the points into energy 'clusters' is applied and our model assumes that the cross section is constant within the energy binning or size of the cluster. Thus we have

$$R(\sqrt{s} = E_i^{(k,m)}) = R_i^{(k,m)} \pm \left[\left(\mathrm{d}R_i^{(k,m)} \right)^2 + \left(\mathrm{d}f_k R_i^{(k,m)} \right)^2 \right]^{\frac{1}{2}}, \tag{2.25}$$

where $R_i^{(k,m)}$ is the R value for the i^{th} data point from experiment k in cluster m and $E_i^{(k,m)}$ is its corresponding energy; $\mathrm{d}f_k$ is the common systematic error (as a percentage) of the data points from experiment k, any additional systematic error are added in quadrature to the statistical error and their total is given by $\left(\mathrm{d}R_i^{(k,m)} \right)^2$. This setup of the errors allows for the non-linear χ^2 fitting function that will be explained in the next section. Then a weighted average for cluster m is given by

$$R_m = \left[\sum_k \sum_{i=1}^{N^{(k,m)}} \frac{R_i^{(k,m)}}{\left(\mathrm{d}\tilde{R}_i^{(k,m)} \right)^2} \right] \left[\sum_k \sum_{i=1}^{N^{(k,m)}} \frac{1}{\left(\mathrm{d}\tilde{R}_i^{(k,m)} \right)^2} \right]^{-1}, \tag{2.26}$$

where

$$\mathrm{d}\tilde{R}_i^{(k,m)} = \sqrt{\left(\mathrm{d}R_i^{(k,m)} \right)^2 + \left(\mathrm{d}f_k R_i^{(k,m)} \right)^2} \tag{2.27}$$

[1]The $\eta\omega$ channel is an exception since we do not have access to the actual data, see Section 2.3.8 for details.

and $N^{(k,m)}$ is the total number of data points within cluster m. Similarly, the energy for each cluster center is

$$E_m = \left[\sum_k \sum_{i=1}^{N^{(k,m)}} \frac{E_i^{(k,m)}}{\left(\mathrm{d}\tilde{R}_i^{(k,m)}\right)^2}\right]\left[\sum_k \sum_{i=1}^{N^{(k,m)}} \frac{1}{\left(\mathrm{d}\tilde{R}_i^{(k,m)}\right)^2}\right]^{-1}. \tag{2.28}$$

The R_m computed here are not the final values, instead they are used as initial values of the fit parameters in our χ^2 fitting function, which is explained in the next section. In [61], for each channel, there is always a cluster size defined for the continuum region but other cluster sizes may also be defined for the known resonance regions. However, note that if two data points are separated by an energy binning larger than the defined cluster size, then no clustering between the two data points occur, so the cluster size is effectively the larger energy binning between the two data points. In this work, the process has been improved to include the option of using a more adaptive clustering algorithm. The new algorithm turns the defined cluster sizes to *target* cluster sizes that can be reduced or enlarged based on the energies of the data points. The resulting effect prevents a cluster from getting too large and also tries to group more points together in the continuum regions.

2.1.3 Minimisation

After the data is combined into clusters, the weighted average for cluster m, R_m and the normalisation factor f_k for the k^{th} experiment are fitted using a non-linear χ^2 function,

$$\begin{aligned}\chi^2(R_m, f_k) = &\sum_{k=1}^{N_{\text{exp}}} \left(\frac{1-f_k}{\mathrm{d}f_k}\right)^2 + \\ &\left\{\sum_{m=1}^{N_{\text{clu}}} \sum_{i=1}^{N^{(k,m)}} \left(\frac{R_i^{(k,m)} - f_k R_m}{\mathrm{d}\tilde{R}_i^{(k,m)}}\right)^2\right\}_{\text{w/o cov. mat.}} + \\ &\left\{\sum_{m=1}^{N_{\text{clu}}} \sum_{i=1}^{N^{(k,m)}} \sum_{j=1}^{N^{(k,n)}} \left(R_i^{(k,m)} - f_k R_m\right) C^{-1}(m_i, n_j) \left(R_j^{(k,n)} - f_k R_n\right)\right\}.\end{aligned} \tag{2.29}$$

The input for this are $R_i^{(k,m)}$, $\mathrm{d}R_i^{(k,m)}$ and $\mathrm{d}f_k$ defined earlier and by equation (2.25). The common systematic error of $\mathrm{d}f_k$ may be given in many forms. If the systematic error is given as an overall percentage for all energy regions, then this is simply taken as $\mathrm{d}f_k$. If each data point is assigned an absolute systematic error, the minimum (in percentage) of which is taken as $\mathrm{d}f_k$ and the remaining error (as an absolute number) are included in $\mathrm{d}R_i^{(k,m)}$. If the systematic errors are given as different percentages in different energy regions, they will be converted to an absolute systematic error for each point and the treatment above will be used. Finally, N_{clu} and N_{exp} denote the

total number of clusters and the total number of experiments respectively. Some recent data sets give a covariance matrix for each of their statistical and systematic errors. Their contributions are added separately in the χ^2 function, appearing as the last line in (2.29). Instead of $(1/\mathrm{d}\tilde{R}_i^{(k,m)})^2$ that appears in the second line, the inverse of the covariance matrix $C^{-1}(m_i, n_j)$ for each experiment is used. This 'C' is the sum of the statistical and systematic covariance matrices with the common systematic error subtracted from each element. Thus the subscript 'w/o cov. mat.' in the second line of equation (2.29) is used to indicate they are contribution to χ^2 from experiments that do not give covariance matrices for their errors. This function is then minimised with respect to the fit parameters R_m and f_k via a numeric iteration procedure. So as mentioned earlier, the weighted average R_m computed in equation (2.26) serves as the starting values in this fitting procedure. For the normalisation factors, their initial values are taken as $f_k \equiv 1$. The output from this fitting procedure include the fitted values, $R_m = \bar{R}_m$, $f_k = \bar{f}_k$, a minimised global χ^2 given by χ^2_{min}, local χ^2_m value for each cluster m and a covariance matrix $V(m, n)$ that defines the correlation of errors $\mathrm{d}R_m$ and $\mathrm{d}R_n$ between clusters m and n. For this matrix, the diagonal elements are simply $V(m, m) = (\mathrm{d}R_m)^2$ while in general, $V(m, n)$ satisfies

$$V(m, n) = (\mathrm{d}R_m)(\mathrm{d}R_n)\rho_{\mathrm{corr}}(m, n) \tag{2.30}$$

so the correlation factors $\rho_{\mathrm{corr}}(m, m) \equiv 1$. The goodness of the overall fit can be estimated from

$$\frac{\chi^2_{\mathrm{min}}}{\mathrm{d.o.f.}} = \frac{\chi^2_{\mathrm{min}}}{N_{\mathrm{tot}} - N_{\mathrm{clu}} - N_{\mathrm{exp}}} \tag{2.31}$$

The degree of freedom (d.o.f.) is the total number of data points minus the number of fitted parameters, N_{clu} for R_m and N_{exp} for f_k.

In [61, 62], if $\chi^2_{\mathrm{min}}/\mathrm{d.o.f.}$ is greater than unity then the final error after integration would be inflated by $\sqrt{\chi^2_{\mathrm{min}}/\mathrm{d.o.f.}}$. However, this prescription may be improved by using the local χ^2 and inflate the error of each cluster. More precisely, the covariance matrix $V(m, n)$ should be inflated given the following:

- if $\chi^2_m/\mathrm{d.o.f.} > 1$ and $\chi^2_n/\mathrm{d.o.f.} > 1$,

$$\tilde{V}(m, n) = V(m, n) \cdot \sqrt{\chi^2_m/\mathrm{d.o.f.}} \cdot \sqrt{\chi^2_n/\mathrm{d.o.f.}}; \tag{2.32}$$

- if $\chi^2_m/\mathrm{d.o.f.} > 1$ only, then

$$\tilde{V}(m, n) = V(m, n) \cdot \left(\chi^2_m/\mathrm{d.o.f.}\right). \tag{2.33}$$

The d.o.f. for a local χ^2 is simply the total number of data points in the cluster minus one. The effect of the local χ^2 on the fit can be seen from Figs. 2.2 and 2.3. Points from mock data 1 and 2 have the same statistical and percentage systematic error but

disagrees at two places. Mock data 5 are identical to mock data 2 except for the larger statistical and much larger systematic errors. Therefore we see that in places where the two data sets disagree, there is an inflation of the error band due to the usage of local χ^2. In Fig. 2.2, the inflation is much greater because both data sets are equally precise leading to small re-normalisations, therefore the size of the error band is a reflection of the disparity between the two data at those points. For Fig. 2.3, points from mock data 5 are less precise and the larger systematic errors mean they get a larger re-normalisation downwards. Therefore the smaller error inflation reflects the fact that mock data 5 are less precise. As for how much the local χ^2 impacts the error after integration i.e. the error on a_μ, Table 2.2 shows that the effect for actual data is not huge but nevertheless noticeable. Thus in this work, we have chosen to use the local χ^2 prescription.

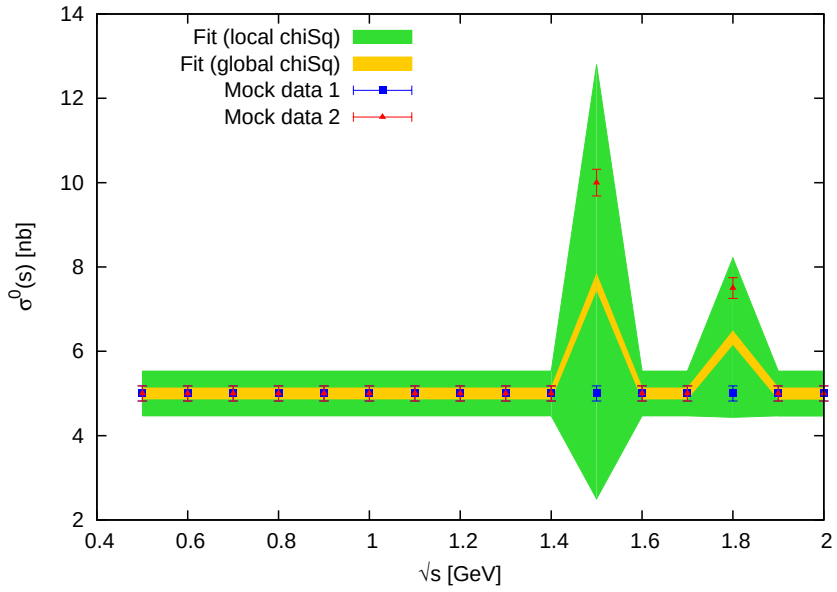

Fig. 2.2: Plot to demonstrate the effect of the local χ^2 fit. The light (yellow) band represents the original fit as was used in [61,62], where only the final error is inflated by $\sqrt{\chi^2_{\text{min}}/\text{d.o.f.}}$ after integration. The dark (green) band is the new fit, where the error is inflated locally i.e. on the level of the cluster.

2.1.4 Integration

Once the fitting procedure is complete, then a_μ and its error can be found by integration using the trapezoid rule. Ignoring the constants in equation (1.52), the integral between two arbitrary energies E_a and E_b is then,

$$I = \int_{E_a^2}^{E_b^2} \frac{\mathrm{d}s}{s} R_{\text{had}}(s) K(s) = 2 \int_{E_a}^{E_b} \frac{\mathrm{d}E}{E^2} E R_{\text{had}}(E^2) K(E^2) = \bar{I} \text{ with error } \Delta\bar{I}. \quad (2.34)$$

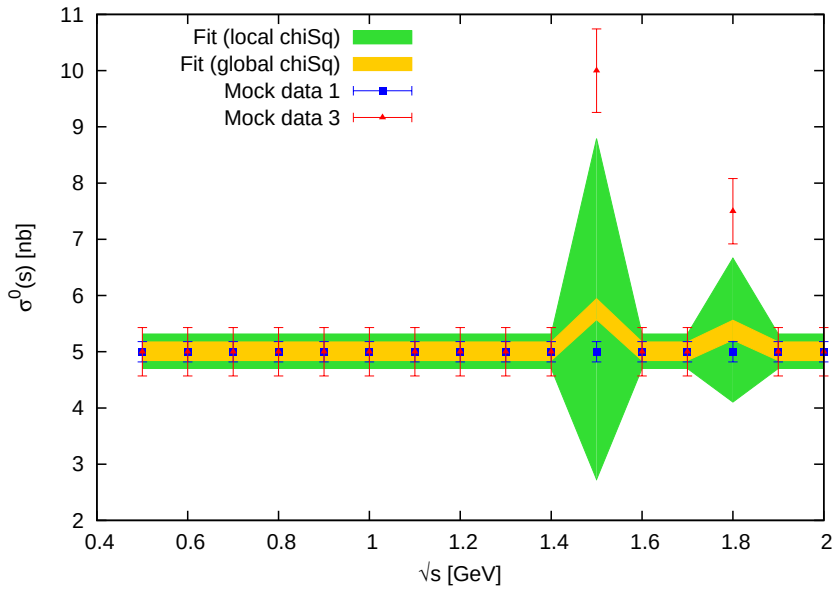

Fig. 2.3: Same as Fig. 2.2 except that Mock data 5 have larger statistical and systematic errors than Test data 2.

Channel	global $\chi^2_{\rm min}$/d.o.f.	globally infl. err.	locally infl. err.	'global – local'
$\pi^+\pi^-$	1.4	3.06	3.09	-0.03
$\pi^+\pi^-\pi^0$	3.0	1.08	0.99	$+0.10$
$4\pi(2\pi^0)$	1.3	1.19	1.26	-0.07
$4\pi(\text{no}\,\pi^0)$	1.7	0.49	0.47	$+0.02$
K^+K^-	1.9	0.57	0.46	$+0.11$
$K^0_SK^0_L$	0.8	0.16	0.16	-0.003
$5\pi(1\pi^0)$	1.2	0.09	0.09	0
$6\pi(2\pi^0)$	4.0	0.39	0.24	$+0.16$

Table 2.2: Global $\chi^2_{\rm min}$/d.o.f., globally and locally inflated error (in units of 10^{-10}) of a_μ and their differences for several channels. The range of integration is 0.305 to 2 GeV.

Since $R_{\rm had}(E^2)$ is parametrised by $R_{\rm had}(E_m^2) = \bar{R}_m$ with cluster center E_m, so lets suppose $E_m < E_a < E_{m+1}$ which is less than $E_{n-1} < E_b < E_n$. The integral can then be estimated with trapezoid rule

$$\begin{aligned}\bar{I} = &2\left(\frac{E_{m+1}-E_a}{2E_a}\bar{R}_aK_a + \frac{E_{m+2}-E_a}{2E_{m+1}}\bar{R}_{m+1}K_{m+1}\right) + \\ &2\left(\sum_{l=m+2}^{n-2}\frac{E_{l+1}-E_{l-1}}{2E_l}\bar{R}_lK_l\right) + \\ &2\left(\frac{E_b-E_{n-2}}{2E_{n-1}}\bar{R}_{n-1}K_{n-1} + \frac{E_b-E_{n-1}}{2E_b}\bar{R}_bK_b\right),\end{aligned} \tag{2.35}$$

where $K_l = K(E_l^2)$ and $\bar{R}_a, \bar{R}_b$ are found using linear interpolation. The error of the integral is estimated via the inflated covariance matrix $\tilde{V}$

$$(\Delta\bar{I})^2 = \sum_{p=m}^{n}\sum_{q=m}^{n} \frac{\partial\bar{I}}{\partial\bar{R}_p}\tilde{V}(p,q)\frac{\partial\bar{I}}{\partial\bar{R}_q} \tag{2.36}$$

$$= \sum_{p,q=m}^{n} \left(\frac{E_{p+1}-E_{p-1}}{E_p}K_p\right)\tilde{V}(p,q)\left(\frac{E_{q+1}-E_{q-1}}{E_q}K_q\right). \tag{2.37}$$

Note that in order to match equation (2.35),

$$\begin{aligned} p = m &\rightarrow E_{p-1} = E_a \text{ and } E_p = E_a \\ p = m+1 &\rightarrow E_{p-1} = E_a \\ p = n-1 &\rightarrow E_{p+1} = E_b \\ p = n &\rightarrow E_{p+1} = E_b \text{ and } E_p = E_b \end{aligned}$$

and similarly for the index q. In addition, since $\bar{R}_a$ and $\bar{R}_b$ are interpolated, their correlations and errors are not defined in $\tilde{V}(p,q)$. Although one may find interpolated values for $\tilde{V}(a,a)$ or $\tilde{V}(b,b)$, the meaning of interpolating $\tilde{V}(a,q)$ or $\tilde{V}(p,b)$ is less clear. Therefore the following method is used so that the border terms in equation (2.37) are no longer ill-defined. Let $X_a = \bar{R}_a K_a$, then demand $X_a = \bar{R}_m\tilde{K}_m$ and solve for $\tilde{K}_m$, which is some modified value of K_m. Similarly, this is done for $X_b = \bar{R}_b K_b$. Therefore, if $\bar{R}_m\tilde{K}_m$ and $\bar{R}_n\tilde{K}_n$ is used instead of $\bar{R}_a K_a$ and $\bar{R}_b K_b$ in equation (2.35), the value of $\bar{I}$ remains the same and more importantly, all terms in equation (2.37) are now well defined.

2.1.5 Remarks

Choosing the size or energy binning of the clusters is an important issue. If it is too small, then the problem of the precise data being overwhelmed mentioned in Section 2.1.2 applies and if it is too large, some structures such as resonance peaks might become too smeared or missed entirely. So the cluster size is effectively a parametrisation on the shape and normalisation of R_{had}.

This may be demonstrated with the help of a toy model using two data sets shown in Fig. 2.4.The first data set have 16 points with large statistical ($\sim 17\%$) and systematic (25%) errors, while the second data set only have 3 points but they are very precise ($\sim$ 3% statistical error and 2.5% systematic error). From Fig. 2.4 we can see what happens to the fit with two different choices of clustering. The plot on top shows the fit using a cluster size of 5 MeV. Only one point from the precise data set is combined with the imprecise data, so the fit still follows the imprecise points with an unphysical looking dip near the peak. The combination with the single more precise point leads to a re-normalisation of both data sets, with a factor of 1/1.1528 for the imprecise data and 1/0.9982 for the precise one. The difference between the two factors reflect the

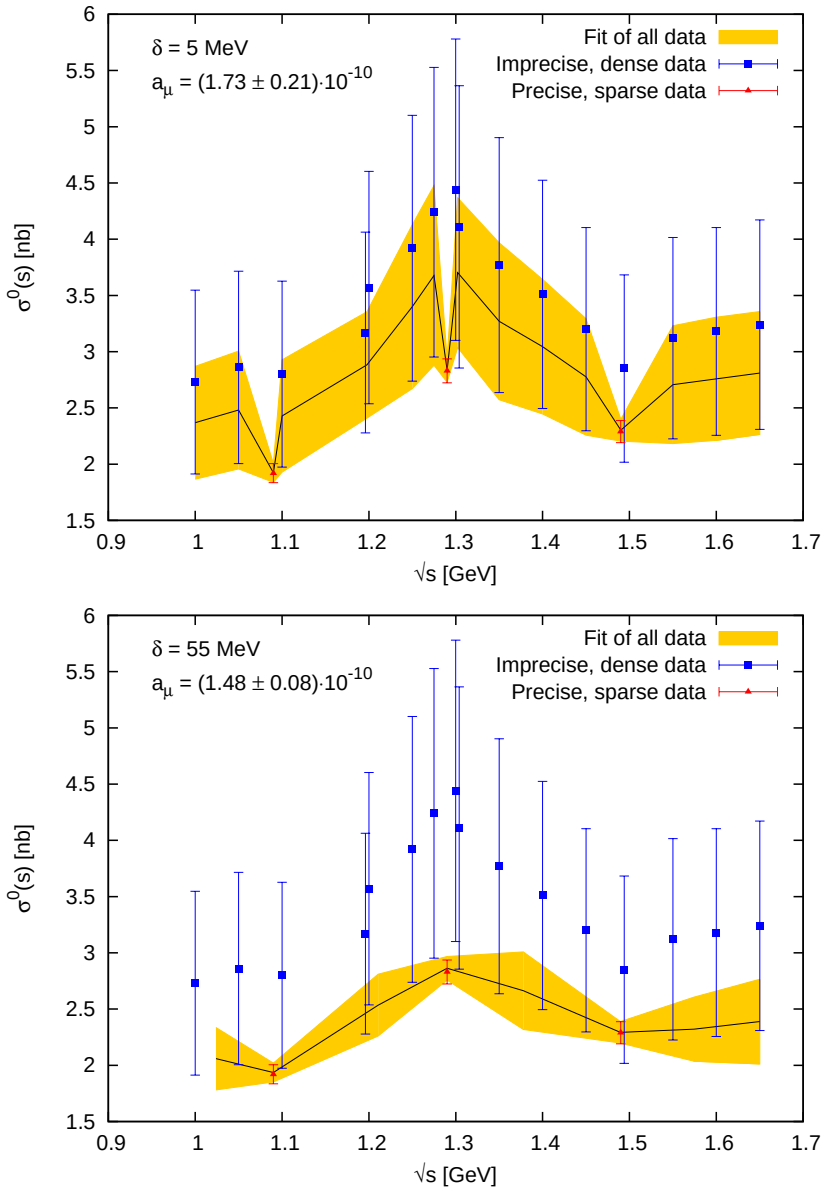

Fig. 2.4: Plots of two mock data and their fits to demonstrate the importance of choosing the appropriate cluster size. The top graph shows how numerous imprecise data can dominate the fit if the cluster size is too small. The graph on the bottom shows the fit with a larger cluster size, allowing the fewer but more precise data to contribute their weights. The error bars on the data represent the sum in quadrature of statistical and systematic errors.

difference between systematic errors of the two data sets. The plot on the bottom gives the fit when a cluster size of 55 MeV is used. Now all three points of the precise data are combined with the imprecise data points, and their weighting is illustrated by way the fit follows the precise data. The normalisation factors are now 1/1.3563 and 1/0.9951 for the imprecise and precise data sets respectively. Finally, the resulting a_μ and errors from integrating over the two fits using trapezoid rule shows that with a larger cluster

size, the mean was reduce by about 15% and the decrease in error was more than 50%. This of course, comes with the assumption that the cross section is constant within the larger 55 MeV interval. Now to assist us in choosing a better cluster size, we have the ability to produce a scan through a range of cluster or target cluster sizes in the continuum. The output of this scan include values for global $\chi^2_{\rm min}$/d.o.f., a_μ and its error. An actual example of this is shown by Fig. 2.11.

2.2 Results overview

In this work, we use measurements for 26 different hadronic final states or 'exclusive' channels and data for the $e^+e^- \to$ all hadrons process or 'inclusive' channel. These form the contributions to $a_\mu^{\rm had,\ LOVP}$ that are purely based on data and are described in Section 2.3. In addition to those exclusive channels, there are some final states that are not measured by experiments. However, the contribution from these channels can be determined by approximate relations to the appropriate cross section data, based on isospin symmetries of the final state particles. They are known as the 'isospin' channels and in this work, we follow the isospin relations derived in [78], which gives 11 different isospin channels using contributions from 15 exclusive channels as input, see Section 2.4 for details. This setup or isospin analysis is different to the one used in HMNT (03) [61] and (06) [62], where there were 4 isospin channels based on different isospin relations to the ones used in this work. Other non-data based contributions to $a_\mu^{\rm had,\ LOVP}$ including predictions using chiral perturbation theory (ChPT), J/ψ, ψ' and Υ resonances and perturbative QCD (pQCD) are detailed in Section 2.5. Now we can calculate $a_\mu^{\rm had,\ LOVP}$ (or $R_{\rm had}$) up to $\sqrt{s} = 2$ GeV by summing the a_μ results (or cross section data) from all the exclusive and isospin channels. This is usually called 'the sum of exclusive'. The calculation can also be done for $1.43 \lesssim \sqrt{s} \leq 11.09$ GeV by using the cross section data for the inclusive channel. Hence in the energy region $1.43 \lesssim \sqrt{s} \leq 2$ GeV, there is an overlap between inclusive and sum of exclusive, where the two methods can be compared, see Section 2.6. It should be noted that the total number of distinct final states that contribute in the sum of all exclusive (and isospin) channels is 27. This is due to the way the isospin relations uses the exclusive channels as input: some need to be counted as separate channels and summed accordingly, while others do not and some appear in more than one isospin relation (see Section 2.4, and Table 2.6 for details.) Finally, the total contribution to $a_\mu^{\rm had,\ LOVP}$ will be summarised in Section 2.8.

2.3 Data based channels

2.3.1 The $\pi^0\gamma$ channel

Although the $e^+e^- \to \pi^0\gamma$ channel defines the lower limit of the dispersion relation (1.52) with $\sqrt{s_{\rm th}} = m_\pi$, the data sets available [122–124] only encompass the energy region $0.60 \leq \sqrt{s} \leq 1.31$ GeV. Their contribution to $a_\mu^{\rm had}$ after combination and integration is,

$$a_\mu^{\pi^0\gamma}(0.60 \leq \sqrt{s} \leq 1.31 \text{ GeV}) = (4.54 \pm 0.14) \times 10^{-10} \tag{2.38}$$

See Fig. 2.5 for the result of the combination and fitting procedure. For energies below 0.60 GeV, chiral perturbation theory (ChPT) is used, see Section 2.5.1 for details.

2.3.2 The $\pi^+\pi^-$ channel

The $e^+e^- \to \pi^+\pi^-$ channel accounts for over 70% of $a_\mu^{\text{had, LOVP}}$, making it the largest and the most important contribution. This dominance comes from the $\rho(\to \pi^+\pi^-)$ intermediate state due to the weighting of the kernel function (1.50) and the cross section of the data. This channel has been measured from experiments using the direct scan method (by adjusting the e^+e^- beam energy), such as the recent, very precise results from CMD-2 and SND in Novosibirsk (see [125] for a brief review). Since 2005 however, analyses using the radiative return method[2] have also become available. KLOE (05) [127] was the first published results for the $\pi^+\pi^-$ channel based on this method and it was in fair agreement with other analyses from Novosibirsk apart from slight shape differences. However, it was these differences that prevented the KLOE (05) data from being combined on the bin-to-bin level in [62]. Thus they were only combined with the other data sets *after* integration. This is not preferred since not all data sets were treated equally and the error estimate may not have been completely realistic. Therefore as reported in [128], this analysis treats all the data sets in the same way, i.e. following the combination and fitting procedure as outlined in sections 2.1.2 and 2.1.3.

We now use 23 data sets [129–150] in total, and we apply FSR corrections, as discussed in Section 2.1.1, to [135–149]. There are three new results based on radiative return methods from KLOE [129,130][3] and BaBar [131]. These experiments provide full covariance matrices for statistical and systematic errors, which prompted the change to our non-linear χ^2 function (2.29). The energy range covered by the data sets is $0.305 \leq \sqrt{s} \leq 3.0$ GeV.

The effect of new radiative return data in the new fit can be seen in Fig. 2.6 showing the ρ-dominant region from about 0.6 to 0.95 GeV. The light (yellow) band

[2] See [126] for a review of this approach along with further references and results.

[3] The KLOE (08) data [130] supersede their 2005 results [127] but the KLOE (10) analysis is independent from the one in 2008.

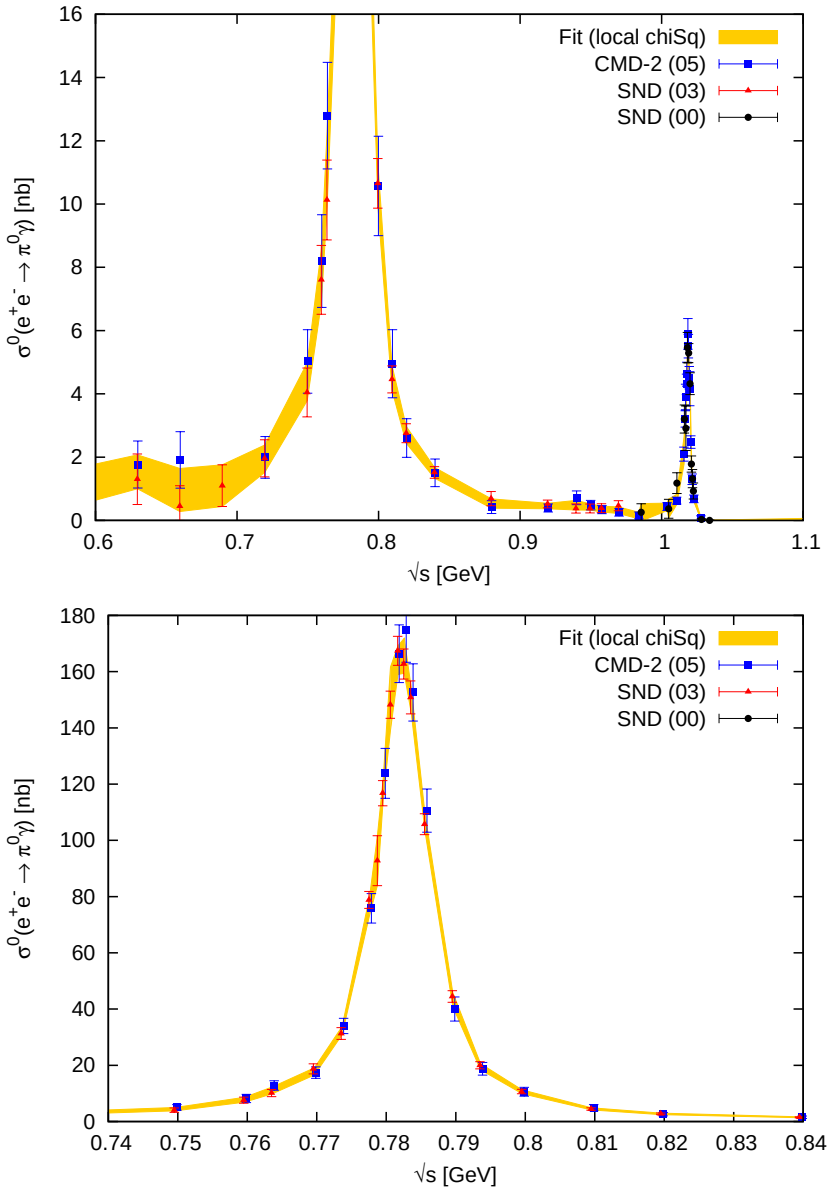

Fig. 2.5: The $e^+e^- \to \pi^0\gamma$ cross section, the (green) band shows the behaviour of the cross section after clustering and fitting with local χ^2 error inflation. The lower plot is an enlargement of the ω resonance region.

represents the result of our fit of all data. The dark (green) band is the new radiative return data from BaBar [131] and the data from KLOE [129, 130] are shown by the markers in the graph. Fig. 2.7 displays an enlargement of the $\rho - \omega$ interference region along with data from CMD-2 [133, 150] and SND [134]. Fig. 2.8 shows the low energy region close to threshold where the BaBar data have become a very valuable addition amongst the other less precise results. The prediction from ChPT is also shown, which is in agreement with the new fit and used in the energy region below 0.305 GeV, see Section 2.5.1 for details. From these figures, it should be apparent that the two

analyses from KLOE, which agree amongst themselves, are lower than the BaBar data. Furthermore, this tension causes the fit to interpolate between BaBar and KLOE. Nonetheless, the global $\chi^2_{\rm min}$/d.o.f. for the fit is ~ 1.4, which suggests the actual fit quality is still quite good. The differences between the three radiative return data sets and the fit can be demonstrated more clearly by their normalised differences as shown in Fig. 2.9. The differences of KLOE (08,10) and BaBar (09) compared to the fit *without* their presence can be seen from a similar plot in Fig. 2.10.

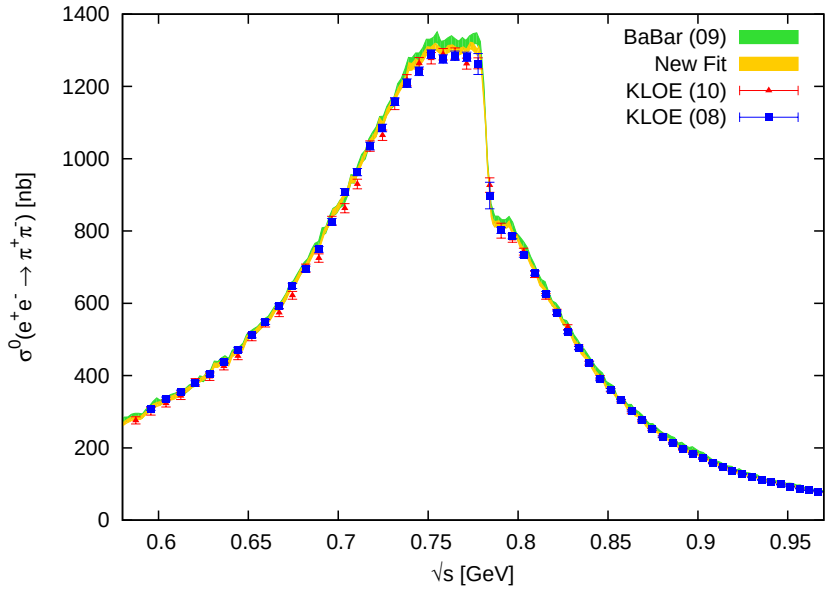

Fig. 2.6: Cross section plot of the $e^+e^- \to \pi^+\pi^-$ channel in the ρ-dominant region. Light (yellow) band: fit of all the data. Dark (green) band: radiative return data from BaBar [131]. Data from KLOE [129, 130] are shown with the markers as noted in the legend.

There are now a very large number of data points (879 in total) in this channel, of which more than half (337 data points from BaBar along with 75 and 60 points from the two KLOE analyses) comes from the new radiative return data sets. Therefore it is important to discuss the issue of fit stability with respect to different energy clustering. The increase in the number of data points means it is possible to adopt a very fine clustering that drastically reduces any biases from assumptions about the cross section. Nevertheless, there is still a dependence on the way data is combined, specifically the way data points are clustered together varies depends on the target energy cluster size δ, which may change the shape of the resulting fit. Fig. 2.11 shows this dependence on this δ from 1 to 5 MeV: the solid (red) line is the global $\chi^2_{\rm min}$/d.o.f.; the dashed (red) line displays the inflated error of the $\pi^+\pi^-$ contribution to $a_\mu^{\rm had,\ LOVP}$ (in units of 10^{-10}); finally the dotted (blue) line represents the corresponding mean value of $a_\mu^{\pi^+\pi^-}$ (again in units of 10^{-10}). From the graph, it can be seen that:

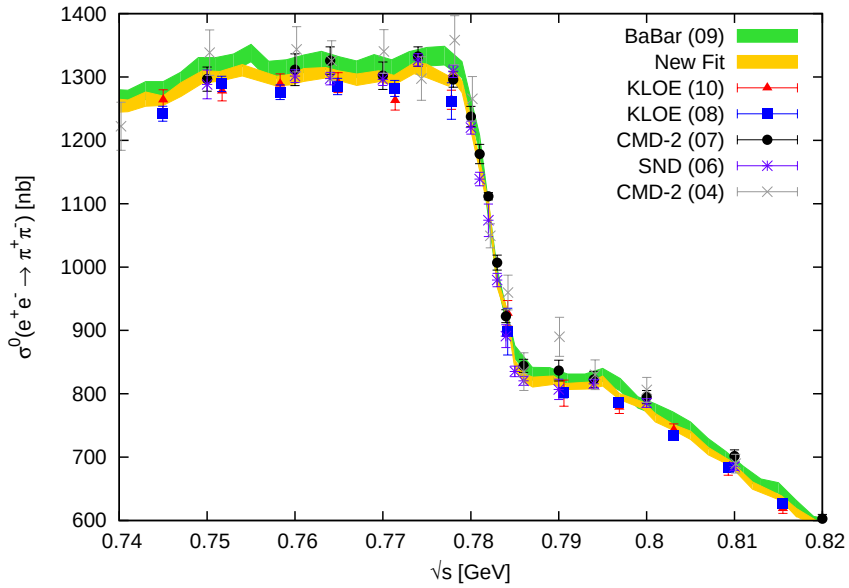

Fig. 2.7: This is the same as Fig. 2.6 except the $\rho - \omega$ interference region is enlarged. Important results from CMD-2 [133, 150] and SND [134] are also shown along with the radiative return data.

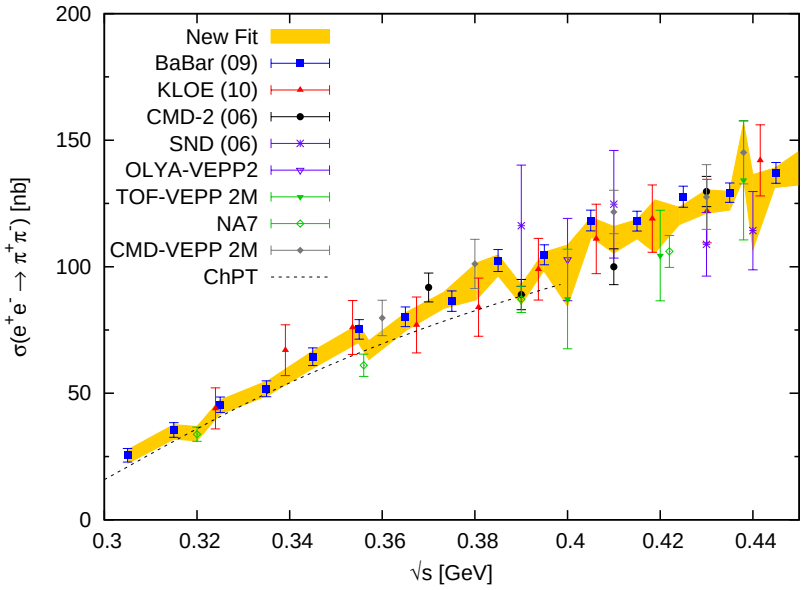

Fig. 2.8: This is the low energy tail of the $\pi^+\pi^-$ channel. The light (yellow) band is the result of the fit with data sets. Important data sets in this region are displayed by the markers indicated in the legend. The dashed line shows what chiral perturbation theory (ChPT) predicts, which is used from the threshold energy $\sqrt{s_{\rm th}}$ up to the first BaBar point at 0.305 GeV.

- it is preferable to take the target cluster size δ up to about 2 MeV due to the fit quality and the size of the error;

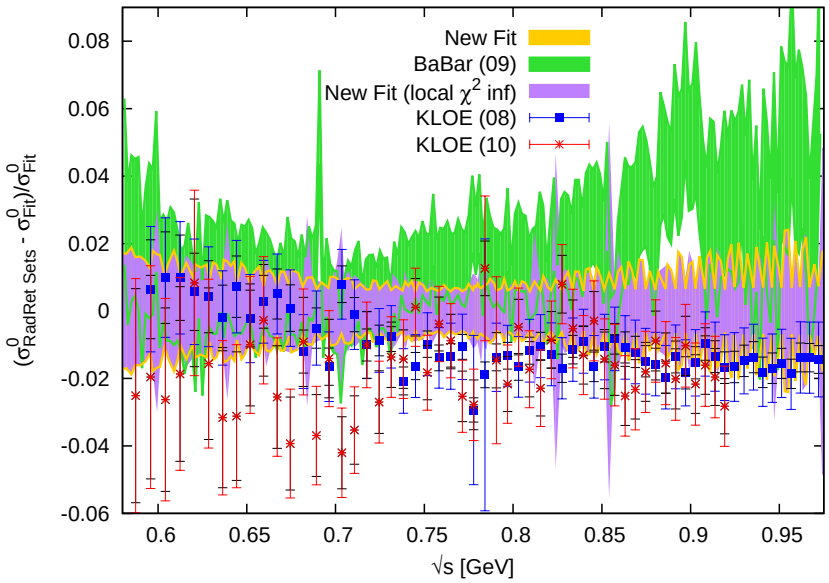

Fig. 2.9: Difference plot (normalised against the fit of all data) between the radiative return data from KLOE [129,130], BaBar [131] and the fit. The (lilac) band symmetric around the x-axis represents the error of the fit given by the diagonal elements of the covariance matrix and then inflated by the local χ^2. The light (yellow) thick lines highlight the error band of the fit without error inflation.

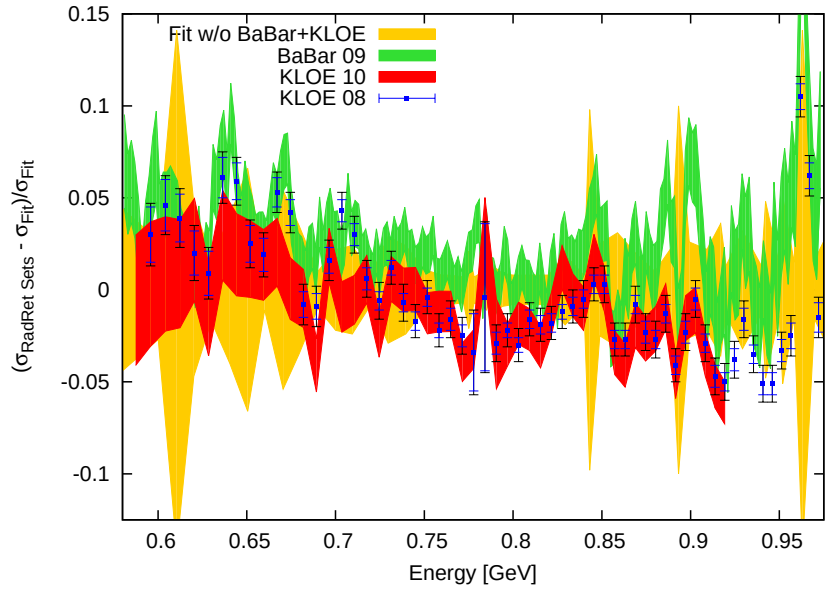

Fig. 2.10: Similar to Fig. 2.9, except it is with the fit that does not include the new radiative return data. Note the larger y-scale compared to Fig. 2.9.

- larger cluster sizes are disadvantageous because of the increase in χ^2_{min}/d.o.f. overshadows any reduction in the error before error inflation;
- the mean for $a_\mu^{\pi^+\pi^-}$ fluctuates by about 1σ within the range of the target δ.

Therefore, a target cluster size of $\delta = 1.5$ MeV was chosen since it gives the best fit quality, the smallest inflated error and a mean value for $a_\mu^{\pi^+\pi^-}$ that is neither too high nor too low in the possible choice of results. Using this choice we obtain by integrating

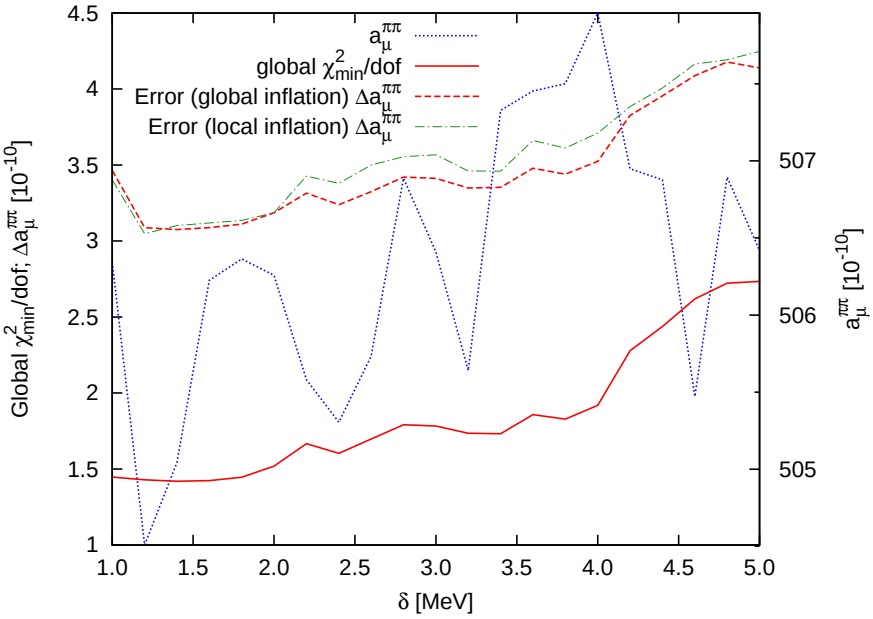

Fig. 2.11: Influence of the target cluster size δ on the global χ^2_{min}/d.o.f. (solid red line, left scale), the globally inflated error $\Delta a_\mu^{\pi^+\pi^-}$ (dashed red line, left scale) and the mean $a_\mu^{\pi^+\pi^-}$ (dotted blue, right scale). The dash-dotted (green) line represents the values of $\Delta a_\mu^{\pi^+\pi^-}$ with local error inflation. The $a_\mu^{\pi^+\pi^-}$ displayed here is calculated in the energy range $0.305 \leq \sqrt{s} \leq 2.0$ GeV.

up to 2 GeV, the upper limit for exclusive channels,

$$a_\mu^{\pi^+\pi^-}(0.305 \leq \sqrt{s} \leq 2 \text{ GeV}) = (505.77 \pm 3.09) \times 10^{-10}. \tag{2.39}$$

However, in order to compare the effect of including these new radiative return data, a low energy limit of 0.32 GeV has to be used since only the BaBar data goes down to 0.305 GeV. Using the new limit

$$a_\mu^{\pi^+\pi^-}(0.32 \leq \sqrt{s} \leq 2 \text{ GeV}) = (504.23 \pm 2.97) \times 10^{-10}, \tag{2.40}$$

and if the new radiative return sets are excluded but δ is still kept at 1.5 MeV,

$$a_\mu^{\pi^+\pi^-,\text{ w/o Rad. Ret.}}(0.32 \leq \sqrt{s} \leq 2 \text{ GeV}) = (501.26 \pm 4.48) \times 10^{-10}. \tag{2.41}$$

Hence the radiative return data causes a considerable increase to the result without their presence. Furthermore, without the data from KLOE and BaBar the fit actually favours a larger target cluster size of 4.2 MeV (which was used in [62]) giving,

$$a_\mu^{\pi^+\pi^-,\text{ w/o Rad. Ret.}}(0.32 \leq \sqrt{s} \leq 2 \text{ GeV}) = (498.65 \pm 3.28) \times 10^{-10}. \tag{2.42}$$

This rather significant increase is not unexpected given the plot in Fig. 2.10. The BaBar data is consistently larger compared to the fit apart from a few places, while the two KLOE data sets are on average, level with the fit. Furthermore, although the small increase in precision from adding these new radiative return data may seem odd given these data have relatively small errors, this is merely a reflection of the tension between the data sets discussed earlier.

Finally to complete the comparison, it is necessary to look at a restricted energy range, $0.5958 \leq \sqrt{s} \leq 0.9192$ GeV, where KLOE and BaBar data sets completely overlap with the other data. In this range, the KLOE data sets give

$$a_\mu^{\pi^+\pi^-}(\text{KLOE (08)}) = (376.3 \pm 3.4) \times 10^{-10} \tag{2.43}$$

$$a_\mu^{\pi^+\pi^-}(\text{KLOE (10)}) = (373.4 \pm 3.3) \times 10^{-10}, \tag{2.44}$$

which is in fair agreement. BaBar on the other hand is much higher

$$a_\mu^{\pi^+\pi^-}(\text{BaBar (09)}) = (384.4 \pm 2.8) \times 10^{-10}, \tag{2.45}$$

which is expected given what is shown in Figs. 2.6 and 2.9. For the combination of the data sets without the radiative return data,

$$a_\mu^{\pi^+\pi^-}(\text{w/o Rad.Ret.}) = (376.0 \pm 2.6) \times 10^{-10}, \tag{2.46}$$

using the same energy range with the larger, favoured choice of $\delta = 4.2$ MeV. Taking the weighted average of these numbers would give a value of $(377.9 \pm 1.5) \times 10^{-10}$. In comparison, combining all data before integration in this energy range along with the preferred $\delta = 1.5$ MeV gives,

$$a_\mu^{\pi^+\pi^-}(\text{All data}) = (380.0 \pm 2.2) \times 10^{-10}. \tag{2.47}$$

These two results are superb examples in showing some of the problems of combining data *after* integration as stated in Section 2.1.2. The smaller error in the weighted average is not representative of the tensions between the data sets discussed before. Furthermore, the lower mean does not reflect the true weighting of the more precise BaBar data. Therefore in this analysis, all the $\pi^+\pi^-$ data will be combined before integration when calculating their contribution to the SM prediction of a_μ.

2.3.3 The $\pi^+\pi^-\pi^0$ channel

The $e^+e^- \to \pi^+\pi^-\pi^0$ channel is the second largest contribution to $a_\mu^{\text{had, LOVP}}$, but it is an order of magnitude smaller than the largest. For this channel, we now use a total of 13 data sets, [146,150–158] including three scans from the recent CMD-2 analysis [151] not present in [62]. Fig. 2.12 is a log plot showing the new fit using local χ^2 and nearly all the data up to 2.4 GeV. The two large peaks are the ω and ϕ resonances, which

can be seen more clearly in Fig. 2.13. Although the energy range covered by all data is $0.48 \leq \sqrt{s} \leq 2.99$ GeV, all data points below 0.66 GeV are discarded and ChPT is used instead, see Section 2.5.1. This is done due to the lack of quality experimental data, which is illustrated by Fig. 2.14. Thus the contribution to $a_\mu^{\text{had, LOVP}}$ up to 2 GeV for this channel is

$$a_\mu^{\pi^+\pi^-\pi^0}(0.66 \leq \sqrt{s} \leq 2 \text{ GeV; Data}) = (47.51 \pm 0.99) \times 10^{-10}. \tag{2.48}$$

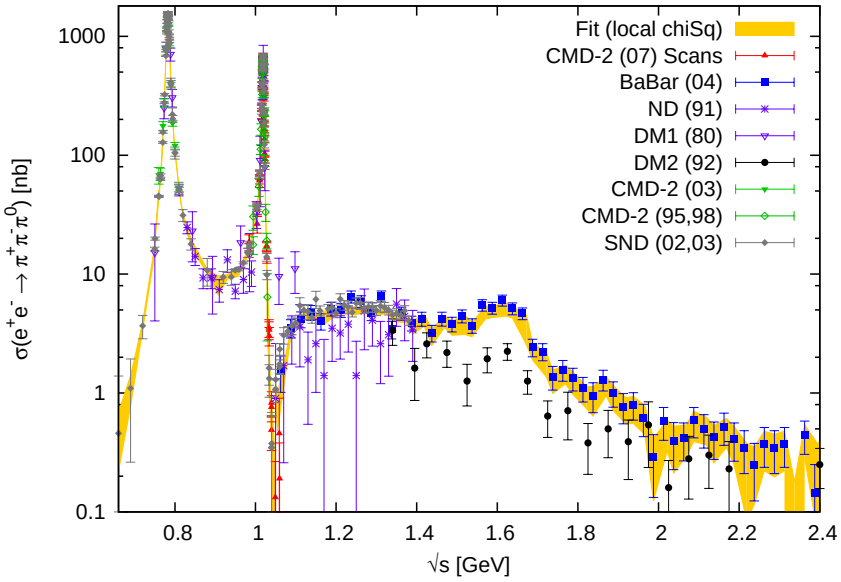

Fig. 2.12: Plot of the $\pi^+\pi^-\pi^0$ channel from 0.66 to 2.4 GeV clearly showing the ω and ϕ resonances. The new fit with local χ^2 inflation is shown by the (yellow) band and the most important data are indicated by the markers.

2.3.4 The 4π channels

The 4π channels only involve the $\pi^+\pi^-\pi^+\pi^-$ and $\pi^+\pi^-\pi^0\pi^0$ final states since $e^+e^- \to \gamma^* \to 4\pi^0$ is forbidden due to charge conjugation symmetry.

For the $2\pi^+2\pi^-$ channel, there have been no new data sets since [62]. However, due to the slight change in clustering size, the use of local χ^2 error inflation and our updated VP correction routines, there are small changes in the numerics. There is a total of 14 data sets [146, 159–171] and the result of their combination and fitting can be seen in Fig. 2.15. The presence of the more precise BaBar data [159] has not changed the fit very much. However, as noted in Table 1 of [62], the total error after integration has been improved significantly. Their contribution to a_μ, up to 2 GeV is,

$$a_\mu^{2\pi^+2\pi^-}(\sqrt{s} \leq 2 \text{ GeV}) = (14.65 \pm 0.47) \times 10^{-10}. \tag{2.49}$$

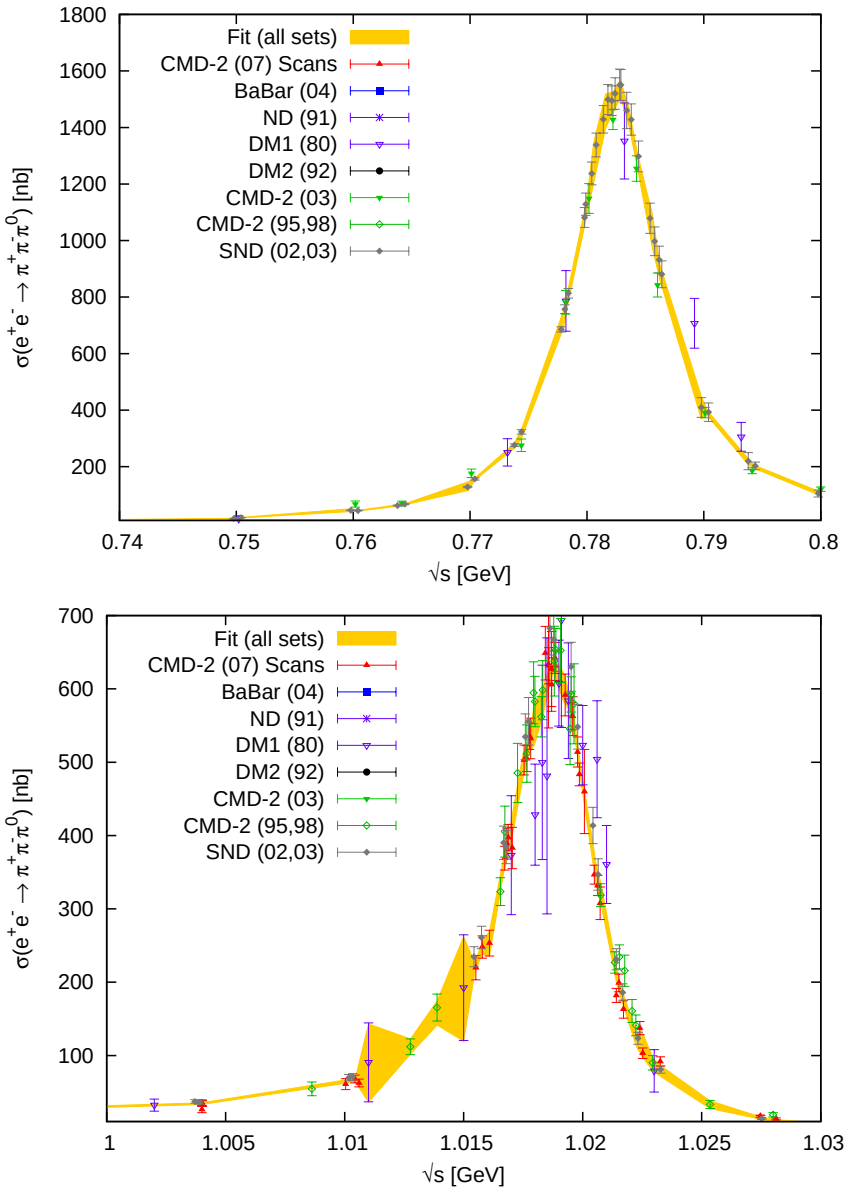

Fig. 2.13: Enlargement of the ω and ϕ resonance region in the $\pi^+\pi^-\pi^0$ channel.

Compared to the result from [62], which was integrated up to 1.43 GeV, the error has marginally increased by 0.02×10^{-10} while the mean has stayed the same.

For the $\pi^+\pi^-2\pi^0$ channel, there are 8 data sets [160, 164, 168, 171–175] covering the energy region from 0.915 to 2.4 GeV. All of these data are present since [61] but due to the same type of changes mentioned in the $2\pi^+2\pi^-$ channel, there are again small differences in the numerics. The cluster size have been increased from 10 to 16 MeV and the contribution is

$$a_\mu^{\pi^+\pi^-2\pi^0}(\sqrt{s} \leq 2 \text{ GeV; This work}) = (20.37 \pm 1.26) \times 10^{-10} \tag{2.50}$$

$$a_\mu^{\pi^+\pi^-2\pi^0}(\sqrt{s} \leq 2 \text{ GeV; HMNT (03)}) = (20.55 \pm 1.22) \times 10^{-10}. \tag{2.51}$$

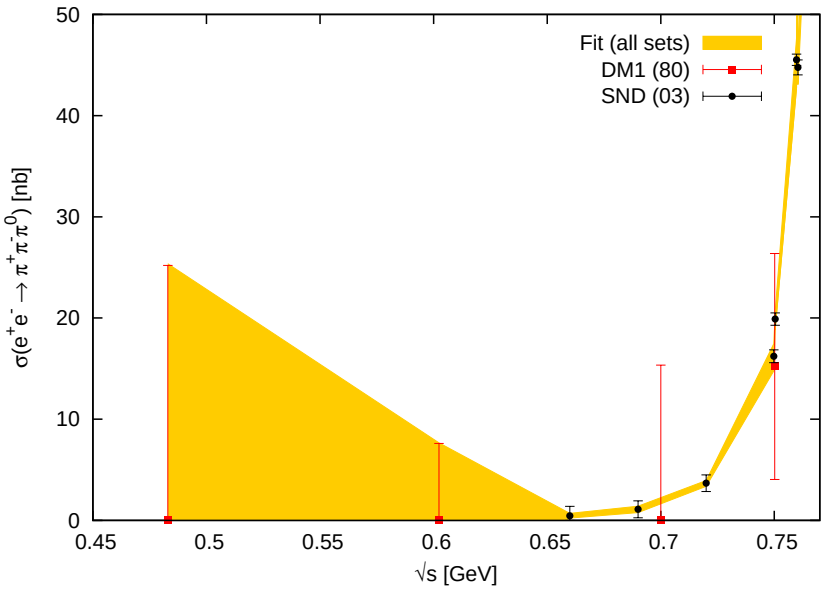

Fig. 2.14: The low energy region of the $\pi^+\pi^-\pi^0$ channel, showing the poor quality of data below 0.66 GeV.

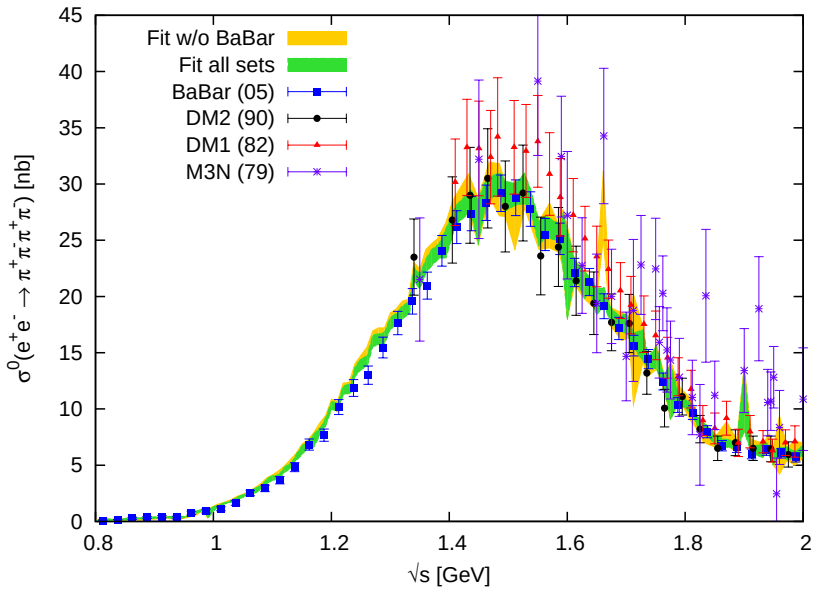

Fig. 2.15: Cross section plot of the $\pi^+\pi^-\pi^+\pi^-$ channel.

Fig. 2.16 illustrates the fit and most of the data sets for this channel. It is clear the data in this channel do not agree very well and preliminary data from BaBar shown in [78] can improve the fit significantly. However at this time, we do not have access to this data.

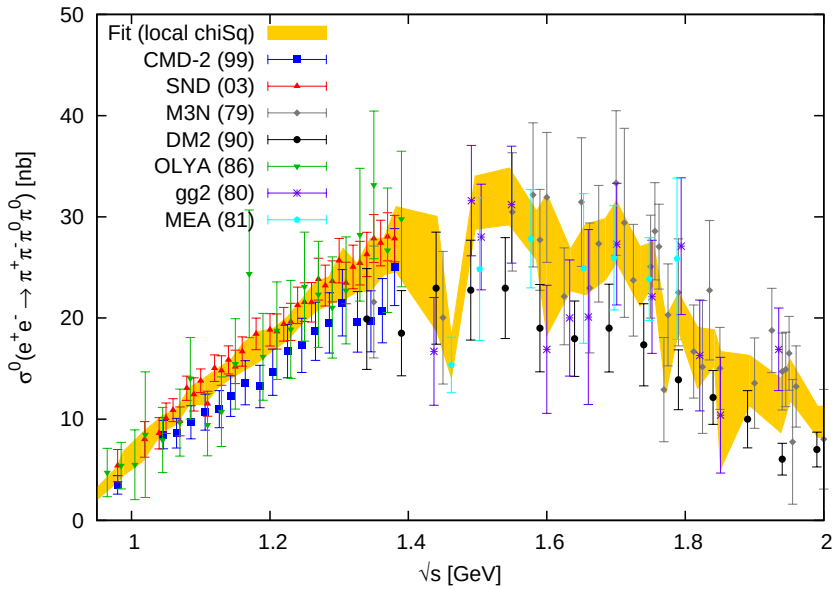

Fig. 2.16: Cross section plot of the $\pi^+\pi^-2\pi^0$ channel.

2.3.5 The $5\pi, 6\pi$ channels

The following 5π and 6π final states are directly measured by data: $\pi^+\pi^-\pi^+\pi^-\pi^0$, $\pi^+\pi^-\pi^0\pi^0\pi^0$, $\pi^+\pi^-\pi^+\pi^-\pi^+\pi^-$, and $\pi^+\pi^-\pi^+\pi^-\pi^0\pi^0$. The $\pi^+\pi^-\pi^0\pi^0\pi^0\pi^0$ final state is derived from isospin relations and the $e^+e^- \to 6\pi^0$ final state is forbidden due to charge conjugation symmetry. For all the data based channels, their contributions are part of the input for the new set of isospin channels and not summed separately.

For the $2\pi^+2\pi^-\pi^0$ final state we now use 6 data sets [146, 161, 174–177], including new data from BaBar [176]. The old M3N data set [160] was removed because it is incompatible with the new BaBar data and is only available from a thesis. In addition, the data from DM1 [177] have been revised to include the non-resonant background. The cluster size have also been decreased from 30 MeV to 24 MeV. Fig. 2.17 shows the new fit including the BaBar data as well as the fit from HMNT (03) [61]. Here we see that the new very precise BaBar data completely dominates the fit. The M3N data that was excluded in the new fit is shown on the graph for reference. Integrating up to 2 GeV, the new fit gives

$$a_\mu^{2\pi^+2\pi^-\pi^0}(\text{This work}) = (1.42 \pm 0.09) \times 10^{-10}, \tag{2.52}$$

which is much lower and more precise than the value from [61] due to the new data from BaBar,

$$a_\mu^{2\pi^+2\pi^-\pi^0}(\text{HMNT (03)}) = (2.85 \pm 0.25) \times 10^{-10}. \tag{2.53}$$

Note again that in this work, this channel will not contribute directly, instead the results will be used as input for the $(2\pi^+2\pi^-\pi^0)_{\text{no }\eta}$ isospin relation. The subscript

'no η' means contributions from $\eta(\to \pi^+\pi^-\pi^0)\pi^+\pi^-$ is excluded, see Section 2.4 for details.

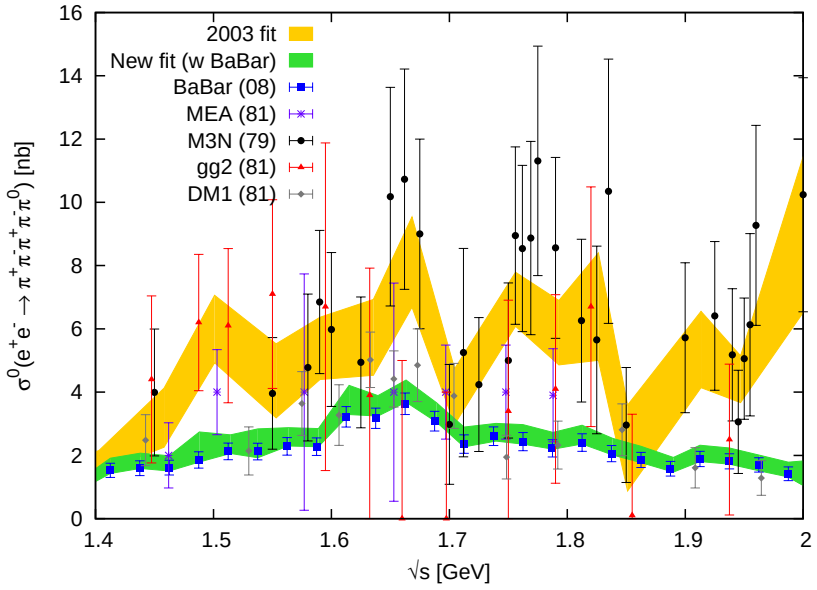

Fig. 2.17: Cross section plot of the $e^+e^- \to 2\pi^+2\pi^-\pi^0$ final state. Note that the M3N data set in the plot is not used in the new fit.

The $\pi^+\pi^-3\pi^0$ final state will no longer use the single set of data from M3N [160]. Instead, it will be estimated in the form of $(\pi^+\pi^-3\pi^0)_{\text{no }\eta}$ using an isospin relation.

For the $2\pi^+2\pi^-2\pi^0$ channel, we use 4 data sets [161,174,175,178] including again, new data from BaBar [178]. Like before, the data from M3N is no longer used in the new fit. Furthermore, a set of data from DM2 [179] is now also excluded. It is incompatible with the new data from BaBar, causing the entire fit to be artificially shifted too much upwards and completely missing the BaBar data from about 1.6 to 2 GeV as shown in Fig. 2.19. Fig. 2.18 shows the new fit including the BaBar data and excluding the M3N and DM2 data, which are still plotted for reference. Note also the cluster size has been increased from 10 to 26 MeV. Now the contribution to a_μ up to 2 GeV from this channel is

$$a_\mu^{2\pi^+2\pi^-2\pi^0}(\text{This work}) = (1.89 \pm 0.24) \times 10^{-10}, \tag{2.54}$$

$$a_\mu^{2\pi^+2\pi^-2\pi^0}(\text{HMNT (03)}) = (3.32 \pm 0.29) \times 10^{-10}. \tag{2.55}$$

Again the results are much lower than before as the fit now prefers to follow the new, lower BaBar data. The minor reduction in error is a reflection of the inconsistency between the new and older data sets. Note that contribution from this channel will be used as input for the $(2\pi^+2\pi^-2\pi^0)_{\text{no }\eta}$ isospin relation and not summed separately.

In the $3\pi^+3\pi^-$ channel, we use 5 data sets [160,161,178–180], of which BaBar again has provided a new measurement [178]. Fig. 2.20 shows the fit for this final state. Note

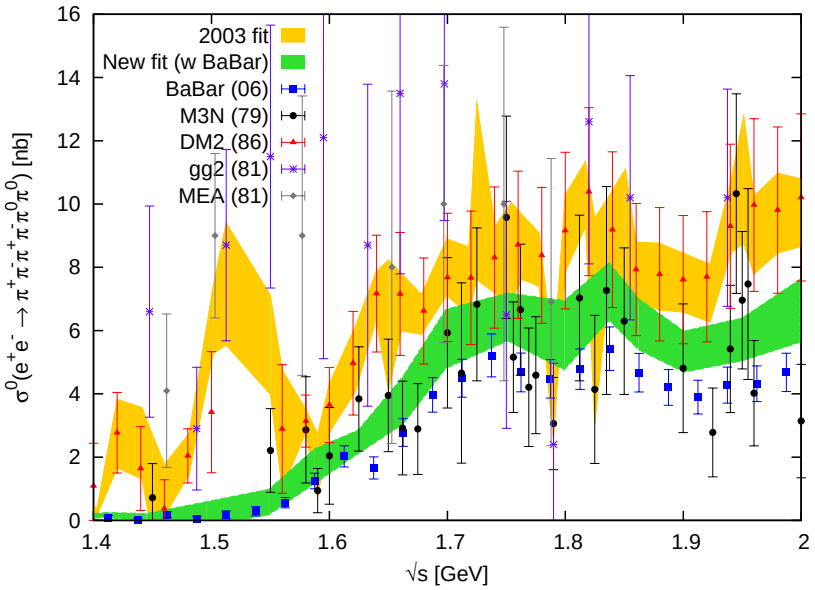

Fig. 2.18: Plot of the $2\pi^+2\pi^-2\pi^0$ channel showing the new fit including BaBar and the old fit from HMNT (03). The data from M3N [160] and DM2 [179] are excluded in the new fit but are plotted for reference.

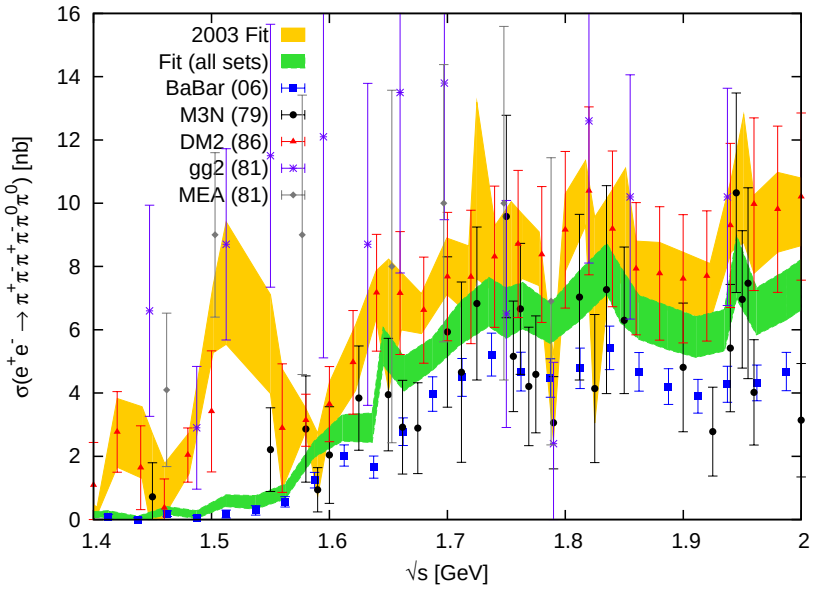

Fig. 2.19: Plot of the $2\pi^+2\pi^-2\pi^0$ channel if the new fit includes the M3N and DM2 data sets. It shows how these data artificially pulls the fit upwards, and no longer encompasses the more precise data from BaBar.

that the M3N and DM2 data are *included* in the new fit in this case, however the first point in the M3N data was not used since it was anomalously large with an equally large error (1.56 ± 1.11 nb). Once again the cluster size have changed, from 40 MeV to 18 MeV since the new BaBar data have a much finer binning. Up to 2 GeV, the

contribution from this channel compared to 2003 give,

$$a_\mu^{3\pi^+3\pi^-}(\sqrt{s} \leq 2 \text{ GeV; This work}) = (0.28 \pm 0.02) \times 10^{-10} \tag{2.56}$$

$$a_\mu^{3\pi^+3\pi^-}(\sqrt{s} \leq 2 \text{ GeV; HMNT (03)}) = (0.22 \pm 0.02) \times 10^{-10}. \tag{2.57}$$

The increase in mean is expected due to the slightly higher BaBar data, which causes more tension in the fit so the error is only reduced by 0.006×10^{-10}.

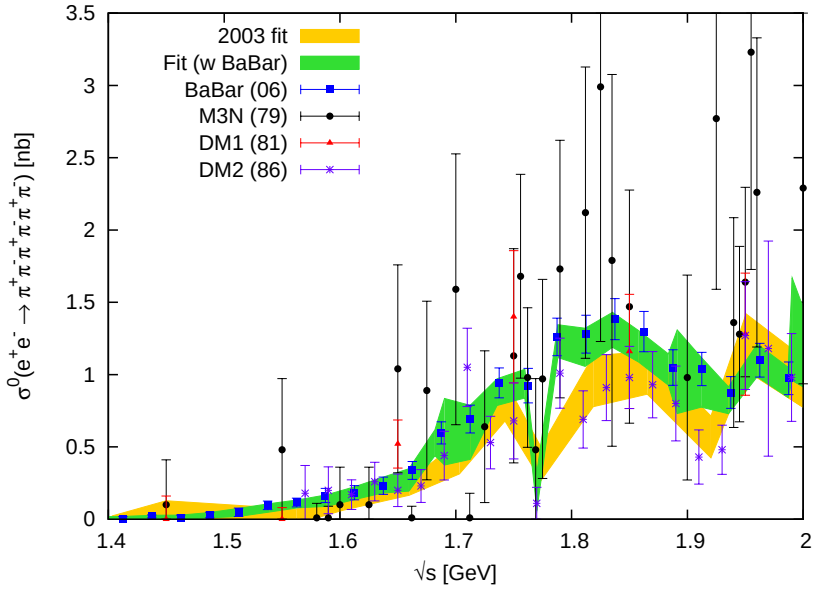

Fig. 2.20: Plot of the $3\pi^+3\pi^-$ channel. The new fit is higher than the fit from HMNT (03) due to the inclusion of the new BaBar data.

2.3.6 The KK channels

The KK channels include the K^+K^- and $K_S^0K_L^0$ final states. The K^+K^- channel now uses 13 sets of data [143, 145, 146, 155, 181–187] including two new scans from CMD-2 [181] and a new measurement from SND [182]. Fig. 2.21 shows the fit including all the new data sets, the most important data in this channel are also displayed. Fig. 2.22 zooms into the ϕ resonance region, which gives the greatest contribution in this channel. Integrating up to 2 GeV,

$$a_\mu^{K^+K^-}(\sqrt{s} \leq 2 \text{ GeV; This work}) = (22.15 \pm 0.46) \times 10^{-10} \tag{2.58}$$

$$a_\mu^{K^+K^-}(\sqrt{s} \leq 2 \text{ GeV; HMNT (03)}) = (22.35 \pm 0.77) \times 10^{-10}. \tag{2.59}$$

So the mean in this new analysis has remained roughly the same while the uncertainty has decreased significantly compared to 2003.

For the $K_S^0K_L^0$ channel, there is 1 new set of data from SND [188] since HMNT (03) taking the total up to 11 data sets [173, 187–190]. Fig. 2.23 displays the new fit along

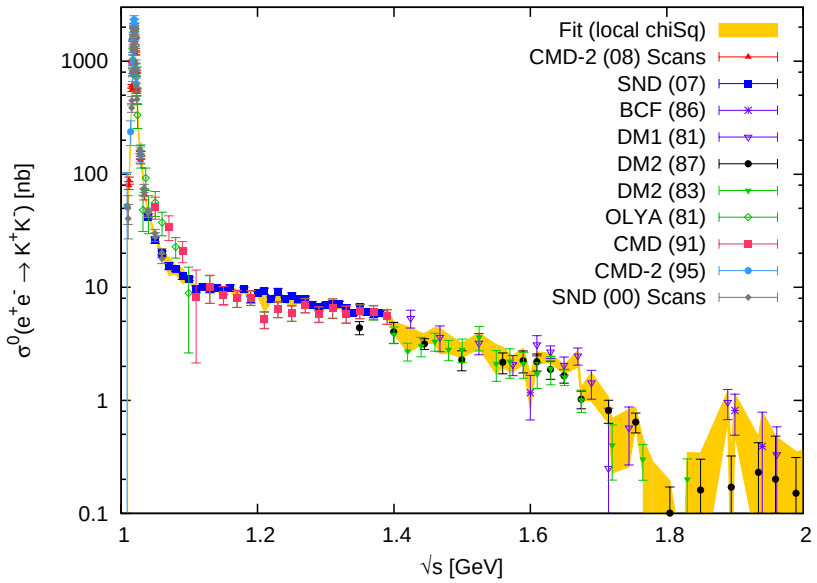

Fig. 2.21: Plot of the entire energy range for the K^+K^- channel including the ϕ resonance. The most relevant data sets are shown by the points in the graph.

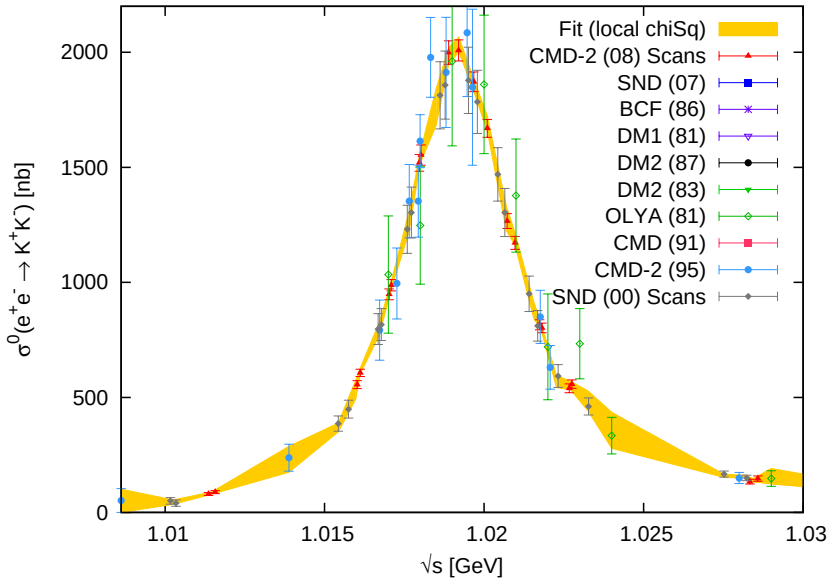

Fig. 2.22: Enlargement of the ϕ resonance region in the K^+K^- channel.

with all the data in this channel, while Fig. 2.24 zooms in on the ϕ resonance region with the data sets in that region listed. Comparing with HMNT (03)

$$a_\mu^{K_S^0 K_L^0}(\sqrt{s} \leq 2 \text{ GeV; This work}) = (13.33 \pm 0.16) \times 10^{-10} \tag{2.60}$$

$$a_\mu^{K_S^0 K_L^0}(\sqrt{s} \leq 2 \text{ GeV; HMNT (03)}) = (13.30 \pm 0.32) \times 10^{-10}, \tag{2.61}$$

the mean value has only changed marginally while the error has decreased by half.

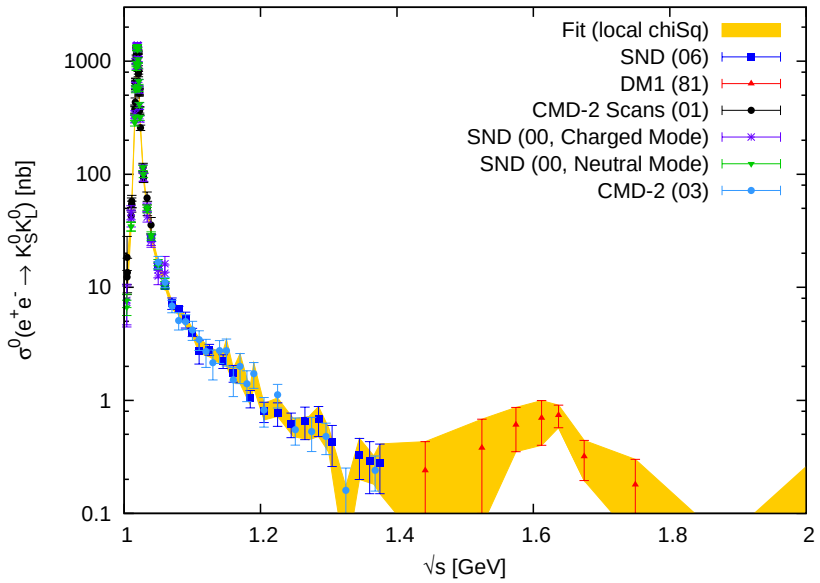

Fig. 2.23: Plot of the $K_S^0 K_L^0$ channel up to 2 GeV including the ϕ resonance region. All data sets are shown by the points in the graph.

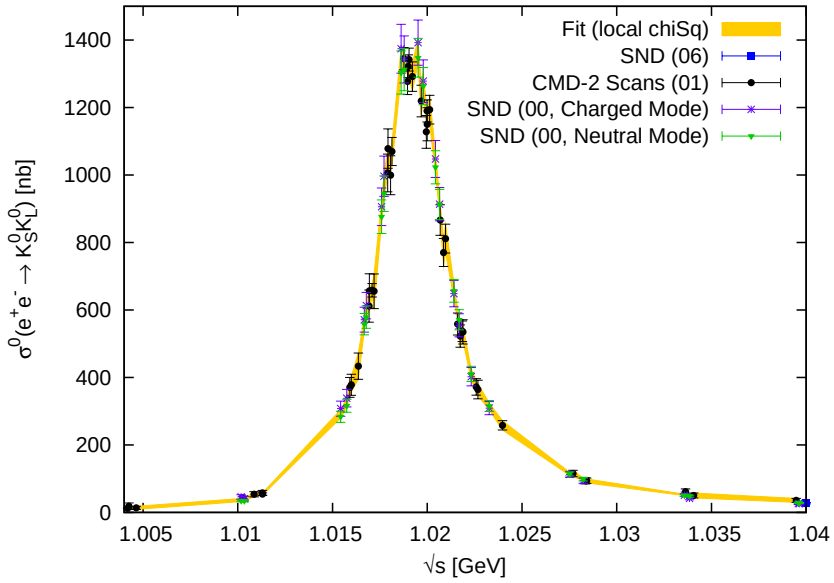

Fig. 2.24: Enlargement of the ϕ resonance region in the $K_S^0 K_L^0$ channel.

2.3.7 $KK + n\pi$ channels

The final states here include $K_S^0 K^{\pm}\pi^{\mp}$, $K^*K\pi$, $K^+K^-\pi^+\pi^-$, $K^+K^-\pi^0\pi^0$ and finally $K^+K^-\pi^+\pi^-\pi^0$. Their contributions are all used as input in the new isospin analysis to compute the $K\bar{K}\pi$, $K\bar{K}2\pi$ and $K\bar{K}3\pi$ isospin channels. Data for the $K_S^0 K^{\pm}\pi^{\mp}$ final state are no longer used since it will be estimated as part of the $K\bar{K}\pi$ isospin channel. Similarly, the old and imprecise data for the $K_S^0 X$ channel (X denotes any hadronic

state), which were used for the $K\bar{K}2\pi$ iso-spsin channel, are no longer needed due to a new isospin relation for $K\bar{K}2\pi$.

For the $K^0_S K^\pm\pi^\mp$ channel, we use 4 data sets in total, 1 from DM1 [191], 2 from DM2 [192, 193] and a new measurement from BaBar [194]. The cluster size in the continuum have been decreased from 40 to 18 MeV and the new fit can be seen along with all the data can be seen in Fig. 2.25. Once again, the more precise BaBar data have the most influence on the fit. Integrating up to 2 GeV we have,

$$a_\mu^{K^0_S K^\pm\pi^\mp}(\sqrt{s} \leq 2 \text{ GeV; This work}) = (0.91 \pm 0.05) \times 10^{-10} \tag{2.62}$$

$$a_\mu^{K^0_S K^\pm\pi^\mp}(\sqrt{s} \leq 2 \text{ GeV; HMNT (03)}) = (1.00 \pm 1.11) \times 10^{-10}. \tag{2.63}$$

The more precise BaBar data have helped to reduce the error in this channel by more than 50%. This result will be part of the input for the $K\bar{K}\pi$ isospin relation, so it will not be summed separately.

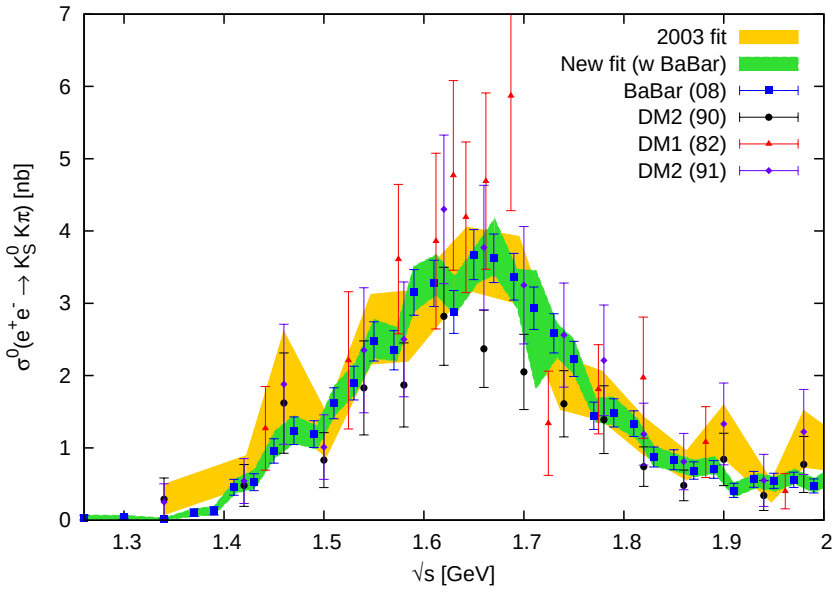

Fig. 2.25: Plot of the $K^0_S K^\pm\pi^\mp$ channel. The darker (green) band shows the new fit including BaBar and using local χ^2. The lighter (yellow) band replicates fit using HMNT (03) data and settings.

The $K^*K\pi$ and $K^+K^-\pi^0\pi^0$ channels have 2 data sets each, and they all come from the same two new measurements by BaBar [195,196]. Their contributions up to 2 GeV are

$$a_\mu^{K^*K\pi}(\sqrt{s} \leq 2 \text{ GeV}) = (0.78 \pm 0.03) \times 10^{-10} \tag{2.64}$$

$$a_\mu^{K^+K^-\pi^0\pi^0}(\sqrt{s} \leq 2 \text{ GeV}) = (0.16 \pm 0.01) \times 10^{-10}. \tag{2.65}$$

These results form part of the input for the $K\bar{K}2\pi$ isospin relation and not summed separately. So there is no actual double counting between $K^*K\pi$ and $K^0_S K^\pm\pi^\mp$ channels.

For the $K^+K^-\pi^+\pi^-$ final state, we use a total of 5 data sets where one comes from DM1 [197], another is from DM2 [192] and the last three are from BaBar [159,195,196], of which [195,196] are new measurements since HMNT (06). Fig. 2.26 shows the result of the fit and all the data sets. Once again, the new more precise data from BaBar dictates the shape and normalisation of the fit. The contribution up to 2 GeV is

$$a_\mu^{K^+K^-\pi^+\pi^-}(\sqrt{s} \leq 2 \text{ GeV}) = (0.99 \pm 0.04) \times 10^{-10}. \tag{2.66}$$

In HMNT (03) and (06), contribution from this channel was not used in any way at all because it was already included in the old $K\bar{K}2\pi$ isospin relation. However in this work, the $K^+K^-\pi^+\pi^-$ contribution is used as one of the inputs for the new $K\bar{K}2\pi$ isospin relation. Hence, this channel is used, but its contribution is not summed separately.

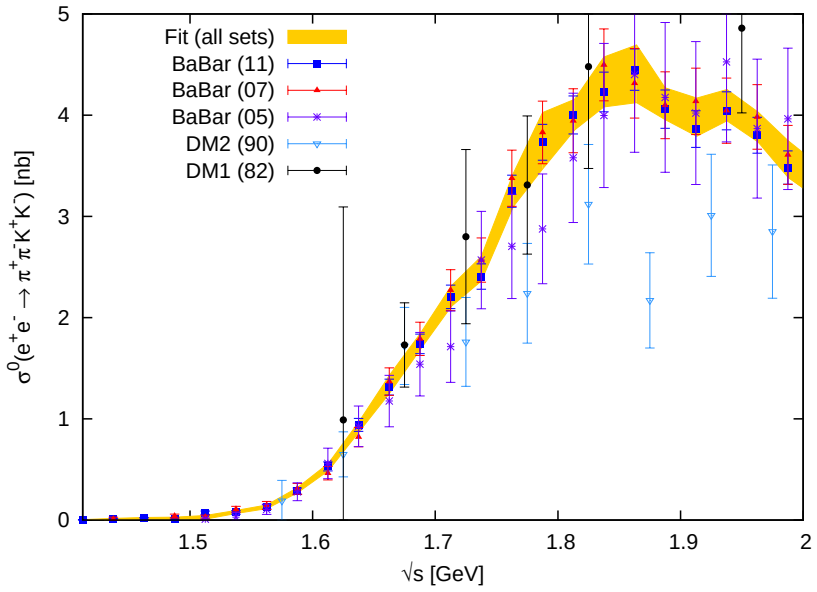

Fig. 2.26: Plot of the $K^+K^-\pi^+\pi^-$ channel showing the new fit as well as all the data sets.

Finally, the $K^+K^-\pi^+\pi^-\pi^0$ channel is measured recently by BaBar [176], giving a single data set. It has a small contribution up to 2 GeV

$$a_\mu^{K^+K^-\pi^+\pi^-\pi^0}(\sqrt{s} \leq 2 \text{ GeV}) = (0.09 \pm 0.01) \times 10^{-10}, \tag{2.67}$$

which is used as part of the input for the $K\bar{K}3\pi$ isospin relation and not added separately.

2.3.8 The η, ω, ϕ channels

The channels represented here are $\eta\gamma$, $\eta\pi^+\pi^-$, $\eta 2\pi^+2\pi^-$, $\eta\omega$, $\omega(\to \pi^0\gamma)\pi^0$, $\omega\pi^+\pi^-$, $\eta\phi$, $\phi\pi^0$, $\phi\pi^+\pi^-$, and $\phi(\to$ unaccounted).

We use 8 data sets [122, 124, 155, 198–201] for the $\eta\gamma$ final state, where the two scans from SND [198] are re-analyses of [202]. These re-analyses replaces the earlier SND scans [202] added in HMNT (06). Figs. 2.27 and 2.28 shows the new fit and most of the data. The cluster size in the continuum is now 2.5 MeV compared to 10 MeV in 2006 and the contribution from this channel is,

$$a_\mu^{\eta\gamma}(0.66 \leq \sqrt{s} \leq 1.36 \text{ GeV}) = (0.69 \pm 0.02) \times 10^{-10}. \tag{2.68}$$

Compared to HMNT (06), the mean value has gone down by 0.02×10^{-10} and the error has decreased by 0.01×10^{-10}.

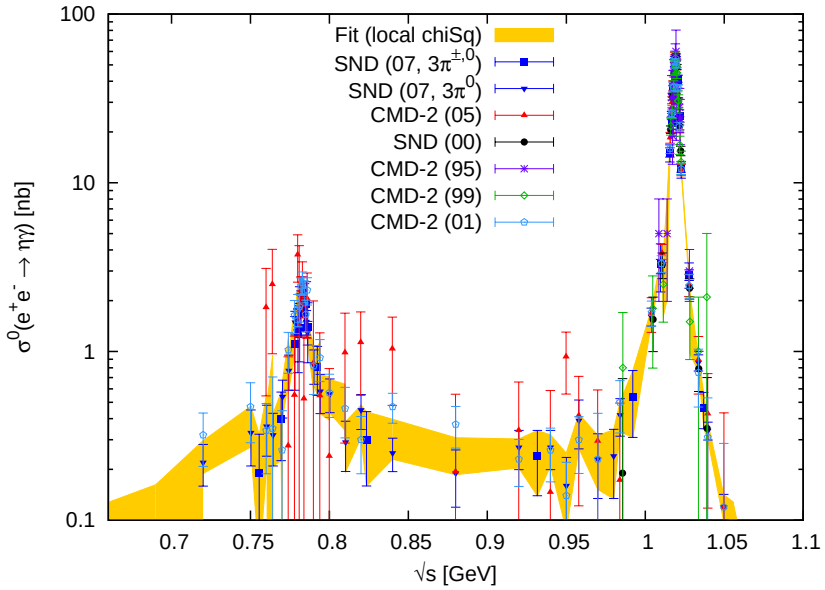

Fig. 2.27: Plot of the $\eta\gamma$ channel up to 1.1 GeV including the ϕ resonance region, the most relevant data points are displayed.

There are no new data for the $\eta\pi^+\pi^-$ channel since HMNT (03). The two existing sets of data are from DM2 [203] and CMD-2 [204]. The cluster size have been increased from 30 MeV to 55 MeV, and integrating up to 2 GeV,

$$a_\mu^{\eta\pi^+\pi^-}(1.29 \leq \sqrt{s} \leq 2 \text{ GeV}) = (0.98 \pm 0.24) \times 10^{-10}. \tag{2.69}$$

Note we no longer multiply this result by a factor of $1 - \mathcal{B}(\eta \to \pi^+\pi^-\pi^0) - \mathcal{B}(\eta \to 3\pi^0)$ due to the new isospin analysis, see Section 2.4 for details.

The $\eta 2\pi^+ 2\pi^-$ final state was only recently measured by BaBar [176]. The total contribution up to 2 GeV is

$$a_\mu^{\eta 2\pi^+ 2\pi^-}(1.3375 \leq \sqrt{s} \leq 2 \text{ GeV}) = (0.11 \pm 0.02) \times 10^{-10}. \tag{2.70}$$

The $\eta\omega$ channel comes from the BaBar measurement [178] of the $2\pi^+2\pi^-2\pi^0$ final state. First, the $2\pi^+2\pi^-2\pi^0$ events are filtered, so only those that come from $\eta\omega$ decays

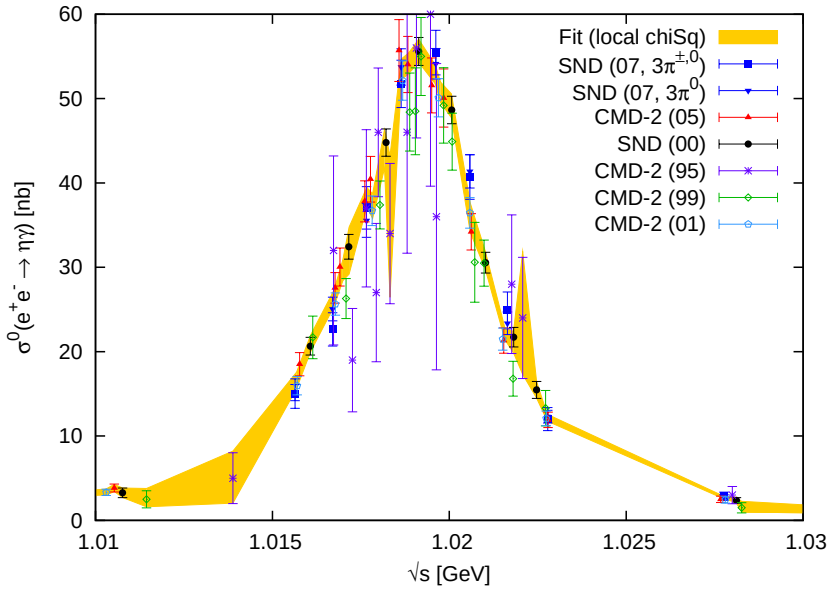

Fig. 2.28: Enlargement of the ϕ resonance region in the $\eta\gamma$ channel.

are kept. Then the background is subtracted and corrections to the cross section from the relevant η, ω decays are applied. Finally the resulting data, which are shown in Fig. 19 of [178], are fitted with a resonance type parametrisation using equations (6) and (7) of [178],

$$\sigma_{e^+e^-\to\eta\omega}(s) = \frac{F(s)}{s^{3/2}} \frac{m^5\Gamma_0^2\sigma_0}{F(m^2)((s-m^2)^2+s\Gamma_0^2)}. \tag{2.71}$$

where the fitted parameters are mass m, width Γ_0 and resonance peak σ_0. Now

$$F(s) = \left(\sqrt{\frac{(s+m_\eta^2-m_\omega^2)^2}{4s} - m_\eta^2}\right)^3, \tag{2.72}$$

is a phase space function of the η (or ω) momentum in the rest frame of the $\eta\omega$ system. Since the data from Fig. 19 of the BaBar paper is not available to us, we have decided to use the result of their parametrisation for this channel i.e. equation (2.71) with $m = 1.645 \pm 0.008$ GeV, $\Gamma_0 = 0.114 \pm 0.014$ GeV and $\sigma_0 = 3.08 \pm 0.33$ nb. Specifically, we have created a pseudo data set using equation (2.71) based on the energy binning of the $2\pi^+2\pi^-2\pi^0$ data. The first pseudo-data point is 1.3325 GeV, since there is no phase space for the energy bin below. The absolute errors for the fit parameters as well as the masses of η and ω were converted to percentage errors and added in quadrature for use as the common systematic error f_k. The resulting contribution up to 2 GeV is,

$$a_\mu^{\eta\omega}(1.3325 \le \sqrt{s} \le 2 \text{ GeV}) = (0.43 \pm 0.07) \times 10^{-10}. \tag{2.73}$$

For the $\omega(\to \pi^0\gamma)\pi^0$ final state, we use 9 data sets [146,164,173,205–209] with a new measurement from KLOE [205]. The $\omega(\to \pi^+\pi^-)\pi^0$ and $\omega(\to \pi^+\pi^-\pi^0)\pi^0$ final states

are not considered because they are already accounted for in the corresponding 3π and 4π channels. Therefore after applying the branching ratio $\mathcal{B}(\omega \to \pi^0\gamma) = 0.0828$ [23], the contribution from this channel and those from HMNT (03) are

$$a_\mu^{\omega(\to\pi^0\gamma)\pi^0}(\sqrt{s} \leq 2 \text{ GeV; This work}) = (0.77 \pm 0.03) \times 10^{-10} \tag{2.74}$$

$$a_\mu^{\omega(\to\pi^0\gamma)\pi^0}(\sqrt{s} \leq 2 \text{ GeV; HMNT (03)}) = (0.83 \pm 0.03) \times 10^{-10}. \tag{2.75}$$

Note that the lower mean in this work is due to a combination of the change in cluster size from 20 to 11 MeV and update in branching ratio from 0.087 to 0.0828. The new KLOE data had a minimal effect.

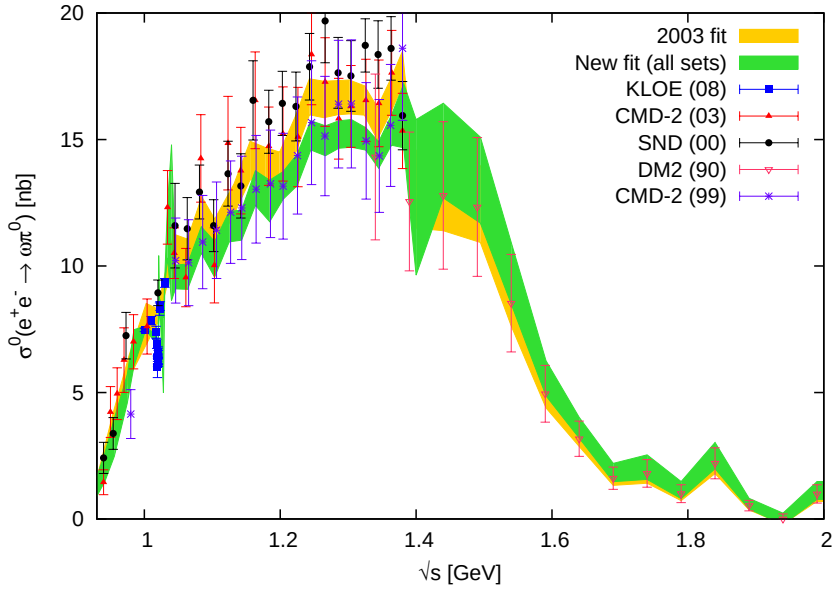

Fig. 2.29: Plot of the $\omega\pi^0$ channel up to 2 GeV. The most relevant data are displayed.

We use 3 data sets [154, 177, 204] for the $\omega\pi^+\pi^-$ channel giving

$$a_\mu^{\omega\pi^+\pi^-}(1.29 \leq \sqrt{s} \leq 2 \text{ GeV}) = (0.79 \pm 0.10) \times 10^{-10}. \tag{2.76}$$

We do not multiply this result by any branching ratio since it will used as input in the new $\omega\pi\pi$ isospin relation and not summed directly. See Fig. 2.30

Data for the $\eta\phi$ [176,194], $\phi\pi^0$ [194] and $\phi\pi^+\pi^-$ [195,196] final states all come from new or recent measurements by BaBar. Their contributions up to 2 GeV are,

$$a_\mu^{\eta\phi}(1.57 \leq \sqrt{s} \leq 2 \text{ GeV}) = (0.46 \pm 0.03) \times 10^{-10} \tag{2.77}$$

$$a_\mu^{\phi\pi^0}(1.25 \leq \sqrt{s} \leq 2 \text{ GeV}) = (0.04 \pm 0.01) \times 10^{-10} \tag{2.78}$$

$$a_\mu^{\phi\pi^+\pi^-}(1.4875 \leq \sqrt{s} \leq 2 \text{ GeV}) = (0.14 \pm 0.01) \times 10^{-10}. \tag{2.79}$$

These contributions above are used as input in the $K\bar{K}3\pi$, $K\bar{K}\pi$ and $K\bar{K}2\pi$ isospin relations respectively. However, the contributions for the $\phi\pi^0$ and $\phi\pi^+\pi^-$ final states are not added separately in the sum due to the way they are used in the isospin relation.

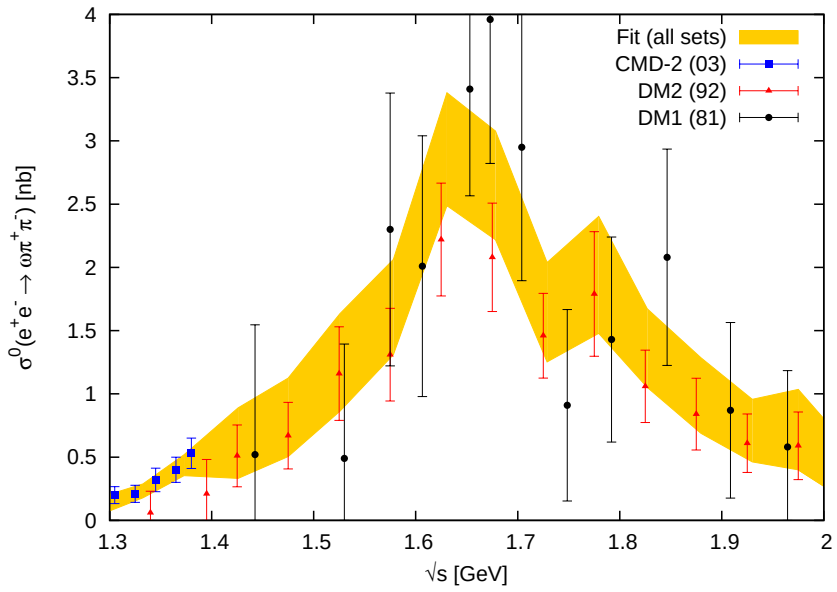

Fig. 2.30: Plot of the $\omega\pi^+\pi^-$ channel up to 2 GeV. All data are displayed.

Finally, the $\phi(\rightarrow$ unaccounted) channel represents the final states not included in the $\phi \rightarrow K^+K^-$, $K^0_SK^0_L$, 3π, $\eta\gamma$, $\pi^0\gamma$, $\pi^+\pi^-$, $\omega\pi^0$, $\pi^+\pi^-\gamma$ and $2\pi^+2\pi^-$ decay processes, which make up $(100 - 99.873)\%$ [23] of the ϕ decay branching ratio. Hence the unaccounted modes can be calculated by first computing a_μ^ϕ and then multiply the result by 1.27×10^{-3}. In the ϕ region defined by $2m_{K^\pm} \leq \sqrt{s} \leq 1.03$ GeV,[4] where $m_{K^\pm} = 493.677$ MeV [23],

$$a_\mu^{\phi\rightarrow K^+K^-} = 15.96 \times 10^{-10}. \tag{2.80}$$

Since $\mathcal{B}(\phi \rightarrow K^+K^-) = 0.489$,

$$a_\mu^\phi = \frac{a_\mu^{\phi\rightarrow K^+K^-}}{\mathcal{B}(\phi \rightarrow K^+K^-)} = 32.64 \times 10^{-10} \tag{2.81}$$

therefore

$$a_\mu^{\phi(\rightarrow\text{unaccounted})} = a_\mu^\phi \cdot 1.27 \times 10^{-3} = (0.04 \pm 0.04) \times 10^{-10}, \tag{2.82}$$

where the error is assigned to be 100% of the result.

2.3.9 The $p\bar{p}$, $n\bar{n}$ channels

The proton and neutron have just low enough mass so their baryon pair final states can contribute below 2 GeV. For the $p\bar{p}$ channel, we use 6 data sets, from FENICE [210,211], DM1 [212], DM2 [213, 214] and BaBar [215]. In the $n\bar{n}$ channel, we use 2 data sets

[4]The actual lower limit is 1.008624 GeV because there is no data below this energy where any contribution would be negligible anyway due to the smallness of the cross section.

from FENICE [210, 216]. The contributions from these channels are,

$$a_\mu^{p\bar{p}}(\sqrt{s} \leq 2 \text{ GeV}) = (0.06 \pm 0.00) \times 10^{-10} \tag{2.83}$$

$$a_\mu^{n\bar{n}}(\sqrt{s} \leq 2 \text{ GeV}) = (0.07 \pm 0.02) \times 10^{-10}. \tag{2.84}$$

2.3.10 The $e^+e^- \to$ all hadrons channel

In the region $1.43 \lesssim \sqrt{s} < 2$ GeV, we use 4 sets of data [217–220], all of which were used in HMNT (03) [61]. Fig. 2.31 shows the fit of these sets along with all but the M3N data [219], which consists of a single point. Note that the $\gamma\gamma 2$ [217], MEA [218] and ADONE [220] data have been corrected for missing two-body final states, specifically, $\pi^+\pi^-$, K^+K^- and $K_S^0K_L^0$. The data from M3N [219] has already taken these missing contributions as part of the error. In addition, we must add contributions from purely neutral final states that are unaccounted, namely $\omega(\to \pi^0\gamma)\pi^0$ and $K_S^0(\to 2\pi^0)K_L^0\pi^0$. Therefore, the contribution to $a_\mu^{\text{had, LOVP}}$ in this region from this work and [61] are

$$a_\mu^{\text{incl}}(1.43 \lesssim \sqrt{s} \leq 2 \text{ GeV; This work}) = (31.99 \pm 2.43) \times 10^{-10} \tag{2.85}$$

$$a_\mu^{\text{incl}}(1.43 \lesssim \sqrt{s} \leq 2 \text{ GeV; HMNT (03)}) = (31.91 \pm 2.42) \times 10^{-10}. \tag{2.86}$$

The slight change in the mean is due to adding the missing contributions since they are estimated from data in the exclusive channels.

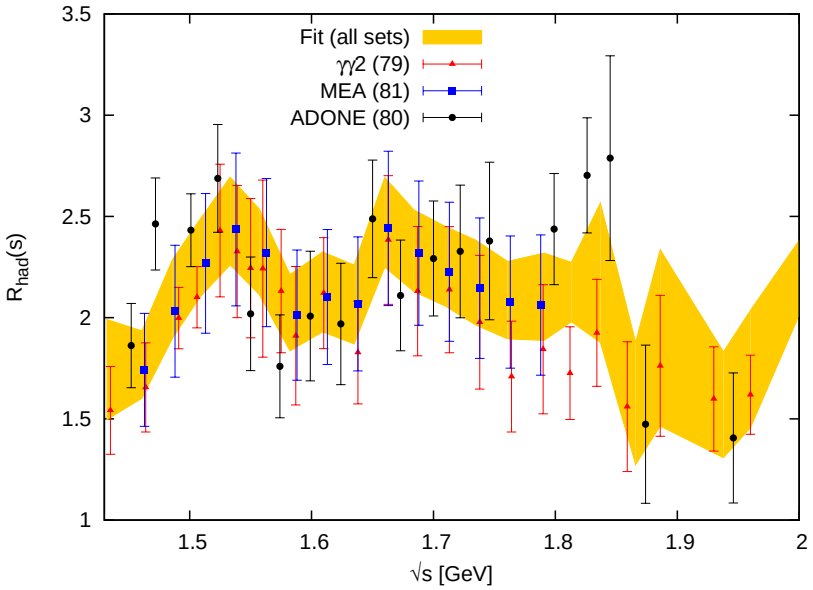

Fig. 2.31: R value plot of the $e^+e^- \to$ all hadrons channel between 1.43 and 2 GeV showing the fit along with the most relevant sets of data.

Between 2 and 11.09 GeV, we use 16 data sets [221–235], of which 2 sets from BES [221, 222] and 1 set from CLEO [223] are new compared to [62]. There is an additional data set, a R_b (i.e. normalised $e^+e^- \to b\bar{b}$) measurement from BaBar [236]

in the energy region $10.54-11.20$ GeV that has *not* been included yet. This data needs to be stripped of initial state radiation (ISR) and have R_{udsc} added before it can be used. This process and the results are described in Section 3.4 later on. Note that this data will have minimal impact on a_μ due to the weighting of the kernel function, thus not including it in the main $g-2$ analysis is not a major issue. Fig. 2.32 shows the new fit in the whole region along with the most important data sets. Although the data in this region is suppressed by the kernel (1.50), their contribution to a_μ is the third largest, after the $\pi^+\pi^-\pi^0$ and $\pi^+\pi^-$ channels. Comparing the direct integration of the new fit in this region to that of [62], we have

$$a_\mu^{\text{incl}}(2 \leq \sqrt{s} \leq 11.09 \text{ GeV; This work}) = (41.40 \pm 0.87) \times 10^{-10} \tag{2.87}$$

$$a_\mu^{\text{incl}}(2 \leq \sqrt{s} \leq 11.09 \text{ GeV; HMNT (06)}) = (42.75 \pm 1.08) \times 10^{-10}. \tag{2.88}$$

This difference is partly due to the new data sets and partly due to the finer cluster size implemented for the peak structures from 3.73 to 4.6 GeV in the new fit. This can be seen from Fig. 2.33, where the new fit, shown by the light (yellow) band, is clearly a better fit than the dark (green) band representing the fit used in [62]. The bottom graph is quite reflective of the smaller a_μ value in this work, since the fit from [62] is consistently higher in this whole region. Fig. 2.34 magnifies the energy region close to 2 GeV, where the new fit, shown again as the light (yellow) band and some of the data are compared to pQCD, represented by the thin dark (red) band. Of particular interest is how the three points from the new BES II [221] data closely match the prediction from pQCD. Thus between 2.6 and 3.73 GeV, we have decided to use pQCD with an inflated error band based on the percentage uncertainties from the three BES II data points. With this setup, the contribution to a_μ is then

$$a_\mu^{\text{incl+pQCD}}(2 \leq \sqrt{s} \leq 11.09 \text{ GeV}) = (41.19 \pm 0.82) \times 10^{-10}. \tag{2.89}$$

If we trust pQCD rather than data down to 2 GeV then a_μ in the region $2 \leq \sqrt{s} \leq 2.6$ GeV would give $(14.49 \pm 0.13) \times 10^{-10}$ rather than $(15.69 \pm 0.63) \times 10^{-10}$. However, since this work is data-driven, we have decided not to use pQCD in this region.

2.4 The isospin channels

2.4.1 Introduction

Some subleading final states such as $K\bar{K} + n\pi$, still lack experimental measurement but in principle can contribute to a_μ. Thus, we are led to use approximate relations to known cross sections based on isospin symmetries to estimate their contribution. These relations are based on Pais isospin classes, which was first introduced in [237]. In this work, we no longer use the 4 isospin relations from [61]. Instead, we follow new isospin relations derived in [78]. There are now 11 separate isospin channels (see Sections 2.4.2

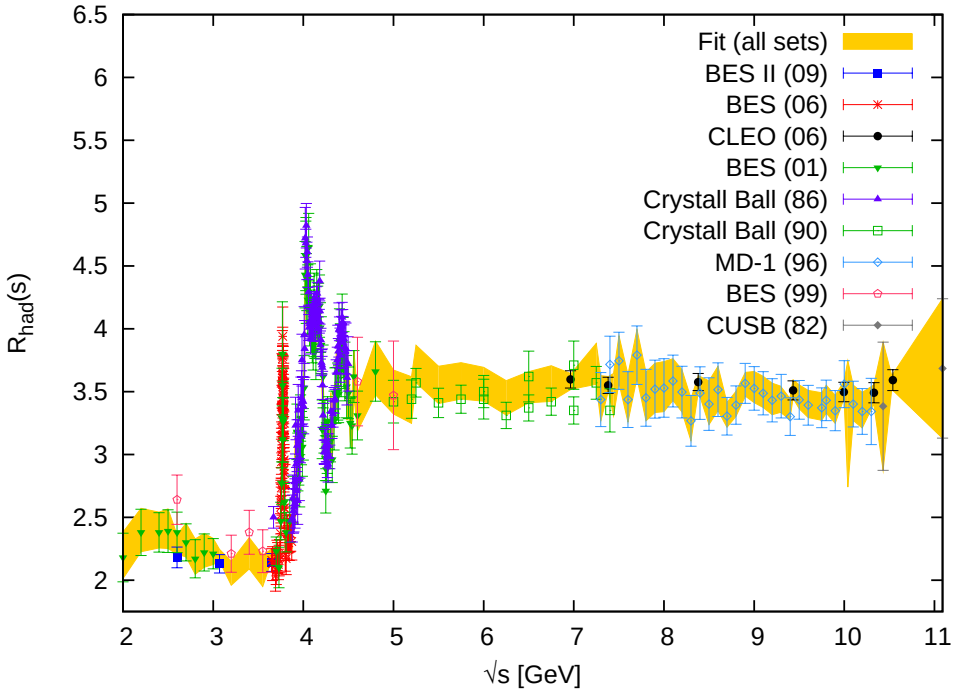

Fig. 2.32: R value plot of the $e^+e^- \to$ all hadrons channel between 2 and 11.09 GeV illustrating the new fit shown in the light (yellow) band along with the most relevant data sets.

to 2.4.7 for a detailed breakdown), we sometimes use our internal numbering schemes to label them as shortcuts in the following sections. Table 2.3 summarises their contributions up to 2 GeV along with a comparison with the old results from [61]. As noted in earlier sections, the 5π and 6π channels estimated in this work do not contain contributions from η decays. They are added in separately from the $\eta\pi^+\pi^-$ final state and new channels $\eta\omega$, $\eta\phi$, $\eta 2\pi^+2\pi^-$ and $\eta\pi^+\pi^-2\pi^0$. The resulting downward shift of the total contribution in Table 2.3 is due to the new BaBar data in the $2\pi^+2\pi^-\pi^0$ and $2\pi^+2\pi^-2\pi^0$ channels as shown in Figs. 2.17 and 2.18. The use of new isospin relations had a minimal impact there. Furthermore, the error of the new $K\bar{K}2\pi$ isospin relation is significantly lower compared to that of the old relation, which was by far the most dominant source of error in the region just below 2 GeV. In the future, data from VEPP-2000 in will provide further information in this energy region, including the $K\bar{K}\pi$ and $K\bar{K}3\pi$ channels.

2.4.2 The 5π related channels

The $(2\pi^+2\pi^-\pi^0)_{\text{no}\,\eta}$ final state (iso11)

This final state is given by,

$$a_\mu((2\pi^+2\pi^-\pi^0)_{\text{no}\,\eta}) = a_\mu(2\pi^+2\pi^-\pi^0) - a_\mu(\eta\pi^+\pi^-)\mathcal{B}(\eta \to \pi^+\pi^-\pi^0) \tag{2.90}$$

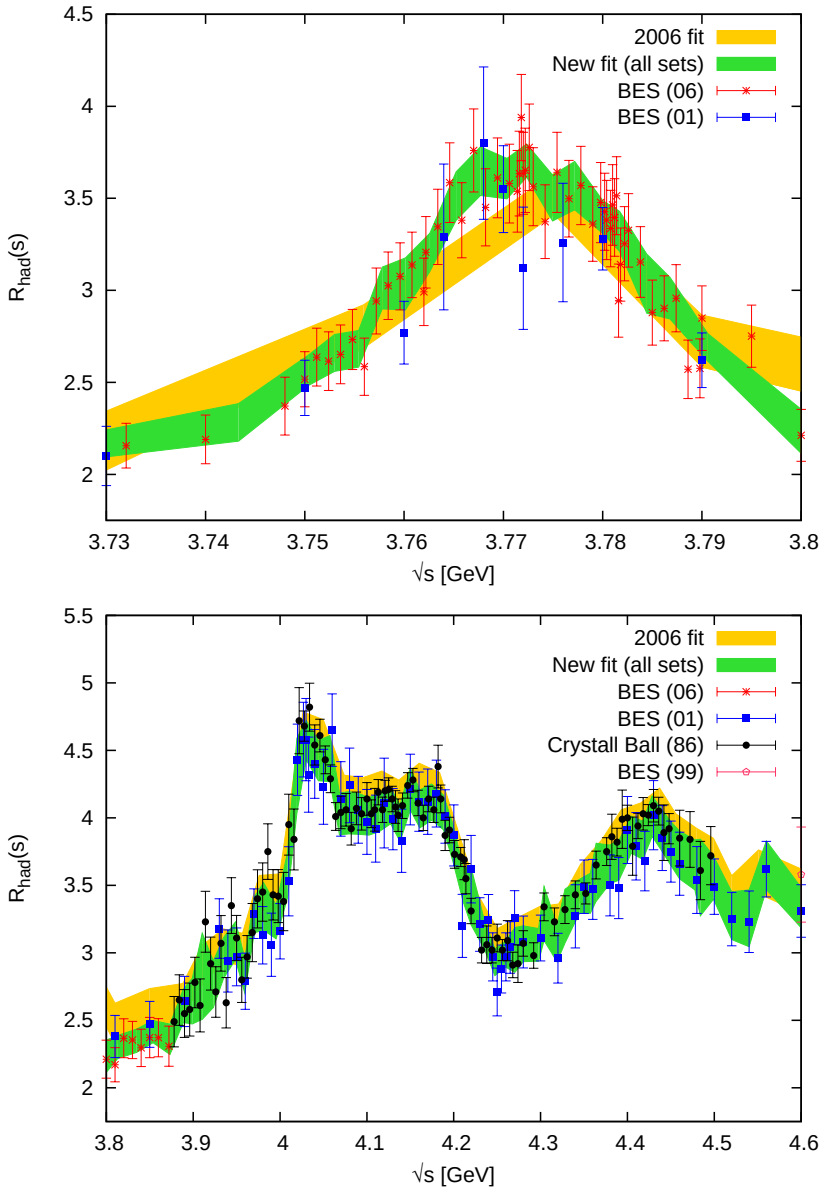

Fig. 2.33: The top graph shows the enlargement of the $\psi(3770)$ peak while the bottom graph shows the other peak structures between 3.8 and 4.6 GeV. The new fit is now shown by the dark (green) band while the fit used in [62] is the light (yellow) band. The most important data sets in those regions are displayed. Note the suppressed zero and the slight difference in the y-scales of both graphs.

where data for the $2\pi^+2\pi^-\pi^0$ (ch14) and $\eta\pi^+\pi^-$ (ch1) states need to be used. The 'no η' means the contribution from $\eta\pi^+\pi^-$ with $\eta \to \pi^+\pi^-\pi^0$ is excluded. The error for this contribution involves a linear correlation with the $\eta\pi^+\pi^-$ state (ch1) only since ch14, as stated in Section 2.3.5, is not added in the sum separately. Therefore the total error for these two final states is given by

$$\delta a_\mu(\mathrm{ch1+iso11}) = \left\{[\delta a_\mu(\mathrm{ch14})]^2 + [(1-B_{11})\delta a_\mu(\mathrm{ch1})]^2 + a_\mu(\mathrm{ch1})\delta B_{11}]^2\right\}^{\frac{1}{2}}, \quad (2.91)$$

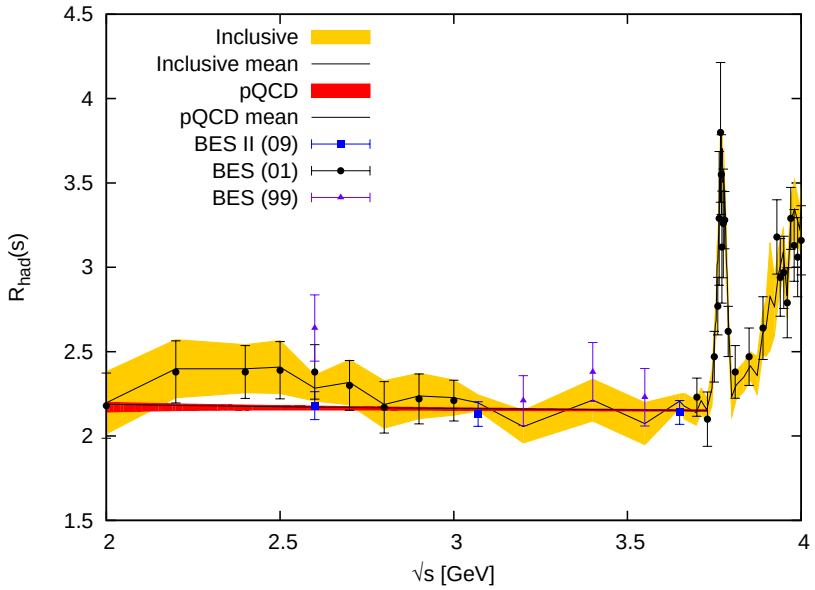

Fig. 2.34: R value plot of the e^+e^- → all hadrons channel between 2 and 4 GeV displaying the fit in the light (yellow) band compared to prediction of pQCD in the dark (red) band. The error band for the pQCD includes the uncertainty on $\alpha_s(M_Z^2)$ and variation of the renormalisation scale μ between $s/2 \leq \mu^2 \leq 2s$. The peak in the graph is the $\psi(3770)$, but J/ψ and ψ' are not resolved by data so they are added in as narrow resonances separately.

where $B_{11} = \mathcal{B}(\eta \to \pi^+\pi^-\pi^0) = 0.2274$ and $\delta B_{11} = 0.0028$ [23]. Hence the contribution to $a_\mu^{\text{had, LOVP}}$ from this channel up to 2 GeV is

$$a_\mu^{(2\pi^+2\pi^-\pi^0)_{\text{no}\,\eta}}(\sqrt{s} \leq 2 \text{ GeV}) = (1.20 \pm 0.20) \times 10^{-10}, \tag{2.92}$$

where the error includes linear correlation with the $\eta\pi^+\pi^-$ state, but is not added separately in the sum due to further correlation with next final state.

The $(\pi^+\pi^-3\pi^0)_{\text{no}\,\eta}$ final state (iso12)

This is the $\pi^+\pi^-3\pi^0$ state where the contribution from $\eta(\to \pi^+\pi^-\pi^0)2\pi^0$ is excluded. Since the $\eta 2\pi^0$ state is forbidden by charge conjugation symmetry, the following relation is used to determine this $(\pi^+\pi^-3\pi^0)_{\text{no}\,\eta}$ channel,

$$a_\mu((\pi^+\pi^-3\pi^0)_{\text{no}\,\eta}) = \frac{1}{2} a_\mu((2\pi^+2\pi^-\pi^0)_{\text{no}\,\eta}). \tag{2.93}$$

Therefore iso12 is linearly correlated with iso11 and ch1, and the total error for all three channels is given by,

$$\delta a_\mu(\text{ch1} + \text{iso11} + \text{iso12}) = \big\{[1.5\delta a_\mu(\text{ch14})]^2 + [(1 - 1.5B_{11})\delta a_\mu(\text{ch1})]^2 + [1.5a_\mu(\text{ch1})\delta B_{11}]^2\big\}^{\frac{1}{2}}. \tag{2.94}$$

Channel	This work	HMNT (03) [61]	approach used in [61]
$K\bar{K}\pi$	2.77 ± 0.15	2.58 ± 0.26	sum of $K^+K^-\pi^0$, $K^0_{S,L}K\pi$, $K^0_SK^0_L\pi^0$
$K\bar{K}2\pi$	3.31 ± 0.58	3.63 ± 1.34	different relation based on K^0_SX final state
$K\bar{K}3\pi$	$0.08 \pm 0.02^*$	-	not accounted for
$\omega(\to \text{npp})K\bar{K}$	$0.01 \pm 0.04^\dagger$	-	not accounted for
$(2\pi^+2\pi^-\pi^0)_{\text{no }\eta}$	$1.20 \pm 0.10^*$	2.85 ± 0.25	purely data-based, incl. η
$(\pi^+\pi^-3\pi^0)_{\text{no }\eta}$	$0.60 \pm 0.05^\dagger$	1.19 ± 0.33	based only on M3N data, incl. η
$\omega(\to \text{npp})2\pi$	0.11 ± 0.02	0.07 ± 0.01	only $\omega(\to \pi^0\gamma)\pi^+\pi^-$ based on data
$3\pi^+3\pi^-$ (data)	0.28 ± 0.02	0.22 ± 0.02	same as this work
$(2\pi^+2\pi^-2\pi^0)_{\text{no }\eta}$	$1.80 \pm 0.24^*$	3.32 ± 0.29	purely data based, incl. η
$(\pi^+\pi^-4\pi^0)_{\text{no }\eta}$	0.28 ± 0.28	0.12 ± 0.12	different relation, incl. η
$\omega(\to \text{npp})3\pi$	$0.22 \pm 0.04^\dagger$	-	not estimated
$\eta\pi^+\pi^-$ (data)	$0.98 \pm 0.24^*$	0.49 ± 0.07	$\eta \to 3\pi$ excluded
$\eta\omega$ (data)	$0.42 \pm 0.07^*$	n/a	no data, not estimated separately
$\eta\phi$ (data)	$0.46 \pm 0.03^*$	n/a	no data, not estimated separately
$\eta2\pi^+2\pi^-$ (data)	0.11 ± 0.02	n/a	no data, not estimated separately
$\eta\pi^+\pi^-2\pi^0$	0.11 ± 0.06	n/a	not estimated separately
Total	12.73 ± 0.75	14.47 ± 1.54	

Table 2.3: Contributions to a_μ from exclusive channels for energies up 2 GeV, estimated using isospin relations following [78] and as discussed in the text. For comparison, the results of the original analysis are also given. Note: * indicates the error is not summed separately due to linear correlation with another channel; † means the error includes contributions from other linearly correlated channels, see the individual channel breakdown for details.

Therefore, the contribution from this channel is

$$a_\mu^{(\pi^+\pi^-3\pi^0)_{\text{no }\eta}}(\sqrt{s} \leq 2 \text{ GeV}) = (0.60 \pm 0.21) \times 10^{-10}, \tag{2.95}$$

where the error includes correlations with $\eta\pi^+\pi^-$ and $(2\pi^+2\pi^-\pi^0)_{\text{no}\,\eta}$ states, and contributes to the sum.

The $\omega(\to$ non-pure pionic states$)2\pi$ final state (iso13)

This is the contribution from the $\omega\pi\pi$ final state (where $\pi\pi$ can be $\pi^+\pi^-$ and $\pi^0\pi^0$), followed by ω decaying into non-purely pionic (npp) states. This means the decay products are not $\pi^+\pi^-\pi^0$ or $\pi^+\pi^-$, and thus are dominated by $\pi^0\gamma$. The following

relation is used to compute this final state,

$$a_\mu(\omega(\to \text{npp})2\pi) = \frac{3}{2} a_\mu(\omega\pi^+\pi^-)\mathcal{B}(\omega \to \text{npp}) \tag{2.96}$$

where [23]

$$\begin{aligned}\mathcal{B}(\omega \to \text{npp}) &= (1 - \mathcal{B}(\omega \to \pi^+\pi^-\pi^0) - \mathcal{B}(\omega \to \pi^+\pi^-)) &(2.97)\\ &= (1 - 0.892 - 0.0153) \\ &= 0.0927 &(2.98)\end{aligned}$$

and we use data to determine the $\omega\pi^+\pi^-$ final state (ch7) as discussed in Section 2.3.8. The error for this channel is then

$$\delta a_\mu(\text{iso13}) = \left\{[1.5\delta a_\mu(\text{ch7})]^2 + [1.5 a_\mu(\text{ch7})\delta B_{13}]^2\right\}^{\frac{1}{2}}, \tag{2.99}$$

with $B_{13} = \mathcal{B}(\omega \to \text{npp})$ and

$$\delta B_{13} = \left\{[\delta\mathcal{B}(\omega \to \pi^+\pi^-\pi^0)]^2 + [\delta\mathcal{B}(\omega \to \pi^+\pi^-)]^2\right\}^{\frac{1}{2}}, \tag{2.100}$$

where $\delta\mathcal{B}(\omega \to \pi^+\pi^-\pi^0) = 0.007$ and[5] $\delta\mathcal{B}(\omega \to \pi^+\pi^-) = 0.0012$ [23]. There is no linear correlation with ch7 since it is not added separately in the sum. Therefore the contribution from this channel is

$$a_\mu^{\omega(\to\text{npp})2\pi}(\sqrt{s} \leq 2 \text{ GeV}) = (0.11 \pm 0.02) \times 10^{-10}. \tag{2.101}$$

The $\eta\pi^+\pi^-$ final state (iso14)

This is simply the $\eta\pi^+\pi^-$ (ch1) channel discussed in Section 2.3.8.

2.4.3 The 6π related channels

The $(2\pi^+2\pi^-2\pi^0)_{\text{no}\,\eta}$ final state (iso21)

For this final state the contribution from $\eta(\to \pi^+\pi^-\pi^0)\omega(\to \pi^+\pi^-\pi^0)$ is excluded,

$$a_\mu((2\pi^+2\pi^-2\pi^0)_{\text{no}\,\eta}) = a_\mu(2\pi^+2\pi^-2\pi^0) - a_\mu(\eta\omega)\mathcal{B}(\eta \to \pi^+\pi^-\pi^0)\mathcal{B}(\omega \to \pi^+\pi^-\pi^0) \tag{2.102}$$

where data for the $2\pi^+2\pi^-2\pi^0$ (ch15) and $\eta\omega$ (ch26) are used. There is linear correlation with ch26 (but not ch15) thus the error for these two channels is given by

$$\delta a_\mu(\text{ch26+iso21}) = \left\{[\delta a_\mu(\text{ch15})]^2 + [(1-B_{21})\delta a_\mu(\text{ch26})]^2 + [a_\mu(\text{ch26})\delta B_{21}]^2\right\}^{\frac{1}{2}}, \tag{2.103}$$

where $B_{21} = \mathcal{B}(\eta \to \pi^+\pi^-\pi^0)\mathcal{B}(\omega \to \pi^+\pi^-\pi^0)$ and

$$\begin{aligned}\delta B_{21} = \Big\{&[\mathcal{B}(\eta \to \pi^+\pi^-\pi^0)\delta\mathcal{B}(\omega \to \pi^+\pi^-\pi^0)]^2 + \\ &[\mathcal{B}(\omega \to \pi^+\pi^-\pi^0)\delta\mathcal{B}(\eta \to \pi^+\pi^-\pi^0)]^2\Big\}^{\frac{1}{2}}. &(2.104)\end{aligned}$$

[5] The $\delta\mathcal{B}(\omega \to \pi^+\pi^-)$ value used here is symmetrised from the original asymmetrical errors in PDG2010 [23].

Up to 2 GeV, this channel gives

$$a_\mu^{(2\pi^+2\pi^-2\pi^0)_{\text{no}\,\eta}}(\sqrt{s} \leq 2 \text{ GeV}) = (1.80 \pm 0.24) \times 10^{-10}, \tag{2.105}$$

where the error includes linear correlation with the $\eta\omega$ state, but is not added separately due to further correlation with the $\omega(\to \text{npp})3\pi$ final state.

The $(\pi^+\pi^-4\pi^0)_{\text{no}\,\eta}$ final state (iso22)

This final state is given by,

$$a_\mu((\pi^+\pi^-4\pi^0)_{\text{no}\,\eta}) = 0.0625 a_\mu(3\pi^+3\pi^-) + 0.145 a_\mu((2\pi^+2\pi^-2\pi^0)_{\text{no}\,\eta}), \tag{2.106}$$

where we use data for the $3\pi^+3\pi^-$ final state as stated in Section 2.3.5. Due to the uncertainty of this relation, the error is taken as 100% of the contribution itself. Thus we have,

$$a_\mu^{(\pi^+\pi^-4\pi^0)_{\text{no}\,\eta}}(\sqrt{s} \leq 2 \text{ GeV}) = (0.28 \pm 0.28) \times 10^{-10}. \tag{2.107}$$

The old isospin relation in [61] was given by

$$a_\mu(\pi^+\pi^-4\pi^0) = 0.031 a_\mu(2\pi^+2\pi^-2\pi^0) + 0.0931 a_\mu(3\pi^+3\pi^-), \tag{2.108}$$

where the contribution from η decays are included. However, the old relation actually gave a smaller contribution to $a_\mu^{\text{had, LOVP}}$,

$$a_\mu^{\pi^+\pi^-4\pi^0}(\sqrt{s} \leq 2 \text{ GeV}) = (0.12 \pm 0.12) \times 10^{-10}. \tag{2.109}$$

The $3\pi^+3\pi^-$ final state (iso23)

This is simply the $3\pi^+3\pi^-$ channel as discussed in Section 2.3.5.

The $\omega(\to$ non-pure pionic state$)3\pi$ final state (iso24)

This is the contribution from the $\omega 3\pi$ final state where the ω decays to non-purely pionic (npp) states. It can be calculated using following relation,

$$a_\mu(\omega(\to \text{npp})3\pi) = 1.145 a_\mu(2\pi^+2\pi^-2\pi^0) \frac{\mathcal{B}(\omega \to \text{npp})}{\mathcal{B}(\omega \to \pi^+\pi^-\pi^0)}, \tag{2.110}$$

where there is an error of ± 0.145 on the factor of 1.145. Since this uses data from the $2\pi^+2\pi^-2\pi^0$ (ch15) final state (see Section 2.3.5 for details), there is linear correlation with iso21. Hence the total error of ch26, iso21, iso22 is given by,

$$\begin{aligned}\delta a_\mu(\text{ch26} + \text{iso21} + \text{iso24}) = \big\{ &[(1 + B_{24})\delta a_\mu(\text{ch15})]^2 + [(1 - B_{21})\delta a_\mu(\text{ch26})]^2 + \\ &[a_\mu(\text{ch15})\delta B_{24}]^2 + [a_\mu(\text{ch26})\delta B_{21}]^2 \big\}^{\frac{1}{2}}.\end{aligned} \tag{2.111}$$

Now

$$B_{24} = 1.145\frac{\mathcal{B}(\omega \to \text{npp})}{\mathcal{B}(\omega \to \pi^+\pi^-\pi^0)} \tag{2.112}$$
$$= 1.145 B'_{24}$$

with

$$\delta B_{24} = \left\{(1.145B'_{24})^2 + (0.145\delta B'_{24})^2\right\}^{\frac{1}{2}}, \tag{2.113}$$

and

$$\delta B'_{24} = \left\{ \left[\frac{\mathcal{B}(\omega \to \pi^+\pi^-) - 1}{(\mathcal{B}(\omega \to \pi^+\pi^-\pi^0))^2} \cdot \delta\mathcal{B}(\omega \to \pi^+\pi^-\pi^0) \right]^2 + \left[-\frac{\delta\mathcal{B}(\omega \to \pi^+\pi^-)}{\mathcal{B}(\omega \to \pi^+\pi^-\pi^0)} \right] \right\}^{\frac{1}{2}}. \tag{2.114}$$

Therefore we have the following contribution for this channel,

$$a_\mu^{\omega(\to \text{npp})3\pi}(\sqrt{s} \leq 2 \text{ GeV}) = (0.23 \pm 0.04) \times 10^{-10}, \tag{2.115}$$

where the uncertainty consists the combined errors from $\eta\omega$ and $(2\pi^+2\pi^-2\pi^0)_{\text{no}\,\eta}$ final states with linear correlation.

The $\eta\omega$ final state (iso25)

This is simply the $\eta\omega$ (ch26) channel detailed in Section 2.3.8, which was found using a Breit-Wigner type parametrisation from [178].

2.4.4 The $K\bar{K}\pi$ channel

This channel (iso31) includes all possible combinations of the following final states: $K^+K^-\pi^0$, $K^0_SK^0_L\pi^0$, $K^0_SK^\pm\pi^\mp$, $K^0_LK^\pm\pi^\mp$ along with a small contribution from $\phi\pi^0$. This is given by the following relation,

$$a_\mu(K\bar{K}\pi) = 3a_\mu(K^0_SK^\pm\pi^\mp) + a_\mu(\phi\pi^0)\mathcal{B}(\phi \to K\bar{K}). \tag{2.116}$$

with $\mathcal{B}(\phi \to K\bar{K}) = \mathcal{B}(\phi \to K^+K^-) + \mathcal{B}(\phi \to K^0K^0)$. We use data for the $K^0_SK^\pm\pi^\mp$ (ch5) and $\phi\pi^0$ (ch28) final states as discussed in Sections 2.3.7 and 2.3.8 respectively. Therefore the error for this channel is given by

$$\delta a_\mu(K\bar{K}\pi) = \left\{[3a_\mu(\text{ch5})]^2 + [B_{31}\delta a_\mu(\text{ch28})]^2 + [a_\mu(\text{ch28})\delta B_{31}]^2\right\}^{\frac{1}{2}}, \tag{2.117}$$

where

$$B_{31} = \mathcal{B}(\phi \to K^+K^-) + \mathcal{B}(\phi \to K^0K^0) \tag{2.118}$$
$$= 0.489 + 0.342 \tag{2.119}$$

and

$$\delta B_{31} = \left\{[\delta\mathcal{B}(\phi \to K^+K^-)]^2 + [\delta\mathcal{B}(\phi \to K^0K^0)]^2\right\}^{\frac{1}{2}} \tag{2.120}$$
$$= \sqrt{0.005^2 + 0.004^2}. \tag{2.121}$$

Thus contribution is then

$$a_\mu^{K\bar{K}\pi}(\sqrt{s} \leq 2 \text{ GeV}) = (2.77 \pm 0.15) \times 10^{-10}. \tag{2.122}$$

In [61], the closest analogue to this isospin channel was the sum of the four final states mentioned at the beginning of the previous paragraph. Two of these are isospin relations based on the other two measured final states,

$$a_\mu^{K^+K^-\pi^0}(\sqrt{s} \leq 2 \text{ GeV}) = (0.29 \pm 0.07) \times 10^{-10}, \tag{2.123}$$
$$a_\mu^{K_S^0K^\pm\pi^\mp}(\sqrt{s} \leq 2 \text{ GeV}) = (1.00 \pm 0.11) \times 10^{-10}, \tag{2.124}$$
$$a_\mu^{K_S^0K_L^0\pi^0}(\sqrt{s} \leq 2 \text{ GeV}) = a_\mu^{K^+K^-\pi^0}(\sqrt{s} \leq 2 \text{ GeV}), \tag{2.125}$$
$$a_\mu^{K_L^0K^\pm\pi^\mp}(\sqrt{s} \leq 2 \text{ GeV}) = a_\mu^{K_S^0K^\pm\pi^\mp}(\sqrt{s} \leq 2 \text{ GeV}). \tag{2.126}$$

The sum of these gives $(2.58 \pm 0.26) \times 10^{-10}$, and simply adding the $\phi\pi^0$ contribution to this will not make up the difference with the new isospin relation. This is probably due to the fact that $K_S^0K_L^0\pi^0$ in general does not equal to $K^+K^-\pi^0$ stated in [78].

2.4.5 The $K\bar{K}2\pi$ channel

This channel (iso41) includes all possible combinations of the following final states: $K^+K^-\pi^0\pi^0$, $K^+K^-\pi^+\pi^-$, $K^0K^0\pi^+\pi^-$, $K^+\pi^-K^0\pi^0$ etc. and their charge conjugates. This is given by the following relation,

$$a_\mu(K\bar{K}2\pi) = 9[a_\mu(K^+K^-\pi^0\pi^0) - a_\mu(\phi\pi^0\pi^0)] + \frac{9}{4}a_\mu(K^*K^\pm\pi^\mp) + \frac{3}{2}a_\mu(\phi\pi^+\pi^-) + a_\mu(K\bar{K}\rho), \tag{2.127}$$

where

$$a_\mu(\phi\pi^0\pi^0) = \frac{1}{2}a_\mu(\phi\pi^+\pi^-). \tag{2.128}$$

In addition, it is also assumed that

$$a_\mu(K\bar{K}\rho) = 4a_\mu(K^+K^-\rho), \tag{2.129}$$

with 100% error. Furthermore, $K^+K^-\rho$ is calculated from

$$a_\mu(K^+K^-\rho) = a_\mu(K^+K^-\pi^+\pi^-) - a_\mu(K^*K^\pm\pi^\mp) - a_\mu(\phi\pi^+\pi^-)\mathcal{B}(\phi \to K^+K^-). \tag{2.130}$$

Therefore (2.127) can be re-written as,

$$a_\mu(K\bar{K}2\pi) = 9a_\mu(K^+K^-\pi^0\pi^0) + \frac{9}{4}a_\mu(K^*K^\pm\pi^\mp) - 3a_\mu(\phi\pi^+\pi^-) + 4[a_\mu(K^+K^-\pi^+\pi^-) - a_\mu(K^*K^\pm\pi^\mp) - a_\mu(\phi\pi^+\pi^-)\mathcal{B}(\phi \to K^+K^-)]. \tag{2.131}$$

We use data for the following final states: $K^+K^-\pi^0\pi^0$ (ch23), $K^*K^\pm\pi^\mp$ (ch30), $K^+K^-\pi^+\pi^-$ (ch11) and $\phi\pi^+\pi^-$ (ch29), which were detailed in Sections 2.3.7 and 2.3.8. Therefore the error for this channel is given by

$$\delta a_\mu(K\bar{K}2\pi) = \left\{ [3\delta a_\mu(\text{ch23})]^2 + [3\delta a_\mu(\text{ch29})]^2 + \left[\frac{9}{4}\delta a_\mu(\text{ch30})\right]^2 + [\delta a_\mu(K\bar{K}\rho)]^2 \right\}^{\frac{1}{2}}, \tag{2.132}$$

with $\delta a_\mu(K\bar{K}\rho) = 4a_\mu(K^+K^-\rho)$. Now the total contribution to this final state is

$$a_\mu^{K\bar{K}2\pi}(\sqrt{s} \leq 2 \text{ GeV}) = (3.31 \pm 0.58) \times 10^{-10}. \tag{2.133}$$

In [61] the $K\bar{K}2\pi$ isospin channel was based on a different relation to different known measured final states. By definition

$$K\bar{K}2\pi = (K_S^0K_L^0 + K_S^0K_S^0 + K_L^0K_L^0)(\pi\pi) + (K_S^0 + K_L^0)(K\pi\pi) + (K^+K^-)(\pi\pi), \tag{2.134}$$

where $\pi\pi$ stands for $\pi^+\pi^-$ or $\pi^0\pi^0$ and $K\pi\pi$ is $K^+\pi^-\pi^0$ or $K^-\pi^+\pi^0$. Noting that

$$\begin{aligned} 2K_S^0X &= K_S^0X + K_L^0X \\ &= 2K_S^0K_L^0 + 2(K_S^0K_L^0 + K_S^0K_S^0 + K_L^0K_L^0)(\pi + \pi\pi) + (K_S^0 + K_L^0)(K\pi + K\pi\pi), \end{aligned} \tag{2.135}$$

where $K\pi$ is $K^+\pi^-$ or $K^-\pi^+$ and X denotes any hadronic state. The $K\bar{K}2\pi$ isospin relation can then be expressed as,

$$\begin{aligned} K\bar{K}2\pi =& 2K_S^0X - 2K_S^0K_L^0 - (K_S^0K_L^0 + K_S^0K_S^0 + K_L^0K_L^0)(2\pi + \pi\pi) - \\ & 2K_S(K\pi) + (K^+K^-)(\pi\pi) \\ =& 2[K_S^0X - K_S^0K_L^0 - K^+K^-\pi - K_S^0(K\pi)]. \end{aligned} \tag{2.136}$$

However for the K_S^0X final state, there is only one set of data from an old DM1 measurement that appeared in a thesis [238], which gives a contribution of

$$a_\mu^{K_S^0X}(\sqrt{s} \leq 2 \text{ GeV}) = (3.20 \pm 0.66) \times 10^{-10}. \tag{2.137}$$

This error is around an order of magnitude larger compared those from the other final states used in the relation. Hence, the contribution to $a_\mu^{\text{had, LOVP}}$ using this relation is

$$a_\mu^{K\bar{K}2\pi(\text{old})}(\sqrt{s} \leq 2 \text{ GeV}) = (3.63 \pm 1.34) \times 10^{-10}. \tag{2.138}$$

The error, which includes linear correlation between the channels used in the isospin relation, is huge. It was in fact, the second largest error from a single channel and is bigger than the error of the new isospin relation by more than a factor of two. Therefore, it was an easy decision to discard the old relation.

2.4.6 The $K\bar{K}3\pi$ related channels

The $K\bar{K}3\pi$ final state (iso51)

This includes the $(K^+K^-\pi^+\pi^-\pi^0)_{\mathrm{no}\,\eta}$ and $(K^0\bar{K}^0\pi^+\pi^-\pi^0)_{\mathrm{no}\,\eta}$ states resulting from $K^+K^-\omega$ dominance and excluding the $\eta\phi$ contribution. The missing modes not covered by the $K^+K^-\omega$ dominance should be small below 2 GeV and are ignored. First,

$$a_\mu((K^+K^-\pi^+\pi^-\pi^0)_{\mathrm{no}\,\eta}) = a_\mu(K^+K^-\pi^+\pi^-\pi^0) - a_\mu(\eta\phi)\mathcal{B}(\phi\to K^+K^-)\mathcal{B}(\eta\to\pi^+\pi^-\pi^0) \tag{2.139}$$

and then we assume

$$a_\mu((K^0\bar{K}^0\pi^+\pi^-\pi^0)_{\mathrm{no}\,\eta}) = a_\mu((K^+K^-\pi^+\pi^-\pi^0)_{\mathrm{no}\,\eta}), \tag{2.140}$$

with a systematic error that is 50% of the mean of $a_\mu((K^+K^-\pi^+\pi^-\pi^0)_{\mathrm{no}\,\eta})$. Hence in total, this channel can be expressed as

$$a_\mu(K\bar{K}3\pi) = 2[a_\mu(K^+K^-\pi^+\pi^-\pi^0) - a_\mu(\eta\phi)\mathcal{B}(\phi\to K^+K^-)\mathcal{B}(\eta\to\pi^+\pi^-\pi^0)], \tag{2.141}$$

where we use data for the $K^+K^-\pi^+\pi^-\pi^0$ (ch24) and $\eta\phi$ (ch27) final states as described in Sections 2.3.7 and 2.3.8. Since ch24 is not summed separately, there is only linear correlation with ch27. Thus the total error (assuming $\delta a_\mu((K^0\bar{K}^0\pi^+\pi^-\pi^0)_{\mathrm{no}\,\eta}) = 0.5a_\mu((K^+K^-\pi^+\pi^-\pi^0)_{\mathrm{no}\,\eta})$), is given by

$$\delta a_\mu(\mathrm{ch27}+\mathrm{iso51}) = \big\{[\delta a_\mu(\mathrm{ch24})]^2 + [(1-B_{51})\delta a_\mu(\mathrm{ch27})]^2 + [a_\mu(\mathrm{ch27})\delta B_{51}]^2 + [\delta a_\mu((K^0\bar{K}^0\pi^+\pi^-\pi^0)_{\mathrm{no}\,\eta})]^2\big\}^{\frac{1}{2}}, \tag{2.142}$$

where

$$B_{51} = \mathcal{B}(\phi\to K^+K^-)\mathcal{B}(\eta\to\pi^+\pi^-\pi^0) \tag{2.143}$$

and

$$\delta B_{51} = \big\{[\mathcal{B}(\eta\to\pi^+\pi^-\pi^0)\delta\mathcal{B}(\phi\to K^+K^-)]^2 + [\mathcal{B}(\phi\to K^+K^-)\delta\mathcal{B}(\phi\to\pi^+\pi^-\pi^0)]^2\big\}^{\frac{1}{2}}. \tag{2.144}$$

Alternatively, the error can be calculated by assuming 100% linear correlation between the data based channels in $a_\mu((K^+K^-\pi^+\pi^-\pi^0)_{\mathrm{no}\,\eta})$ and $a_\mu((K^0\bar{K}^0\pi^+\pi^-\pi^0)_{\mathrm{no}\,\eta})$

$$\delta a_\mu(\mathrm{ch27}+\mathrm{iso51(alt)}) = \big\{[2\delta a_\mu(\mathrm{ch24})]^2 + [(1-2B_{51})\delta a_\mu(\mathrm{ch27})]^2 + [2a_\mu(\mathrm{ch27})\delta B_{51}]^2\big\}^{\frac{1}{2}}, \tag{2.145}$$

which gives something that is slightly smaller than Eq. (2.142) when the terms are substituted with actual numbers. Thus we take the more conservative error estimate and the contribution is,

$$a_\mu^{K\bar{K}3\pi}(\sqrt{s}\le 2\ \mathrm{GeV}) = (0.08\pm 0.04)\times 10^{-10}. \tag{2.146}$$

However, the error is not added separately due to another correlation with the following channel.

The $\omega(\to \text{npp})K\bar{K}$ final state (iso52)

The following relation is used to compute this contribution

$$a_\mu(\omega(\to \text{npp})K\bar{K}) = a_\mu(K\bar{K}3\pi) \cdot \frac{\mathcal{B}(\omega \to \text{npp})}{\mathcal{B}(\omega \to \pi^+\pi^-\pi^0)}. \tag{2.147}$$

Hence, there is linear correlation with ch27 and iso51 and the total error can be expressed as

$$\begin{aligned}\delta a_\mu(\text{ch27} + \text{iso51} + \text{iso52}) = \big\{&[(1+B_{52})\delta a_\mu(\text{ch24})]^2 + \\ &[(1-B_{51}-B_{51}B_{52})\delta a_\mu(\text{ch27})]^2 + \\ &[(1+B_{52})a_\mu(\text{ch27})\delta B_{51}]^2 + \\ &[a_\mu(\text{ch24})\delta B_{52}]^2 + [a_\mu(\text{ch27})\delta B_{52}]^2 + \\ &[(1+B_{52})\delta a_\mu((K^0\bar{K}^0\pi^+\pi^-\pi^0)_{\text{no}\,\eta})]^2\big\}^{\frac{1}{2}},\end{aligned} \tag{2.148}$$

where $B_{52} = B'_{24}$ and $\delta B_{52} = \delta B'_{24}$. The contribution from this channel is

$$a_\mu^{\omega(\to\text{npp})K\bar{K}}(\sqrt{s} \le 2 \text{ GeV}) = (0.01 \pm 0.04) \times 10^{-10}, \tag{2.149}$$

where the error contains the combined uncertainties of the $\eta\phi$, $K\bar{K}3\pi$ and $\omega(\to \text{npp})K\bar{K}$ final states with linear correlation.

The $\eta\phi$ final state (iso53)

This is simply the $\eta\phi$ (ch27) final state as discussed in Section 2.3.8.

2.4.7 The $\eta 4\pi$ channels

The $\eta 2\pi^+2\pi^-$ final state (iso61)

This is simply the $\eta 2\pi^+2\pi^-$ (ch25) channel as described in Section 2.3.8.

The $\eta\pi^+\pi^-2\pi^0$ final state (iso62)

The following relation is assumed,

$$a_\mu(\eta\pi^+\pi^-2\pi^0) = a_\mu(\eta 2\pi^+2\pi^-) \tag{2.150}$$

with the error taken as 50% of $a_\mu(\eta 2\pi^+2\pi^-)$. Therefore the contribution from this channel is

$$a_\mu^{\eta\pi^+\pi^-2\pi^0}(\sqrt{s} \le 2 \text{ GeV}) = (0.11 \pm 0.06) \times 10^{-10}. \tag{2.151}$$

2.5 Other contributions

Other contributions include predictions ChPT, pQCD and narrow resonances. The method used to calculate them remain unchanged from the previous analysis [61].

2.5.1 Chiral perturbation theory predictions

As mentioned earlier, certain exclusive channels have additional contributions from ChPT in the energy region below the experimental measurements. The first is the $\pi^0\gamma$ channel in the region $m_\pi \leq \sqrt{s} < 0.6$ GeV. We describe the $\pi^0\gamma\gamma$ vertex by a Weiss-Zumino-Witten (WZW) local interaction term

$$\mathcal{L}_{\text{WZW}} = -\frac{\alpha}{8\pi f_\pi}\pi^0 e^{\mu\nu\rho\sigma}F_{\mu\nu}F_{\rho\sigma}, \tag{2.152}$$

where $f_\pi \simeq 92.4$ MeV is the pion decay constant. We also assume ω meson dominance because ω meson exchange is what couples $\pi^0\gamma$ to the electromagnetic current. Thus as used in [239]

$$\sigma_{\text{VMD}}(e^+e^- \to \pi^0\gamma) = \frac{8\pi\alpha\Gamma(\pi^0 \to 2\gamma)}{3m_\pi^3}\left(1-\frac{m_\pi^2}{s}\right)^3\left(\frac{m_\omega^2}{m_\omega^2 - s}\right)^2, \tag{2.153}$$

and the contribution to $a_\mu^{\text{had, LOVP}}$ is

$$a_\mu^{\pi^0\gamma}(m_\pi \leq \sqrt{s} < 0.6 \text{ GeV; ChPT}) = (0.13 \pm 0.01) \times 10^{-10}. \tag{2.154}$$

Second we have the $\pi^+\pi^-$ channel where contribution from ChPT is calculated in the energy range $2m_\pi \leq \sqrt{s} < 0.305$ GeV. We write the pion form factor $F_\pi(s)$ as

$$F_\pi(s) = 1 + \frac{1}{6}\langle r^2\rangle_\pi s + c_\pi s^2 + \mathcal{O}(s^3), \tag{2.155}$$

where the coefficients are fitted [240] from space-like pion scattering data [241]

$$\langle r^2\rangle_\pi = 0.431 \pm 0.026 \text{ fm}^2, \quad \text{and} \quad c_\pi = 3.2 \pm 1.0 \text{ GeV}^{-4}. \tag{2.156}$$

Therefore the contribution from ChPT is,

$$a_\mu^{\pi^+\pi^-}(2m_\pi \leq \sqrt{s} < 0.305 \text{ GeV; ChPT}) = (0.87 \pm 0.02) \times 10^{-10}. \tag{2.157}$$

Note that Fig. 2.8 shows how the prediction from ChPT matches with the $\pi^+\pi^-$ data.

The third is the $\pi^+\pi^-\pi^0$ final state. Due to the lack of good quality data below $\sqrt{s} < 0.66$ GeV as mentioned before, we use results from [242, 243] giving

$$a_\mu^{\pi^+\pi^-\pi^0}(3m_\pi \leq \sqrt{s} < 0.66 \text{ GeV; ChPT}) = (0.01 \pm 0.00) \times 10^{-10}. \tag{2.158}$$

Finally we have the $\eta\gamma$ channel where ChPT is used in the region $m_\eta \leq \sqrt{s} < 0.66$ GeV. The method is summarised in Appendix A of [61], which resulted in a contribution to $a_\mu^{\text{had, LOVP}}$ that is less than 10^{-12}. Therefore it is completely insignificant.

2.5.2 J/ψ, ψ' and Υ resonance contributions

The contributions of narrow resonances from J/ψ, ψ' and $\Upsilon(1S-6S)$ states are added in manually using the zero-width approximation since they are not resolved by data,

$$\sigma(e^+e^- \to V) = 12\pi^2 \frac{\Gamma^0_{ee}}{M_V}\delta(s - M_V^2). \tag{2.159}$$

Here V represents the various resonances, and $\Gamma^0_{ee} = C_{\rm res}\Gamma(V \to e^+e^-)$ is the bare electronic width of V, stripped of photon VP effects and FSR corrections with the correction factor C_{res} as mentioned in earlier in Section 2.1.1,

$$C_{\rm res} = \left(\frac{\alpha}{\alpha_{\rm no\,V}(M_V^2)}\right)^2 \left(1 + \frac{3}{4}\frac{\alpha}{\pi}\right)^{-1}. \tag{2.160}$$

The contributions from these resonances are,

$$a_\mu(J/\psi) = (6.24 \pm 0.16) \times 10^{-10}, \tag{2.161}$$

$$a_\mu(\psi') = (1.56 \pm 0.05) \times 10^{-10}, \tag{2.162}$$

$$a_\mu(\Upsilon(1S-6S)) = (0.10 \pm 0.00) \times 10^{-10}. \tag{2.163}$$

2.5.3 Perturbative QCD contributions

As mentioned before, we use pQCD in the energy domains $2.6 \le \sqrt{s} \le 3.73$ GeV and $\sqrt{s} > 11.09$ GeV, where the former has already been accounted for in Eq. (2.89). The contribution to $a_\mu^{\rm had,\ LOVP}$ from the latter is

$$a_\mu^{\rm pQCD}(\sqrt{s} > 11.09\ {\rm GeV}) = (2.11 \pm 0.00) \times 10^{-10}, \tag{2.164}$$

where the error includes uncertainties of $\alpha_s(M_Z^2)$ (dominant), pole masses of the top and bottom quarks, and varying the renormalisation scale between $\sqrt{s}/2 \le \mu \le 2\sqrt{s}$.

2.6 Inclusive vs Exclusive

As stated earlier, in the energy region $1.43 \lesssim \sqrt{s} \le 2$ GeV we can either use the sum of all exclusive channels or data for the inclusive channel, which allows a comparison between the two approaches. When this was done in [61], a discrepancy was found where the contribution to a_μ from the sum of exclusive channels was larger than that of the inclusive,

$$a_\mu^{\rm excl}(1.43 \lesssim \sqrt{s} \le 2\ {\rm GeV};\ {\rm HMNT\ (03)}) = 35.68 \pm 1.71 \tag{2.165}$$

$$a_\mu^{\rm incl}(1.43 \lesssim \sqrt{s} \le 2\ {\rm GeV};\ {\rm HMNT\ (03)}) = 31.91 \pm 2.42. \tag{2.166}$$

Fig. 2.35, which is reproduced from Figure 4 of [61], compares the $R_{\rm had}$ values of the inclusive channel with the sum of exclusive channels in 2003. We see that the sum of

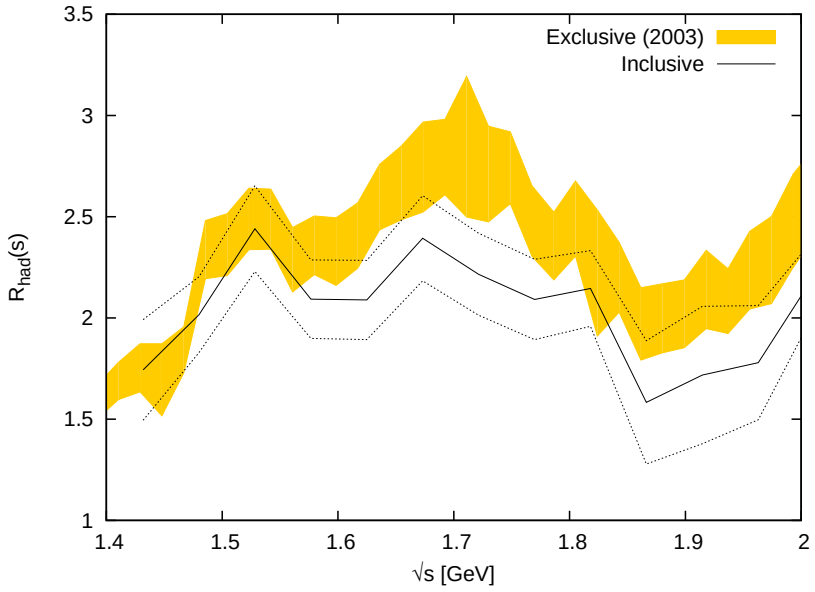

Fig. 2.35: $R_{\rm had}(s)$ behaviour of inclusive data versus the sum of exclusive final states from HMNT (03).

exclusive is consistently higher than inclusive from about 1.6 GeV, but they share a similar shape.

From our partial update of [61, 62] reported at the PhiPsi09 conference in Beijing [244], the sum of exclusive was reduced to

$$a_\mu^{\rm excl}(1.43 \lesssim \sqrt{s} \leq 2 \text{ GeV; PhiPsi09}) = 35.04 \pm 1.62. \tag{2.167}$$

There was no change in the contribution from inclusive, so the discrepancy remains. Now in this work, the sum of exclusive have been reduced further along with a significant improvement in the error,

$$a_\mu^{\rm excl}(1.43 \lesssim \sqrt{s} \leq 2 \text{ GeV; This work}) = 34.61 \pm 1.11 \tag{2.168}$$

$$a_\mu^{\rm incl}(1.43 \lesssim \sqrt{s} \leq 2 \text{ GeV; This work}) = 31.99 \pm 2.43. \tag{2.169}$$

However, the discrepancy still has not disappeared, which can also be seen in the updated $R_{\rm had}$ plot of inclusive versus sum of exclusive in Fig. 2.36. There, the sum of exclusive from [61] is now represented by the (blue) dashed lines while the sum of exclusive from this work is the (yellow) band, with a solid (red) line representing the mean. In this analysis, the exclusive sum as compared to [61], is unsurprisingly lower in most regions. However, it now has a different shape, with a much flatter tail that better matches the data from inclusive above 2 GeV. A detailed breakdown of the changes can be seen in Table 2.4. There are fluctuations of the mean both upwards and downwards, resulting in some cancellations giving the moderate decrease in the sum of exclusive shown.

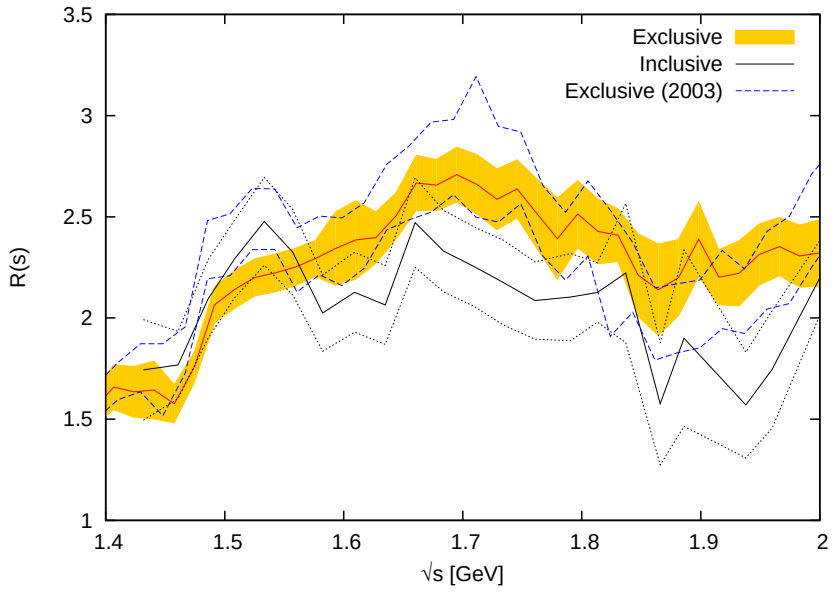

Fig. 2.36: Updated $R_{\rm had}(s)$ plot showing the behaviour inclusive data (dotted line) versus the sum of exclusive final states ((yellow) band) from this work. The dashed (blue) lines indicate the error band of the old exclusive sum from HMNT (03) [61].

Channel	This work	HMNT (03) [61]	Difference
$\pi^+\pi^-2\pi^0$	10.80 ± 0.77	10.84 ± 0.73	-0.04
$2\pi^+2\pi^-$	8.64 ± 0.28	8.61 ± 0.30	$+0.03$
$5\pi, 6\pi$(incl. η)	5.92 ± 0.41	7.65 ± 0.43	-1.73
$K\bar{K}\pi$	2.69 ± 0.15	2.48 ± 0.23	$+0.21$
$K\bar{K}2\pi$	3.31 ± 0.58	3.63 ± 1.32	-0.32
$\pi^+\pi^-\pi^0$	1.25 ± 0.07	0.61 ± 0.09	$+0.64$
Others	1.99 ± 0.17	1.86 ± 0.56	$+0.13$
Sum of excl.	34.61 ± 1.11	35.68 ± 1.71	-1.08
Inclusive	31.99 ± 2.43	31.91 ± 2.42	$+0.08$
Weighted avg.	34.15 ± 1.10		

Table 2.4: Contributions to a_μ from the most important channels in the region from 1.43 to 2 GeV. The numbers given in the second column ('This work') are our new results based on the updated compilation, whereas the column labelled 'HMNT (03)' refers to our old analysis [61]. The last column gives the difference, which, due to changes in the treatment of radiative corrections, is also present in the combination of the inclusive data, for which no new data sets are available. The last three lines give the different options for use of data in this region: sum of exclusive channels (our preferred choice), inclusive data, or the weighted average. (All values in units of 10^{-10}.)

The reason for this discrepancy is unknown. Double counting could have occurred in the sum of exclusive, as numerous final states are added together. However, it is not clear where this occurs as any misidentification of the final states should be accounted for properly by the experiments themselves. The lack of neutral final states in the inclusive data is another possible reason since they are hard for experiments to see.

However as mentioned earlier, the missing neutrals are already estimated and added in. Hence, in order to choose between the two ways of counting the contribution to $a_\mu^{\text{had, LOVP}}$ for $1.43 \lesssim \sqrt{s} \leq 2$ GeV, [61] conducted a QCD sum rule analysis and found that the use of inclusive data is preferable. In this work, an improved analysis has been performed, the details and the results are presented in the following section.

2.7 QCD sum rule analysis

2.7.1 Introduction

In order to check if inclusive or the sum of exclusive data should be used in the energy region $1.43 \lesssim \sqrt{s} \leq 2$ GeV, we update the QCD sum rule analysis performed in [61]. Now QCD sum rules were first introduced by Shifman, Vainstein and Zakharov [245–247], where they were used to measure condensates - the vacuum expectation values of operators from the operator product expansion (OPE). In this work, the sum rules are based on the analyticity of the vacuum polarisation function $\Pi(s)$, which implies

$$\int_{s_{\text{th}}}^{s_0} \mathrm{d}s R_{\text{had}}(s) f(s) = \int_C \mathrm{d}s D(s) g(s) \tag{2.170}$$

for a non-singular function $f(s)$. The circular contour C has radius s_0, and C along with the line segments l_+ and l_- (which have length $s_0 - s_{\text{th}}$) shown in Fig. 2.37 make up the whole contour C'. Finally, the function $g(s)$ can be determined once $f(s)$ is chosen. Now $R_{\text{had}}(s)$ is

$$R_{\text{had}}(s) = 12\pi \frac{\operatorname{Im}\Pi(s)}{s}, \tag{2.171}$$

and $D(s)$, the Adler function is defined by

$$D(s) \equiv -12\pi^2 s \frac{\mathrm{d}}{\mathrm{d}s}\left(\frac{\Pi(s)}{s}\right). \tag{2.172}$$

Therefore, if experimental data are used for $R_{\text{had}}(s)$ and $D(s)$ is determined from theory, then we can check the consistency of data against theory. Specifically, if s_0 is chosen large enough to allow $D(s)$ to be found using QCD, then the data that appears as $R_{\text{had}}(s)$ can be checked for $s \leq s_0$. This is done by first calculating the left hand side (LHS) of the sum rule. Then, a well known, fundamental parameter of the theory that appears in $D(s)$ is fitted (varied) until the right hand side (RHS) of the sum rule matches the LHS. The value of the parameter is then compared to its known world average. The parameter in our case is $\alpha_s(M_Z^2)$, the running of the QCD coupling at the Z-boson mass. Furthermore by tuning $f(s)$, we can emphasise the contribution of $R_{\text{had}}(s)$ to the sum rule from the energy region of interest (i.e. $1.43 \lesssim \sqrt{s} \leq 2$ GeV), which improves the discriminating ability of the sum rules since 'contamination' of data from other energy domains would be reduced. In this work, our choices of s_0 as shown later on, differs from those in the previous analysis [61]. However, they are still below

the open charm threshold (i.e. $\sqrt{s_0} < 3.73$ GeV) so we can still use the three-flavour ($n_f = 3$) QCD expression for the Adler function. Thus, the J/ψ and ψ' resonance contributions to $R_{\rm had}(s)$ still do not need to be taken into account.

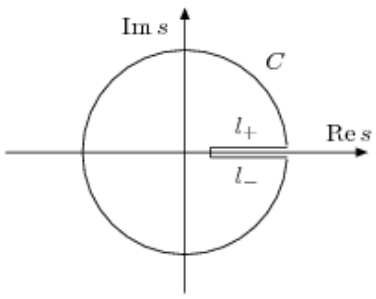

Fig. 2.37: Contour C for the r.h.s. of the sum rule relation.

2.7.2 Sum rules with different choices of $f(s)$

To begin, let us consider the simplest case where $f(s) = 1$. Using the definition of $R(s)$,

$$\begin{aligned}\int_{s_{\rm th}}^{s_0} {\rm d}s\, R_{\rm had}(s) &= 12\pi \int_{s_{\rm th}}^{s_0} {\rm d}s \frac{{\rm Im}\,\Pi(s)}{s} \\ &= \frac{12\pi}{2i}\left(\int_{s_{\rm th}+i\epsilon}^{s_0+i\epsilon} {\rm d}s - \int_{s_{\rm th}-i\epsilon}^{s_0-i\epsilon} {\rm d}s\right)\frac{\Pi(s)}{s}, \end{aligned} \tag{2.173}$$

where the second line is a result of the Schwarz reflection principle $\Pi(s)/s = (\Pi(s^*)/s^*)^*$. Hence it can be seen that the above equation goes over the contour $C' - C$,

$$\int_{s_{\rm th}}^{s_0} {\rm d}s\, R_{\rm had}(s) = -6\pi i\left(\int_{C'} {\rm d}s - \int_C {\rm d}s\right)\frac{\Pi(s)}{s}. \tag{2.174}$$

In the equation above the first term vanishes by Cauchy's Integral theorem because $\Pi(s)/s$ is holomorphic inside C'. Integrating by parts on the second term gives,

$$\int_{s_{\rm th}}^{s_0} {\rm d}s\, R_{\rm had}(s) = 6\pi i\left\{\Big[\Pi(s)\Big]_{s_0+i\epsilon}^{s_0-i\epsilon} - \int_C {\rm d}s\, s\frac{\rm d}{{\rm d}s}\left(\frac{\Pi(s)}{s}\right)\right\}. \tag{2.175}$$

It is easy to see that the integrand in the equation above is $\sim D(s)$ and the first term is $12\pi {\rm Im}\,\Pi(s_0) = s_0 R_{\rm had}(s_0)$, which can be re-written as an integral of $D(s)s_0/s$ over C. First, use the differentiated version of Eq. (2.171), which gives

$$\int_{s_{\rm th}}^{s_0} {\rm d}s \frac{\rm d}{{\rm d}s} R_{\rm had}(s) = 6\pi i \int_C {\rm d}s \frac{\rm d}{{\rm d}s}\left(\frac{\Pi(s)}{s}\right) \tag{2.176}$$

by following the same logic that produced Eqs. (2.173) and (2.174). Then by applying the Second Fundamental Theorem of Calculus on the LHS,

$$\begin{aligned} R_{\rm had}(s_0) - R_{\rm had}(s_{\rm th}) &= 6\pi i \int_C {\rm d}s\, D(s)\frac{-1}{12\pi^2 s}, \\ R_{\rm had}(s_0) &= -\frac{i}{2\pi}\int_C {\rm d}s\, D(s)\frac{1}{s}. \end{aligned} \tag{2.177}$$

where in the last step we used the fact that $R_{\rm had}(s_{\rm th}) = 0$ by definition. Finally we arrive at the following relation,

$$\int_{s_{\rm th}}^{s_0} {\rm d}s\, R_{\rm had}(s) = \frac{i}{2\pi} \int_C {\rm d}s\, D(s) \left(1 - \frac{s_0}{s}\right). \tag{2.178}$$

Now let $f(s) = (s/s_0)^n$ where $n \geq 0$, then by following the same logic as above it is easy to see that

$$\int_{s_{\rm th}}^{s_0} {\rm d}s\, R_{\rm had}(s) \left(\frac{s}{s_0}\right)^n = \frac{i}{2\pi} \int_C {\rm d}s\, \frac{D(s)}{n+1} \left[\left(\frac{s}{s_0}\right)^n - \frac{s_0}{s}\right]. \tag{2.179}$$

For our sum rule analysis, we use $f(s) = (1 - s/s_0)^m (s/s_0)^n$ where $m, n \geq 0$ and $m + n \leq 2$, thus the sum relations are different linear combinations of Eq. (2.179)

$$\int_{s_{\rm th}}^{s_0} {\rm d}s\, R_{\rm had}(s) = \frac{i}{2\pi} \int_C {\rm d}s \left[1 - \frac{s_0}{s}\right] D(s), \tag{2.180}$$

$$\int_{s_{\rm th}}^{s_0} {\rm d}s\, R_{\rm had}(s) \frac{s}{s_0} = \frac{i}{2\pi} \int_C {\rm d}s\, \frac{1}{2} \left[\frac{s}{s_0} - \frac{s_0}{s}\right] D(s), \tag{2.181}$$

$$\int_{s_{\rm th}}^{s_0} {\rm d}s\, R_{\rm had}(s) \left(1 - \frac{s}{s_0}\right) = \frac{i}{2\pi} \int_C {\rm d}s \left[-\frac{1}{2}\frac{s}{s_0} + 1 - \frac{1}{2}\frac{s_0}{s}\right] D(s), \tag{2.182}$$

$$\int_{s_{\rm th}}^{s_0} {\rm d}s\, R_{\rm had}(s) \left(\frac{s}{s_0}\right)^2 = \frac{i}{2\pi} \int_C {\rm d}s\, \frac{1}{3} \left[\left(\frac{s}{s_0}\right)^2 - \frac{s_0}{s}\right] D(s), \tag{2.183}$$

$$\int_{s_{\rm th}}^{s_0} {\rm d}s\, R_{\rm had}(s) \left(1 - \frac{s}{s_0}\right) \frac{s}{s_0} = \frac{i}{2\pi} \int_C {\rm d}s \left[-\frac{1}{3}\left(\frac{s}{s_0}\right)^2 + \frac{1}{2}\frac{s}{s_0} - \frac{1}{6}\frac{s_0}{s}\right] D(s), \tag{2.184}$$

$$\int_{s_{\rm th}}^{s_0} {\rm d}s\, R_{\rm had}(s) \left(1 - \frac{s}{s_0}\right)^2 = \frac{i}{2\pi} \int_C {\rm d}s \left[\frac{1}{3}\left(\frac{s}{s_0}\right)^2 - \frac{s}{s_0} + 1 - \frac{1}{3}\frac{s_0}{s}\right] D(s). \tag{2.185}$$

Hence these relations can be labelled by $(m, n, \sqrt{s_0})$ and in order to do the integrals on the RHS, we need to know the functional form of $D(s)$.

2.7.3 Updated prediction for $D(s)$

Using QCD, the contribution to Adler D function can be expressed as the sum

$$D(s) = D_0(s) + D_m(s) + D_{np}(s). \tag{2.186}$$

$D_0(s)$ is the prediction from three-flavour massless QCD, $D_m(s)$ is a small correction from the quark mass and $D_{np}(s)$ is a very small non-perturbative effect estimated from condensates.

The massless QCD contribution is given by [248],

$$D_0(s) = N_c \sum_f Q_f^2 \left[1 + d_0 a_s(s) + d_1 a_s^2(s) + \tilde{d}_2 a_s^3(s) + \tilde{d}_3 a_s^4(s) + \mathcal{O}(a_s^5)\right], \tag{2.187}$$

which is one order higher in α_s compared to the analysis [61]. Here, the QCD running coupling appears in $a_s(s) = \alpha_s(s)/\pi$ and

$$d_0 = 1, \tag{2.188}$$

$$\begin{aligned} d_1 &= \left(\frac{365}{24} - 11\zeta_3\right) - \left(\frac{11}{12} - \frac{2}{3}\zeta_3\right) n_f \\ &\simeq 1.985707 - 0.115295 n_f, \end{aligned} \tag{2.189}$$

$$\begin{aligned} \tilde{d}_2 = &\left(\frac{87092}{288} - \frac{1103}{4}\zeta_3 + \frac{275}{6}\zeta_5\right) + \left(-\frac{7847}{216} + \frac{262}{9}\zeta_3 - \frac{25}{9}\zeta_5\right) n_f + \\ &\left(\frac{151}{162} - \frac{19}{27}\zeta_3\right) n_f^2 + \left(\frac{55}{72} - \frac{5}{3}\zeta_3\right) \frac{\left(\sum_f Q_f\right)^2}{N_c \sum_f Q_f^2} \\ \simeq &-0.636936 - 1.200134 n_f - 0.005178 n_f^2 - 1.239539 \frac{\left(\sum_f Q_f\right)^2}{N_c \sum_f Q_f^2} + \frac{\beta_0^2 \pi^2}{48}, \end{aligned} \tag{2.190}$$

$$\tag{2.191}$$

with

$$\begin{aligned} \tilde{d}_3 = &\left(\frac{144939499}{20736} - \frac{5693495}{864}\zeta_3 + \frac{5445}{8}\zeta_3^2 + \frac{65945}{288}\zeta_5 - \frac{7315}{48}\zeta_7\right) + \\ &\left(-\frac{13044007}{10368} + \frac{12205}{12}\zeta_3 - 55\zeta_3^2 + \frac{29675}{432} + \frac{665}{72}\zeta_7\right) n_f + \\ &\left(\frac{1045381}{15552} - \frac{40655}{864}\zeta_3 + \frac{5}{6}\zeta_3^2 - \frac{260}{27}\zeta_7\right) n_f^2 + \\ &\left(-\frac{6131}{5832} + \frac{203}{324}\zeta_3 + \frac{5}{18}\zeta_5\right) n_f^3 \\ \simeq &\, 135.792 - 34.440 n_f + 1.8753 n_f^2 - 0.01009 n_f^3, \end{aligned} \tag{2.192}$$

which was found in 2008 by [249]. Here $N_c = 3$ is the number of colours and the sum f in the $\tilde{d}_2$ term is the sum over flavours (i.e. u,d, s). So $Q_f = 2/3$, $-1/3$, $-1/3$, are the electric charges of the u, d and s quark respectively. In addition, the ζ_is are the Riemann Zeta functions and

$$\beta_0 = 11 - \frac{2}{3} n_f, \tag{2.193}$$

which is the first coefficient of the β-function, see Eq. (2.198).

There have been no changes to the expressions of both $D_m(s)$ and $D_{np}(s)$. The quark mass correction is given by

$$D_m(s) = -3 \sum_f Q_f^2 \frac{m_f(s)^2}{s} \left[6 + 28 a_s(s) + (294.8 - 12.3 n_f) a_s^2(s)\right], \tag{2.194}$$

where we have used $m_s((2\text{ GeV})^2) = 105$ MeV in the $\overline{\text{MS}}$ scheme [23], while the mass

of u and d quarks are taken as zero. The contribution from condensates read

$$D_{np}(s) = 3\sum_f Q_f^2 \left\{ \frac{2\pi^2}{3}\left[1 - \frac{11}{18}a_s(s)\right]\frac{\langle a_s GG\rangle}{s^2} + 8\pi^2\left[1 - a_s(s)\right]\frac{\langle m_f \bar{q}_f q_f\rangle}{s^2} + \frac{32\pi^2}{27}a_s(s)\sum_k \frac{\langle m_k \bar{q}_k q_k\rangle}{s^2} + 12\pi^2\frac{\langle \mathcal{O}_6\rangle}{s^3} + 16\pi^2\frac{\langle \mathcal{O}_8\rangle}{s^4}\right\}, \tag{2.195}$$

where we take,

$$\langle a_s GG\rangle = 0.037 \pm 0.019 \text{ (GeV)}^4 \tag{2.196}$$

by following [250]. In addition,

$$\langle m_s \bar{q}_s q_s\rangle = -f_\pi^2 m_K^2 \tag{2.197}$$

where $f_\pi \simeq 92.4$ MeV is the pion decay constant and $m_K = 493.667$ MeV [23]. We neglect the $\langle \mathcal{O}_6\rangle$ and $\langle \mathcal{O}_8\rangle$ condensates since their contributions to $D_{np}(s)$ are very small.

2.7.4 Expansion of the QCD coupling

The QCD coupling $\alpha_s(s)$ appears prominently in $D(s)$ and it can be expressed as an expansion of itself at some reference scale e.g. $\mu^2 = s_0$. This approximation simplifies the contour integral on the RHS of the sum rule. The expansion can be found using the renormalisation group equation

$$\frac{\partial a_s}{\partial \ln \mu^2} = -\frac{\beta_0}{4}a_s^2 - \frac{\beta_1}{8}a_s^3 - \frac{\beta_2}{128}a_s^4 - \frac{\beta_3}{256}a_s^5 - \cdots, \tag{2.198}$$

where the coefficients are

$$\beta_0 = 11 - \frac{2}{3}n_f \tag{2.199}$$

$$\beta_1 = 51 - \frac{19}{3}n_f \tag{2.200}$$

$$\beta_2 = 2857 - \frac{5033}{9}n_f + \frac{325}{27}n_f^2 \tag{2.201}$$

$$\beta_3 = \left(\frac{149753}{6} + 3564\zeta_3\right) - \left(\frac{1078361}{162} + \frac{6508}{27}\right)n_f + \left(\frac{50065}{162} + \frac{6472}{81}\zeta_3\right)n_f^2 + \frac{1093}{729}n_f^3. \tag{2.202}$$

The convention for β_0, β_1 and β_2 is the same as the PDG [23] while the form of β_3 is taken from [251]. We want to find the expansion to $\mathcal{O}(a_s^4)$, which matches the order we know $D_0(s)$ to. Thus we solve the RGE by making the following ansatz

$$a_s(s) = a_s(s_0) + (c_{11}L_0)\,a_s^2(s_0) + \left(c_{21}L_0 + c_{22}L_0^2\right)a_s^3(s_0) + \left(c_{31}L_0 + c_{32}L_0^2 + c_{33}L_0^3\right)a_s^4(s_0) + \mathcal{O}(a_s^5), \tag{2.203}$$

where $L_0 = \ln(s/s_0)$ and c_{ij} $(i,j = 1,2,3\ i \leq j)$ are unknown constants. This is reasonable since the expansion to $\mathcal{O}(a_s^3)$ determined in [61] is

$$a_s(s) = a_s(s_0) - \frac{\beta_0}{4} L_0\, a_s^2(s_0) - \left(\frac{\beta_1}{8} L_0 - \frac{\beta_0^2}{16} L_0^2\right) a_s^3(s_0) + \mathcal{O}(a_s^4). \tag{2.204}$$

Now take $\mu^2 = s$, then the LHS of the RGE (2.198) after applying the ansatz is,

$$\begin{aligned}(\text{LHS of (2.198)}) &= \frac{\partial}{\partial \ln s} a_s(s) \\ &= c_{11} a_s^2(s_0) + (c_{21} + 2c_{22} L_0)\, a_s^3(s_0) + \\ &\quad \left(c_{31} + 2c_{32} L_0 + 3c_{33} L_0^2\right) a_s^4(s_0) + \mathcal{O}(a_s^5).\end{aligned} \tag{2.205}$$

Similarly, the RHS is

$$\begin{aligned}(\text{RHS of (2.198)}) = &- \frac{\beta_0}{4} \left[a_s(s_0) + (c_{11} L_0)\, a_s^2(s_0) + \left(c_{21} L_0 + c_{22} L_0^2\right) a_s^3(s_0) + \mathcal{O}(a_s^4)\right]^2 \\ &- \frac{\beta_1}{8} \left[a_s(s_0) + (c_{11} L_0)\, a_s^2(s_0) + \mathcal{O}(a_s^3)\right]^3 \\ &- \frac{\beta_2}{128} \left[a_s(s_0) + \mathcal{O}(a_s^2)\right]^4 + \mathcal{O}(a_s^5).\end{aligned} \tag{2.206}$$

Hence by comparing equations (2.205) and (2.206), we can determine the unknown constants c_{ij}. The most trivial solutions are the c_{i1} terms, since they are proportional to $L_0^{(1-1)} a_s^{i+1}$

$$c_{11} = -\frac{\beta_0}{4}, \quad c_{21} = -\frac{\beta_1}{8}, \quad c_{31} = -\frac{\beta_2}{128}. \tag{2.207}$$

Next, the c_{i2} unknowns are found by comparing terms $\sim L_0^{(2-1)} a_s^{i+1}$

$$2c_{22} = -\frac{\beta_0}{4} 2c_{11}, \qquad 2c_{32} = -\frac{\beta_0}{4} 2c_{21} - \frac{\beta_1}{8} 3c_{11}, \tag{2.208}$$

$$c_{22} = \frac{\beta_0^2}{16}, \qquad c_{32} = 5\frac{\beta_1 \beta_0}{64}. \tag{2.209}$$

Finally, by comparing terms $\sim L_0^{3-1} a_s^4$,

$$3c_{33} = -\frac{\beta_0}{4} 2c_{22} - \frac{\beta_0}{4} c_{11}^2, \tag{2.210}$$

$$c_{33} = -\frac{\beta_0^3}{64}. \tag{2.211}$$

Therefore putting it all together,

$$\begin{aligned}a_s(s) = a_s(s_0) - \frac{\beta_0}{4} L_0\, a_s^2(s_0) - \left(\frac{\beta_1}{8} L_0 - \frac{\beta_0^2}{16} L_0^2\right) a_s^3(s_0) - \\ \left(\frac{\beta_2}{128} L_0 - 5\frac{\beta_1 \beta_0}{64} L_0^2 + \frac{\beta_0^3}{64} L_0^3\right) a_s^4(s_0) - \mathcal{O}(a_s^5).\end{aligned} \tag{2.212}$$

2.7.5 Computing the RHS of the sum rules

Now that we have an expansion for $\alpha_s(s)$ in terms of $\alpha_s(s_0)$, we can finally calculate the RHS of the sum rules. First, we express $D_0(s)$ in terms of $\alpha_s(s_0)$. Using Eq. (2.212) we derive,

$$a_s^2(s) = a_s^2(s_0) - 2\frac{\beta_0}{4}L_0 a_s^3(s_0) - \left[2\left(\frac{\beta_1}{8}L_0 - \frac{\beta_0^2}{16}L_0^2\right) - \frac{\beta_0^2}{16}L_0^2\right] a_s^4(s_0) + \mathcal{O}(a_s^5), \tag{2.213}$$

$$a_s^3(s) = a_s^3(s_0) - 3\frac{\beta_0}{4}L_0 a_s^4(s_0) + \mathcal{O}(a_s^5), \tag{2.214}$$

$$a_s^4(s) = a_s^4(s_0) + \mathcal{O}(a_s^5). \tag{2.215}$$

Then substitution into Eq. (2.187) gives,

$$\begin{aligned} D_0(s) = N_c \sum_f Q_f^2 \Bigg\{ & 1 + d_0 a_s(s_0) + \left[d_1 - \frac{\beta_0}{4}L_0\right] a_s^2(s_0) + \\ & \left[\tilde{d}_2 - \left(\frac{\beta_1}{8} + \frac{d_1\beta_0}{2}\right)L_0 + \frac{\beta_0^2}{16}L_0^2\right] a_s^3(s_0) + \\ & \left[\tilde{d}_3 - \left(\frac{\beta_2}{128} + \frac{d_1\beta_1}{4} + 3\frac{\tilde{d}_2\beta_0}{4}\right)L_0 + \right. \\ & \left. \left(5\frac{\beta_1\beta_0}{64} + 3\frac{d_1\beta_0^2}{16}\right)L_0^2 - \frac{\beta_0^3}{64}L_0^3\right] a_s^4(s_0) + \mathcal{O}(a_s^5) \Bigg\}. \end{aligned} \tag{2.216}$$

When this is placed into the RHS the terms that contain the integration variables are proportional to $(L_0)^p(s/s_0)^q$ where $p = 1, 2, 3$ and $q = -1, 0, 1, 2$. The calculations of these integrals are found in Appendix A. Second, for $D_m(s)$ and $D_{np}(s)$, we take $a_s(s) = a_s(s_0)$ since their contributions are very small. Finally, the explicit expressions for the RHS can then be constructed from the following pieces. First we have the

massless $n_f = 3$ QCD contributions,

$$\int_C \mathrm{d}s \frac{s_0}{s} D_0(s) = 2\pi i s_0 N_c \sum_f Q_f^2 \Big\{ 1 + a_s(s_0) + d_1 a_s^2(s_0) + \left[\tilde{d}_2 - \frac{\pi^2}{3} L_{22}\right] a_s^3(s_0) + \left[\tilde{d}_3 - \frac{\pi^2}{3} L_{32}\right] a_s^4(s_0) + \mathcal{O}(a_s^5) \Big\}, \quad (2.217)$$

$$\int_C \mathrm{d}s\, D_0(s) = -\pi i s_0 N_c \sum_f Q_f^2 \Big\{ 2L_{11} a_s^2(s_0) + \Big[2L_{21} + 4L_{22}\Big] a_s^3(s_0) + \Big[2L_{31} + 4L_{32} + 2(6-\pi^2) L_{33}\Big] a_s^4(s_0) + \mathcal{O}(a_s^5) \Big\}, \quad (2.218)$$

$$\int_C \mathrm{d}s \frac{s}{s_0} D_0(s) = -\pi i s_0 N_c \sum_f Q_f^2 \Big\{ L_{11} a_s^2(s_0) + \Big[L_{21} + L_{22}\Big] a_s^3(s_0) + \left[L_{31} + L_{32} + \left(\frac{3}{2} - \pi^2\right)\right] a_s^4(s_0) + \mathcal{O}(a_s^5) \Big\}, \quad (2.219)$$

$$\int_C \mathrm{d}s \left(\frac{s}{s_0}\right)^2 D_0(s) = -\pi i s_0 N_c \sum_f Q_f^2 \left\{ \frac{2}{3} L_{11} a_s^2(s_0) + \left[\frac{2}{3} L_{21} + \frac{4}{9} L_{22}\right] a_s^3(s_0) + \left[\frac{2}{3} L_{31} + \frac{4}{9} L_{32} + \frac{2}{3}\left(\frac{2}{3} - \pi^2\right) L_{33}\right] a_s^4(s_0) + \mathcal{O}(a_s^5) \right\}, \quad (2.220)$$

where

$$L_{11} = \frac{\beta_0}{4}, \quad (2.221)$$

$$L_{21} = \frac{\beta_1}{8} + \frac{d_1 \beta_0}{2}, \qquad L_{22} = \frac{\beta_0^2}{16}, \quad (2.222)$$

$$L_{31} = \frac{\beta_2}{128} + \frac{d_1 \beta_1}{4} + 3\frac{\tilde{d}_2 \beta_0}{4}, \qquad L_{32} = 5\frac{\beta_1 \beta_0}{64} + 3\frac{d_1 \beta_0^2}{16}, \qquad L_{33} = \frac{\beta_0^3}{64}. \quad (2.223)$$

Then quark mass corrections are given by,

$$\int_C \mathrm{d}s \frac{s_0}{s} D_m(s) = 24\pi i N_c \sum_f Q_f^2 m_f^2(s_0) a_s(s_0) + \mathcal{O}(m_f^2 a_s^2), \quad (2.224)$$

$$\int_C \mathrm{d}s\, D_m(s) = 4\pi i N_c \sum_f Q_f^2 m_f^2(s_0)(3 + 14 a_s(s_0)) + \mathcal{O}(m_f^2 a_s^2), \quad (2.225)$$

$$\int_C \mathrm{d}s \frac{s}{s_0} D_m(s) = -24\pi i N_c \sum_f Q_f^2 m_f^2(s_0) a_s(s_0) + \mathcal{O}(m_f^2 a_s^2), \quad (2.226)$$

$$\int_C \mathrm{d}s \left(\frac{s}{s_0}\right)^2 D_m(s) = -12\pi i N_c \sum_f Q_f^2 m_f^2(s_0) a_s(s_0) + \mathcal{O}(m_f^2 a_s^2). \quad (2.227)$$

Finally, the contributions from the condensates are

$$\int_C \mathrm{d}s \frac{s_0}{s} D_{np}(s) = \frac{\pi i}{4} N_c \sum_f Q_f^2 \frac{\beta_0}{s_0} \left[-\frac{11\pi^2}{27} \langle a_s GG \rangle - 8\pi^2 \langle m_f \bar{q}_f q_f \rangle + \frac{32\pi^2}{27} \sum_k \langle m_k \bar{q}_k q_k \rangle \right] a_s^2(s_0), \tag{2.228}$$

$$\int_C \mathrm{d}s \, D_{np}(s) = \frac{\pi i}{2} N_c \sum_f Q_f^2 \frac{\beta_0}{s_0} \left[-\frac{11\pi^2}{27} \langle a_s GG \rangle - 8\pi^2 \langle m_f \bar{q}_f q_f \rangle + \frac{32\pi^2}{27} \sum_k \langle m_k \bar{q}_k q_k \rangle \right] a_s^2(s_0), \tag{2.229}$$

$$\int_C \mathrm{d}s \frac{s}{s_0} D_{np}(s) = 2\pi i N_c \sum_f Q_f^2 \frac{1}{s_0} \left[\frac{2\pi^2}{3} \left(1 - \frac{11}{18} a_s(s_0) \right) \langle a_s GG \rangle + 8\pi^2 (1 - a_s(s_0)) \langle m_f \bar{q}_f q_f \rangle + \frac{32\pi^2}{27} a_s(s_0) \sum_k \langle m_k \bar{q}_k q_k \rangle \right], \tag{2.230}$$

$$\int_C \mathrm{d}s \left(\frac{s}{s_0} \right)^2 D_{np}(s) = -\frac{\pi i}{2} N_c \sum_f Q_f^2 \frac{\beta_0}{s_0} \left[-\frac{11\pi^2}{27} \langle a_s GG \rangle - 8\pi^2 \langle m_f \bar{q}_f q_f \rangle + \frac{32\pi^2}{27} \sum_k \langle m_k \bar{q}_k q_k \rangle \right] a_s^2(s_0). \tag{2.231}$$

2.7.6 Results

In HMNT (03) [61], $\sqrt{s_0} = 3.0$, 3.73 GeV, which meant the energy region that we are interested in only accounted for $\sim 13 - 30\%$ of the total contribution (see e.g. Figure 19 in [61]). In this work, we have decided to use 2.0 and 2.6 GeV as our choices for $\sqrt{s_0}$, which gives the region of interest much more weight ($\sim 26 - 55\%$). Fig. 2.38 gives an idea of weighting of the different sum rules by plotting the value for the various $f(s)$ (including the Jacobian factor) considered in this analysis against the energy $\sqrt{s}$. We can see that the $(1,0)$ sum rule for $\sqrt{s_0} = 2$ GeV and $(2,0)$ sum rules for $\sqrt{s_0} = 2$, 2.6 GeV do not give lots of weight to the energy region of interest, hence they are not used. In addition, the $(0,1)$ and $(0,2)$ sum rules are also ignored similar to [61].

Since we want to fit $\alpha_s(M_Z^2)$ but $\alpha_s(s_0)$ appears in $D(s)$, we used the latest `rhad` routine [252], which includes the latest contributions of $\mathcal{O}(\alpha_s^4)$, to turn $\alpha_s(M_Z^2)$ into $\alpha_s(s_0)$ with the correct running and matching. The results of the fitting using the various sum rules can be seen in Fig. 2.39. The error bars on the sum rules are the result of varying the experimental data within their combined systematic and statistic errors. They are much larger than the uncertainties from pQCD, which were estimated by comparing the results using $\mathcal{O}(\alpha_s^3)$ precision to the ones using $\mathcal{O}(\alpha_s^4)$. Results using the inclusive data are shown on the top half of the graph, while the sum of exclusive results are on the bottom half. The band represents the PDG2010 world average and error for $\alpha_s(M_Z^2) = 0.1184 \pm 0.0007$ [23]. It is clear that the sum rules now favour the

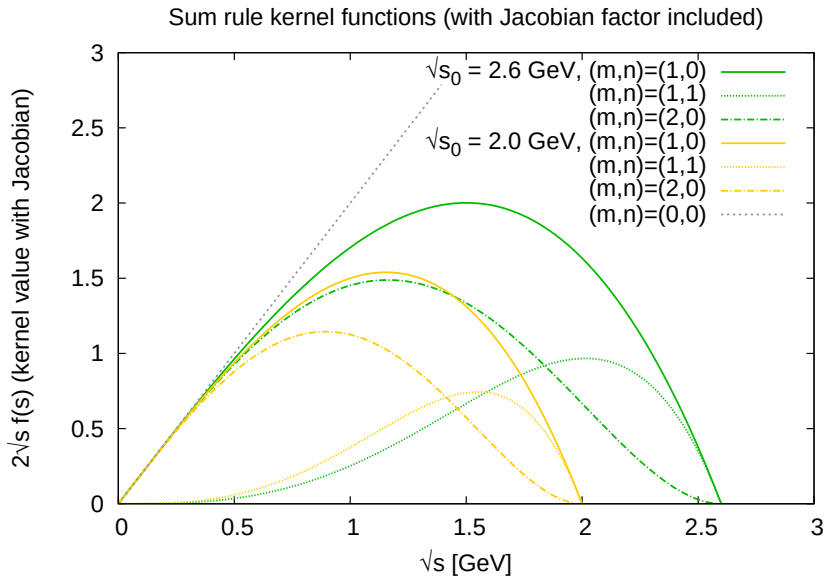

Fig. 2.38: Plot of sum rule $f(s)$ weight function with Jacobian factor included.

more precise sum of exclusive channels rather than the inclusive data. This is not just due to the changes in the $1.43 \lesssim \sqrt{s} \leq 2$ GeV energy region, as the data in there are only a part of the total contribution to the sum rules (the percentages of their contributions are listed in the brackets in Fig. 2.39). Changes to data in the ρ-resonance region and above 2 GeV for example, are also responsible. In light of this result, and the recent, significant improvements in the exclusive channels, we have decided to use the sum of exclusive in the energy region $1.43 \lesssim \sqrt{s} \leq 2$ GeV. This leads to a large improvement in the error for this region but also an upward shift of the mean value, see Table 2.4.

2.8 Total contribution to $a_\mu^{\text{had, LOVP}}$

The total contribution to $a_\mu^{\text{had, LOVP}}$ from the various energy regions and channels are summarised in Tables 2.5 to 2.8 below. The final result, with the choice of using the sum of exclusive (and isospin) channels in the energy region $1.43 \lesssim \sqrt{s} \leq 2$ GeV is

$$a_\mu^{\text{had, LOVP}} = (694.91 \pm 3.72_{\text{exp}} \pm 2.10_{\text{rad}}) \times 10^{-10}, \tag{2.232}$$

where the first error is due to statistical and systematic uncertainties in the experimental data and the second error is from our treatment of the radiative corrections and vacuum polarisation. Table 2.5 lists all the contributions and the energy regions they cover, which directly make up the result above. It also lists the new data sets that did not appear in HMNT (03) [61] and HMNT (06) [62]. Note that the number of exclusive channels from this table and the number of channels in Table 2.3 add up to 27, i.e. the total number of distinct exclusive and isospin that contribute directly to $a_\mu^{\text{had, LOVP}}$ mentioned in Section 2.2. Table 2.6 lists all the measured final states that

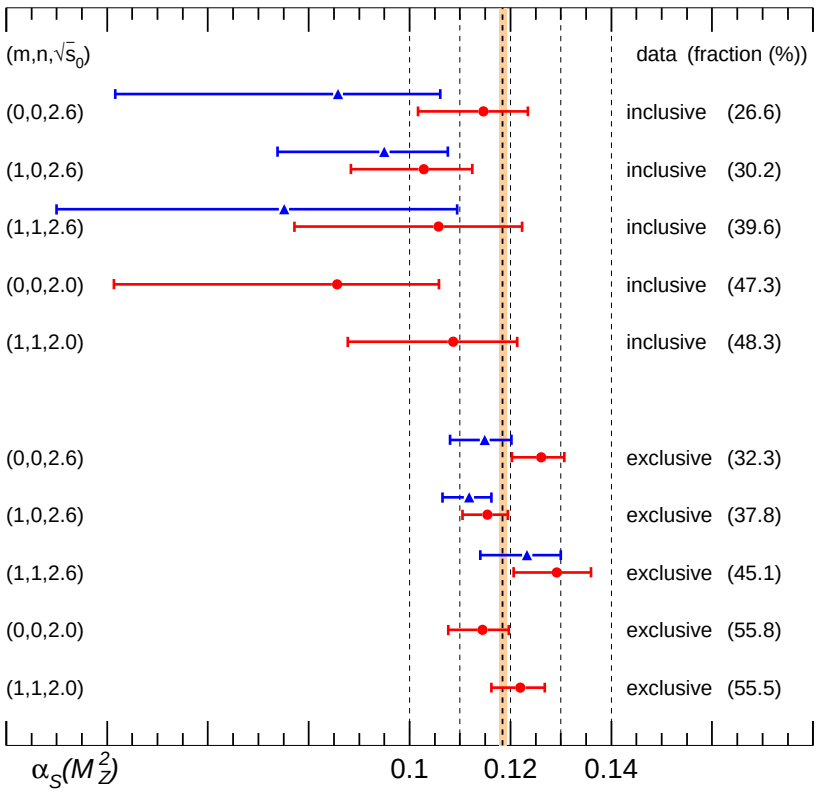

Fig. 2.39: Results of fitting $\alpha_s(M_Z^2)$ using sum rules ((2.180), (2.182) and (2.184)) with various choices of $(m, n, \sqrt{s_0})$, and different input data in the energy range $1.43 \lesssim \sqrt{s} \leq 2$ GeV. Top half: using inclusive data; bottom half: using the updated sum of exclusive channels. Results that uses data only are shown by the (red) round markers and those that uses pQCD above 2 GeV have (blue) triangle markers. The thin (orange) band displays the world average and error of $\alpha_s(M_Z^2)$ from PDG2010 [23].

are used to make up the contribution from the sum of the isospin channels. The last column shows the isospin channel they are used in and changes to the data set(s) used from the previous analyses. Note that the number of channels in this table and the number of exclusive channels in Table 2.5 add up to 26, i.e. the number of measured final states that is used in this work, which was first stated at the start of Section 2.2.

2.8.1 Comparison with HMNT (06)

Table 2.7 compares the contribution from different energy regions from this work to the analysis in 2006 [62]. Note that in this table, the lower integration limit is 0.32 GeV instead of 0.305 GeV to facilitate the comparison. From the last column it is clear that the differences between the two analyses partly cancel. However, the presence of new radiative return data from BaBar and KLOE makes the increase in the 0.32 to 1.43

Contribution	$a_\mu \times 10^{10}$	Energy region	New data set(s)
ChPT, 2π	0.87 ± 0.02	$2m_\pi - 0.305$ GeV	-
ChPT, 3π	0.01 ± 0.00	$3m_\pi - 0.66$ GeV	-
ChPT, $\pi^0\gamma$	0.13 ± 0.01	$m_\pi - 0.60$ GeV	-
ChPT, $\eta\gamma$	0.00 ± 0.00	$m_\eta - 0.66$ GeV	-
$\phi \rightarrow$ unaccounted	0.04 ± 0.04	-	-
Exclusive states	-	$0.305 - 2.00$ GeV	See below
$\pi^0\gamma$	4.54 ± 0.14	$0.60 - 1.31$ GeV	-
$\pi^+\pi^-$	505.77 ± 3.09	$0.305 - 2.00$ GeV	KLOE [129, 130], BaBar [131]
$\pi^+\pi^-\pi^0$	47.51 ± 0.99	$0.66 - 2.00$ GeV	CMD-2 scans [151]
$2\pi^+2\pi^-$	14.65 ± 0.47	$0.6125 - 2.00$ GeV	-
$\pi^+\pi^-2\pi^0$	20.37 ± 1.26	$0.915 - 2.00$ GeV	-
K^+K^-	22.15 ± 0.46	$1.0086 - 2.00$ GeV	CMD-2 [181], SND [182]
$K^0_S K^0_L$	13.33 ± 0.16	$1.0037 - 2.00$ GeV	SND [188]
$\eta\gamma$	0.69 ± 0.02	$0.66 - 1.36$ GeV	SND scans [198]
$\omega(\rightarrow \pi^0\gamma)\pi^0$	0.77 ± 0.03	$0.9200 - 2.00$ GeV	KLOE [205]
$p\bar{p}$	0.06 ± 0.00	$1.8887 - 2.00$ GeV	-
$n\bar{n}$	0.07 ± 0.02	$1.9154 - 2.00$ GeV	-
Isospin states	12.73 ± 0.75	-	See Section 2.4 for details
Inclusive channel	41.19 ± 0.82	$2.0 - 11.09$ GeV	BES [221, 222], CLEO [223]
$J/\psi + \psi'$	7.80 ± 0.16	-	-
$\Upsilon(1S - 6S)$	0.10 ± 0.00	-	-
pQCD	2.11 ± 0.00	$11.09 - \infty$ GeV	-
Total	694.91 ± 3.72	$m_\pi - \infty$ GeV	-

Table 2.5: Summary of the explicit contributions that make up the total value of $a_\mu^{\text{had, LOVP}}$ used in this work. The last column also gives any new data set(s) not present in the previous analyses [61,62]. The sum of contributions from isospin channels is taken from Table 2.3, where the individual contributions can also be found. All the measured final states that contributed to the sum of the isospin channels are listed separately in Table 2.6.

GeV region dominate over the changes in other energies. Keeping in mind that [62] used inclusive data in the region 1.43 to 2 GeV and the change in the inclusive data above 2 GeV are also important, so $a_\mu^{\text{had, LOVP}}$ from this work is almost 0.9σ larger compared to the one used in [62]. However, the increase would only be slight if [62] used exclusive rather than inclusive in the region 1.43 to 2 GeV. This is because the new sum of exclusive in this region has seen a significant decrease as shown.

2.8.2 Comparison with DHMZ (10)

Table 2.8 gives the comparison of the results from exclusive channels in this work with those used in the analysis from Davier *et al.* [78] in the region 0.305 to 1.8 GeV.

Channel	$a_\mu \times 10^{10}$	Energy region	Notes
$2\pi^+2\pi^-\pi^0$	1.42 ± 0.09	$1.0127 - 2.00$ GeV	Used in $(2\pi^+2\pi^-\pi^0)_{\mathrm{no}\,\eta}$ Data: +BaBar [176]; −M3N [160].
$3\pi^+3\pi^-$	0.28 ± 0.02	$1.3125 - 2.00$ GeV	Used in $(\pi^+\pi^-4\pi^0)_{\mathrm{no}\,\eta}$; also summed separately. Data: +BaBar [178]
$2\pi^+2\pi^-2\pi^0$	1.89 ± 0.24	$1.3223 - 2.00$ GeV	Used in $(2\pi^+2\pi^-2\pi^0)_{\mathrm{no}\,\eta}$ and $(\pi^+\pi^-4\pi^0)_{\mathrm{no}\,\eta}$ and $\omega(\to \mathrm{npp})3\pi$. Data: +BaBar [178]; −M3N [160], −DM2 [179].
$K^0_S K^\pm\pi^\mp$	0.91 ± 0.05	$1.26 - 2.00$ GeV	Used in $K\bar{K}\pi$. Data: +BaBar [194].
$K^*K\pi$ (new)	0.78 ± 0.03	$1.5875 - 2.00$ GeV	Used in $K\bar{K}2\pi$. Data: +BaBar [195, 196].
$K^+K^-\pi^+\pi^-$	0.99 ± 0.04	$1.4125 - 2.00$ GeV	Used in $K\bar{K}2\pi$. Data: +BaBar [195, 196].
$K^+K^-2\pi^0$ (new)	0.16 ± 0.01	$1.46 - 2.00$ GeV	Used in $K\bar{K}2\pi$. Data: +BaBar [195, 196].
$K^+K^-\pi^+\pi^-\pi^0$ (new)	0.09 ± 0.01	$1.6125 - 2.00$ GeV	Used in $K\bar{K}3\pi$; Data: +Babar [176].
$\eta\pi^+\pi^-$	0.98 ± 0.24	$1.2946 - 2.00$ GeV	Used in $(2\pi^+2\pi^-\pi^0)_{\mathrm{no}\,\eta}$ and $(\pi^+\pi^-3\pi^0)_{\mathrm{no}\,\eta}$; also summed separately.
$\eta 2\pi^+2\pi^-$ (new)	0.11 ± 0.02	$1.3375 - 2.00$ GeV	Used in $\eta\pi^+\pi^-2\pi^0$; also summed separately. Data: +BaBar [176].
$\eta\omega$ (new)	0.43 ± 0.07	$1.3325 - 2.00$ GeV	Used in $(2\pi^+2\pi^-2\pi^0)_{\mathrm{no}\,\eta}$ and $(\pi^+\pi^-4\pi^0)_{\mathrm{no}\,\eta}$; also summed separately. Data: +BaBar [178] (BW fit).
$\eta\phi$ (new)	0.46 ± 0.03	$1.5693 - 2.00$ GeV	Used in $K\bar{K}3\pi$, $\omega(\to \mathrm{npp})K\bar{K}$; also summed separately. Data: +BaBar [176, 194].
$\omega\pi^+\pi^-$	0.79 ± 0.10	$1.2923 - 2.00$ GeV	Used in $\omega(\to \mathrm{npp})2\pi$.
$\phi\pi^0$ (new)	0.04 ± 0.01	$1.25 - 2.00$ GeV	Used in $K\bar{K}2\pi$. Data: +BaBar [194].
$\phi\pi^+\pi^-$ (new)	0.14 ± 0.01	$1.4875 - 2.00$ GeV	Used in $K\bar{K}2\pi$. Data: +BaBar [195, 196].

Table 2.6: Summary of the measured final states that contributed to the sum of isospin channels that appeared in Tables 2.3 and 2.5. Channels that did not appear in the previous analyses [61, 62] are labelled by 'new' in brackets. The last column lists which isospin channel they were used in and whether they have to be added separately in the sum. Finally, a new (removed) data set is preceded by a '+' ('−') sign.

Contribution	This work	HMNT (06) [62]	difference
$2m_\pi - 0.32\,\text{GeV}$ (ChPT, 2π)	2.36 ± 0.05	2.36 ± 0.05	± 0.00
$3m_\pi - 0.66\,\text{GeV}$ (ChPT, 3π)	0.01 ± 0.00	0.01 ± 0.00	± 0.00
$m_\pi - 0.60\,\text{GeV}$ (ChPT, $\pi^0\gamma$)	0.13 ± 0.01	0.13 ± 0.01	± 0.00
$m_\eta - 0.69\,\text{GeV}$ (ChPT, $\eta\gamma$)	0.00 ± 0.00	0.00 ± 0.00	± 0.00
$\phi \to$ unaccounted modes	0.04 ± 0.04	0.06 ± 0.06	-0.02
$0.32 - 1.43\,\text{GeV}$	606.50 ± 3.35	601.96 ± 3.19	$+4.54$
$1.43 - 2\,\text{GeV}$ (excl. only)	34.61 ± 1.11	36.38 ± 1.66	-1.77
$1.43 - 2\,\text{GeV}$ (incl. only)	31.99 ± 2.43	32.05 ± 2.43	-0.06
$1.43 - 2\,\text{GeV}$ (incl.-excl. avg.)	34.15 ± 1.01	n/a	n/a
$2 - 11.09\,\text{GeV}$	41.19 ± 0.82	42.75 ± 1.08	-1.56
$J/\psi + \psi'$	7.80 ± 0.16	7.90 ± 0.16	-0.10
$\Upsilon(1\text{S} - 6\text{S})$	0.10 ± 0.00	0.10 ± 0.00	± 0.00
$11.09 - \infty\,(\text{pQCD})$	2.11 ± 0.00	2.11 ± 0.00	± 0.00
Sum (excl.–excl.–incl.)	694.86 ± 3.71	693.77 ± 3.84	$+1.09$
Sum (excl.–incl.–incl.)	692.25 ± 4.23	689.44 ± 4.17	$+2.81$
Sum (excl.–avg.–incl.)	694.40 ± 3.67	n/a	n/a

Table 2.7: Contributions to $a_\mu^{\text{had, LOVP}}$ obtained in this work compared to the values used in our analysis [62]. The last column gives the differences. (All values in units of 10^{-10}.) The first four lines give our predictions of contributions close to threshold where no data are available and are based on chiral perturbation theory (ChPT), see Section 2.5.1 for details. For $2.6 \leq \sqrt{s} \leq 3.73$ GeV pQCD with errors comparable to those of the latest BES data is used as default for this work, see the discussion in the text. The different choices quoted in the last three lines refer to the energy regions below 1.43 GeV, for $1.43 \lesssim \sqrt{s} \leq 2$ GeV and above.

Note that for the $\pi^+\pi^-$ result, we have included the contribution from ChPT theory since [78] extended the $\pi^+\pi^-$ data to threshold and included this extra contribution in their result. From the table we see that there is reasonable agreement between the two results, where the one in this work is moderately higher. Nevertheless, for individual contributions there are still differences that are on the order of the error, for example, $\pi^+\pi^-$, $\pi^+\pi^-\pi^0$ and K^+K^- channels. These differences presumably come from the different choices in selecting, processing, combining and integrating the data between our groups. The total result for the leading order hadronic contribution to a_μ are

$$a_\mu^{\text{had, LOVP}}(\text{This Work}) = (694.9 \pm 4.3) \times 10^{-10}, \tag{2.233}$$

$$a_\mu^{\text{had, LOVP}}(\text{DHMZ (10)}) = (692.3 \pm 4.2) \times 10^{-10}, \tag{2.234}$$

where the individual error components have been added in quadrature. Part of the difference (1.22×10^{-10}) is already accounted for in Table 2.8. Most of the remaining difference comes from the use of pQCD by Davier *et al.* between 1.8 and 3.7 GeV. If we use pQCD from 1.8 to 3.7 GeV, our result would be lower by 1.28×10^{-10}. The rest of the difference ($\sim 0.1 \times 10^{-10}$) could be from our use of ChPT for the $\pi^0\gamma$ and $\pi^+\pi^-\pi^0$ channels since Davier *et al.* was not explicit on this matter with only the remark

Channel	This work	DHMZ (10) [78]	Difference
$\eta\pi^+\pi^-$	0.88 ± 0.10	1.15 ± 0.19	-0.27
K^+K^-	22.09 ± 0.46	21.63 ± 0.73	0.46
$K^0_S K^0_L$	13.32 ± 0.16	12.96 ± 0.39	0.36
$\omega\pi^0$	0.76 ± 0.03	0.89 ± 0.07	-0.13
$\pi^+\pi^-$	506.52 ± 3.09	507.80 ± 2.84	-1.28
$2\pi^+2\pi^-$	13.50 ± 0.44	13.35 ± 0.53	0.15
$3\pi^+3\pi^-$	0.11 ± 0.01	0.12 ± 0.01	-0.01
$\pi^+\pi^-\pi^0$	47.38 ± 0.99	46.00 ± 1.48	1.38
$\pi^+\pi^-2\pi^0$	18.62 ± 1.15	18.01 ± 1.24	0.61
$\pi^0\gamma$	4.54 ± 0.14	4.42 ± 0.19	0.12
$\eta\gamma$	0.69 ± 0.02	0.64 ± 0.02	0.05
$\eta 2\pi^+2\pi^-$	0.02 ± 0.00	0.02 ± 0.01	0.00
$\eta\omega$	0.38 ± 0.06	0.47 ± 0.06	-0.09
$\eta\phi$	0.33 ± 0.03	0.36 ± 0.03	-0.03
$\phi(\rightarrow$ unaccounted)	0.04 ± 0.04	0.05 ± 0.00	-0.01
Sum of isospin channels	5.98 ± 0.42	6.06 ± 0.46	-0.08
Total	635.15 ± 3.53	633.93 ± 3.61	1.22

Table 2.8: Contributions to a_μ (in units of 10^{-10}) in the energy region from 0.305 to 1.8 GeV from exclusive channels: Results based on the data compilation as used in this analysis compared to the results as given by Davier *et al.* [78]. Note that the ChPT contribution for the $\pi^+\pi^-$ channel is also included in the $\pi^+\pi^-$ result from this analysis since Davier *et al.* included a similar estimate in their result.

"We also perform a reestimation of missing low-energy contributions using results on cross sections and process dynamics from BABAR". Otherwise, it is probably due to rounding of the numbers but either way this is inconsequential.

Chapter 3

The running of the QED coupling and its value at the Z-boson mass

3.1 Introduction

The QED coupling α is one of the most fundamental quantities in physics, and as mentioned in Section 1.3, its value at the zero momentum transfer has been measured with a very high precision. However, when calculating processes that involve a virtual photon exchange at high energies, most of the radiative corrections can be absorbed into the running or effective coupling $\alpha(q^2)$ [119], where q^2 is the virtuality of the exchanged photon.

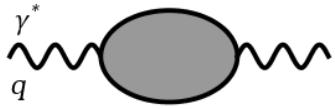

Fig. 3.1: Vacuum polarisation diagram with momentum transfer q.

The running of the QED coupling can be thought of as the screening of the electric charge, and is therefore affected by the energy of the probing photon. Hence it is subject to photon vacuum polarisation effects with momentum transfer q^2, such as the one shown in Fig. 3.1. However, time-like ($q^2 = s > 0$) and space-like ($q^2 = -s < 0$) momentum transfers give rise to different effects. For $\alpha(q^2 = s)$, the running coupling follows the structure of the hadronic spectrum including resonances at low energy. However, for $\alpha(q^2 = -s)$ it is a smooth function in those regions. These differences can be as high as a few percent in certain places, hence, for calculations that require high precision, they cannot be neglected. For example, in the treatment of the e^+e^- hadronic annihilation data mentioned earlier, computing the VP corrections to the data requires precise knowledge of both $\alpha(s)$ and $\alpha(-s)$ in order to arrive at the most accurate and precise determination for the muon $g-2$. Furthermore, these can also be used for the precise determination of $\alpha(q^2)$ as explained below and also, in particular, $\alpha(M_Z^2)$. The QED coupling at the Z-boson mass M_Z is the least precise of the set of

parameters, $[G_F, M_Z, \alpha(M_Z^2)]$ that are normally perceived to define the EW sector of the SM. Therefore, one of the main limiting factors in precision electroweak physics is the uncertainty on $\alpha(M_Z^2)$, which affects for example, the indirect calculation of the mass of the Higgs boson.

3.2 Computing $\alpha(q^2)$ and $\Delta\alpha^{(5)}_{\rm had}(q^2)$

We use the same description of the running of the QED coupling from Eq. (2.1) except the VP function will be given in terms of $\Pi'(s)$ rather than $\tilde{\Pi}$,

$$\alpha(q^2) = \frac{\alpha}{1 - \Delta\alpha(q^2)} = \frac{\alpha}{1 + e^2 \mathrm{Re}\,\Pi'(q^2)}. \tag{3.1}$$

Again $\mathrm{Re}\,\Pi'(q^2)$ is the real part of the photon VP function, and corresponds to defining the effective charge by summing the 1-particle irreducible 'blobs' to arbitrary order (see Fig. 2.1). We break the quantity $\Delta\alpha(q^2)$ into three separate pieces as was done in Eq. (2.3),

$$\Delta\alpha(q^2) = \Delta\alpha_{\rm lep}(q^2) + \Delta\alpha^{(5)}_{\rm had}(q^2) + \Delta\alpha_{\rm top}(q^2). \tag{3.2}$$

The leptonic and top quark contributions can be calculated perturbatively, however the five flavour hadronic contribution, $\Delta\alpha^{(5)}_{\rm had}(q^2)$, contains non-perturbative effects and cannot be computed reliably using pQCD. Therefore, using the same prescription defined in Section 1.5.2 we can write,

$$\mathrm{Re}\,\Pi'(q^2) = \frac{q^2}{\pi}\mathcal{P}\int_{s_{\rm th}}^{\infty} \mathrm{d}s \frac{\mathrm{Im}\,\Pi'(s)}{s(s - q^2)}, \tag{3.3}$$

where $\mathcal{P}$ denotes taking the principal value for $q^2 > s_{\rm th}$. With the use of the optical theorem again we arrive at the dispersion relation for $\Delta\alpha$,

$$\Delta\alpha^{(5)}_{\rm had}(q^2) = -\frac{\alpha q^2}{3\pi}\mathcal{P}\int_{s_{\rm th}}^{\infty} \mathrm{d}s \frac{R_{\rm had}(s)}{s(s - q^2)}. \tag{3.4}$$

Here $R_{\rm had}(s)$ has the same definition as Eq. (1.53), and the same compilation of e^+e^- hadronic annihilation data along with pQCD, ChPT, treatment of narrow resonances etc, used in the determination of a_μ can be applied to $R_{\rm had}$ in this case.

However, for computing $\Delta\alpha^{(5)}_{\rm had}(q^2)$ the integration of $R_{\rm had}(s)$ is done on a specific grid of energies s_i . Thus $R_{\rm had}(s)$ takes the form

$$R_{\rm had}(s) = R_{\rm had}(s_i) + (s - s_i)\frac{R_{\rm had}(s_{i+1}) - R_{\rm had}(s_i)}{s_{i+1} - s_i}, \tag{3.5}$$

for $s_i < s < s_{i+1}$. This means Eq. (3.4) can be expressed as

$$\Delta\alpha^{(5)}_{\rm had}(q^2) = -\frac{\alpha q^2}{3\pi}\sum_{i=1}^{N-1}\mathcal{P}\int_{s_i}^{s_{i+1}}{\rm d}s\frac{R_{\rm had}(s)}{s(s-q^2)} \tag{3.6}$$

$$= -\frac{\alpha}{3\pi}\sum_{i=1}^{N-1}\frac{1}{s_{i+1}-s_i}\Bigg\{\Big[s_iR_{\rm had}(s_{i+1}) - s_{i+1}R_{\rm had}(s_i)\Big]\ln\frac{s_{i+1}}{s_i} + \Big[(q^2-s_i)R_{\rm had}(s_{i+1}) - (q^2-s_{i+1})R_{\rm had}(s_i)\Big]\ln\left|\frac{q^2-s_{i+1}}{q^2-s_i}\right|\Bigg\}, \tag{3.7}$$

where N is the total number of grid points. It is easy to see that the 'singularities' at $q^2 = s_i$ cancel between adjacent intervals. The calculation of the error proceeds exactly as the $g-2$ case described in Section 2.1.4. The error from radiative corrections is, of course, also treated the same way.

3.3 Results

Fig. 3.2 displays the results of $\Delta\alpha^{(5)}_{\rm had}(q^2)/\alpha$ in both the time-like $q^2 = s > 0$ (top graph) and space-like $q^2 = -s < 0$ (bottom graph) cases.[1] The bands show the uncertainty of the results due to all the errors associated with the use of the data mentioned above. The dashed line in the top graph is the central value for the space-like result, drawn for comparison purposes. The large structures exhibited by the time-like result follows the hadronic resonances. Thus it is flat once the running is above the Υ states, where the time-like and space-like results are almost identical[2]. Note that in regions very close to narrow resonances for the time-like case, the idea of an effective charge through the summation of the 1PI blobs is no longer valid. Since $\Delta\alpha \sim \mathcal{O}(1)$, Eq. (3.1) is no longer compatible with this summation due to the radius of convergence. This is the reason that when removing VP effects that dress narrow resonances, $\alpha_{{\rm no}\,V}(s)$, the running coupling with the contribution from the narrow resonances removed is used. Further details regarding the running of the QED coupling in different energy regions, along with discussions and comparisons with other works are not finalised yet and will be presented in our upcoming paper [253].

Using the same compilation of $e^+e^- \to$ hadrons data (along with pQCD and other contributions) as in the a_μ analysis, the five-flavour hadronic contribution to the running of the QED coupling at the Z boson mass is

$$\Delta\alpha^{(5)}_{\rm had}(M_Z^2) = (276.26 \pm 1.16_{\rm exp} \pm 0.74_{\rm rad}) \times 10^{-4}. \tag{3.8}$$

[1] These graphs actually show preliminary results because they have included an additional set of the data (BaBar R_b measurement [236]) that was not present in the main $g-2$ analysis (see Section 2.3.10). The inclusion of this data is described in Section 3.4 below and details on our determination of $\Delta\alpha^{(5)}_{\rm had}(q^2)$ and $\alpha(q^2)$ with this data included will be published in an upcoming paper [253].

[2] For example, at $s = M_Z^2$, $\Delta\alpha(M_Z^2) - \Delta\alpha(-M_Z^2) \sim -4 \times 10^{-5}$.

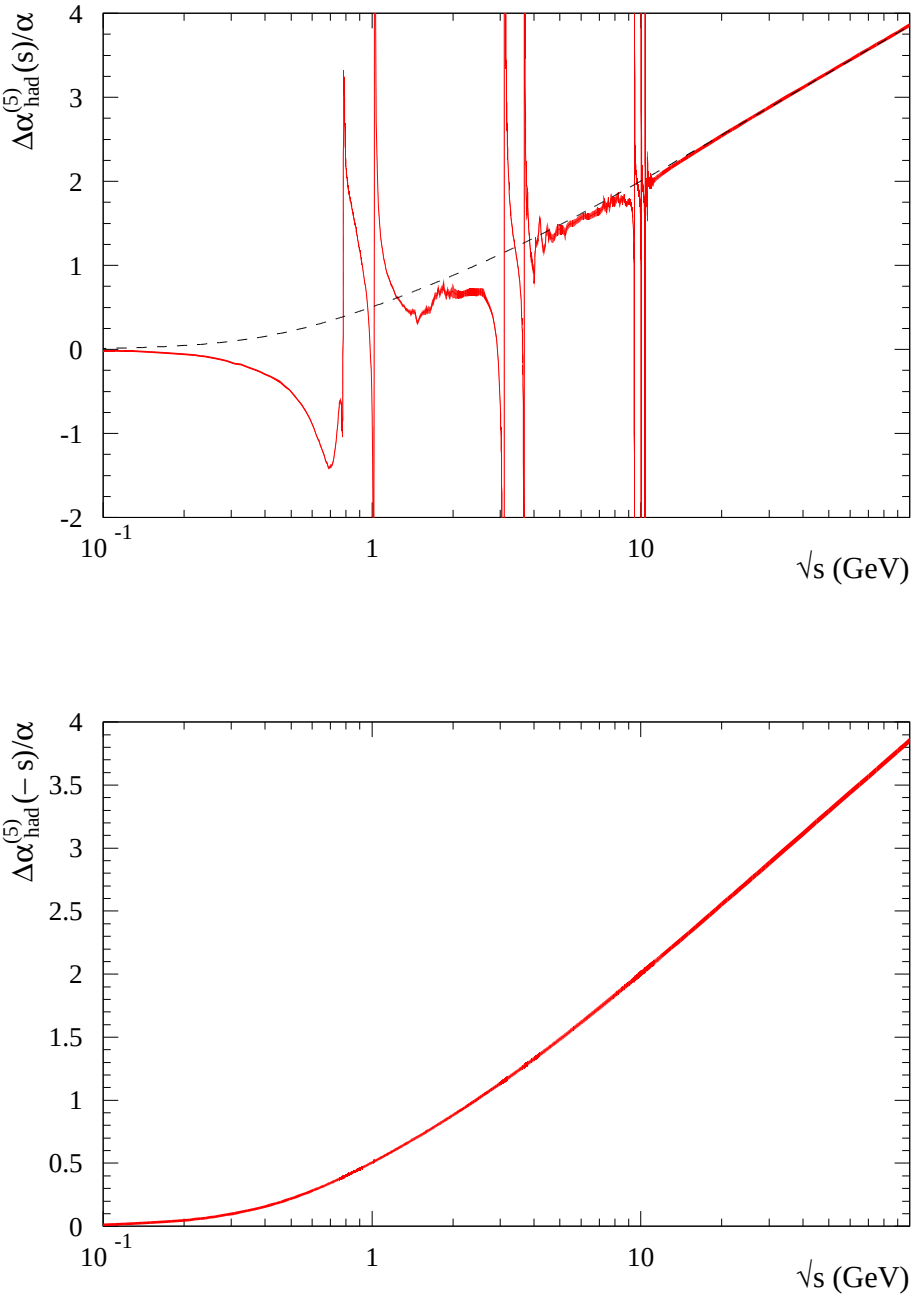

Fig. 3.2: Plots of the hadronic contributions $\Delta\alpha^{(5)}_{\rm had}(q^2)/\alpha$ to the running of the QED coupling. The results for the time-like $q^2 = s > 0$ case is shown in the top graph by the (red) band. The space-like $q^2 = -s < 0$ case is shown in the bottom graph and as a dashed line in the top graph for comparison.

Summing this with the leptonic [254] and top quark [255–257] contributions

$$\Delta\alpha_{\rm lep}(M_Z^2) = 314.98 \times 10^{-4}, \tag{3.9}$$

$$\Delta\alpha_{\rm top}(M_Z^2) = -(0.728 \pm 0.014) \times 10^{-4}, \tag{3.10}$$

where the mass of the top quark is taken as $m_t = (172.6 \pm 1.6)$ GeV [23], we arrive at the final result for the running of the QED coupling at the Z-boson mass,

$$\alpha(M_Z^2)^{-1} = 128.944 \pm 0.019. \tag{3.11}$$

This is a noticeable improvement from the previous analysis [62], whose result is

$$\alpha(M_Z^2)^{-1} = 128.937 \pm 0.030. \tag{3.12}$$

Thus the error has been reduced by a factor of just over one third.

Group, year, ref.	$\Delta\alpha^{(5)}_{\rm had}(M_Z^2)$	Remarks
Kühn+Steinhauser (98) [258]	0.02775 ± 0.00017	pQCD
Martin *et al.* (00) [259]	0.02738 ± 0.00020	data driven
Troconiz+Yndurain (05) [260]	0.02749 ± 0.00012	pQCD
Burkhardt+Pietrzyk (05) [261]	0.02758 ± 0.00035	data driven
HMNT (06) [62]	0.02768 ± 0.00022	data driven
Jegerlehner (08) [262]	0.027594 ± 0.000219	data driven/pQCD
	0.027515 ± 0.000149	Adler function ($\sqrt{s_0} = 2.5$ GeV)
Jegerlehner (10) [263]	0.027498 ± 0.000135	Adler function ($\sqrt{s_0} = 2.5$ GeV)
Davier *et al.* (10) [78]	0.02750 ± 0.00010	pQCD from $1.8 < \sqrt{s} < 3.7$ GeV
HLMNT (11), this work	0.027626 ± 0.000138	data driven

Table 3.1: Results for $\Delta\alpha^{(5)}_{\rm had}(M_Z^2)$ from different groups. The column 'remarks' indicates if the analysis is mainly relying on data as input in the dispersion integral (3.4) or if pQCD is used outside the resonance regions; another approach proposed by Jegerlehner is based on the use of the Adler D function, thus reducing the dependence on data and improving the error.

Table 3.1 compares the result for $\Delta\alpha^{(5)}_{\rm had}(M_Z^2)$ from this work with recent determinations from other groups. Note that result from Davier *et al.* is noticeably lower than this work. The reason is due to their use of pQCD from 1.8 to 3.7 GeV. In the $a_\mu^{\rm had,\,LOVP}$ analysis, this has already made a visible difference between Davier *et al.* and this work, where the weighting of this energy region is suppressed (see Fig. 4.2) due to the $g-2$ kernel. Thus in this case where the weighting of this energy region is much larger, it has created an even bigger difference between the two analyses.

It is also worth noting that the $\Delta\alpha^{(5)}_{\rm had}(M_Z^2)$ result from this work is slightly higher but much more precise than the default prediction used by the LEP Electroweak Working group [261] for their precision fits [265]. This is can be seen from the graph in Fig. 3.3, which is also known as the 'Blue-band plot'. It summarises the indirect determination on the mass of the Higgs boson. The effect of the new $\alpha(M_Z^2)$ value in this work is shown by the steeper parabola with the (red) solid line. The resulting fit for the mass of the Higgs is [264]

$$m_H = \left(91^{+30}_{-23}\right)\ \text{GeV}, \tag{3.13}$$

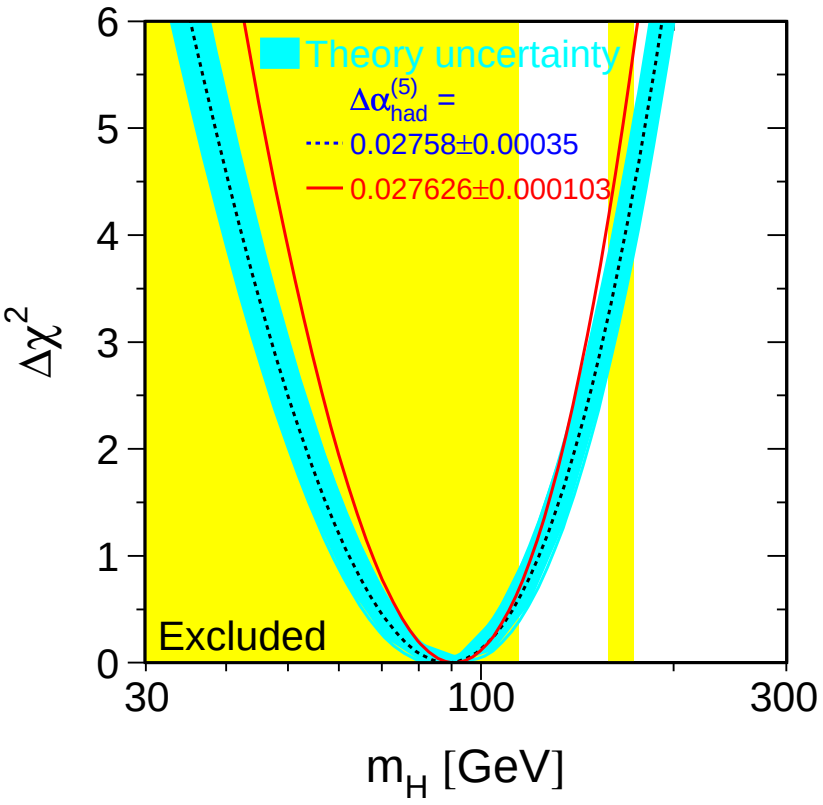

Fig. 3.3: 'Blue-band plot' from the LEP EWWG: The dark (blue) band with the dashed line shows the default EW precision data fit result (July 2010), whereas the solid (red) parabola is obtained by using our new value for $\Delta\alpha^{(5)}_{\rm had}(M_Z^2)$ [264].

which can be compared to

$$m_H = \left(89^{+35}_{-26}\right) \text{ GeV}, \tag{3.14}$$

the value from using the default option (July 2010)[3]. Therefore by also taking into account the excluded regions (shown by the (yellow) shaded rectangles) from direct Higgs searches by LEP and Tevatron, this might be indicating another problem for the SM, which is however, less compelling than the $g-2$ deviation.

3.4 Inclusion of the BaBar R_b data

The BaBar collaboration recently measured the quantity R_b between 10.54 GeV and 11.20 GeV [236]. This analysis is very precise and contains lots of data points, which will improve the quality of the measurement in this previously sparsely populated region. However, before this data can be used here, we must correct the data by removing

[3]The latest fit from the Working Group gives $m_H = \left(92^{+34}_{-26}\right)$ GeV, see [265].

the initial state radiation (ISR) and the radiative tails of the resonances from the $\Upsilon(1S-4S)$ states. We follow the procedure outlined in [266], where the data was used for a different purpose.

First, the tails of the $\Upsilon(1S-3S)$ resonances were subtracted using the data provided in the supplementary material from [236]. To calculate the tail of the $\Upsilon(4S)$ resonance, the following Breit-Wigner function was used

$$\sigma(s) = 12\pi \frac{\Gamma_{ee}(\Upsilon(4S))\Gamma_{\text{tot}}(\Upsilon(4S))}{(s-M^2)^2 + M^2\Gamma^2_{\text{tot}}(\Upsilon(4S))}. \tag{3.15}$$

Here $M = 10.58$ GeV, the mass of the $\Upsilon(4S)$ state, $\Gamma_{ee}(\Upsilon(4S)) = 0.272 \times 10^{-6}$ GeV, the electronic width and $\Gamma_{\text{tot}}(\Upsilon(4S)) = 20.5 \times 10^{-3}$ GeV, an energy-independent total width. However, since the BaBar data includes ISR, the $\Upsilon(4S)$ tail must also be 'convoluted' with ISR before it can be subtracted. In order to do this, we use the following integral to calculate the cross section (σ_{ISR}) including ISR effects,

$$\sigma_{\text{ISR}}(s) = \int_{z_0}^{1} \mathrm{d}z\, G(z)\sigma(sz). \tag{3.16}$$

$G(z)$ is the radiator function in the form presented by equation (3) in [267], which was based on the resummed next-to-next-to-leading order result from [268],

$$G(z) = \beta \cdot (1-z)^{\beta-1} \cdot e^{\delta_{yfs}} \cdot F \cdot (\delta_C^{V+S} + \delta_C^H(z)). \tag{3.17}$$

Define $L = \ln(s/m_e^2)$ and $a = \alpha/\pi$ then

$$\beta = 2a(L-1) \tag{3.18}$$

$$F = \frac{e^{-\beta\gamma_E}}{\Gamma(1+\beta)} \tag{3.19}$$

$$\delta_{yfs} = a\left(\frac{L}{2} - 1 + 2\zeta(2)\right) \tag{3.20}$$

$$\delta_C^{V+S} = 1 + a(L-1) + \frac{1}{2}(aL)^2 \tag{3.21}$$

$$\delta_C^H(z) = -\frac{1-z^2}{2} + aL\left(-\frac{1}{4}(1+3z^2)\ln(z) - 1 + z\right), \tag{3.22}$$

where γ_E is the Euler-Mascheroni constant and $\zeta(2) = \pi^2/6$. The variable z is defined through

$$\frac{s_0}{s} = z_0 \leq z \leq 1, \tag{3.23}$$

so the invariant mass of the system (after correcting for ISR) is sz. Here we took $\sqrt{s_0} = 10.5408$ GeV, corresponding to the energy of the first BaBar point. With the radiative tail of $\Upsilon(4S)$ 'convoluted' with ISR, it is then subtracted from the BaBar data, which was converted from R_b to nano-barns. Finally, we have to remove or 'de-convolute' ISR effects from the BaBar data. From equation (3.16), we can solve for σ iteratively if σ_{ISR} have been given as data. Let us define $\delta G(z) \equiv G(z) - \delta(1-z)$

and $\sigma_0(s) \equiv \sigma_{\rm ISR}(s)$, so the starting (zeroth iteration) cross section corresponds to the cross section including ISR. Then in the $i^{\rm th}$ iteration,

$$\sigma_i(s) = \sigma_0(s) - \int_{z_0}^{1} {\rm d}z\, \delta G(z) \sigma_{i-1}(sz). \tag{3.24}$$

Since the cross section comes from data points, which are discrete, we can re-write the above equation as

$$\sigma_i(s_n) = \sigma_0(s_n) - \sum_{k=1}^{n} \int_{z_{k-1}}^{z_k} {\rm d}z\, \delta G(z) \sigma_{i-1}(s_n z). \tag{3.25}$$

Here, n (and k) is the index of the data points, thus $z_k = s_k/s_n$ and $z_n = 1$. For the lower bound, $z_0 = s_0/s_n = 10.6178^2/s_n$, corresponding to the energy where the cross section vanishes i.e. $\sigma_0(s_0) = 0$. Note that $z = s/s_n$ is still continuous so $s_0 \leq s \leq s_n$ (or $s_{k-1} \leq s \leq s_k$ within each integral in the sum) in equation (3.25). This means $\sigma_{i-1}(s_n z)$ is continuous and we calculate its value using linear interpolation based on neighbouring data points. Thus for $z_{k-1} \leq z \leq z_k$

$$\sigma_{i-1}(s_n z) = \sigma_{i-1}(s_k) - (e_k - e(z)) \frac{\sigma_{i-1}(s_k) - \sigma_{i-1}(s_{k-1})}{e_k - e_{k-1}}, \tag{3.26}$$

where e_k is the energy of the $k^{\rm th}$ cross section so $e(z) = \sqrt{z s_n} = \sqrt{s}$. For this procedure, we have taken the number of iterations, i, to be 50, giving results[4] that seem to be stable up to a precision of 10^{-5}. Specifically, there is no difference between $\sigma_{50}(s_n)$ and $\sigma_{100}(s_n)$ in the $5^{\rm th}$ decimal place for all n. To check the correctness of the results, we placed $\sigma_{50}(s_n)$ in equation (3.16) and found that the output agree with $\sigma_0(s_n)$ in the $5^{\rm th}$ decimal place[5].

The determination of the error of the BaBar data without ISR, is not completely trivial. In the BaBar paper [236], they construct a full covariance matrix using

$$V_{ij} = [\delta\sigma^2_{\rm stat}(s_j) + \delta\sigma^2_{\rm unc}(s_j)]\delta_{ij} + \delta\sigma_{\rm corr}(s_i)\delta\sigma_{\rm corr}(s_j), \tag{3.27}$$

where $\delta\sigma_{\rm stat}$, $\delta\sigma_{\rm unc}$ and $\delta\sigma_{\rm corr}$ are the statistical, uncorrelated and correlated systematic uncertainties respectively. Hence if we can express $\sigma_i(s_n)$ in terms of $\sigma_0(s_k)$ i.e.

$$\sigma_i(s_n) = \sum_{k=1}^{n} C^i_{nk} \sigma_0(s_k), \tag{3.28}$$

then we can write an equivalent equation to (2.36) and compute the error for each $\sigma_i(s_n)$. This also has the added benefit of being another check on the correctness of

[4] The results are roughly $O(10^{-1})$ and the errors, which will be discussed later, are $O(10^{-2})$

[5] In [266], they found differences of less than 0.5% after 5 iterations.

$\sigma_i(s_n)$ themselves. In order to do this, recall that

$$\begin{aligned}\sigma_i(s_n) &= \sigma_0(s_n) - \int_{z_0}^{1} \mathrm{d}z\,[G(z) - \delta(1-z)]\sigma_{i-1}(s_n z) \\ &= \sigma_0(s_n) - \sum_{k=1}^{n} \int_{z_{k-1}}^{z_k} \mathrm{d}z\, G(z) \left[\sigma_{i-1}(s_k) - (e_k - e(z))\frac{\sigma_{i-1}(s_k) - \sigma_{i-1}(s_{k-1})}{e_k - e_{k-1}}\right] \\ &\quad + \sigma_{i-1}(s_n) \\ &= \sigma_0(s_n) - \sum_{k=1}^{n} \left\{ I_k \sigma_{i-1}(s_k) - \tilde{I}_k \left[\sigma_{i-1}(s_k) - \sigma_{i-1}(s_{k-1})\right]\right\} + \sigma_{i-1}(s_n), \qquad (3.29)\end{aligned}$$

where

$$I_k = \int_{z_{k-1}}^{z_k} \mathrm{d}z\, G(z) \quad \text{and} \quad \tilde{I}_k = I_k \frac{e_k - e(z)}{e_k - e_{k-1}}. \qquad (3.30)$$

Hence in the first iteration,

$$\sigma_1(s_n) = \sum_{k_1=1}^{n} (\delta_{nk_1} - I_{k_1} + \tilde{I}_{k_1})\sigma_0(s_{k_1}) - \sum_{k_1=1}^{n} \tilde{I}_{k_1}\sigma_0(s_{k_1-1}) + \sigma_0(s_n) \qquad (3.31)$$

Since $\sigma_0(s_0) = 0$, the sum in the second term above now starts at $k_1 = 2$. Thus the term itself, through the manipulation of the summation index, can then be re-written as

$$\begin{aligned}\sum_{k_1=2}^{n} \tilde{I}_{k_1}\sigma_0(s_{k_1-1}) &= \sum_{k_1=1}^{n-1} \tilde{I}_{k_1+1}\sigma_0(s_{k_1}) \\ &= \sum_{k_1=1}^{n} [1 - \theta(k_1 - (n-1))]\tilde{I}_{k_1+1}\sigma_0(s_{k_1}), \qquad (3.32)\end{aligned}$$

where θ is the Heaviside function. Let $C^0_{nk_1} = \delta_{nk_1} - I_{k_1} + \tilde{I}_{k_1}$, then

$$\begin{aligned}\sigma_1(s_n) &= \sum_{k_1=1}^{n} \left\{ C^0_{nk_1} - [1 - \theta(k_1 - (n-1))]\tilde{I}_{k_1+1} + \delta_{nk_1}\right\}\sigma_0(s_{k_1}) \\ &= \sum_{k_1=1}^{n} C^1_{nk_1}\sigma_o(s_{k_1}). \qquad (3.33)\end{aligned}$$

For the next iteration,

$$\begin{aligned}\sigma_2(s_n) &= \sum_{k_2=1}^{n} C^0_{nk_2}\sigma_1(s_{k_2}) - \sum_{k_2=1}^{n-1} \tilde{I}_{k_2+1}\sigma_1(s_{k_2}) + \sigma_0(s_n) \\ &= \sum_{k_2=1}^{n} \left\{ C^0_{nk_2} - [1 - \theta(k_2 - (n-1))]\tilde{I}_{k_2+1}\right\}\sigma_1(s_{k_2}) + \sigma_0(s_n). \qquad (3.34)\end{aligned}$$

Now let $C_{nk_j} = C^0_{nk_j} - [1 - \theta(k_j - (n-1))]\tilde{I}_{k_j+1}$ and using (3.33),

$$\begin{aligned}\sigma_2(s_n) &= \sum_{k_2=1}^{n} \sum_{k_1=1}^{k_2} \left(C_{nk_2}C^1_{k_2k_1} + \delta_{nk_1}\right)\sigma_0(s_{k_1}) \\ &= \sum_{k_2=1}^{n} \sum_{k_1=1}^{k_2} C^2_{nk_1}\sigma_0(s_{k_1}). \qquad (3.35)\end{aligned}$$

Hence in general for the m^{th} iteration,

$$\sigma_m(s_n) = \sum_{k_m=1}^{n} ... \sum_{k_1=1}^{k_2} \left(C_{nk_m} C^{m-1}_{k_m k_1} + \delta_{nk_1} \right) \sigma_0(s_{k_1})$$
$$= \sum_{k_m=1}^{n} ... \sum_{k_1=1}^{k_2} C^m_{nk_1} \sigma_0(s_{k_1}). \tag{3.36}$$

Therefore the uncertainty for each data point without ISR is then given by

$$(\delta\sigma_m(s_n))^2 = \sum_{a=1}^{n}\sum_{b=1}^{n} \frac{\partial\sigma_m(s_n)}{\partial\sigma_0(s_a)} V_{ab} \frac{\partial\sigma_m(s_n)}{\partial\sigma_0(s_b)} \tag{3.37}$$
$$= \sum_{a=1}^{n}\sum_{b=1}^{n} C^m_{na} V_{ab} C^m_{nb}. \tag{3.38}$$

In addition, the results from equation (3.36) match the ones calculated using the iteration procedure. The final step in this 'de-convolution' involves subtracting the photon VP effects. Recall that the BaBar R_b data was converted to cross section measurements when subtracting the $\Upsilon(4S)$ tail and that for this measurement, BaBar used the *bare* $e^+e^- \to \mu^+\mu^-$ process for normalisation. Thus, this corresponds to case (1) in how to correct for VP effects from Section 2.1.1. So

$$R_{b,\text{ w/o ISR}}(s) = \frac{3s}{4\pi\alpha^2(s)} \sigma_m(s), \tag{3.39}$$

where the running of $\alpha(s)$ was taken as a constant with the value of $\alpha^2(s) = \alpha^2/0.929$ within the energy region covered by the BaBar data points. This was done because $\alpha(s)$ does not vary by a lot in this region, hence it is akin to applying a small effect on to a small correction of α itself, which can be ignored. Fig. 3.4 shows the result of the whole 'de-convolution' procedure, this matches the results shown in Figure 1 of [266].

With the BaBar R_b data 'de-convoluted' of ISR, we can then add R_{udsc} and include it as a data set in the inclusive channel. This is done with the help of the `rhad` program again, where the quantity $R_{\text{had}}(s) - R_t(s) - R_b(s)$ was calculated at the energies of the BaBar data points[6] and then added to them. The result of including this BaBar R_b data in the fit can be seen in Fig. 3.5. It is clear from the fit shown by the (yellow) band that much more structure can now be observed in this energy region, which was populated by only a couple of old data points previously. The (red) curved line displays the result of adding the $\Upsilon(5S)$ and $\Upsilon(6S)$ resonances (calculated using a Breit-Wigner parametrisation) incoherently to R_{udsc} values (from the program `rhad`). This shows that adding these contributions on the level of the cross section is a poor approximation. Interference effects on the amplitude level plays an important role here and the different contributions must be summed coherently. Since the new BaBar R_b data is able to

[6]Note that $R_t(s) \equiv 0$ since the energies used are too low for the top quark to have any measurable contribution.

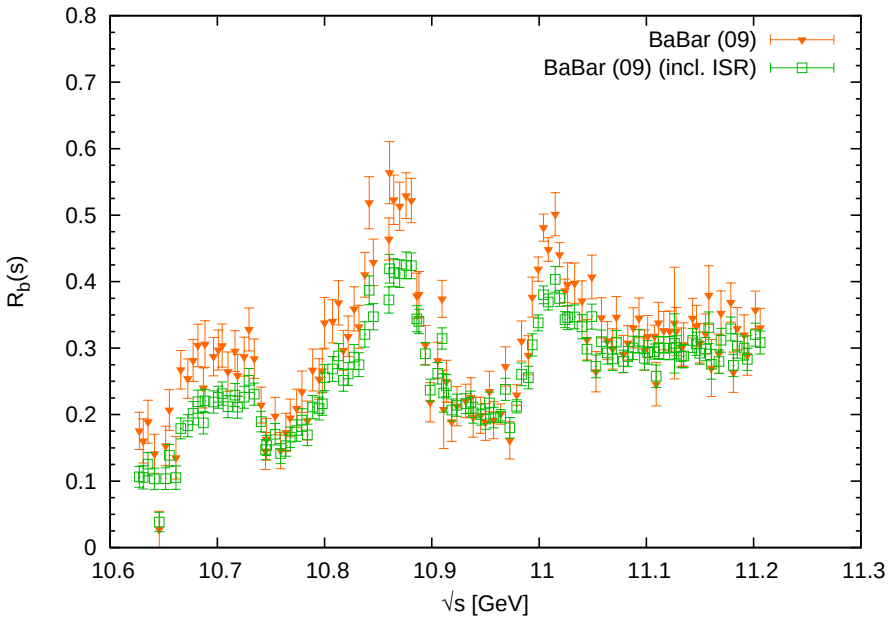

Fig. 3.4: Plot of the BaBar R_b data (with the radiative tails of the $\Upsilon(1S-4S)$ resonances subtracted) before and after removing ISR.

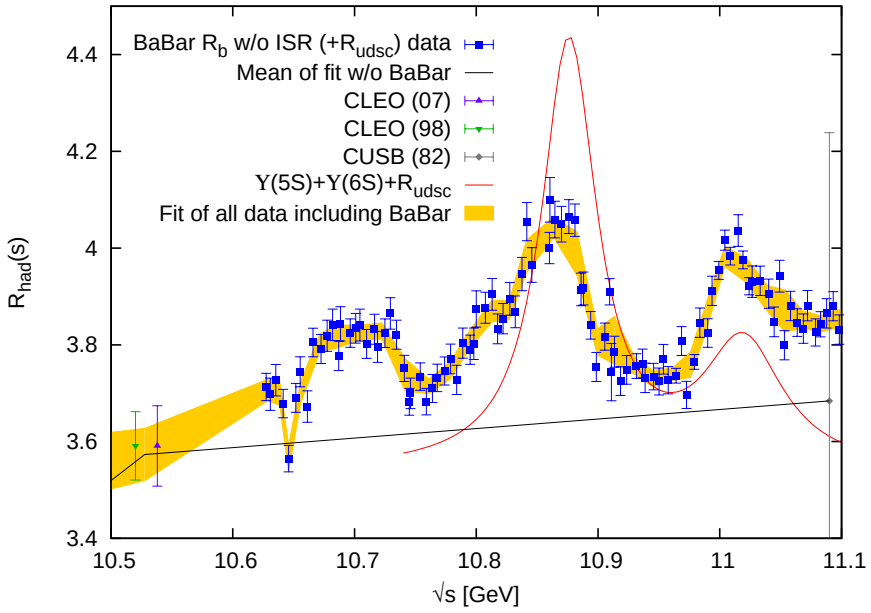

Fig. 3.5: Fit of all $R_{\rm had}$ data after including the BaBar R_b data with ISR removed. The data points of all the experiments in this region are indicated by the markers. The (black) line represent the mean of the fit before including the BaBar data. The (red) curved line with two peaks shows the result of incoherently adding the $\Upsilon(5S)$ and $\Upsilon(6S)$ resonances with R_{udsc}.

resolve the resonances of these two Υ states, there is no longer any need to add them separately in future analyses. Due to the weighting of the $g-2$ kernel function, this will

have minimal impact on the a_μ result. However, for $\Delta\alpha^{(5)}_{\rm had}(q^2)$ and $\alpha(q^2)$, the effects from this change will be more important and they will be presented in our upcoming paper [253].

Chapter 4

Conclusions and outlook

4.1 The SM prediction of the muon $g-2$

4.1.1 Total hadronic contribution

The leading order hadronic vacuum polarisation contribution to a_μ using the updated methodology, updated data compilation along with contributions from pQCD, ChPT and narrow resonances is determined to be

$$a_\mu^{\text{had, LOVP}} = (694.91 \pm 3.72_{\text{exp}} \pm 2.10_{\text{rad}}) \times 10^{-10}, \tag{4.1}$$

where the first error comes from experimental data and the second error comes from the treatment of radiative corrections. For the higher order hadronic vacuum polarisation contribution, the individual results from the three classes of diagrams are

$$a_\mu^{\text{had, HOVP(a)}} = (-20.61 \pm 0.11_{\text{exp}} \pm 0.07_{\text{rad}}) \times 10^{-10}, \tag{4.2}$$

$$a_\mu^{\text{had, HOVP(b)}} = (9.94 \pm 0.06_{\text{exp}} \pm 0.03_{\text{rad}}) \times 10^{-10}, \tag{4.3}$$

$$a_\mu^{\text{had, HOVP(c)}} = (0.34 \pm 0.01_{\text{exp}} \pm 0.00_{\text{rad}}) \times 10^{-10}. \tag{4.4}$$

Adding these together and keeping in mind that the errors from (a) and (b) are almost completely anti-correlated and are thus subtracted linearly, the total HOVP contribution to a_μ is

$$a_\mu^{\text{had, HOVP}} = (-9.84 \pm 0.06_{\text{exp}} \pm 0.04_{\text{rad}}) \times 10^{-10}. \tag{4.5}$$

For the hadronic light-by-light contribution, we have elected to use the recent compilation from Prades, de Rafael and Vainshtein [112],

$$a_\mu^{\text{had, LbL}} = (10.5 \pm 2.6) \times 10^{-10}, \tag{4.6}$$

which is equivalent to the recent result from Nyffeler and Jegerlehner, [11, 111],

$$a_\mu^{\text{had, LbL}} = (11.6 \pm 4.0) \times 10^{-10}. \tag{4.7}$$

Therefore the total hadronic contribution to a_μ comes to

$$a_\mu^{\text{had}} = (695.6 \pm 4.9) \times 10^{-10}. \tag{4.8}$$

The total uncertainty is calculated as follows. Since the LOVP and HOVP contributions are almost completely anti-correlated, their errors are added linearly with a relative minus sign. Then the uncertainty from the LbL contribution is added quadratically.

4.1.2 Total contribution to a_μ and comparisons

For the QED contribution to a_μ we use the value from [9, 34]

$$a_\mu^{\mathrm{QED}} = (11\,658\,471.808 \pm 0.015) \times 10^{-10}, \tag{4.9}$$

as stated in Section 1.3. For the electroweak sector, we use

$$a_\mu^{\mathrm{EW}} = (15.4 \pm 0.2) \times 10^{-10} \tag{4.10}$$

from [55]. Thus adding these to the total hadronic contribution from above we arrive at

$$a_\mu^{\mathrm{SM}} = (11\,659\,182.8 \pm 4.9) \times 10^{-10}, \tag{4.11}$$

where the errors have been added in quadrature. This result is now even more precise than the formidable experimental measurement from BNL [10]. Recently there was a slight change in the ratio of the muon-to-proton magnetic moment published from CODATA [269]. This means the experimental value for a_μ is now slightly increased [270, 271]

$$a_\mu^{\mathrm{EXP}} = (11\,659\,208.9 \pm 6.3) \times 10^{-10}, \tag{4.12}$$

which leads to a difference of

$$a_\mu^{\mathrm{EXP}} - a_\mu^{\mathrm{SM}} = (26.1 \pm 8.0) \times 10^{-10}, \tag{4.13}$$

corresponding to a 3.3σ discrepancy.

Fig. 4.1 gives the comparison between some recent SM predictions from various groups (shown by the markers) and the latest world average of the experimental value of a_μ ((orange) band), which is dominated by the results from the BNL experiment. It is clear that in spite of the changes in recent years, the different SM predictions agree quite well with each other. Furthermore, the discrepancy in this observable have consolidated at a level of more than 3σ. Although this discrepancy is not large enough to establish a definitive deviation from the SM, it should be noted that all the contributions have been carefully checked[1]. In addition, it is becoming more challenging to explain this discrepancy by altering the hadronic data to increase the total hadronic contribution. Since this would result in more tension with the EW precision fits of the SM and the limits on the mass of the Higgs boson [274, 275].

[1] Although the very recent developments in the hadronic light-by-light contribution need to be investigated further.

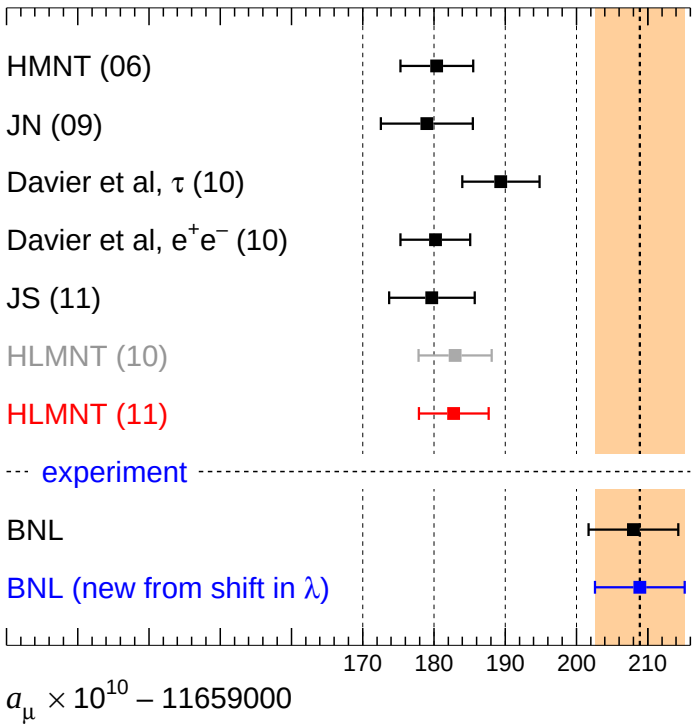

Fig. 4.1: Standard model predictions of a_μ by several groups compared to the measurement from BNL [10, 270, 271]. The SM predictions are from HMNT (06) [62], JN (09) [11], Davier *et al.* [78], JS (11) [82], HLMNT (10) [272, 273], and HLMNT (11) is this work. Note that the value from Jegerlehner and Szafron includes τ spectral function data, which, in their approach, are fully consistent with and confirm the e^+e^- data. HLMNT (10) is a preliminary version of this work, presented at conferences [272, 273], but before the full updated data set was available.

4.2 The running of the QED coupling at the Z-boson mass

With the same compilation of hadronic data, we have also been able to compute the updated prediction of the five-flavour hadronic contribution to the running of the QED coupling, with a value of

$$\Delta\alpha^{(5)}_{\rm had}(M_Z^2) = (276.26 \pm 1.38) \times 10^{-4} \tag{4.14}$$

at the Z-boson mass. This updates the prediction of the running of the QED coupling itself, whose value at the Z scale is,

$$\alpha(M_Z^2)^{-1} = 128.944 \pm 0.019. \tag{4.15}$$

Fig. 4.2 shows that the contribution to $\Delta\alpha^{(5)}_{\rm had}(M_Z^2)$ receives very different weightings from the energy of the hadronic data compared to $a_\mu^{\rm had,\,LOVP}$. There is much less

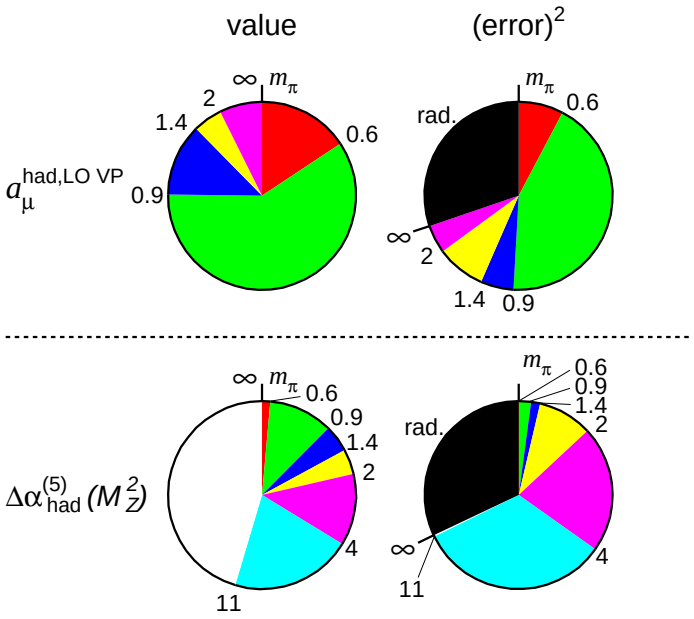

Fig. 4.2: The pie diagrams in the left- and right-hand columns show the fractions of the total contributions and (errors)^2, respectively, coming from various energy intervals in the dispersion integrals (1.52) and (3.4). The pie diagrams for the LO hadronic contribution to $g-2$, shown in the first row, correspond to sub-contributions with energy boundaries at $m_\pi, 0.6, 0.9, 1.4, 2$ GeV and ∞, whereas for the hadronic contribution to the QED coupling, shown in the second row, the boundaries are at $m_\pi, 0.6, 0.9, 1.4, 2, 4, 11.09$ GeV and ∞. In the (error)^2 pie diagrams we also included the (error)^2 arising from the treatment of the radiative corrections to the data.

emphasis on the low energy regions, while the single biggest contribution comes from above 11 GeV. Using the this updated value of $\Delta\alpha^{(5)}_{\text{had}}(M_Z^2)$, the EW precision fits of the SM gives a more constrained mass limit for the Higgs boson. The SM preferred value at 68% confidence level is now

$$m_H = \left(91^{+30}_{-23}\right)\ \text{GeV}, \tag{4.16}$$

which lies in a region excluded by the direct searches.

4.3 Summary

This work was aiming to obtain the most accurate and precise determination of the anomalous magnetic moment of the muon $a_\mu = (g-2)/2$ and for the QED coupling at the Z-boson mass. These are two are quantities in the SM of particle physics. In particular, the a_μ discrepancy between the experimental measurement and theoretical prediction is arguably the best clue at present for new physics beyond the SM.

Currently, the greatest source of uncertainty for the predictions come from the leading order hadronic vacuum polarisation contribution. This analysis employs a data-drive approach to tackle this issue by making use of as many e^+e^- hadronic annihilation measurements as possible. The combination of measurements from different experiments in a reliable and consistent manner is achieved using a flexible clustering algorithm, with local χ^2 inflation where necessary. From the top pie graphs in Fig. 4.2, the single largest central value and error of the LO VP contribution to a_μ, both originate from the e^+e^- energy region between 0.6 and 0.9 GeV, where the $\pi^+\pi^-$ final state dominates.

The new radiative return data from BaBar and KLOE had a limited effect in decreasing the uncertainty of the $\pi^+\pi^-$ channel given the level of precision of these data. This is due to tension between data from the different measurements. In particular, the BaBar data is significantly larger than ones from KLOE at energies above 0.8 GeV. Thus, there is much room for improvement and investigation from future measurements.

Other new data using both direct scan and radiative return methods have improved the description of the energy region below 2 GeV, especially for channels with high multiplicities. In addition, the use of new isospin relations derived by [78] have significantly reduced the error from channels not measured by experiments. Therefore this analysis has revisited the issue of choosing either the sum of exclusive final states or data from the $e^+e^- \to$ all hadrons inclusive channel for the energy region $1.43 \lesssim \sqrt{s} \leq 2$ GeV. There is a discrepancy between these two choices, where the sum of exclusive data is more precise but higher than the inclusive data. Thus in a previous analysis [61], QCD sum rules were used to discriminate between them. This procedure has also been refined with an updated Adler function and better sum rule choices. Hence, along with the updated data compilation, this analysis now finds good agreement of the sum rules with the world average for $\alpha_s(M_Z^2)$ when the sum of exclusive channels is used, and less agreement with the use of inclusive data. This reverses the finding of [61] and thus the sum of exclusive channels is now the default choice. However, it is worth noting that the sum of exclusive data is still higher than the inclusive data, and the shapes of their hadronic R-ratio plot are still different.

Moreover, in the energy region between 2.6 GeV and the charm threshold, new data from BES are in near perfect agreement with predictions from pQCD. Hence it was decided that pQCD with a relative error corresponding to that from the BES data should be used in this region. If the use of pQCD is extended further down to 2 GeV, then the central value for a_μ would be shifted down slightly (1.2×10^{-10}) and the sum rules would favour the use of exclusive data even more (see Fig. 2.39).

With all these choices and refinements taken into account, this work arrives at the results shown in the sections above. There is, however, one set of data that did not make it into the main results. In the energy region 10.54 to 11.20 GeV, BaBar have

taken a detailed measurement of R_b. However, this data includes initial state radiation, which must be removed before the data can be used. This was done by following the procedure described in [266]. R_{usdc} values was then added to this data so it can be used as part of the inclusive channel. Due to the weighting of the $g-2$ kernel, this will have minimal impact on the central value and uncertainty of a_μ. However, it will be very useful for the calculation of the QED coupling, as the energy region this data covers was not measured very well at all with only a couple of data points present. The effect of including this BaBar R_b measurement on the running of the QED coupling will be presented in a forthcoming paper [253].

4.4 Outlook

There are numerous interesting prospects for improvement in both the theoretical and experimental side associated with the determination of the muon $g-2$. Regarding further measurements of $e^+e^- \to$ hadrons, the new CMD-3 and SND direct scan experiments at the VEPP-2000 collider in Novosibirsk are already taking data [276]. They will provide crucial cross checks in the energy region between $1-2$ GeV, especially for hadronic final states with high multiplicities. Moreover the KEDR experiment at the VEPP-4M collider are planning to take inclusive $R(s)$ measurements up to 10 GeV. This will provide very useful information and checks for the relatively sparsely populated higher energy regions. In addition, the BES-III experiment at the BEPCII collider in Beijing are also going ahead with measurements of R at higher energies. Furthermore, more radiative return data from KLOE and BaBar are also expected. Further in the future, there is a strong possibility for an upgraded DAΦNE detector [277] and Super-B factories. These experiments will be pivotal in improving the precision of the theoretical determinations of the hadronic vacuum polarisation contributions. The very recent results on the τ versus e^+e^- data are very interesting and show encouraging signs of fully resolving this issue in the future, and further improving the precision of the hadronic vacuum polarisation contribution to a_μ.

Regarding the hadronic light-by-light contribution, the proposed $\gamma\gamma$ physics programme at the upcoming KLOE-2 experiment could be very useful. By measuring the $\gamma\gamma$ transition form factors of pseudoscalars, it will provide better constraints on these objects and hopefully help to improve the model predictions. Furthermore, Lattice QCD looks promising in providing an independent determination of $a_\mu^{\text{had, LbL}}$ in the near future. It will be very interesting to see how their results compare with the mainstream, model dependent calculations.

The next generation of experiments for measuring a_μ, which are striving for approximately four fold increase in precision compared to BNL, are being planned at Fermilab (E989) [278] and J-PARC [279]. Therefore, improvements to the theoretical calculation of a_μ^{had} are critical if the SM prediction of a_μ is to match the precision set by the new

experiments. With this aim in mind the methodology of this analysis may also need to be improved to include inter-experiment and inter-channel correlations. Some of these refinements and prospects of course will also help with the determination of the running of the QED coupling.

Lastly, the QCD sum rule analysis that is performed in this work have the potential to be used for precise determinations of certain parameters within QCD. For example, condensates are important for the study of low energy hadronic physics, however they are not very well determined. For some, even their signs may be in disagreement between different determinations [66, 280]. Condensates such as $\langle GG \rangle$ enter the sum rule as part of the non-perturbative contribution to the Adler function. Therefore, by keeping the condensate of interest as a free parameter but keeping other constants such as $\alpha_s(M_Z^2)$ fixed, the e^+e^- hadronic annihilation data can then be used to determine that condensate. In the same spirit $\alpha_s(M_Z^2)$ can also be determined this way. Furthermore, a fit with multiple parameters that simultaneously determines all the objects of interest can also be done and may be preferred. With the increasing precision of the e^+e^- data, this method has the potential to become quite competitive provided that a suitable set of sum rules can be found.

Appendix A

Sum rule integrals

A.1 Integrals for $D_0(s)$ contributions

This section will list integrals of the form

$$\int_C \mathrm{d}s \left(\ln \frac{-s}{s_0}\right)^p \left(\frac{s}{s_0}\right)^q, \tag{A.1}$$

where the contour C runs counterclockwise from $s = s_0 + i\epsilon$ to $s = s_0 - i\epsilon$ on a circle of radius s_0, centered on the origin in the complex s-plane. Therefore we can parametrise s using the angle θ,

$$s = -s_0 e^{i\theta}, \quad (-\pi \leq \theta \leq \pi) \tag{A.2}$$

$$\mathrm{d}s = -is_0 e^{i\theta} \mathrm{d}\theta. \tag{A.3}$$

Take $(p, q) = (0, -1)$ as an example,

$$\int_C \mathrm{d}s \frac{s_0}{s} = \int_{-\pi}^{\pi} \mathrm{d}\theta \, is_0 = 2\pi i s_0. \tag{A.4}$$

However, we require $p = 1, 2, 3$ and $q = -1, 0, 1, 2$ thus for $q = -1$

$$\int_C \mathrm{d}s \ln \left(\frac{-s}{s_0}\right) \left(\frac{s_0}{s}\right) = 0, \tag{A.5}$$

$$\int_C \mathrm{d}s \ln^2 \left(\frac{-s}{s_0}\right) \left(\frac{s_0}{s}\right) = -\frac{2}{3}\pi^3 i s_0, \tag{A.6}$$

$$\int_C \mathrm{d}s \ln^3 \left(\frac{-s}{s_0}\right) \left(\frac{s_0}{s}\right) = 0. \tag{A.7}$$

For $q = 0$,

$$\int_C \mathrm{d}s \ln \left(\frac{-s}{s_0}\right) = 2\pi i s_0, \tag{A.8}$$

$$\int_C \mathrm{d}s \ln^2 \left(\frac{-s}{s_0}\right) = -4\pi i s_0, \tag{A.9}$$

$$\int_C \mathrm{d}s \ln^3 \left(\frac{-s}{s_0}\right) = (12\pi - 2\pi^3) i s_0. \tag{A.10}$$

For $q = 1$,

$$\int_C \mathrm{d}s \ln\left(\frac{-s}{s_0}\right)\left(\frac{s}{s_0}\right) = \pi i s_0, \tag{A.11}$$

$$\int_C \mathrm{d}s \ln^2\left(\frac{-s}{s_0}\right)\left(\frac{s}{s_0}\right) = -\pi i s_0, \tag{A.12}$$

$$\int_C \mathrm{d}s \ln^3\left(\frac{-s}{s_0}\right)\left(\frac{s}{s_0}\right) = \left(\frac{3}{2}\pi - \pi^3\right) i s_0. \tag{A.13}$$

For $q = 2$,

$$\int_C \mathrm{d}s \ln\left(\frac{-s}{s_0}\right)\left(\frac{s}{s_0}\right)^2 = \frac{2}{3}\pi i s_0, \tag{A.14}$$

$$\int_C \mathrm{d}s \ln^2\left(\frac{-s}{s_0}\right)\left(\frac{s}{s_0}\right)^2 = -\frac{4}{9}\pi i s_0, \tag{A.15}$$

$$\int_C \mathrm{d}s \ln^3\left(\frac{-s}{s_0}\right)\left(\frac{s}{s_0}\right)^2 = \left(\frac{4}{9}\pi - \frac{2}{3}\pi^3\right) i s_0. \tag{A.16}$$

A.2 Integrals for $D_m(s)$ and $D_{np}(s)$ contributions

$$\int_C \mathrm{d}s \frac{1}{s^2} \ln\left(\frac{-s}{s_0}\right) = -2\pi i \frac{1}{s_0}, \tag{A.17}$$

$$\int_C \mathrm{d}s \frac{1}{s^3} \ln\left(\frac{-s}{s_0}\right) = -\pi i \frac{1}{s_0^2}. \tag{A.18}$$

Other required integrals can be found above.

Bibliography

[1] J. S. Schwinger, "On Quantum electrodynamics and the magnetic moment of the electron," *Phys. Rev.* **73** (1948) 416–417.

[2] H. Foley and P. Kusch, "On the Intrinsic Moment of the Electron," *Phys.Rev.* **73** (1948) 412–412.

[3] W. Gerlach and O. Stern, "Experimental proof of the magnetic moment of the silver atom," *Z.Phys.* **8** (1922) 110–111.

[4] S. Goudschmidt and G. Uhlenbeck, "Spinning electrons and the structure of spectra," *Nature* **117** (1926) 264–265.

[5] P. A. Dirac, "The Quantum theory of electron," *Proc.Roy.Soc.Lond.* **A117** (1928) 610–624.

[6] F. Halzen and A. D. Martin, *Quarks and Leptons: An Introductory Course in Modern Particle Physics*. John Wiley & Sons, 1984.

[7] V. B. Berestetskii, O. N. Krokhin, and A. K. Khelbnikov *Sov.Phys.JETP* **3** (1956) 761.

[8] D. Hanneke, S. Fogwell, and G. Gabrielse, "New Measurement of the Electron Magnetic Moment and the Fine Structure Constant," *Phys. Rev. Lett.* **100** (2008) 120801, `arXiv:0801.1134 [physics.atom-ph]`.

[9] T. Aoyama, M. Hayakawa, T. Kinoshita, and M. Nio, "Revised value of the eighth-order QED contribution to the anomalous magnetic moment of the electron," *Phys. Rev.* **D77** (2008) 053012, `arXiv:0712.2607 [hep-ph]`.

[10] **Muon (g-2)** Collaboration, G. W. Bennett *et al.*, "Final report of the muon E821 anomalous magnetic moment measurement at BNL," *Phys. Rev.* **D73** (2006) 072003, `arXiv:hep-ex/0602035`.

[11] F. Jegerlehner and A. Nyffeler, "The Muon g-2," *Phys.Rept.* **477** (2009) 1–110, `arXiv:0902.3360 [hep-ph]`.

[12] G. Charpak, F. Farley, R. Garwin, T. Muller, J. Sens, *et al.*, "Measurement of the anomalous magnetic moment of the muon," *Phys.Rev.Lett.* **6** (1961) 128–132.

[13] J. Bailey, W. Bartl, G. Von Bochmann, R. Brown, F. Farley, *et al.*, "Precision measurement of the anomalous magnetic moment of the muon," *Phys.Lett.* **B28** (1968) 287–290.

[14] J. Bailey, W. Bartl, G. von Bochmann, R. Brown, F. Farley, *et al.*, "Precise Measurement of the Anomalous Magnetic Moment of the Muon," *Nuovo Cim.* **A9** (1972) 369–432.

[15] **CERN-Mainz-Daresbury** Collaboration, J. Bailey *et al.*, "Final Report on the CERN Muon Storage Ring Including the Anomalous Magnetic Moment and the Electric Dipole Moment of the Muon, and a Direct Test of Relativistic Time Dilation," *Nucl.Phys.* **B150** (1979) 1.

[16] R. Carey, W. Earle, E. Efstathiadis, M. Hare, E. Hazen, *et al.*, "New measurement of the anomalous magnetic moment of the positive muon," *Phys.Rev.Lett.* **82** (1999) 1632–1635.

[17] **Muon (g-2)** Collaboration, H. Brown *et al.*, "Improved measurement of the positive muon anomalous magnetic moment," *Phys.Rev.* **D62** (2000) 091101, `arXiv:hep-ex/0009029`.

[18] **Muon (g-2)** Collaboration, H. Brown *et al.*, "Precise measurement of the positive muon anomalous magnetic moment," *Phys.Rev.Lett.* **86** (2001) 2227–2231, `arXiv:hep-ex/0102017`.

[19] **Muon (g-2)** Collaboration, G. Bennett *et al.*, "Measurement of the positive muon anomalous magnetic moment to 0.7 ppm," *Phys.Rev.Lett.* **89** (2002) 101804, `arXiv:hep-ex/0208001 [hep-ex]`.

[20] **Muon (g-2)** Collaboration, G. Bennett *et al.*, "Measurement of the negative muon anomalous magnetic moment to 0.7 ppm," *Phys.Rev.Lett.* **92** (2004) 161802, `arXiv:hep-ex/0401008 [hep-ex]`.

[21] V. Bargmann, L. Michel, and V. Telegdi, "Precession of the polarization of particles moving in a homogeneous electromagnetic field," *Phys.Rev.Lett.* **2** (1959) 435.

[22] B. W. Montague, "Polarized beams in high-energy e^+e^- storage rings," *Phys.Rept.* **113** (1984) 1–96.

[23] **Particle Data Group** Collaboration, K. Nakamura *et al.*, "Review of particle physics," *J. Phys.* **G37** (2010) 075021.

[24] T. Kinoshita, B. Nizic, and Y. Okamoto, "Eighth order QED contribution to the anomalous magnetic moment of the muon," *Phys. Rev.* **D41** (1990) 593–610.

[25] A. Petermann, "Fourth order magnetic moment of the electron," *Helv.Phys.Acta* **30** (1957) 407–408.

[26] C. M. Sommerfield, "Magnetic Dipole Moment of the Electron," *Phys.Rev.* **107** (1957) 328–329.

[27] T. Kinoshita, "New value of the α^3 electron anomalous magnetic moment," *Phys.Rev.Lett.* **75** (1995) 4728–4731.

[28] S. Laporta and E. Remiddi, "The Analytical value of the electron $(g-2)$ at order α^3 in QED," *Phys.Lett.* **B379** (1996) 283–291, `arXiv:hep-ph/9602417`.

[29] M. Caffo, S. Turrini, and E. Remiddi, "Higher-order radiative corrections to electron anomaly in qed: a remark on asymptotic behavior of vacuum polarization insertions and explicit analytic values of the first six ladder graphs," *Nucl.Phys.* **B141** (1978) 302.

[30] J.-P. Aguilar, D. Greynat, and E. De Rafael, "Muon Anomaly from Lepton Vacuum Polarization and The Mellin-Barnes Representation," *Phys.Rev.* **D77** (2008) 093010, `arXiv:0802.2618 [hep-ph]`.

[31] T. Kinoshita and W. Lindquist, "Eighth Order Anomalous Magnetic Moment of the electron," *Phys.Rev.Lett.* **47** (1981) 1573.

[32] V. Hughes and T. Kinoshita, "Anomalous g values of the electron and muon," *Rev.Mod.Phys.* **71** (1999) S133–S139.

[33] T. Aoyama, M. Hayakawa, T. Kinoshita, and M. Nio, "Revised value of the eighth-order electron $g-2$," *Phys.Rev.Lett.* **99** (2007) 110406, `arXiv:0706.3496 [hep-ph]`.

[34] T. Kinoshita and M. Nio, "The tenth-order QED contribution to the lepton g-2: Evaluation of dominant α^5 terms of muon g-2," *Phys. Rev.* **D73** (2006) 053007, `arXiv:hep-ph/0512330`.

[35] T. Aoyama, M. Hayakawa, T. Kinoshita, and M. Nio, "Tenth-Order QED contribution to Lepton Anomalous Magnetic Moment - Fourth-Order Vertices Containing Sixth-Order Vacuum-Polarization Subdiagrams," *Phys.Rev.* **D83** (2011) 053002, `arXiv:1101.0459 [hep-ph]`.

[36] T. Aoyama, M. Hayakawa, T. Kinoshita, and M. Nio, "Tenth-Order Lepton Anomalous Magnetic Moment - Sixth-Order Vertices Containing Vacuum-Polarization Subdiagrams," arXiv:1105.5200 [hep-ph].

[37] M. Hayakawa. Work presented by Thomas Teubner on behalf of Masashi Hayakawa at *PhiPsi11, International Workshop on e^+e^- collisions from Phi to Psi, Novosibirsk, Russia, 19–22 September 2011.*

[38] P. Mohr and B. Taylor, "CODATA recommended values of the fundamental physical constants: 1998," *Rev.Mod.Phys.* **72** (2000) 351–495.

[39] H. H. Elend *Phys.Lett.* **20** (1966) 682. Erratum-ibid. **21** (1966) 720.

[40] M. Passera, "The Standard model prediction of the muon anomalous magnetic moment," *J.Phys.G* **G31** (2005) R75–R94, arXiv:hep-ph/0411168 [hep-ph].

[41] T. Kinoshita and M. Nio, "Improved α^4 term of the muon anomalous magnetic moment," *Phys.Rev.* **D70** (2004) 113001, arXiv:hep-ph/0402206.

[42] G. 't Hooft, "Renormalization of Massless Yang-Mills Fields," *Nucl.Phys.* **B33** (1971) 173–199.

[43] G. 't Hooft, "Renormalizable Lagrangians for Massive Yang-Mills Fields," *Nucl.Phys.* **B35** (1971) 167–188.

[44] G. 't Hooft and M. Veltman, "Combinatorics of gauge fields," *Nucl.Phys.* **B50** (1972) 318–353.

[45] R. Jackiw and S. Weinberg, "Weak interaction corrections to the muon magnetic moment and to muonic atom energy levels," *Phys.Rev.* **D5** (1972) 2396–2398.

[46] I. Bars and M. Yoshimura, "Muon magnetic moment in a finite theory of weak and electromagnetic interaction," *Phys.Rev.* **D6** (1972) 374–376.

[47] G. Altarelli, N. Cabibbo, and L. Maiani, "The Drell-Hearn sum rule and the lepton magnetic moment in the Weinberg model of weak and electromagnetic interactions," *Phys.Lett.* **B40** (1972) 415.

[48] W. A. Bardeen, R. Gastmans, and B. Lautrup, "Static quantities in Weinberg's model of weak and electromagnetic interactions," *Nucl.Phys.* **B46** (1972) 319–331.

[49] K. Fujikawa, B. Lee, and A. Sanda, "Generalized Renormalizable Gauge Formulation of Spontaneously Broken Gauge Theories," *Phys.Rev.* **D6** (1972) 2923–2943.

[50] T. Kukhto, E. Kuraev, Z. Silagadze, and A. Schiller, "The Dominant two loop electroweak contributions to the anomalous magnetic moment of the muon," *Nucl.Phys.* **B371** (1992) 567–596.

[51] S. L. Adler and D. Boulware, "Anomalous commutators and the triangle diagram," *Phys.Rev.* **184** (1969) 1740–1744.

[52] J. Bell and R. Jackiw, "A PCAC puzzle: $\pi^0 \to \gamma\gamma$ in the sigma model," *Nuovo Cim.* **A60** (1969) 47–61.

[53] W. A. Bardeen, "Anomalous Ward identities in spinor field theories," *Phys.Rev.* **184** (1969) 1848–1857.

[54] A. Czarnecki, B. Krause, and W. J. Marciano, "Electroweak corrections to the muon anomalous magnetic moment," *Phys.Rev.Lett.* **76** (1996) 3267–3270, arXiv:hep-ph/9512369.

[55] A. Czarnecki, W. J. Marciano, and A. Vainshtein, "Refinements in electroweak contributions to the muon anomalous magnetic moment," *Phys. Rev.* **D67** (2003) 073006, arXiv:hep-ph/0212229. [Erratum-ibid. **D73** (2006) 119901].

[56] M. Knecht, S. Peris, M. Perrottet, and E. De Rafael, "Electroweak hadronic contributions to the muon (g-2)," *JHEP* **0211** (2002) 003, arXiv:hep-ph/0205102 [hep-ph].

[57] T. Blum and S. Chowdhury, "Hadronic contributions to g-2 from the lattice," *Nucl.Phys.Proc.Suppl.* **189** (2009) 251–256.

[58] P. Rakow *private communication* . See also talk at Lattice 2008, Williamsburg, Virginia, USA, 14-19 July 2008.

[59] T. Goecke, C. S. Fischer, and R. Williams, "Hadronic light-by-light scattering in the muon g-2: a Dyson-Schwinger equation approach," *Phys.Rev.* **D83** (2011) 094006, arXiv:1012.3886 [hep-ph].

[60] S. J. Brodsky and E. De Rafael, "Suggested boson - lepton pair couplings and the anomalous magnetic moment of the muon," *Phys.Rev.* **168** (1968) 1620–1622.

[61] K. Hagiwara, A. D. Martin, D. Nomura, and T. Teubner, "Predictions for $g-2$ of the muon and $\alpha_{\rm QED}(M_Z^2)$," *Phys. Rev.* **D69** (2004) 093003, arXiv:hep-ph/0312250.

[62] K. Hagiwara, A. D. Martin, D. Nomura, and T. Teubner, "Improved predictions for g-2 of the muon and $\alpha_{\rm QED}(M_Z^2)$," *Phys. Lett.* **B649** (2007) 173–179, arXiv:hep-ph/0611102.

[63] R. Alemany, M. Davier, and A. Hocker, "Improved Determination of the Hadronic Contribution to the Muon (g-2) and to $\alpha(M_Z^2)$ Using new Data from Hadronic τ Decays," *Eur. Phys. J.* **C2** (1998) 123–135, arXiv:hep-ph/9703220.

[64] **ALEPH** Collaboration, R. Barate *et al.*, "Measurement of the spectral functions of vector current hadronic tau decays," *Z.Phys.* **C76** (1997) 15–33.

[65] **ALEPH** Collaboration, R. Barate *et al.*, "Measurement of the spectral functions of axial-vector hadronic τ decays and determination of $\alpha_s(M_\tau^2)$ from hadronic τ decays," *Eur.Phys.J.* **C4** (1998) 409–431.

[66] **ALEPH Collaboration** Collaboration, S. Schael *et al.*, "Branching ratios and spectral functions of τ decays: Final ALEPH measurements and physics implications," *Phys.Rept.* **421** (2005) 191–284, arXiv:hep-ex/0506072 [hep-ex].

[67] **OPAL** Collaboration, K. Ackerstaff *et al.*, "Measurement of the strong coupling constant α_s and the vector and axial vector spectral functions in hadronic tau decays," *Eur.Phys.J.* **C7** (1999) 571–593, arXiv:hep-ex/9808019 [hep-ex].

[68] **CLEO** Collaboration, S. Anderson *et al.*, "Hadronic structure in the decay $\tau^- \to \pi^-\pi^0\nu_\tau$," *Phys.Rev.* **D61** (2000) 112002, arXiv:hep-ex/9910046 [hep-ex].

[69] **Belle** Collaboration, M. Fujikawa *et al.*, "High-Statistics Study of the $\tau^- \to \pi^-\pi^0\nu_\tau$ Decay," *Phys.Rev.* **D78** (2008) 072006, arXiv:0805.3773 [hep-ex].

[70] W. Marciano and A. Sirlin, "Electroweak Radiative Corrections to τ Decay," *Phys.Rev.Lett.* **61** (1988) 1815–1818.

[71] E. Braaten and C.-S. Li, "Electroweak radiative corrections to the semihadronic decay rate of the τ lepton," *Phys.Rev.* **D42** (1990) 3888–3891.

[72] R. Decker and M. Finkemeier, "Short and long distance effects in the decay $\tau \to \pi\nu_\tau(\gamma)$," *Nucl.Phys.* **B438** (1995) 17–53, arXiv:hep-ph/9403385 [hep-ph].

[73] J. Erler, "Electroweak radiative corrections to semileptonic τ decays," *Rev.Mex.Fis.* **50** (2004) 200–202, arXiv:hep-ph/0211345 [hep-ph].

[74] V. Cirigliano, G. Ecker, and H. Neufeld, "Radiative τ decay and the magnetic moment of the muon," *JHEP* **0208** (2002) 002, arXiv:hep-ph/0207310 [hep-ph].

[75] M. Davier, S. Eidelman, A. Hocker, and Z. Zhang, "Confronting spectral functions from e^+e^- annihilation and τ decays: Consequences for the muon magnetic moment," *Eur.Phys.J.* **C27** (2003) 497–521, arXiv:hep-ph/0208177 [hep-ph].

[76] M. Davier, S. Eidelman, A. Hocker, and Z. Zhang, "Updated estimate of the muon magnetic moment using revised results from e^+e^- annihilation," *Eur.Phys.J.* **C31** (2003) 503–510, arXiv:hep-ph/0308213 [hep-ph].

[77] M. Davier *et al.*, "The Discrepancy Between τ and e^+e^- Spectral Functions Revisited and the Consequences for the Muon Magnetic Anomaly," *Eur. Phys. J.* **C66** (2010) 127–136, arXiv:0906.5443 [hep-ph].

[78] M. Davier, A. Hoecker, B. Malaescu, and Z. Zhang, "Reevaluation of the hadronic contributions to the muon $g-2$ and to $\alpha(M_Z^2)$," *Eur. Phys. J.* **C71** (2011) 1515, arXiv:1010.4180 [hep-ph].

[79] M. Benayoun, P. David, L. DelBuono, and O. Leitner, "A Global Treatment Of VMD Physics Up To The ϕ: I. e^+e^- Annihilations, Anomalies And Vector Meson Partial Widths," *Eur. Phys. J.* **C65** (2010) 211–245, arXiv:0907.4047 [hep-ph].

[80] M. Benayoun, P. David, L. DelBuono, and O. Leitner, "A Global Treatment Of VMD Physics Up To The phi: II. tau Decay and Hadronic Contributions To g-2," *Eur. Phys. J.* **C68** (2010) 355–379, arXiv:0907.5603 [hep-ph].

[81] M. Benayoun, L. Del Buono, P. David, and O. Leitner, "Can VMD improve the estimate of the muon g-2 ?," *Chin. Phys.* **C34** (2010) 698–704, arXiv:0912.1248 [hep-ph].

[82] F. Jegerlehner and R. Szafron, "$\rho^0 - \gamma$ mixing in the neutral channel pion form factor $F_\pi^{(e)}(s)$ and its role in comparing e^+e^- with τ spectral functions," *Eur. Phys. J.* **C71** (2011) 1632, arXiv:1101.2872 [hep-ph].

[83] M. Benayoun, P. David, L. DelBuono, and F. Jegerlehner, "Upgraded Breaking Of The HLS Model: A Full Solution to the $\tau^- e^+ e^-$ and ϕ Decay Issues And Its Consequences On g-2 VMD Estimates," arXiv:1106.1315 [hep-ph].

[84] B. Krause, "Higher-order hadronic contributions to the anomalous magnetic moment of leptons," *Phys. Lett.* **B390** (1997) 392–400, arXiv:hep-ph/9607259.

[85] **Crystal Ball** Collaboration, D. Williams *et al.*, "Production of the pseudoscalars π^0, η, and η' in the reaction $\gamma\gamma \to \gamma\gamma$,". SLAC-PUB-4580, (1988).

[86] S. Weinberg, "Phenomenological Lagrangians," *Physica* **A96** (1979) 327. Festschrift honoring Julian Schwinger on his 60th birthday.

[87] J. Gasser and H. Leutwyler, "Chiral Perturbation Theory to One Loop," *Annals Phys.* **158** (1984) 142.

[88] J. Gasser and H. Leutwyler, "Chiral Perturbation Theory: Expansions in the Mass of the Strange Quark," *Nucl.Phys.* **B250** (1985) 465.

[89] J. Calmet, S. Narison, M. Perrottet, and E. de Rafael, "Higher Order Hadronic Corrections to the Anomalous Magnetic Moment of the Muon," *Phys.Lett.* **B61** (1976) 283.

[90] T. Kinoshita, B. Nizic, and Y. Okamoto, "Hadronic Contributions to the Anomalous Magnetic Moment of the Muon," *Phys.Rev.* **D31** (1985) 2108.

[91] E. de Rafael, "Hadronic contributions to the muon g-2 and low-energy QCD," *Phys.Lett.* **B322** (1994) 239–246, `arXiv:hep-ph/9311316`.

[92] M. Hayakawa, T. Kinoshita, and A. I. Sanda, "Hadronic light by light scattering contribution to muon g-2," *Phys.Rev.* **D54** (1996) 3137–3153, `arXiv:hep-ph/9601310`.

[93] M. B. Einhorn, "On the hadronic contribution to light by light scattering," *Phys.Rev.* **D49** (1994) 1668–1671, `arXiv:hep-ph/9308254 [hep-ph]`.

[94] J. Bijnens, E. Pallante, and J. Prades, "Hadronic light by light contributions to the muon g-2," *Phys.Rev.Lett.* **75** (1995) 1447–1450. [Erratum-ibid. **75** (1995) 3781].

[95] J. Bijnens, E. Pallante, and J. Prades, "Analysis of the hadronic light by light contributions to the muon g-2," *Nucl.Phys.* **B474** (1996) 379–420. [Erratum-ibid. **626** (2002) 410].

[96] K. Melnikov and A. Vainshtein, *Theory of the Muon Anomalous Magnetic Moment*. Springer, NY, (2006).

[97] J. Bijnens, C. Bruno, and E. de Rafael, "Nambu-Jona-Lasinio like models and the low-energy effective action of QCD," *Nucl.Phys.* **B390** (1993) 501–541, `arXiv:hep-ph/9206236 [hep-ph]`.

[98] J. Bijnens, E. de Rafael, and H.-q. Zheng, "Low-energy behavior of two point functions of quark currents," *Z.Phys.* **C62** (1994) 437–454, `arXiv:hep-ph/9306323 [hep-ph]`.

[99] G. 't Hooft, "A Planar Diagram Theory for Strong Interactions," *Nucl.Phys.* **B72** (1974) 461. [Ibid. **75** (1974) 461].

[100] E. Witten, "Baryons in the 1/n Expansion," *Nucl.Phys.* **B160** (1979) 57.

[101] H. Leutwyler, "On the $1/N$-expansion in chiral perturbation theory," *Nucl.Phys.Proc.Suppl.* **64** (1998) 223–231, arXiv:hep-ph/9709408 [hep-ph].

[102] R. Kaiser and H. Leutwyler, "Large N_c in chiral perturbation theory," *Eur.Phys.J.* **C17** (2000) 623–649, arXiv:hep-ph/0007101 [hep-ph].

[103] M. Hayakawa and T. Kinoshita, "Pseudoscalar pole terms in the hadronic light by light scattering contribution to muon g - 2," *Phys.Rev.* **D57** (1998) 465–477. [Erratum-ibid. **66** (2002) 019902].

[104] M. Bando, T. Kugo, and K. Yamawaki, "Nonlinear Realization and Hidden Local Symmetries," *Phys.Rept.* **164** (1988) 217–314.

[105] M. Knecht and A. Nyffeler, "Hadronic light by light corrections to the muon g-2: The Pion pole contribution," *Phys.Rev.* **D65** (2002) 073034, arXiv:hep-ph/0111058.

[106] M. Knecht, A. Nyffeler, M. Perrottet, and E. de Rafael, "Hadronic light by light scattering contribution to the muon g-2: An Effective field theory approach," *Phys.Rev.Lett.* **88** (2002) 071802, arXiv:hep-ph/0111059.

[107] I. R. Blokland, A. Czarnecki, and K. Melnikov, "Pion pole contribution to hadronic light by light scattering and muon anomalous magnetic moment," *Phys.Rev.Lett.* **88** (2002) 071803, arXiv:hep-ph/0112117 [hep-ph].

[108] M. Ramsey-Musolf and M. B. Wise, "Hadronic light by light contribution to muon g-2 in chiral perturbation theory," *Phys.Rev.Lett.* **89** (2002) 041601, arXiv:hep-ph/0201297.

[109] K. Melnikov and A. Vainshtein, "Hadronic light-by-light scattering contribution to the muon anomalous magnetic moment revisited," *Phys.Rev.* **D70** (2004) 113006, arXiv:hep-ph/0312226.

[110] J. Bijnens and J. Prades, "The Hadronic Light-by-Light Contribution to the Muon Anomalous Magnetic Moment: Where do we stand?," *Mod.Phys.Lett.* **A22** (2007) 767–782, arXiv:hep-ph/0702170.

[111] A. Nyffeler, "Hadronic light-by-light scattering in the muon g-2: A New short-distance constraint on pion-exchange," *Phys.Rev.* **D79** (2009) 073012, arXiv:0901.1172 [hep-ph].

[112] J. Prades, E. de Rafael, and A. Vainshtein, "Hadronic Light-by-Light Scattering Contribution to the Muon Anomalous Magnetic Moment," arXiv:0901.0306 [hep-ph].

[113] R. Boughezal and K. Melnikov, "Hadronic light-by-light scattering contribution to the muon magnetic anomaly: constituent quark loops and QCD effects," arXiv:1104.4510 [hep-ph].

[114] T. Goecke, C. S. Fischer, and R. Williams, "Leading-order calculation of hadronic contributions to the muon $g-2$ using the Dyson-Schwinger approach," arXiv:1107.2588 [hep-ph].

[115] G.-C. Cho, K. Hagiwara, Y. Matsumoto, and D. Nomura, "The MSSM confronts the precision electroweak data and the muon $g-2$," arXiv:1104.1769 [hep-ph].

[116] F. Jegerlehner, "Muon $g-2$ update," *Nucl. Phys. Proc. Suppl.* **181-182** (2008) 26–31.

[117] F. Jegerlehner, "Precision measurements of $\sigma_{\rm hadronic}$ for $\alpha_{\rm eff}(E)$ at ILC energies and $(g-2)_\mu$," *Nucl. Phys. Proc. Suppl.* **162** (2006) 22–32, arXiv:hep-ph/0608329.

[118] M. Davier, "The Hadronic contribution to $(g-2)_\mu$," *Nucl.Phys.Proc.Suppl.* **169** (2007) 288–296, arXiv:hep-ph/0701163 [hep-ph].

[119] M. Gell-Mann and F. Low, "Quantum electrodynamics at small distances," *Phys.Rev.* **95** (1954) 1300–1312.

[120] J. S. Schwinger, *Particles, sources, and fields. Vol. 3.* Redwood City, USA: Addison-Wesley, (1989). p.99.

[121] M. Drees and K.-i. Hikasa, "Scalar top production in e^+e^- annihilation," *Phys.Lett.* **B252** (1990) 127–134.

[122] **CMD-2** Collaboration, R. R. Akhmetshin *et al.*, "Study of the Processes $e^+e^- \to \eta\gamma$, $e^+e^- \to \pi^0\gamma \to 3\gamma$ in the c.m. Energy Range 600–1380 MeV at CMD-2," *Phys. Lett.* **B605** (2005) 26–36, arXiv:hep-ex/0409030.

[123] **SND** Collaboration, M. N. Achasov *et al.*, "Experimental study of the $e^+e^- \to \pi^0\gamma$ process in the energy region $\sqrt{s} = 0.60 - 0.97$ GeV," *Phys. Lett.* **B559** (2003) 171–178, arXiv:hep-ex/0302004.

[124] **SND** Collaboration, M. N. Achasov *et al.*, "Experimental study of the processes $e^+e^- \to \phi \to \eta\gamma$, $\pi^0\gamma$ at VEPP-2M," *Eur. Phys. J.* **C12** (2000) 25–33.

[125] **CMD-2, SND** Collaboration, F. Ignatov, "CMD-2 and SND results on $e^+e^- \to$ hadrons cross sections," *Nucl. Phys. Proc. Suppl.* **181-182** (2008) 101–105.

[126] S. Actis *et al.*, "Quest for precision in hadronic cross sections at low energy: Monte Carlo tools vs. experimental data," *Eur. Phys. J.* **C66** (2010) 585–686, arXiv:0912.0749 [hep-ph].

[127] **KLOE** Collaboration, A. Aloisio *et al.*, "Measurement of $\sigma(e^+e^- \to \pi^+\pi^-\gamma)$ and extraction of $\sigma(e^+e^- \to \pi^+\pi^-)$ below 1-GeV with the KLOE detector," *Phys. Lett.* **B606** (2005) 12–24, arXiv:hep-ex/0407048.

[128] K. Hagiwara, R. Liao, A. D. Martin, D. Nomura, and T. Teubner, "$(g-2)_\mu$ and $\alpha(M_Z^2)$ re-evaluated using new precise data," *J. Phys.* **G38** (2011) 085003, arXiv:1105.3149 [hep-ph].

[129] **KLOE** Collaboration, F. Ambrosino *et al.*, "Measurement of $\sigma(e^+e^- \to \pi^+\pi^-)$ from threshold to 0.85 GeV^2 using Initial State Radiation with the KLOE detector," *Phys. Lett.* **B700** (2011) 102–110, arXiv:1006.5313 [hep-ex].

[130] **KLOE** Collaboration, F. Ambrosino *et al.*, "Measurement of $\sigma(e^+e^- \to \pi^+\pi^-\gamma(\gamma))$ and the dipion contribution to the muon anomaly with the KLOE detector," *Phys. Lett.* **B670** (2009) 285–291, arXiv:0809.3950 [hep-ex].

[131] **BABAR** Collaboration, B. Aubert *et al.*, "Precise measurement of the $e^+e^- \to \pi^+\pi^-(\gamma)$ cross section with the Initial State Radiation method at BABAR," *Phys. Rev. Lett.* **103** (2009) 231801, arXiv:0908.3589 [hep-ex].

[132] **CMD-2** Collaboration, R. R. Akhmetshin *et al.*, "Measurement of the $e^+e^- \to \pi^+\pi^-$ cross section with the CMD-2 detector in the 370-520 MeV c.m. energy range," *JETP Lett.* **84** (2006) 413–417, arXiv:hep-ex/0610016.

[133] **CMD-2** Collaboration, R. R. Akhmetshin *et al.*, "High-statistics measurement of the pion form factor in the ρ-meson energy range with the CMD-2 detector," *Phys. Lett.* **B648** (2007) 28–38, arXiv:hep-ex/0610021.

[134] **SND** Collaboration, M. N. Achasov *et al.*, "Update of the $e^+e^{\to}\pi^+\pi^-$ cross section measured by SND detector in the energy region $400 < \sqrt{s} < 1000$ MeV," *J. Exp. Theor. Phys.* **103** (2006) 380–384, arXiv:hep-ex/0605013.

[135] **CMD-2** Collaboration, V. M. Aulchenko *et al.*, "Measurement of the pion form factor in the energy range $1.04 - 1.38$ GeV with the CMD-2 detector," *JETP Lett.* **82** (2005) 743–747, arXiv:hep-ex/0603021.

[136] **OLYA** Collaboration, I. B. Vasserman *et al.*, "Measurement of pion form-factor in $e^+e^- \to \pi^+\pi^-$ reaction near production threshold. (In Russian)," *Sov. J. Nucl. Phys.* **30** (1979) 519.

[137] **OLYA** Collaboration, I. B. Vasserman *et al.*, "Pion form-factor measurement in the reaction $e^+e^- \to \pi^+\pi^-$ for energies within the range from 0.4 GeV tO 0.46 GeV," *Yad. Fiz.* **33** (1981) 709–714.

[138] **NA7** Collaboration, S. R. Amendolia *et al.*, "Measurement of the pion form-factor in the timelike region for Q^2 values between .1 GeV/c^2 and .18 GeV/c^2," *Phys. Lett.* **B138** (1984) 454.

[139] **CMD, OLYA** Collaboration, L. M. Barkov *et al.*, "Electromagnetic Pion Form-Factor in the Timelike Region," *Nucl. Phys.* **B256** (1985) 365–384.

[140] **DM1** Collaboration, A. Quenzer *et al.*, "Pion Form-Factor from 480 MeV to 1100 MeV," *Phys. Lett.* **B76** (1978) 512–516.

[141] **DM2** Collaboration, D. Bisello *et al.*, "The pion electromagnetic form-factor in the timelike energy range 1.35 GeV $\leq \sqrt{s} \leq$ 2.4 GeV," *Phys. Lett.* **B220** (1989) 321.

[142] **BCF** Collaboration, D. Bollini *et al.*, "The Pion Electromagnetic Form-Factor in the Timelike Range 1.44 GeV^2 – 9.0 GeV^2," *Nuovo Cim. Lett.* **14** (1975) 418.

[143] **MEA** Collaboration, B. Esposito *et al.*, "Momentum Analysis of Kaon and Pion Pairs Produced from Timelike Photons at 1.6-GeV Energy," *Phys. Lett.* **B67** (1977) 239–242.

[144] **MEA** Collaboration, B. Esposito *et al.*, "Measurements of the em timelike form-factors for kaon and pion at $\sqrt{s} = 1.5$ GeV," *Lett. Nuovo Cim.* **28** (1980) 337–342.

[145] **BCF** Collaboration, M. Bernardini *et al.*, "The time-like electromagnetic form factors of the charged pseudoscalar mesons from 1.44 GeV^2 to 9.0 GeV^2," *Phys. Lett.* **B46** (1973) 261–264.

[146] **CMD, ND, ARGUS** Collaboration, S. I. Dolinsky *et al.*, "Summary of experiments with the neutral detector at the e^+e^- storage ring VEPP-2M," *Phys. Rept.* **202** (1991) 99–170.

[147] **OLYA** Collaboration, A. D. Bukin *et al.*, "Pion Form-Factor Measurement by $e^+e^- \to \pi^+\pi^-$ in the Energy Range $2E$ from 0.78 GeV Up to 1.34 GeV," *Phys. Lett.* **B73** (1978) 226–228.

[148] **OLYA** Collaboration, I. A. Koop *Preprint, INP-79-67* (1979) .

[149] **ORSAY-ACO** Collaboration, G. Cosme *et al.*, "Measurement of the electron-positron annihilation cross-section into $\pi^+\pi^-$ at the energies 915, 990 and 1076 MeV,".

[150] **CMD-2** Collaboration, R. R. Akhmetshin *et al.*, "Reanalysis of Hadronic Cross Section Measurements at CMD-2," *Phys. Lett.* **B578** (2004) 285–289, arXiv:hep-ex/0308008.

[151] **CMD-2** Collaboration, R. R. Akhmetshin *et al.*, "Study of $\phi \to \pi^+\pi^-\pi^0$ with CMD-2 detector," *Phys. Lett.* **B642** (2006) 203–209.

[152] **BABAR** Collaboration, B. Aubert *et al.*, "Study of $e^+e^- \to \pi^+\pi - \pi^0$ process using initial state radiation with BABAR," *Phys. Rev.* **D70** (2004) 072004, arXiv:hep-ex/0408078.

[153] **DM1** Collaboration, A. Cordier *et al.*, "Cross-section of the reaction $e^+e^- \to \pi^+\pi^-\pi^0$ for center-of-mass energies from 750 MeV to 1100 MeV," *Nucl. Phys.* **B172** (1980) 13.

[154] **DM2** Collaboration, A. Antonelli *et al.*, "Measurement of the $e^+e^- \to \pi^+\pi^-\pi^0$ and $e^+e^- \to \omega\pi^+\pi^-$ reactions in the energy interval 1350-MeV - 2400-MeV," *Z.Phys.* **C56** (1992) 15–20.

[155] **CMD-2** Collaboration, R. R. Akhmetshin *et al.*, "Measurement of ϕ meson parameters with CMD-2 detector at VEPP-2M collider," *Phys. Lett.* **B364** (1995) 199–206.

[156] **SND** Collaboration, M. N. Achasov *et al.*, "Study of the process $e^+e^- \to \pi^+\pi^-\pi^0$ in the energy region $\sqrt{s}$ from 0.98 to 1.38 GeV.," *Phys. Rev.* **D66** (2002) 032001, arXiv:hep-ex/0201040.

[157] **CMD** Collaboration, L. M. Barkov *et al. Preprint, INP-89-15* (1989) .

[158] **SND** Collaboration, M. N. Achasov *et al.*, "Study of the process $e^+e^- \to \pi^+\pi^-\pi^0$ in the energy region $\sqrt{s}$ below 0.98 GeV," *Phys. Rev.* **D68** (2003) 052006, arXiv:hep-ex/0305049.

[159] **BABAR** Collaboration, B. Aubert *et al.*, "The $e^+e^- \to \pi^+\pi^-\pi^+\pi^-$, $K^+K^-\pi^+\pi^-$, and $K^+K^-K^+K^-$ cross sections at center-of-mass energies 0.5-GeV to 4.5-GeV measured with initial-state radiation," *Phys. Rev.* **D71** (2005) 052001, arXiv:hep-ex/0502025.

[160] **M3N** Collaboration, C. Paulot *Thesis* (1979) . Preprint, LAL-79/14.

[161] **CMD** Collaboration, L. M. Barkov *et al.*, "Study of multiple pion production reactions at the VEPP-2M storage ring using a cryogenic magnetic detector," *Sov. J. Nucl. Phys.* **47** (1988) 248–252.

[162] **DM1** Collaboration, A. Cordier *et al.*, "Study of the $e^+e^- \to \pi^+\pi^-\pi^+\pi^-$ reaction in the 1.4 GeV to 2.18 GeV energy range," *Phys. Lett.* **B109** (1982) 129.

[163] **DM1** Collaboration, A. Cordier *et al.*, "Cross-section of the reaction $e^+e^- \to \pi^+\pi^-\pi^+\pi^-$ for center-of-mass energies from 890 MeV to 1100 MeV," *Phys. Lett.* **B81** (1979) 389.

[164] **DM2** Collaboration, D. Bisello *et al.*, "DM2 results on e^+e^- annihilation into multi - hadrons in the $1350 - 2400$ MeV energy range,". Contributed paper to Int. Conf. on High Energy Physics, Singapore, Aug 2-8, 1990, see also LAL-90/35, Orsay (1990).

[165] **OLYA** Collaboration, L. M. Kurdadze *et al.*, "Study of $e^+e^- \to \pi^+\pi^-\pi^+\pi^-$ reaction at (2 E) up to 1.4 GeV," *JETP Lett.* **47** (1988) 512–515.

[166] $\gamma\gamma 2$ Collaboration, C. Bacci *et al.*, "Measurement of the $e^+e^- \to \pi^+\pi^-\pi^+\pi^-$ cross- section in the ρ' (1600) energy region," *Phys. Lett.* **B95** (1980) 139.

[167] **CMD-2** Collaboration, R. R. Akhmetshin *et al.*, "Total Cross Section of the Process $e^+e^- \to \pi^+\pi^-\pi^+\pi^-$ in the C.M.Energy Range $980 - 1380$ MeV," *Phys. Lett.* **B595** (2004) 101–108, `arXiv:hep-ex/0404019`.

[168] **SND** Collaboration, M. N. Achasov *et al.*, "Analysis of $e^+e^- \to \pi^+\pi^-\pi^+\pi^-$ and $e^+e^- \to \pi^+\pi^-\pi^0\pi^0$ processes in the energy range of $\sqrt{s} = 0.98 - 1.38$ GeV in experiments with a spherical neutral detector," *J. Exp. Theor. Phys.* **96** (2003) 789–800.

[169] **CMD-2** Collaboration, R. R. Akhmetshin *et al.*, "Cross section of the reaction $e^+e^- \to \pi^+\pi^-\pi^+\pi^-$ below 1 GeV at CMD-2," *Phys. Lett.* **B475** (2000) 190–197, `arXiv:hep-ex/9912020`.

[170] **CMD-2** Collaboration, R. R. Akhmetshin *et al.*, "Observation of the $\phi \to \pi^+\pi^-\pi^+\pi^-$ Decay," *Phys. Lett.* **B491** (2000) 81–89, `arXiv:hep-ex/0008019`.

[171] **ORSAY-ACO** Collaboration, G. Cosme *et al.*, "Multi-Pion Production Below 1.1-GeV by e^+e^- Annihilation," *Phys. Lett.* **B63** (1976) 349–351.

[172] **OLYA** Collaboration, L. M. Kurdadze *et al.*, "Study of the reaction $e^+e^- \to \pi^+\pi^-\pi^0\pi^0$ at (2 E) up to 1.4 GeV," *JETP Lett.* **43** (1986) 643–645.

[173] **CMD-2** Collaboration, R. R. Akhmetshin *et al.*, "$a_1(1260)\pi$ dominance in the process $e^+e^- \to 4\pi$ at energies $1.05 - 1.38$ GeV," *Phys. Lett.* **B466** (1999) 392–402, arXiv:hep-ex/9904024.

[174] $\gamma\gamma 2$ Collaboration, C. Bacci *et al.*, "Measurement of hadronic exclusive cross-sections in e^+e^- annihilation from 1.42 GeV to 2.20 GeV," *Nucl. Phys.* **B184** (1981) 31.

[175] **MEA** Collaboration, B. Esposito *et al.*, "Measurement on $\pi^+\pi^-\pi^0\pi^0$, $\pi^+\pi^-\pi^+\pi^-\pi^0$, $\pi^+\pi^-\pi^+\pi^-\pi^0\pi^0$, $\pi^+\pi^-\pi^+\pi^-\pi^+\pi^-$ production cross-sections in e^+e^- annihilation at $1.45 - 1.80$ GeV center-of-mass energy," *Lett. Nuovo Cim.* **31** (1981) 445–452.

[176] **BABAR** Collaboration, B. Aubert *et al.*, "The $e^+e^- \to 2(\pi^+\pi^-)\pi^0$, $2(\pi^+\pi^-)\eta$, $K^+K^-\pi^+\pi^-\pi^0$ and $K^+K^-\pi^+\pi^-\eta$ Cross Sections Measured with Initial-State Radiation," *Phys. Rev.* **D76** (2007) 092005, arXiv:0708.2461 [hep-ex].

[177] **DM1** Collaboration, A. Cordier *et al.*, "Observation of a new isoscalar vector meson in $e^+e^- \to \omega\pi^+\pi^-$ annihilation at 1.65 GeV," *Phys. Lett.* **B106** (1981) 155.

[178] **BABAR** Collaboration, B. Aubert *et al.*, "The $e^+e^- \to 3(\pi^+\pi^-)$, $2(\pi^+\pi^-\pi^0)$ and $K^+K^-2(\pi^+\pi^-)$ cross sections at center-of-mass energies from production threshold to 4.5 GeV measured with initial-state radiation," *Phys. Rev.* **D73** (2006) 052003, arXiv:hep-ex/0602006.

[179] **DM2** Collaboration, M. Schioppa *Thesis, Universita di Roma 'La Sapienza'* (1986) .

[180] **DM1** Collaboration, D. Bisello *et al.*, "Study of the reaction $e^+e^- \to 3\pi^+3\pi^-$ in the total energy range 1400 MeV to 2180 MeV," *Phys. Lett.* **B107** (1981) 145.

[181] **CMD-2** Collaboration, R. R. Akhmetshin *et al.*, "Measurement of $e^+e^- \to \phi \to K^+K^-$ cross section with the CMD-2 detector at VEPP-2M Collider," *Phys. Lett.* **B669** (2008) 217–222, arXiv:0804.0178 [hep-ex].

[182] **SND** Collaboration, M. N. Achasov *et al.*, "Measurement of the $e^+e^- \to K^+K^-$ process cross-section in the energy range $\sqrt{s} = 1.04 - 1.38$ GeV with the SND detector in the experiment at VEPP-2M e^+e^- collider," *Phys. Rev.* **D76** (2007) 072012, arXiv:0707.2279 [hep-ex].

[183] **DM1** Collaboration, B. Delcourt *et al.*, "Study of the reaction $e^+e^- \to K^+K^-$ in the total energy range 1400 MeV to 2060 MeV," *Phys. Lett.* **B99** (1981) 257.

[184] **DM2** Collaboration, D. Bisello *et al.*, "Study of the reaction $e^+e^- \to K^+K^-$ in the energy range $1350 \leqq \sqrt{s} \leqq 2400$ MeV," *Z. Phys.* **C39** (1988) 13.

[185] **DM2** Collaboration, J. E. Augustin *et al.*, "A study of e^+e^- annihilation in the 1400 MeV to 2250 MeV energy range with the magnetic detector DM2 at DCI,". Contributed to Int. Europhysics Conf. on High Energy Physics, Brighton, England, Jul 20-27, 1983.

[186] **OLYA** Collaboration, P. M. Ivanov *et al.*, "Measurement of the charged kaon form-factor in the energy range 1.0 GeV to 1.4 GeV," *Phys. Lett.* **B107** (1981) 297–300.

[187] **SND** Collaboration, M. N. Achasov *et al.*, "Measurements of the parameters of the $\phi(1020)$ resonance through studies of the processes $e^+e^- \to K^+K^-$, K_SK_L, and $\pi^+\pi^-\pi^0$," *Phys. Rev.* **D63** (2001) 072002.

[188] **SND** Collaboration, M. N. Achasov *et al.*, "Experimental study of the reaction $e^+e^- \to K_SK_L$ in the energy range $\sqrt{s} = 1.04 - 1.38$ GeV," *J. Exp. Theor. Phys.* **103** (2006) 720–727, `arXiv:hep-ex/0606057`.

[189] **DM1** Collaboration, F. Mane *et al.*, "Study of the reaction $e^+e^- \to K^0_SK^0_L$ in the total energy range $1.4 - 2.18$ GeV and interpretation of the K^+ and K^0 form-factors," *Phys. Lett.* **B99** (1981) 261.

[190] **CMD-2** Collaboration, R. R. Akhmetshin *et al.*, "Study of the Process $e^+e^- \to K^0_LK^0_S$ in the C.M.Energy Range $1.05 - 1.38$ GeV with CMD-2," *Phys. Lett.* **B551** (2003) 27–34, `arXiv:hep-ex/0211004`.

[191] **DM1** Collaboration, F. Mane *et al.*, "Study of $e^+e^- \to K^0_SK^\pm\pi^\mp$ in the $1.4 - 2.18$ GeV energy range: a new observation of an isoscalar vector meson ϕ' (1.65 GeV)," *Phys. Lett.* **B112** (1982) 178.

[192] **DM2** Collaboration, D. Bisello *et al.*, "e^+e^- annihilation into multihadrons in the $1350 - 2400$ MeV energy range," *Nucl. Phys. Proc. Suppl.* **21** (1991) 111–117. Preprint, LAL-90/71, Orsay.

[193] **DM2** Collaboration, D. Bisello *et al.*, "Observation of an isoscalar vector meson at $\simeq 1650$ MeV/c^2 in the $e^+e^- \to K\bar{K}\pi$ reaction," *Z. Phys.* **C52** (1991) 227–230.

[194] **BABAR** Collaboration, B. Aubert *et al.*, "Measurements of $e^+e^- \to K^+K^-\eta$, $K^+K^-\pi^0$ and $K^0_SK^\pm\pi^\mp$ cross-sections using initial state radiation events," *Phys. Rev.* **D77** (2008) 092002, `arXiv:0710.4451 [hep-ex]`.

[195] **BABAR** Collaboration, J. P. Lees *et al.*, "Cross Sections for the Reactions $e^+e^- \to K^+K^-\pi^+\pi^-$, $K^+K^-\pi^0\pi^0$, and $K^+K^-K^+K^-$ Measured Using Initial-State Radiation," arXiv:1103.3001 [hep-ex].

[196] **BABAR** Collaboration, B. Aubert *et al.*, "The $e^+e^- \to K^+K^-\pi^+\pi^-$, $K^+K^-\pi^0\pi^0$ and $K^+K^-K^+K^-$ Cross Sections Measured with Initial-State Radiation," *Phys. Rev.* **D76** (2007) 012008, arXiv:0704.0630 [hep-ex].

[197] **DM1** Collaboration, A. Cordier *et al.*, "Study of the $e^+e^- \to \pi^+\pi^-k^+k^-$ reaction from $1.4 - 2.18$ GeV," *Phys. Lett.* **B110** (1982) 335.

[198] **SND** Collaboration, M. N. Achasov *et al.*, "Reanalysis of the $e^+e^- \to \eta\gamma$ reaction cross section," *Phys. Rev.* **D76** (2007) 077101, arXiv:0709.1007 [hep-ex].

[199] **SND** Collaboration, M. N. Achasov *et al.*, "First physical results from SND detector at VEPP-2M," *Preprint, BINP-97-78* (1997) , arXiv:hep-ex/9710017.

[200] **CMD-2** Collaboration, R. R. Akhmetshin *et al.*, "Study of the radiative decay $\phi \to \eta\gamma$ with CMD-2 detector," *Phys. Lett.* **B460** (1999) 242–247, arXiv:hep-ex/9907003.

[201] **CMD-2** Collaboration, R. R. Akhmetshin *et al.*, "Study of the Process $e^+e^- \to \eta\gamma$ in c.m. Energy Range $600 - 1380$ MeV at CMD-2," *Phys. Lett.* **B509** (2001) 217–226, arXiv:hep-ex/0103043.

[202] **SND** Collaboration, M. N. Achasov *et al.*, "Study of the $e^+e^- \to \eta\gamma$ process with SND detector at the VEPP-2M e+ e- collider," *Phys. Rev.* **D74** (2006) 014016, arXiv:hep-ex/0605109.

[203] **DM2** Collaboration, A. Antonelli *et al.*, "MEASUREMENT OF THE REACTION $e^+e^- \to \eta\pi^+\pi^-$ IN THE CENTER-OF-MASS ENERGY INTERVAL 1350 TO 2400 MeV," *Phys. Lett.* **B212** (1988) 133.

[204] **CMD-2** Collaboration, R. R. Akhmetshin *et al.*, "Study of the process $e^+e^- \to \pi^+\pi^-\pi^+\pi^-\pi^0$ with CMD-2 detector," *Phys. Lett.* **B489** (2000) 125–130, arXiv:hep-ex/0009013.

[205] **KLOE** Collaboration, F. Ambrosino *et al.*, "Study of the process $e^+e^- \to \omega\pi^0$ in the ϕ-meson mass region with the KLOE detector," *Phys. Lett.* **B669** (2008) 223–228, arXiv:0807.4909 [hep-ex].

[206] **SND** Collaboration, M. N. Achasov *et al.*, "The process $e^+e^- \to \omega\pi^0 \to \pi^0\pi^0\gamma$ up to 1.4 GeV," *Phys. Lett.* **B486** (2000) 29–34, arXiv:hep-ex/0005032.

[207] **ND** Collaboration, S. I. Dolinsky *et al.*, "The reaction $e^+e^- \to \omega\pi^0$ in the center-of-mass energy range from 1.0 to 1.4 GeV," *Phys. Lett.* **B174** (1986) 453–457.

[208] **SND** Collaboration, M. N. Achasov *et al.*, "Investigation of the $e^+e^- \to \omega\pi^0 \to \pi^0\pi^0\gamma$ reaction in the energy domain near the ϕ-meson," *Nucl. Phys.* **B569** (2000) 158–182, arXiv:hep-ex/9907026.

[209] **CMD-2** Collaboration, R. R. Akhmetshin *et al.*, "Study of the Process $e^+e^- \to \omega\pi^0 \to \pi^0\pi^0\gamma$ in c.m. Energy Range 920–1380 MeV at CMD-2," *Phys. Lett.* **B562** (2003) 173–181, arXiv:hep-ex/0304009.

[210] **FENICE** Collaboration, A. Antonelli *et al.*, "The first measurement of the neutron electromagnetic form factors in the timelike region," *Nucl. Phys.* **B517** (1998) 3–35.

[211] **FENICE** Collaboration, A. Antonelli *et al.*, "Measurement of the electromagnetic form-factor of the proton in the timelike region," *Phys. Lett.* **B334** (1994) 431–434.

[212] **DM1** Collaboration, B. Delcourt *et al.*, "Study of the reaction $e^+e^- \to p\bar{p}$ in the total energy range $1925 - 2180$ MeV," *Phys. Lett.* **B86** (1979) 395.

[213] **DM2** Collaboration, D. Bisello *et al.*, "A measurement of $e^+e^- \to \bar{p}p$ for $(1975 \leq \sqrt{s} \leq 2250)$ MeV," *Nucl. Phys.* **B224** (1983) 379.

[214] **DM2** Collaboration, D. Bisello *et al.*, "Baryon pair production in e^+e^- annihilation at $\sqrt{s} = 2.4$ GeV," *Z. Phys.* **C48** (1990) 23–28.

[215] **BABAR** Collaboration, B. Aubert *et al.*, "A Study of $e^+e^- \to p\bar{p}$ using initial state radiation with BABAR," *Phys. Rev.* **D73** (2006) 012005, arXiv:hep-ex/0512023.

[216] **FENICE** Collaboration, A. Antonelli *et al.*, "First measurement of the neutron electromagnetic form- factor in the timelike region," *Phys. Lett.* **B313** (1993) 283–287.

[217] $\gamma\gamma 2$ Collaboration, C. Bacci *et al.*, "Total Cross-Section for Hadronic Production by e^+e^- Annihilation in the Total Center-Of-Mass Energy Range $1.42 - 3.04$ GeV," *Phys. Lett.* **B86** (1979) 234.

[218] **MEA** Collaboration, B. Esposito *et al.*, "Hadronic cross-section in e^+e^- annihilation from $1.45 - 1.80$ GeV," *Lett. Nuovo Cim.* **30** (1981) 65–71.

[219] **M3N** Collaboration, G. Cosme *et al.*, "Hadronic cross-sections study in e^+e^- collisions from $1.350 - 2.125$ GeV," *Nucl. Phys.* **B152** (1979) 215.

[220] **BARYON-ANTIBARYON** Collaboration, M. Ambrosio *et al.*, "Total cross-section for hadron production by electron-positron annihilation at ADONE," *Phys. Lett.* **B91** (1980) 155.

[221] **BES** Collaboration, M. Ablikim *et al.*, "R value measurements for e^+e^- annihilation at 2.60, 3.07 and 3.65 GeV," *Phys. Lett.* **B677** (2009) 239–245, arXiv:0903.0900 [hep-ex].

[222] **BES** Collaboration, M. Ablikim *et al.*, "Measurements of the continuum R_{uds} and R values in e^+e^- annihilation in the energy region between 3.650 and 3.872 GeV," *Phys. Rev. Lett.* **97** (2006) 262001, arXiv:hep-ex/0612054.

[223] **CLEO** Collaboration, D. Besson *et al.*, "Measurement of the Total Hadronic Cross Section in e^+e^- Annihilations below 10.56 GeV," *Phys. Rev.* **D76** (2007) 072008, arXiv:0706.2813 [hep-ex].

[224] **BES** Collaboration, M. Ablikim *et al.*, "Measurements of the cross sections for $e^+e^- \to$ hadrons at 3.650, 3.6648, 3.773 GeV and the branching fraction for $\psi(3770) \to$ non-$D\bar{D}$," *Phys. Lett.* **B641** (2006) 145–155, arXiv:hep-ex/0605105.

[225] **BES** Collaboration, J. Z. Bai *et al.*, "Measurements of the Cross Section for $e^+e^- \to$ hadrons at Center-of-Mass Energies from 2 to 5 GeV," *Phys. Rev. Lett.* **88** (2002) 101802, arXiv:hep-ex/0102003.

[226] **Crystal Ball** Collaboration, A. Osterheld *et al.*, "Measurements of total hadronic and inclusive D^* cross sections in e^+e^- annihilations between 3.87 and 4.5 GeV,". SLAC-PUB-4160, (1986).

[227] **Crystal Ball** Collaboration, C. Edwards *et al.*, "Hadron production in e^+e^- annihilation from $\sqrt{s} = 5$ to7.4 GeV,". SLAC-PUB-5160, (1990).

[228] **Crystal Ball** Collaboration, Z. Jakubowski *et al.*, "Determination of Γ_{ee} of the $\Upsilon(1S)$ and $\Upsilon(2S)$ resonances and measurement of R at $W = 9.39$ GeV," *Z. Phys.* **C40** (1988) 49.

[229] **LENA** Collaboration, B. Niczyporuk *et al.*, "Measurement of R in e^+e^- annihilation for $\sqrt{s}$ between 7.4 and 9.4 GeV," *Zeit. Phys.* **C15** (1982) 299.

[230] **MD-1** Collaboration, A. E. Blinov *et al.*, "The Measurement of R in e^+e^- annihilation at center-of- mass energies between 7.2 and 10.34 GeV," *Z. Phys.* **C70** (1996) 31–38.

[231] **DASP** Collaboration, H. Albrecht *et al.*, "The hadronic cross-section of electron-positron annihilation at 9.5 GeV and the Υ and Υ' resonance parameters," *Phys. Lett.* **B116** (1982) 383.

[232] **CLEO** Collaboration, R. Ammar *et al.*, "Measurement of the total cross section for $e^+e^- \to$ hadrons at $\sqrt{s} = 10.52$ GeV," *Phys. Rev.* **D57** (1998) 1350–1358, arXiv:hep-ex/9707018.

[233] **CUSB** Collaboration, E. Rice *et al.*, "Search for structure in $\sigma(e^+e^- \to \text{hadrons})$ between $\sqrt{s} = 10.34$ and 11.6 GeV," *Phys. Rev. Lett.* **48** (1982) 906–910.

[234] **DHHM** Collaboration, P. Bock *et al.*, "Total cross-section for hadron production by e^+e^- annihilation between 9.4 and 9.5 GeV," *Z. Phys.* **C6** (1980) 125.

[235] **BES** Collaboration, J. Z. Bai *et al.*, "Measurement of the Total Cross Section for Hadronic Production by e^+e^- Annihilation at Energies between $2.6 - 5$ Gev," *Phys. Rev. Lett.* **84** (2000) 594–597, arXiv:hep-ex/9908046.

[236] **BABAR** Collaboration, B. Aubert *et al.*, "Measurement of the $e^+e^- \to b\bar{b}$ cross section between $\sqrt{s} = 10.54$ and 11.20 GeV," *Phys. Rev. Lett.* **102** (2009) 012001, arXiv:0809.4120 [hep-ex].

[237] A. Pais, "The many π-meson problem," *Annals Phys.* **9** (1960) 548–602.

[238] **DM1** Collaboration, F. Mane *Thesis, Université de Paris-Sud* (1982) . Preprint, LAL-82/36.

[239] N. Achasov and A. Kiselev, "Contribution to muon g-2 from the pi0 gamma and eta gamma intermediate states in the vacuum polarization," *Phys.Rev.* **D65** (2002) 097302, arXiv:hep-ph/0202047.

[240] G. Colangelo, M. Finkemeier, and R. Urech, "Tau decays and chiral perturbation theory," *Phys.Rev.* **D54** (1996) 4403–4418, arXiv:hep-ph/9604279 [hep-ph].

[241] **NA7** Collaboration, S. Amendolia *et al.*, "A measurement of the space-like pion electromagnetic form factor," *Nucl.Phys.* **B277** (1986) 168.

[242] E. Kuraev and Z. Silagadze, "Once more about the $\omega \to 3\pi$ contact term," *Phys.Atom.Nucl.* **58** (1995) 1589–1596, arXiv:hep-ph/9502406 [hep-ph].

[243] A. Ahmedov, G. Fedotovich, E. Kuraev, and Z. Silagadze, "Near threshold radiative 3π production in e^+e^- annihilation," *JHEP* **0209** (2002) 008, arXiv:hep-ph/0201157 [hep-ph].

[244] T. Teubner, K. Hagiwara, R. Liao, A. Martin, and D. Nomura, "Update of $g-2$ of the muon and $\Delta\alpha$," *Chinese Phys.* **C34** (2010) 728, arXiv:1001.5401 [hep-ph].

[245] M. A. Shifman, A. I. Vainshtein, and V. I. Zakharov, "QCD and Resonance Physics. Sum Rules," *Nucl. Phys.* **B147** (1979) 385–447.

[246] M. A. Shifman, A. I. Vainshtein, and V. I. Zakharov, "QCD and Resonance Physics: Applications," *Nucl. Phys.* **B147** (1979) 448–518.

[247] M. A. Shifman, A. I. Vainshtein, and V. I. Zakharov, "QCD and Resonance Physics. The $\rho - \omega$ Mixing," *Nucl. Phys.* **B147** (1979) 519.

[248] L. R. Surguladze and M. A. Samuel, "Total hadronic cross-section in e^+e^- annihilation at the four loop level of perturbative QCD," *Phys. Rev. Lett.* **66** (1991) 560–563.

[249] P. A. Baikov, K. G. Chetyrkin, and J. H. Kuhn, "Order α_s^4 QCD Corrections to Z and τ Decays," *Phys. Rev. Lett.* **101** (2008) 012002, `arXiv:0801.1821 [hep-ph]`.

[250] M. Davier and A. Hocker, "Improved determination of $\alpha(M_Z^2)$ and the anomalous magnetic moment of the muon," *Phys. Lett.* **B419** (1998) 419–431, `arXiv:hep-ph/9711308`.

[251] T. van Ritbergen, J. A. M. Vermaseren, and S. A. Larin, "The four-loop beta function in quantum chromodynamics," *Phys. Lett.* **B400** (1997) 379–384, `arXiv:hep-ph/9701390`.

[252] R. V. Harlander and M. Steinhauser, "rhad: A program for the evaluation of the hadronic R-ratio in the perturbative regime of QCD," *Comput. Phys. Commun.* **153** (2003) 244–274, `arXiv:hep-ph/0212294`.

[253] K. Hagiwara, R. Liao, A. D. Martin, D. Nomura, and T. Teubner. In preparation.

[254] M. Steinhauser, "Leptonic contribution to the effective electromagnetic coupling constant up to three loops," *Phys.Lett.* **B429** (1998) 158–161, `arXiv:hep-ph/9803313 [hep-ph]`.

[255] K. Chetyrkin, J. H. Kuhn, and M. Steinhauser, "Heavy quark vacuum polarization to three loops," *Phys.Lett.* **B371** (1996) 93–98, `arXiv:hep-ph/9511430 [hep-ph]`.

[256] K. Chetyrkin, J. H. Kuhn, and M. Steinhauser, "Three loop polarization function and $O(\alpha_s^2)$ corrections to the production of heavy quarks," *Nucl.Phys.* **B482** (1996) 213–240, `arXiv:hep-ph/9606230 [hep-ph]`.

[257] K. Chetyrkin, J. H. Kuhn, and M. Steinhauser, "Heavy quark current correlators to $\mathcal{O}(\alpha_s^2)$," *Nucl.Phys.* **B505** (1997) 40–64, arXiv:hep-ph/9705254 [hep-ph].

[258] J. H. Kuhn and M. Steinhauser, "A Theory driven analysis of the effective QED coupling at M_Z," *Phys.Lett.* **B437** (1998) 425–431, arXiv:hep-ph/9802241 [hep-ph].

[259] A. D. Martin, J. Outhwaite, and M. Ryskin, "A New determination of the QED coupling $\alpha(M_Z^2)$ lets the Higgs off the hook," *Phys.Lett.* **B492** (2000) 69–73, arXiv:hep-ph/0008078 [hep-ph].

[260] J. de Troconiz and F. Yndurain, "The Hadronic contributions to the anomalous magnetic moment of the muon," *Phys.Rev.* **D71** (2005) 073008, arXiv:hep-ph/0402285 [hep-ph].

[261] H. Burkhardt and B. Pietrzyk, "Low energy hadronic contribution to the QED vacuum polarization," *Phys.Rev.* **D72** (2005) 057501, arXiv:hep-ph/0506323 [hep-ph].

[262] F. Jegerlehner, "The Running fine structure constant $\alpha(E)$ via the Adler function," *Nucl.Phys.Proc.Suppl.* **181-182** (2008) 135–140, arXiv:0807.4206 [hep-ph].

[263] F. Jegerlehner. Talk presented at the *LC10 Workshop, INFN/LNF Frascati, Italy, December 2010*.

[264] M. Grunewald. *Private communications*. For a description of the procedure used see: **ALEPH** Collaboration, arXiv:1012.2367 [hep-ex].

[265] For latest results of the 'LEP Electroweak Working Group' (LEP EWWG) see http://lepewwg.web.cern.ch/LEPEWWG/.

[266] K. G. Chetyrkin *et al.*, "Charm and Bottom Quark Masses: an Update," *Phys. Rev.* **D80** (2009) 074010, arXiv:0907.2110 [hep-ph].

[267] K. G. Chetyrkin, J. H. Kuhn, and T. Teubner, "Extracting α_s from electron positron annihilation around 10 GeV," *Phys. Rev.* **D56** (1997) 3011–3018, arXiv:hep-ph/9609411.

[268] S. Jadach and B. Ward, "YFS2: The second order Monte Carlo for fermion pair production at LEP/SLC with the initial state radiation of two hard and multiple soft photons," *Comput.Phys.Commun.* **56** (1990) 351–384.

[269] P. J. Mohr, B. N. Taylor, and D. B. Newell, "CODATA Recommended Values of the Fundamental Physical Constants: 2006," *Rev.Mod.Phys.* **80** (2008) 633–730, arXiv:0801.0028 [physics.atom-ph].

[270] B. Roberts, "Status of the Fermilab Muon (g-2) Experiment," *Chin.Phys.* **C34** (2010) 741–744, arXiv:1001.2898 [hep-ex].

[271] **Particle Data Group** Collaboration, C. Amsler *et al.*, "Review of Particle Physics," *Phys.Lett.* **B667** (2008) 1–1340.

[272] T. Teubner, K. Hagiwara, R. Liao, A. Martin, and D. Nomura, "$g-2$ of the muon and $\Delta\alpha$ re-evaluated," *Nucl.Phys.Proc.Suppl.* **218** (2011) 225–230.

[273] T. Teubner, K. Hagiwara, R. Liao, A. Martin, and D. Nomura, "$(g-2)_\mu$ and $\Delta\alpha$: Recent developments and status report," *AIP Conf.Proc.* **1343** (2011) 340–342.

[274] M. Passera, W. Marciano, and A. Sirlin, "The Muon $g-2$ and the bounds on the Higgs boson mass," *Phys.Rev.* **D78** (2008) 013009, arXiv:0804.1142 [hep-ph].

[275] M. Passera, W. Marciano, and A. Sirlin, "The muon $g-2$ discrepancy: new physics or a relatively light Higgs?," arXiv:1001.4528 [hep-ph].

[276] E. P. Solodov, "First results from the CMD3 Detector at the VEPP2000 Collider," arXiv:1108.6174 [hep-ex].

[277] F. Ambrosino, F. Anulli, D. Babusci, S. Bianco, C. Bini, *et al.*, "Prospects for e^+e^- physics at Frascati between the ϕ and the ψ," *Eur.Phys.J.* **C50** (2007) 729–768, arXiv:hep-ex/0603056 [hep-ex].

[278] R. Carey, K. Lynch, J. Miller, B. Roberts, W. Morse, *et al.*, "The New $(g-2)$ Experiment: A proposal to measure the muon anomalous magnetic moment to ± 0.14 ppm precision,". Spokespersons: David W. Hertzog, B. Lee Roberts.

[279] **J-PARC New g-2/EDM experiment** Collaboration, H. Iinuma, "New approach to the muon $g-2$ and EDM experiment at J-PARC," *J.Phys.Conf.Ser.* **295** (2011) 012032.

[280] A. A. Almasy, K. Schilcher, and H. Spiesberger, "Determination of QCD condensates from tau-decay data," *Eur. Phys. J.* **C55** (2008) 237–248, arXiv:0802.0980 [hep-ph].